Title
Probing Buried and Exposed Interfaces with Submolecular Precision

Author
Thomas, John Christopher

Publication Date
2015

Peer reviewed|Thesis/dissertation

UNIVERSITY OF CALIFORNIA

Los Angeles

Probing Buried and Exposed Interfaces with Submolecular Precision

A dissertation submitted in partial satisfaction of the

requirements for the degree Doctor of Philosophy

in Chemistry

by

John Christopher Thomas, Jr.

2015

ABSTRACT OF THE DISSERTATION

Probing Buried and Exposed Interfaces with Submolecular Precision

by

John Christopher Thomas, Jr.

Doctor of Philosophy in Chemistry

University of California, Los Angeles, 2014

Professor Paul S. Weiss, Chair

The chemistry of nanoscale materials and self-assembled monolayers are largely determined by interfacial properties, structural dimensionality, bonding and lattice structures, and defect types and densities. Bottom-up design strategies differ from prototypical top-down nanofabrication approaches in that the aim is to control and to place single molecules and atoms precisely, which may provide routes to breaking the current lithography limits. Scanning tunneling microscopy (STM) is able to probe the molecular world and to extract information from single molecules, groups of molecules, and even submolecular features. Here, we use STM in both ultrastable and ambient conditions to test the nature of dipolar interactions between molecules, to probe novel

building blocks for assembly, to manipulate surface binding modes, to examine a holey graphene framework against chemical deposition as a means in patterning, and to explore the nature of buried hydrogen-bonding networks in self-assembled monolayer matrices. The simultaneous usage of STM in topographic imaging mode and local barrier height (LBH) mode, in an ultrahigh vacuum ($\leq 10^{-12}$ torr) and low temperature (4 K) environment, enables the measurement of both molecular topography and the buried dipolar interface. Using a block-matching approach, the correlation between molecular apexes and dipolar extrema is computed, thus enabling the visualization of molecular orientations at the submolecular scale. We also use STM in ambient conditions to examine the assembly of *p*-mercaptobenzoic acid derivative of carboranethiol on a Au{111} surface, where the carboxyl-modified carboranethiol backbone provides a surface available for further chemical functionality. Adding a second thiol group attachment in 1,2-carboranedithiol and 9,12-carboranedithiol isomers enables the control of valency between neighboring thiol/thiolate attachment sites. The assembly and manipulation of the two different binding modes using simple acid-base chemistry is evaluated and measured at a local level. Two-dimensional graphene has garnered much interest recently due to extraordinary two-dimensional properties. The design and placement of holes within a protecting sheet is tested against the deposition of molecules, where the holey network acts as a mask that may find use in lithographic processing. Hydrogen bonds also exhibit strong dipoles, where STM in simultaneous topographic and LBH mode may be able to measure the topographic map along with buried amide bond dipoles. We use an amide-containing self-assembled network to evaluate the nature of these 'hidden' networks at the single-molecule scale. The embodiment of this work aims to provide a fundamental understanding of chemical properties at the nanoscale and a complementary tool with averaging and ensemble techniques.

This dissertation of John Christopher Thomas, Jr. is approved.

Richard B. Kaner

Suneel Kodambaka

Paul S. Weiss, Committee Chair

University of California, Los Angeles

2015

For my family

Table of Contents

List of Figures

List of Abbreviations and Symbols

0D	zero-dimensional
1D	one-dimensional
2D	two-dimensional
1AD	1-adamantanethiol
1ATC9	3-mercapto-N-nonylpropionamide
2ATC6	3-mercapto-N-(N'-n-hexylacetamido) propionamide
1O2	*o*-1,2-carboranedithiol
9O12	*o*-9,12-carboranedithiol
1P12	*p*-1,12-carboranedithiol
A/1-p	*p*-carboranethiol
A'	*p*-(mercaptobenzoic acid)-carboranethiol
AFM	atomic force microscopy
BE	binding energy
CCD	charge-coupled device
CCDC	cambridge cystallographic data centre
COOH	carboxyl
CVD	chemical vapor deposition
DFT	density functional theory
DNA	deoxyribonucleic acid
EGaIn	eutectic gallium indium
ESI	electrospray ionization
ET	electron transfer
FFT	fast Fourier transform
FTIR	Fourier transform infrared spectroscopy
FWHM	full width half maximum

GC	gas chromatography
GED	gas-phase electron diffraction
GP	gas-phase
GUI	graphical user interface
HF	Hartree-Fock
HOMO	highest occupied molecular orbital
HOPG	highly ordered pyrolytic graphite
LBH	local barrier height
LUMO	lowest occupied molecular orbital
M1/1-m	*m*-1-carboranethiol
M9	*m*-9-carboranethiol
MPEA	9-(4-mercaptophylethynyl)anthracene
MS	mass spectroscopy
NMR	nuclear magnetic resonance
O1/1-o	*o*-1-carboranethiol
O9	*o*-9-carboranethiol
OPE	oligo(phenylene ethynyl)
PMMA	poly(methyl methacrylate)
ppm	parts per million
S	thiolate
SAM	self-assembled monolayer
SC	single crystal
SeH	selenol
SH	thiol
STM	scanning tunneling microscopy
STS	scanning tunneling spectroscopy
TEM	transmission electron microscopy

UHV	ultrahigh vacuum
VMD	variational mode decomposition
XPS	x-ray photoelectron spectroscopy
XRD	x-ray diffraction
Å	Ångström
cm	centimeter
D	Debye
dz	differential z-height
C	Celsius
eV	electronvolt
e	elementary charge
g	grams
h	hour
ħ	Planck's constant
Ha	Hartree
Hz	hertz
I	current
k	Boltzmann constant
K	kelvin
kcal	kilocalorie
k_t	decay constant
kg	kilogram
kV	kilovolt
L	liter
MHz	megahertz
mbar	millibar
mL	milliliter

mm	millimeter
mM	millimolar
mmol	millimole
ms	millisecond
mTorr	millitorr
min	minute
nA	nanoAmpere
ng	nanogram
nm	nanometer
r	radius
s	second
sccm	standard cubic centimeter
T	Temperature
V	Volt
α	azimuthal angle
δ	surface projection
μL	microliter
θ	polar tilt
φ	work function
ν	frequency of light

Acknowledgments

This dissertation marks the end of my graduate education, and the beginning of a career as a Ph.D. level scientist. The years I have spent researching can only be described as wonderfully extensive and rewarding, where, I can only look back and hope that I have worked in a manner that not only yielded accurate and correct results, but a story with broad impact.

I am very lucky to be one of Prof. Paul Weiss's graduate students. In his lab, I was able to work and to gain experience in an exciting field. Without his guidance and support, none of the work in this dissertation could have been accomplished. Paul is a highly intelligent advisor who has decades of experience in chemical research and as a world-renown leader in the scientific community. He continues to inspire and to push the boundary within the field of nanoscience and beyond.

I would like to thank my thesis committee for all of their help and guidance. Profs. Richard Kaner, Anastassia Alexandrova, and Suneel Kodambaka all provided excellent assistance. Also, Profs. Xianfang Duan, Stanley S. Osher, and Andrea Bertozzi each gave experienced advice and thoughtful criticism that propelled my research into an analytically precise and chemically applied realm. I would also like to thank Dr. Jerome Gilles and Dr. Kevin Kelly for their expert help and discussions. I would also like to thank Adam Kollins at RHK for his invaluable assistance and advice.

The local expert scientific staff at University of California, Los Angeles: Dr. Adam Stieg (Nano and Pico Characterization Lab), Dr. Ivo Atanasov (Electron Imaging Center for NanoMachines), Dr. Jane Strouse (Molecular Instrumentation Center), Dr. Ignacio Martini (Molecular

Instrumentation Center), Shylo Stiteler (Student Machine Shop), and Max Kopelevich (Information Technology Director) have all enabled multiple learning opportunities that can simply be described as forever invaluable.

I would like to also thank some professors at The Pennsylvania State University, where I began my graduate career: Dr. William Castleman, Dr. William Noid, Dr. Lasse Jensen, and Dr. Karl Mueller for the expert knowledge and advice during my time as an entering graduate student.

I thank the US Department of Energy (DE-SC-0005025) for support of instrumentation and methods developed and applied here and (DE-SC-1037004) for the experiments conducted on buried interfaces, as well as the W. M. Keck Foundation for support of analysis methods developed and used. I would also like to thank UCLA for support via an Excellence in Chemistry Research Fellowship from UCLA.

Above all, I would like to thank my family. Without their help and support throughout my childhood and adolescence, none of my schooling and subsequent achievements would be possible. My mom constantly reminds me that, at age 3, I said I wanted to be a scientist. I have, thankfully, been able to become a research scientist who will always be grateful for their inspiration and support during the toughest (greatest) times of my life and graduate career. I would also like to thank my smart and beautiful fiancée, Amy S. Ferreira, for all of her help and amazing support.

VITA

John C. Thomas obtained his BS at the University of Texas at San Antonio in 2008, while performing research in the field of palladium coordination chemistry in the lab of Prof. Judith A. Walmsley. He began his PhD career with Prof. Paul S. Weiss at the Pennsylvania State University with a Bunton-Waller Fellowship in 2008. He helped move the laboratory from Pennsylvania to California in 2010. At the University of California, Los Angeles, he has been supported under a W. M. Keck Foundation Fellowship and the award for Excellence in Chemical Research. His graduate thesis focuses on the scanning tunneling microscopy and spectroscopic imaging of cage molecules for self-assembly, probing buried functionality of self-assembled systems, and extending image capabilities within the scanning tunneling microscope to make novel measurements at molecular and atomic scales. Many of the experiments are performed at low temperature (4 K), in extreme high vacuum, and also at catalytically relevant temperatures.

Select Publications

Hohman, J. N.; Kim, M.; Schüpbach, B.; Kind, M.; **Thomas, J. C.**; Terfort, A.; Weiss, P. S. Dynamic Double Lattice of 1-Adamantaneselenolate Self-Assembled Monolayers on Au {111}. *Journal of the American Chemical Society* **2011**, *133*, 19422–19431.

Zheng, Y. B.; Pathem, B. K.; Hohman, J. N.; **Thomas, J. C.**; Kim, M.; Weiss, P. S. Photoresponsive Molecules in Well-Defined Nanoscale Environments. *Advanced Materials* **2012**, *25*, 302–312.

Claridge, S. A.; Liao, W.-S.; **Thomas, J. C.**; Zhao, Y.; Cao, H.; Cheunkar, S.; Serino, A. C.; Andrews, A. M.; Weiss, P. S. From the Bottom Up: Dimensional Control and Characterization in Molecular Monolayers. *Chemical Society Reviews* **2013**, *42*, 2725–2745.

Claridge, S. A.; **Thomas, J. C.**; Silverman, M. A.; Schwartz, J. J.; Yang, Y.; Wang, C.; Weiss, P. S. Differentiating Individual Amino Acid Residues and Side Chain Orientations in Peptides Using Scanning Tunneling Microscopy. *Journal of the American Chemical Society* **2013**, *135*, 18528–18535.

Kim, J.; Rim, Y. S.; Liu, Y.; Serino, A. C.; **Thomas, J. C.**; Chen, H.; Yang, Y.; Weiss, P. S. Interface Control in Organic Electronics Using Mixed Monolayers of Carboranethiol Isomers. *Nano Letters* **2014**, *14*, 2946–2951.

Hohman, J. N.; **Thomas, J. C.**; Zhao, Y.; Auluck, H.; Kim, M.; Vijselaar, W. J. C.; Kommeren, S.; Terfort, A.; Weiss, P. S. Exchange Reactions between Alkanethiolates and Alkaneselenols on Au{111}. *Journal of the American Chemical Society* **2014**, *136*, 8110–8121.

Thomas, J. C.; Schwartz, J. J.; Hohman, J. N.; Claridge, S. A.; Auluck, H. S.; Serino, A. C.; Spokoyny, A. M.; Tran, G.; Kelly, K. F.; Mirkin, C. A.; Gilles, J.; Osher, S. J.; Weiss, P. S. Defect-Tolerant Aligned Dipoles within Two-Dimensional Plastic Lattices. *ACS Nano* **2015**, *9*, 4734–4742.

Thomas, J. C.; Boldog, I.; Auluck, H. S.; Bereciartua, P.; Dušek, M.; Macháček, J.; Bastl, Z.; Weiss, P. S.; Baše, T. Self-Assembled *p*-Carborane Analog of *p*-Mercaptobenzoic acid on Au{111}. *Chemistry of Materials* **2015**, *27*, 5425–5435.

Gethers, M.; **Thomas, J. C.**; Jiang, S.; Weiss, N.; Goddard, W.; Duan, X.; Weiss, P. S. Holey Graphene as a Weed Barrier. *Submitted* **2015**

Thomas, J. C.; Serino, A. C.; Goronzy, D.; Auluck, H. S.; Dermeinjian, J.; Dadras, J.; Irving, O.; Alexandrova, A. A.; Baše, T.; Weiss, P. S. Acid-Base Control of Valency within Carboranedithiol Self-Assembled Monolayers: Molecules Do the Can-Can. *In preparation* **2015**

Thomas, J. C.; Goronzy, D.; Dragomiretskiy, K.; Zosso, D.; Gilles, J.; Bertozzi, A.; Osher, S. J.; Weiss, P. S. Mapping Buried Hydrogen-Bonding Networks. *In preparation* **2015**

CHAPTER 1

From the Bottom Up: Dimensional Control and Characterization in Molecular Monolayers

1.1 Introduction

Molecular interplay and material poperties at the nanoscale dictate two-dimensional assembly, which, firstly, evolves due to interactions between the surface and the molecular head group, then interactions between nearest-neighbor molecules, and, finally, interactions between next-nearest neighboring molecules progessing towards bulk, ensemble effects. This process can be further manipulated by fine tuning each stage of interaction to control interfacial chemistry, defect type and distribution, lattice and bonding structure, and quantum size effects.

The chemistry and physics of self-assembled monolayers (SAMs) can be understood through the structure and chemical formations at the interface (typical monolayer thickness range from 1-3 nm).[1] Self-assembly, such as the relatively simple *n*-alkanethiol formation on gold, is driven by surface energy minimization on a variety of metals, metal oxides, and other surfaces.[1] In this system, the enthalpy of the gold-sulfur bond formation (~50 kcal/mol) is several times larger than the combined intermolecular interactions between neighboring alkyl backbone and tail groups (1-2 kcal/mol · CH_2, or 10-20 kcal/mol for decanethiol, one common SAM substituent).[2] Here, there is ample room for improvement both in the ability to fine-tune intermolecular interactions, modulate substrate-mediated interactions, and in the intelligent design of materials at all scales.

1.2 Two-Dimensional Structure and Function

Multi-dimensional formation and assembly is fundamental in the fields of nanotechnology, device physics, interfacial chemistry, and in applied biology.[1,3-7] The assembly of *n*-alkanethiolate SAMs on Au{111} proceeds by: an initial 'head group' thiol functionality that binds to the metal substrate, than an alkyl 'backbone' rearrangement, and, finally, a monolayer that forms with variety

of defects originate from surface-SAM interface and intermolecular interactions. The understanding of chemical interplay between assemblies, in all dimensions, can be used to advantage when directing single molecules, linear arrays, and two-dimensional assemblies (Figure 1.1). The exposed methyl (-CH_3) 'tail groups' result in a monolayer with hydrophobic properties, which can be further chemically functionalized to obtain a variety of material properties. The interplay of these three groups embody self-assembly, which yields both a general zoological classification system and optimizable parameters to understand and fine tune interfaces with SAM modification, respectively. Head group bonding is one key parameter, as it plays the first role in assembly via surface attachment.

1.2.1 Molecular Head Group

The head group corresponds to a library of different linker groups which form a strong bond to a surface. This is the first, and arguably, the most critical step in SAM formation, as bond angle, strength, and underlying surface reconstruction play a formidable role in assembly. Self-assembled monolayers were discovered by depositing organic disulfides onto an Au surface.[8-10] Since their discovery, SAMs have been formed on Au,[1,2,7,8] Ag,[8,11] Cu,[8,12] Pd,[13,14] Pt,[15,16] Ni,[12,17] Fe,[12] and even dopable liquid eutectic GaIn,[18] to name a few. Monolayers have also been formed on semiconductor surfaces such as GaAs,[19] GaN,[20,21] Ge,[22] ZnSe,[23] and InP.[24] Self-assembly due to π-π stacking interactions has also been observed on graphitic surfaces.[25-28] Other formations have been observed on oxide substrates, including SiO_2[29,30] and TiO_2.[31,32] The Au{111} surface is well-studied, is easy to obtain and to prepare, is relatively inert, and it binds functionalizable thiols with high affinity and selectivity.[8] Head groups are as varied as the available surface, and include

isocyanide,[33] Si,[34-36] P,[20,37-39] Se,[11,40-43] S,[8,10,44] and also subgroups that enable favorable π-π interactions on highly oriented graphite such as cyclodextrins,[45-48] pentacene,[49,50] and peptides.[51-54]

The nature of the head group/substrate bond is complicated by underlying substrate reconstructions. Thiol on Au is the prototypical head group to substrate bond exhibited in a multitude of precursor forms (thiols, dithiols, thioethers, and disulfides) that have each been shown to lift the herringbone reconstruction of Au{111}. The growing consensus is that thiolate binds to lifted Au adatoms.[55] Recent calculations show that there are multiple different stable surface reconstructions, which all are within ~0.2 eV of one another, including; one sulfur bonded to a three-fold hollow site, one sulfur to a bridge site, one sulfur to one Au adatom, and two sulfurs to one Au adatom.[56-61] Other factors, including the backbone and tail groups, play key roles in determining bond type. These possible formations can help to converge the debate regarding underlying Au reconstructions. Gold cleaves the thiol, R-S-H, bond selectively and readily due to the strength of the Au-S bond, ~44 kcal/mol, which is stronger than the Au-Au bond and thus enabling a large range of functional R groups.[4] Sykes and co-workers have shown that by varying the molecule, and the amount of deposition, the Au herringbone reconstruction can be controllably altered before being completely lifted.[39,62] These interactions can be independently monitored by using scanning tunneling microscopy (STM). The local tunneling work function, and thus largest buried dipole, in a SAM can be probed by varying the tunneling gap distance, simultaneously, in STM topographic and local barrier height (LBH) imaging mode. This enabled the Au-S bond dipole to be measured and compared with regionally bounded topographic images, and proved to be the first local tilt angle measurement within a SAM.[63] This technique has been adapted and applied to cyclohexanethiol on Au{111}, where two types of adsorption sites were proposed, at bridge and atop sites.[64] Recently, both modalities were used to extract single molecular orientations

within a carboranethiol monolayers.[65] Thiols on Ag{111} exhibit different binding properties and the adatom bonding scheme is less stable in comparison with Au unless stabilized by another donor group such as Cl^-.[66] This results in binding on bridge and three-fold hollow binding sites. Silver is also less stable towards oblique bonding geometries, so, *n*-alkanethiols bind near normal with respect to the underlying substrate, where Au formations commonly obtain monolayers with a tilt angle of ~30°.[1,63] Thioethers are also head group options, where the weaker molecule-substrate bond still lifts the Au{111} herringbone and also assemble on Cu{111}, forming monolayers with lower defect density due to the nature of adsorptivity.[67-70]

Emerging new targets for self-assembly include selenoethers, selenols, diselenols, and diselenides.[42,43,71-76] Monolayers formed from selenium head groups have shown greater stability towards oxide degradation and have also shown to possess greater adsorptivity in some cases,[42] where both sulfur and selenium binding can be modulated with tunable backbone groups. Monnell *et al.* showed that, for *n*-alkyl backbones, alkanethiolate monolayers have a lower barrier to tunneling compared with alkaneselenolates, and therefore a higher conductance.[71] Previous measurements have shown Moiré pattern formations as alkaneselenols form densely packed, distorted hexagonal lattices that are incommensurate with the underlying Au substrate with linear missing-row structures.[41] These structures are distinct from *n*-alkanethiol monolayers on Au, which is indicative of a difference in bonding. Later work with 1-adamantaneselenol on Au, shows selenol preferentially attaching to bridge and three-fold hollow sites. Upon annealing, the SAM restructured into two distinct commensurate lattices, as low-conductance molecules assumed a (7 x 7) all-bridge configuration and high conductance molecules formed into rows of dimers with long-range order described by a $(6\sqrt{5} \times 6\sqrt{5})R15°$ unit cell.[42] Diselenides and dithiols have shown to replace thiolate monolayers on Au efficiently, leading to a hypothesis that more efficient reactive

exchange processes in which the immediate availability of a second thiol or selenol entity aids in further substitution.[76] Density functional theory (DFT) calculations comparing self-assembled monolayers of selenols and thiols show a marginal energetic difference in stability between the two, eluding to the backbone and tail groups playing a more significant role in stability.[72] Different backbone lengths (n = 2-6) of *n*-alkaneselenol and *n*-alkanethiol on Au follow the odd/even rule for stability, where the former is more stable. For these backbone lengths, *n*-alkaneselenols were shown to be more stable towards exchange in comparison to *n*-alkanethiols.[73] Diselenides have also shown to adsorb readily to Ag substrates, however, thiol-bound Ag was more stable in comparison to selenol-bound Ag. This was attributed to different bonding configurations, where selenium and sulfur were presumed to be sp^3 and sp, respectively.[11] While selenium and sulfur have similar electronic structure, the substrate bonding is different and numerous effects contribute to overall binding and subsequent stability.

While sulfur and selenium head groups are common in self-assembly, there are still other head groups that can self-assemble on surfaces. Silanes and silicates form on a variety of substrates including biological cells, amorphous surfaces, and silica surfaces.[36] These assemblies are ubiquitous in nature, and have led to the rich field of sol-gel chemistry.[77,78] Other head groups include phosphonates, phosphines, phosphonic acid, alcohols, and peptide assemblies. Jewell *et al.* showed that, in special cases, the hard and soft rules of inorganic chemistry can be applied towards molecule-substrate interaction strengths on the soft Au surface, where measured data revealed the relative order of molecule-gold interaction strength: trimethylphosphine>dibutyl selenide>dibutyl sulfide.[39] This finding is specific towards groups that do not chemisorb as readily as RSH or RSeH, however, trimethylphosphine does lift the Au reconstruction, which indicates strong bond formation.[38] Phosphonic acid groups have shown to form stable structures on Ti and Au substrates

and have been shown to be more stable than trichlorosilanes.[18] Phosphonates and also alkylphosphonic acid have shown to form assemblies on GaN and nitinol (NiTi), respectively.[20,79] Alkylphosphonates have also been shown to assemble on Al_2O_3, TiO_2, ZrO_2, planar mica, and SiO_2,[38] however, full monolayer formation has only been noted in a few cases. Molecule-substrate bonds, here, are not the prevailing factors. Instead, the tail group plays a more dominant role. Baber *et al.* used ultrahigh vacuum and low-temperature conditions to assemble methanol onto Au{111} surfaces to monitor intermolecular hydrogen-bonding networks between tail groups, within formed structures.[80] Conjugated carbon backbone structures on surfaces begin to blur distinctions between the head and tail group, exhibiting charge transport and work function shifts due to varied conjugated backbone lengths.[16,81] Structures such as styrene,[82] pentacene,[49] pyrene,[62] and graphene[50,83] form stable two-dimensional structures on surfaces such as highly ordered pyrolytic graphite (HOPG) and Au{111}. Peptides can also assemble onto surfaces, where deposition can lead to possible methodologies of isolating and studying single peptides or proteins.[52-54,84,85]

The head group of a self-assembled monolayer is the first driving interaction with a surface, and it can play either the dominant or introductory role in assembly. A summary of different assembly classifications is further illustrated in Figure 1.2. Differences in head groups and substrates create dramatically different monolayers, however, the backbone and tail group also play a substantial and arguably larger role in monolayer formation and stabilization.

1.2.2 Molecular Backbone and Tail Group

Reverting back to the prototypical *n*-alkanethiol, as the sulfur first attaches to a surface, the interplay between the neighboring molecules via the carbon backbone begins to play a significant factor as each methyl unit contributes approximately 1 kcal/mol.[12] This results in further

stabilization with increasing chain length due to stacked methyl-methyl interactions. The molecular interactions that govern monolayer formation, listed in increasing strength, are van der Waals, dipole-dipole, and hydrogen bonding. Just as chain length can increase stability, varying the backbone with different functional units can increase or decrease interaction strength, thus leading to greater or weaker monolayer stabilities.

As the number of methyl units on a carbon backbone can increase stability, odd-numbered methyl units have shown to be less stable when compared with even-numbered *n*-alkanethiols.[2] As the chain length increases in *n*-alkanethiols, the range of accessible backbone tilt angles is constrained due to steric effects.[86] Self-assembled monolayers with different backbones that include conjugated units also exhibit similar behavior, as each reconfigures to maximize intermolecular forces.[81] Some of the backbone functional groups include amides, alkenes, alkynes, diacetylene, aryl groups, oligo(phenylene thynylene), oligo(ethylene glycol), sulfones, and azobenzenes.[44,87-89] Adding one methyl unit to benezenethiol creates SAMs that exhibit higher order due increased methyl-methyl interactions, which results in altered thiol-gold bond angles and van der Waals interaction stabilization.[90] Cage molecules encompass another family of thiol-substituted molecules that are defined as rigid, three-dimensional molecular frameworks that enclose space.[91] Some cage molecules of note include adamantanes (and their related constructs that form in structural series towards bulk diamond), carboranes, and decaboranes.[41,91-93] Each cage molecule listed above can be further functionalized with additional thiols creating multiple possible attachment sites. These cage-molecule SAMs have larger nearest-neighbor spacings, when compared with *n*-alkanethiolates, due to steric hinderance and therefore have contrasting SAM-substrate properties that may include different Au binding and tunable interaction potentials.[94] The cage molecule 1-adamantanethiol, with sufficiently low intermolecular

interaction strength, is readily displaced by poly(dimethylsiloxane) stamps inked with 11-mercaptoundecanoic acid, and both 1-adamanthiolate and 2-admantanethiolate are displaced by *n*-dodecanethiolate.[91,92] This is the case for most diamonoid cages, but the situation can vary if stronger intermolecular forces are at play, such as for carboranethiols.

As van der Waals interactions play a significant role in *n*-alkanethiol assembly, replacing the backbone with a large charge offset, originate from the cage center, enables dipole-dipole interactions. Carboranethiols, of the formula $C_2B_{10}H_{12}SH$, have been a recent target for self-assembly, as the hexacoordinated carbon and boron atoms, due to electron-deficient boron hydrides and the delocalized nature in cage bonding, enable control of dipole vector direction and magnitude by simply varying the carbon positions within the cage.[91,95] Some carboranethiols that have been reported for self-assembly are *o*-1-carboranethiol (O1), *o*-9-carboranethiol (O9), *m*-1-carboranethiol (M1), *m*-9-carboranethiol (M9), *o*-1,2-carboranedithiol (1O2), and *p*-1,12-carboranedithiol (1P12).[91,96] Effects of interacting dipole-dipole interactions between M1 and M9 carboranethiols, where M1 has a strong lateral dipole component and M9 has a larger out of plane component with respect to the underlying substrate, were solution deposited onto Au{111}/mica and monitored with STM.[95] Here, scanning tunneling micrographs of M1, M9, and codeposited M1 and M9 proved indistinguishable in topographic images, however, grazing angle Fourier transform infrared (FTIR) spectroscopy was able to monitor the characteristic B-H stretching region and track relative concentrations upon competitive thiol exposure to show that cages with larger in-plane component dipoles are more stable and less susceptible to eviction by other cage isomers or *n*-alkanethiol.[95] Similar interactions have been monitored in styrene assemblies, in vacuum and low temperature conditions, on Au{111}, where a weak interacting dipole drives assembly between interacting styrene molecules at near monolayer coverage.[82]

Recently, these intermolecular interactions were monitored directly within assemblies of carboranethiol on Au{111} using multi-modal STM to reveal the aligned dipolar nature at the interface through the measurement of single-molecule orientations.[65] Just as dipole-dipole interactions affect monolayer integrity, hydrogen bonding between adjacent molecules can significantly increase intermolecular interaction strength, and therefore, SAM stability.

Incorporating a amide functionality group within a molecular backbone, such as 3-mecapto-*N*-nonylpropionamide (1ATC9), adds another type of interaction between proximate molecules. Each amide bond contributes 6 kcal/mol, driving both assembly and morphology.[51,97] Single amide-containing monolayers, composed of 1ATC9, have buried hydrogen-bonding networks that help dictate assembly and, thus, phase separate from *n*-alkanethiol SAM regions in bicomponent films.[98] Assembly of the two- and three-amide counterparts showed that the two amide counterpart, 3-mercapto-N-(N'-n-hexylacetamido) propionamide (2ATC6), phase separated, but the three amide counterpart did not produce ordered monolayers as van der Waals forces were sufficiently decreased.[98,99] There have been two phases imaged under ambient conditions, where the molecule is normal to the surface, and also tilted 18° off the surface normal, where the topographically less protruding tilted phase has a larger microwave difference frequency signal.[100] Both 1ATC9 phases orient to maximize intermolecular hydrogen bonding, with the latter being more thermodynamically stable since, upon annealing, the normal phase will restructure to the tilted phase.[88] Amide bonding networks in SAMs have been theorized and invoked for charge transport across a Ag/SAM//Ga_2O_3/EGaIn contact, and prove to be stable anchoring groups for various terminating functional groups.[101] Hydrogen bonding between methanol groups forms hexamer units and zigzag chains on Au{111}, at sub-monolayer coverage, in vacuum and low temperature.[102] In similar conditions, thioether, also forms hexamer units and linear chains on

Au{111} upon room temperature annealing.[103] These interactions have also been visualized in small model peptides on graphitic surfaces, where small block polypeptides form into stable β-sheets with distinguishable local domains under STM imaging.[54] As hydrogen-bonding networks are ubiquitous in nature, their molecular interplay during assembly may prove an important role in determining biological structure and function at the nanoscale.

Beyond the head group and backbone, another parameter for self-assembly is inputting terminal group functionality, which plays an essential role in SAM properties and dictates much of the chemistry at the exposed interface. Terminal groups can include methyl units, amines, nitriles, carboxylic acid, sulfides, alcohols, ferrocenes, pyrrole, and fullerenes.[1,7,105-112] The conventional methyl terminating group for *n*-alkanethiolate produces a SAM that is hydrophobic, however, simply changing the end group to a hydroxyl unit, the SAM is able to hydrogen bond and is then hydrophilic. Similarly, dipole moments of SAMs can be reversed by using two different terminal substituents, an electron-rich amine, and an electron-poor cyano group.[108] Azobenzene-functionalized SAMs can be used as targets for molecular switches, as azobenzene units will isomerize into trans and cis conformations upon cyclic exposure to ultraviolet (UV) (365 nm) and blue (450 nm) light, respectively.[87,89,111] These terminally functionalized photoswitchable molecules have attracted attention in terms of developing molecular machinery.[113] Carboxyl-terminated hexa(ethylene glycol) alkanethiols have been functionalized with amines, carboxyl groups, biotin, and 5-hydroxytrptophan, and used to immobilize 5-HT_7 receptors and streptavidin onto a surface.[114-117] Other reports have used similar systems to immobilize Au nanoparticles on surfaces, which enabled subsequent tunneling spectroscopy on these previously inaccessible targets.[118] In addition to terminal functionalization, terminal group reactions are possible, where 9-(4-mercaptophylethynyl)anthracene (MPEA) can be inserted into

n-dodecanethiolate matrices and dimerized under UV light at the 9 and 10 positions via [4+4] cycloaddition.[119] Also, pyrrole-terminated SAMs upon plasma exposure, form into polymerized polypyrrole, which continues to be intensely studied for its mechanical and electrical properties.[110] Terminal group functionalization dictates chemistry at the exposed interface of a SAM, and provides a wealth of possible chemistry within the context of self-assembled systems.

1.2.3 Assembled Structures

As discussed above, the assembled structure depends on the head group, backbone, and tail group. Structure further dictates SAM functionality, integrity, and stability. Subsequent assembled formations, in the context of this thesis, rely upon two-dimensional surfaces, where defects, domain boundaries, and vacancies all play roles in how single molecules and assemblies are placed within monolayers and how SAMs can be further functionalized for devices, solar cells, and molecular electronics.

1.2.4 Lattices and Defects for Zero-, One-, and Two-Dimensional Assemblies

Reverting back to *n*-alkanethiolate SAM, linear chains form structures that are tilted off the surface normal by ~30°, which produces quite a number of defects, such as domains that are tilted in different directions from one another, lattice shifted from one another, step edge defects, molecular voids, low-density regions, and vacancy islands between different domains.[1,7,12] Domain boundaries can result from different azimuthal tilt angles and Au attachment offsets.[91] The lattices formed by *n*-alkanethiolate are $(\sqrt{3} \times \sqrt{3})R30°$, with a 4.99 Å hexagonally close-packed nearest-neighbor spacing, and also a $c(4 \times 2)$ superlattice.[4] Single molecules and assemblies have been shown to insert into defect sites within SAMs from exposure to solution or vapor,[10] making defects within monolayers important to exploit and to control. Molecular insertion has been used

to advantage in isolating single molecules, such as molecular switches.[87,89,120-123] While *n*-alkanethiol forms a variety of defects, cage molecules form larger lattices, ~7 Å, and fewer defects due to a larger, nearly spherical backbone, symmetry, and conformational rigidity. Simply changing the thiol position on 1-admantanethiolate to 2-adamantanethiolate, creates SAMs with tilt defects similar to *n*-alkanethiolate that contain vacancy islands and more defects.[92] Assemblies of *tert*-butanethiol on Au{111} exhibited a ($\sqrt{7}$ x $\sqrt{7}$)*R*19° surface lattice structure, where the terminal methyl units play a large role inducing this SAM into a densely packed monolayer with a high defect density.[124] Phase-separated SAMs, in which domains of one molecular group organize together and separate from domains of a different molecular group, can be manipulated with temperature, deposition conditions, and varied surfactants. Phases can be controlled in *n*-alkanethiols by deposition time and temperature, as striped, or lying down, phases are the first steps in the self-assembly process, which lifts the herringbone before densely packing into the ($\sqrt{3}$ x $\sqrt{3}$)*R*30° more upright phase.[1] The substituent, 2-(aryl)-ethanethiol, has been shown to produce a ($5\sqrt{3}$ x 3) structure at room temperature, and restructure into a (23 x 2) unit cell upon annealing.[125] This has also been seen with anthracene-2-thiol on Au{111}, where a ($2\sqrt{3}$ x 4)*rect* unit cell is formed at room temperature and, upon annealing, the molecules form a dilute (4 x 2)-phase due to partial desorption.[126] Nanografting, an atomic force microscopy (AFM) technique, has emerged as another means of controlling the densities of defects in monolayers by simply varying the shaving, or scan speed, of the AFM tip.[127,128] There is a complex library being formed with the plethora of surfactants and surface-modifiable ligands currently available, where novel constructs for intelligent material design are quickly becoming a field unto itself. Controlling the structure and density of defects in monolayers is essential in utilizing SAMs in molecular devices, bottom-up design, and solar cells, where defects are key to controlling charge transport

across interfaces (*e.g.*, batteries).

1.3 Characterization

In this dissertation, the predominant characterization tool used is scanning tunneling microscopy coupled with spectroscopic imaging to probe buried and exposed interfaces of thin film materials. Both Fourier transform infrared spectroscopy and X-ray photoelectron spectroscopy are also employed to monitor characteristic vibronic structure and electronic binding energies, respectfully.

1.3.1 Scanning Tunneling Microscopy and Spectroscopic Imaging

In quantum mechanics, the fundamental principle of quantum tunneling through a classically forbidden barrier provides a route towards monitoring single atomic and molecular surface structure. Scanning tunneling microscopy, for which Binnig and Rohrer received the Nobel Prize in 1986,[129-131] makes use of this phenomena by bringing an atomically sharp tip within tunneling distance to a surface of interest using an applied bias between the two conducting electrodes. The result is a tunneling current, I_t, that can be represented by the equation

$$I_t = Ae^{-2kz},$$

where k is the decay constant, A is the ground state wave function, and z is the tip-sample separation distance.[132] The decay constant can be further represented by the equation

$$k_t = \frac{\sqrt{2m(V-E)}}{\hbar},$$

where m is the mass of an electron (9.11×10^{-31} kg), ħ is plank's constant (4.14×10^{-15} eV·s) divided by 2π, V is the applied bias voltage and E is the energy state of an electron. In the approximation of small V, the equation can be approximated as

$$k_t = \frac{\sqrt{2m\varphi}}{\hbar},$$

where φ is the tunneling work function.

It becomes evident that an applied sinusoidal modulation to the tunneling gap distance would permit the measurement of the tunneling work function as represented by the equation

$$\varphi = c\left(\frac{dln(I_t)}{dz}\right)^2,$$

where c is a constant (0.95). The local barrier height can further related to the largest buried dipole available to the tunneling tip.[133-135] Upon applying a modulation above the response frequency bandwidth of the scanning tunneling microscope feedback loop, the simultaneous acquisition of both topography and the dipolar interface contours can be obtained.[63,65] A schematic that details different uses and modalities of STM is shown in Figure 1.3. This is the principle behind the local barrier height measurements described in Chapters 2, 4, and 6.

1.3.2 Other Techniques

Infrared spectroscopy is a powerful surface technique that can track chemical fingerprints and help deconvolute heterogeneity.[95] We use Fourier transform infrared spectroscopy (FTIR) to track the boron-hydride peak at ~2680 cm^{-1}, which is far enough from the alkanethiolate terminal methyl peak at 2877 cm^{-1} to be a characteristic region in monolayers composed of carboranethiols. This

signature helps to distinguish compositions of different isomeric SAMs and aids in structural arguments.

X-ray photoelectron spectroscopy (XPS) is a surface-sensitive technique that employs specific wavelengths (Al K_α X-rays, E_{photon} = 1486.7 eV) to probe the chemical composition of a sample.[136] Here, we use XPS to determine the characteristic binding energies of gold, sulfur, carbon, boron, and oxygen in SAMs composed of *p*-carboranethiol (A), *p*-(mercaptobenzoic acid)-carboranethiol (A'), *o*-12-carboranedithiol (1O2), and *o*-9,12-carboranedithiol (9O12). Resulting data enables confirmation of SAM stability, the nature of binding, and the relative concentrations of each chemical component within measured samples.

Water contact angle measurements enable surface wettability characteristics at the exposed (solvent or air) interface.[137] Monolayers of *n*-alkanethiols on Au{111} contain increased methyl-methyl interactions at the SAM-environment boundary, which subsequently produces SAMs with large contact angles against water droplets, *i.e.*, hydrophobic. The reverse is true for SAMs composed of 1-mercaptoundecanol, where terminal hydroxyl groups hydrogen bond with solvent and, thus, produce monolayers with small contact angles with water droplets, *i.e.*, hydrophilic. Contact angle hysteresis can be obtained by measuring both advancing and receding measurements, where the difference relates to surface properties.

Transmission electron microscopy (TEM) is a method to image and to characterize samples with high-energy transmitted electrons. Contrast within images obtained is dominated by three types of contrast: diffraction contrast due to local defects and dislocations, phase modulation of the incident electron wave transmitted through a crystal potential, and sensitivity to atomic mass.[138] Here, TEM is used to confirm methodologies for producing holey graphene frameworks.

Diffraction patterns and morphological images obtained enabled the characterization of hole size, hole distribution, and the nature of the graphene interlayer.

X-ray diffraction (XRD) is broadly used to characterize ensemble crystal structures in a wide-array of materials. This technique is commonly coupled with nuclear magnetic resonance (NMR) spectroscopy to confirm and to identify atomic locations within a molecule or larger structure,[93,137] where NMR spectroscopy measures the absorption and release of radio frequency energy by a nucleus in a magnetic field. In this thesis, both techniques are used to characterize *p*-carboranethiol and its *p*-mercaptobenzoic acid derivative. Analysis of atomic positions within the solid state confirmed hydrogen-bonding interactions, which enabled further conformational investigation of the –COOH rotational barrier and complications obtaining molecular resolution with STM. Mass Spectrometry (MS), which operates by measuring the mass to charge ratio and abundance of impending ions on a detector, was also used for confirmation. The gas-phase distribution of the *p*-mercaptobenzoic acid derivative was measured, and used to further confirm elemental composition.

1.4 Perspectives

There is much current research aimed to advance the ever-expanding 'tech' industry and to push Moore's law, defined as doubling the amount of transistors on a wafer every two years, past its current boundary and to create computer processing chips at the single-molecule limit. Furthermore, many characterization techniques are hindered by averaging, where the subtle variations in the nature of interaction at the nanoscale is lost. Scanning probe technology is well equipped to tackle this problem, where each development and newly coupled technique better enables medical doctors, engineers, and scientists to understand fundamental interactions between

atoms and how these interactions form large-scale structures. This thesis attempts to leverage sparse details within large-scale networks, to develop new targets for functionalization, and to design two-dimensional systems precisely from the bottom up.

1.5 Dissertation Overview

This dissertation is organized as follows, Chapter 1 has discussed monolayer formations from the bottom up along with a means for classification and characterization. In Chapter 2, the measurement of defect-tolerant aligned dipoles is discussed. Chapter 3 presents the synthesis and characterization of novel carboxy functionalized *p*-carboranethiol assemblies on Au{111}. Chapter 4 discusses the simple control of valency within monolayers of carboranedithiol. Chapter 5 details the use of a holey graphene transferrable film as a mask against chemical deposition. Chapter 6 uses multi-modal STM to measure and uncover the nature of buried hydrogen bonding networks within amide-containing SAMs. Future prospects of this dissertation are summarized in Chapter 7.

Chapter 1 has been modified based on the following invited review and adapted with permission:

Claridge, S. A.; Liao, W.-S.; Thomas, J. C.; Zhao, Y.; Cao, H. H.; Cheunkar, S.; Serino, A. C.; Andrews, A. M.; Weiss, P. S. From the Bottom Up: Dimensional Control and Characterization in Molecular Monolayers. *Chem. Soc. Rev.* **2013**, 42, 2725–2745.

Chapter 2 has been reformatted from the manuscript:

Thomas, J. C.; Schwartz, J. J.; Hohman, J. N.; Claridge, S. A.; Auluck, H. S.; Serino, A. C.; Spokoyny, A. M.; Tran, G.; Kelly, K. F.; Mirkin, C. A.; Gilles, J.; Osher, S. J.; Weiss, P. S. Defect-Tolerant Aligned Dipoles within Two-Dimensional Plastic Lattices. *ACS Nano* **2015**, *9*, 4734–4742.

Chapter 3 has been reformatted from the manuscript that has been accepted to Chemistry of Materials:

Thomas, J. C.; Boldog, I.; Auluck, H. S.; Bereciartua, P.; Dušek, M.; Macháček, J.; Bastl, Z.; Weiss, P. S.; Baše, T. Self-Assembled *p*-Carborane Analog of *p*-Mercaptobenzoic acid on Au{111}. *Chem. Mater.* **2015**, *27*, 5425–5435.

Chapter 4 has been reformatted from a manuscript in preparation:

Thomas, J. C.; Serino, A. C.; Goronzy, D.; Auluck, H. S.; Dermeinjian, J.; Dadras, J.; Irving, O.; Alexandrova, A. A.; Baše, T.; Weiss, P. S. Acid-Base Control of Valency within Carboranedithiol Self-Assembled Monolayers: Molecules Do the Can-Can. *In preparation* **2015**.

Chapter 5 has been reformatted from a submitted manuscript:

Gethers, M.; Thomas, J. C.; Jiang, S.; Weiss, N.; Goddard, W.; Duan, X.; Weiss, P. S. Holey Graphene as a Weed Barrier. *Submitted* **2015**.

Chapter 6 has been reformatted from a manuscript in preparation:

Thomas, J. C.; Goronzy, D.; Dragomiretskiy, K.; Zosso, D.; Gilles, J.; Bertozzi, A.; Osher, S. J.; Weiss, P. S. Mapping Buried Hydrogen-Bonding Networks. *In preparation* **2015**.

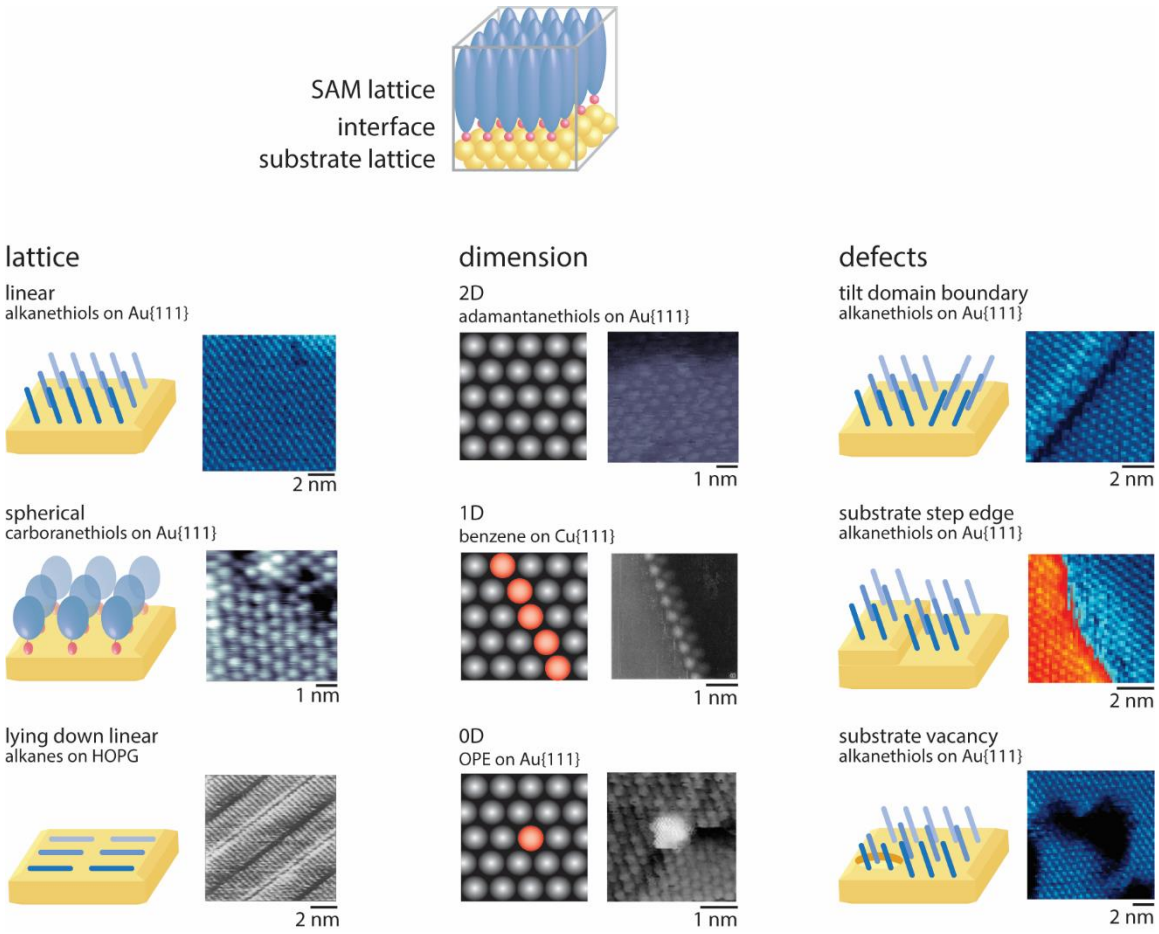

Figure 1.1 The process of self-assembly can be ascribed to substrate-mediated effects and intermolecular interactions, which lead to a complex zoology of possible lattice structures and defects. After adsorption, dimensionality is restricted within the monolayer that enables unique molecular behavior, directional coupling, and single-molecule isolation. Adapted with permission from refs. 120 and 139. Monolayer structural defects can originate from the substrate or molecular interactions, where control of defect type and density can be used to optimize material design at the single-molecule scale. Adapted from ref. 10.

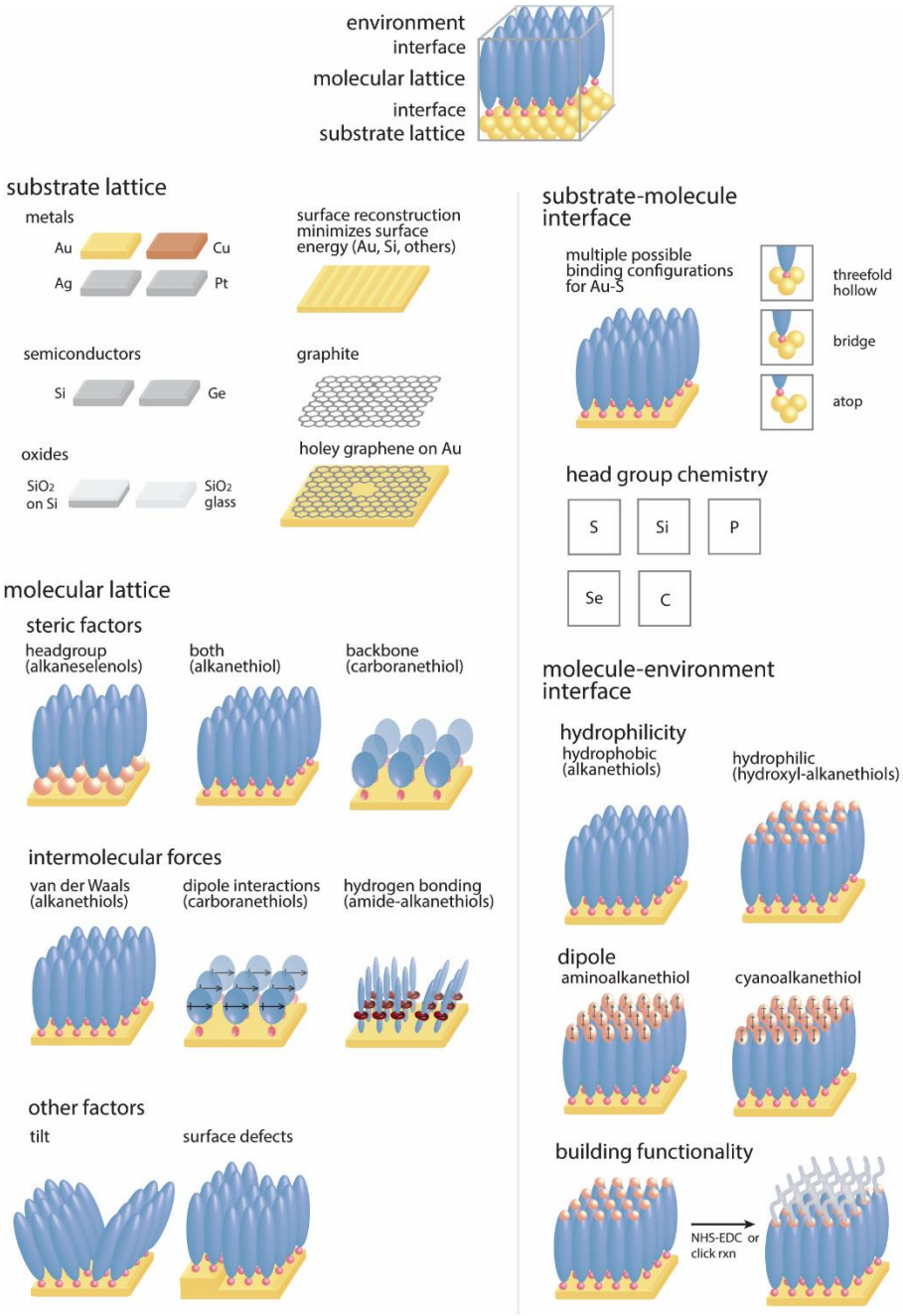

Figure 1.2 Properties within two-dimensional monolayer interfaces are governed by the cooperative effects originate from the molecular lattice, substrate-molecule interface, and the molecule-environment interface.

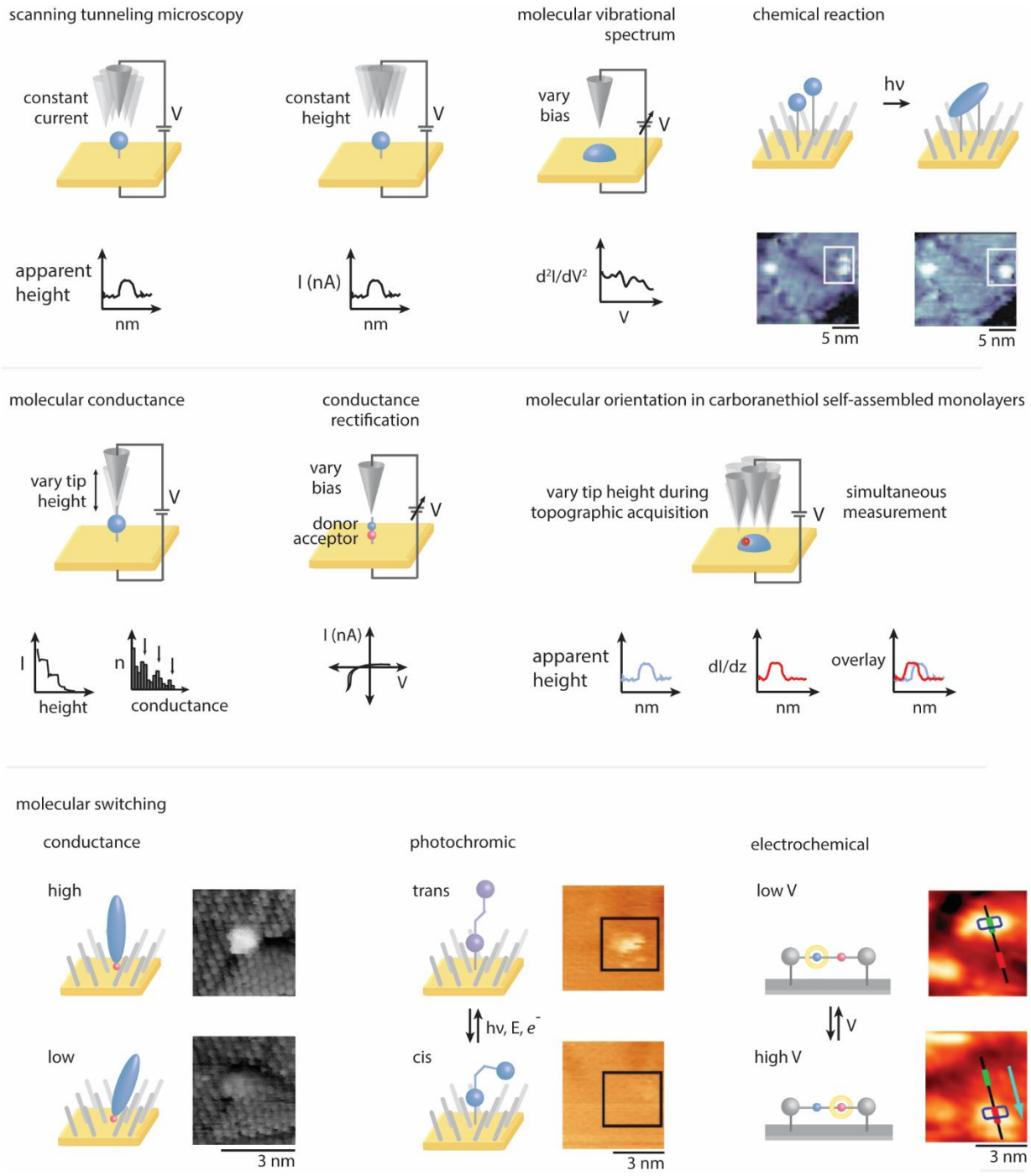

Figure 1.3 Scanning tunneling microscopy (STM), where an atomically sharp is brought in close proximity to a substrate with an applied bias, operates in both constant-current and constant-height mode. Single-molecule spectroscopy can be obtained by measuring current and sweeping through bias energy regimes of interest. A number of possibilities become evident with STM, which include

monitoring chemical reactions at the local scale, measuring break junction currents as the tip is moved away from the surface, and measuring donor-bridge-acceptor molecular rectifiers. Scanning tunneling microscopy in simultaneous topographic and local barrier height mode can measure both the molecular landscape and the dipolar interface, which can be correlated to compute molecular orientations. Molecular interactions are accessible and visible, such as single-molecule conductance switching, photochromic reactions, and electrochemical motion. Adapted with permission from refs. 87, 119, 120, and 140.

1.6 References

1. Love, J. C.; Estroff, L. A.; Kriebel, J. K.; Nuzzo, R. G.; Whitesides, G. M. Self-Assembled Monolayers of Thiolates on Metals as a Form of Nanotechnology. *Chem. Rev*. **2005**, *105*, 1103–1169.

2. Nuzzo, R. G.; Fusco, F. A.; Allara, D. L. Spontaneously Organized Molecular Assemblies. 3. Preparation and Properties of Solution Adsorbed Monolayers of Organic Disulfides on Gold Surfaces. *J. Am. Chem. Soc.* **1987**, *109*, 2358–2368.

3. Jorgenson, W. L.; Swensen, C. J. Optimized Intermolecular Potential Functions for Amides and Peptides. Structure and Properties of Liquid Amides. *J. Am. Chem. Soc.* **1985**, *107*, 569–578.

4. Ulman, A. Formation and Structure of Self-Assembled Monolayers. *Chem. Rev.* **1996**, *96*, 1533–1544.

5. Okawa, Y.; Aono, M. Materials Science: Nanoscale Control of Polymerization. *Nature* **2011**, *409*, 683–684.

6. Claridge, S. A.; Schwartz, J. J.; Weiss, P. S. Electrons, Photons, and Force: Quantitative Single-Molecule Measurements from Physics to Biology. *ACS Nano* **2011**, *5*, 693–729.

7. Claridge, S. A.; Liao, W.-S.; Thomas, J. C.; Zhao, Y.; Cao, H. H.; Cheunkar, S.; Serino, A. C.; Andrews, A. M.; Weiss, P. S. From the Bottom-Up: Dimensional Control and Characterization in Molecular Monolayers. *Chem. Soc. Rev.* **2013**, *42*, 2725–2745.

8. Nuzzo, R. G.; Allara, D. L. Adsorption of Bifunctional Organic Disulfides on Gold Surfaces. *J. Am. Chem. Soc.* **1983**, *105*, 4481–4483.

9. Nuzzo, R. G. Comparison of the Structures and Wetting Properties of Self-Assembled Monolayers of *n*-Alkanethiols on the Coinage Metal Surfaces, Cu, Ag, Au. *J. Am. Chem. Soc.* **1991**, *113*, 7152–7167.

10. Weiss, P. S. Functional Molecules and Assemblies in Controlled Environments: Formation and Measurements. *Acc. Chem. Res.* **2008**, *41*, 1772–1781.

11. Shaporenko, A.; Ulman, A.; Terfort, A.; Zharnikov, M. Self-Assembled Monolayers of Alkaneselenolates on (111) Gold and Silver. *J. Phys. Chem. B* **2005**, *109*, 3898–3906.

12. Vericat, C.; Vela, M. E.; Benitez, G.; Carro, P.; Savarezza, R. C. Self-Assembled Monolayers of Thiols and Dithiols on Gold: New Challenges for a Well-Known System. *Chem. Soc. Rev.* **2010**, *39*, 1805–1834.

13. Azzaroni, O.; Vela, M. E.; Fonticelli, M.; Benitez, G.; Carro, P.; Blum, B.; Salvarezza, R. C. Electrodesorption Potentials of Self-Assembled Monolayers of Alkanethiolates on Palladium. *J. Phys. Chem. B* **2003**, *107*, 13446–13454.

14. Love, J. C.; Wolfe, D. B.; Haasch, R.; Chabinyc, M. L.; Paul, K. E.; Whitesides, G. M.; Nuzzo, R. G. Formation and Structure of Self-Assembled Monolayers of Alkanethiolates on Palladium. *J. Am. Chem. Soc.* **2003**, *125*, 2597–2609.

15. Zangmeister, C. D.; Picraux, L. B.; van Zee, R. D.; Yao, Y.; Tour, J. M. Energy-Level Alignment and Work Function Shifts for Thiol-Bound Monolayers of Conjugated Molecules Self-Assembled on Ag, Cu, Au, and Pt. *Chem. Phys. Lett.* **2007**, *442*, 390–393.

16. Floridia Addato, M. a. A.; Rubert, A. A.; Benitez, G. A.; Fonticelli, M. H.; Carrasco, J.; Carro, P.; Salvarezza, R. C. Alkanethiol Adsorption on Platinum: Chain Length Effects on the Quality of Self-Assembled Monolayers. *J. Am. Phys. Chem. C* **2011**, *115*, 17788–17798.

17. Bengio, S.; Fonticelli, M.; Benitez, G.; Creus, A. H.; Carro, P.; Ascolani, H.; Zampieri, G.; Blum, B.; Salvarezza, R. C. Electrochemical Self-Assembly of Alkanethiolate Molecules on Ni(111) and Polycrystalline Ni Surfaces. *J. Phys. Chem. B* **2005**, *109*, 23450–23460.

18. Hohman, J. N.; Ki, M.; Wadworth, G. A.; Bednar, H. R.; Jiang, J.; LeThai, M. A.; Weiss, P. S. Directing Substrate Morphology via Self-Assembly: Ligand-Mediated Scission of Gallium-Indium Microspheres to the Nanoscale. *Nano Lett.* **2011**, *11*, 5140–5110.

19. McGuiness, C. L.; Shaporenko, A.; Mars, C. K.; Uppili, S.; Zharnikov, M.; Allara, D. L. Molecular Self-Assembly at Bare Semiconductor Surfaces: Preparation and Characterization of Highly Organized Octadecanethiolate Monolayers on GaAs(001). *J. Am. Chem. Soc.* **2006**, *128*, 5231–5243.

20. Mani, G.; Johnson, D. M.; Marton, D.; Dougherty, V. L.; Feldman, M. D.; Patel, D.; Ayon, A. A.; Agrawal, C. M. Stability of Self-Assembled Monolayers of Alkylphosphonic Acid on Titanium and Gold. *Languir* **2008**, *24*, 6774–6784.

21. Ito, T.; Forman, S. M.; Cao, C.; Li, F.; Eddy C. R., Jr.; Mastro, M. A.; Holm, R. T.; Henry, R. L.; Hohn, K. L.; Edgar, J. H. Self-Assembled Monolayers of Alkylphosphonic Acid on GaN Substrates. *Langmuir* **2008**, *24*, 6630–6635.

22. Hohman, J. N.; Kim, M.; Bednar, H. R.; Lawrence, J. A.; McClanahan, P. D.; Weiss, P. S. Simple, Robust Molecular Self-Assembly on Germanium. *Chem. Sci.* **2011**, *2*, 1334–1343.

23. Noble-Luginbuhl, A. R.; Nuzzo, R. G. Assembly and Characterization of SAMs Formed by the Adsorption of Alkanethiols on Zinc Selenide Substrates. *Langmuir* **2001**, *17*, 3937–3944.

24. Lim, H.; Carraro, C.; Maboudian, R.; Pruessner, M. W.; Ghodssi, R. Chemical and Thermal Stability of Alkanethiol and Sulfur Passivated InP(100). *Langmuir* **2004**, *20*, 743–747.

25. De Feyter, S.; De Schryver, F. C. Two-Dimensional Supramolecular Self-Assembly Probed by Scanning Tunneling Microscopy. *Chem. Soc. Rev.* **2003**, *32*, 139–150.

26. De Feyter, S.; De Schyver, F. C. Self-Assembly at the Liquid/Solid Interface: STM Reveals. *J. Phys. Chem. B* **2005**, *109*, 4290–4302.

27. Xu, L.; Miao, X.; Yung, X.; Deng, W. Two-Dimensional Self-Assembled Molecular Structures Formed by the Competition of van der Waals Forces and Dipole-Dipole Interactions. *J. Phys. Chem. C* **2012**, *116*, 1061–1069.

28. Xue, Y.; Zimmt, M. B. Patterned Monolayer Self-Assembly Programmed by Side Chain Shape: Four Component Gratings. *J. Am. Chem. Soc.* **2012**, *134*, 4513–4516.

29. Correa-Duarte, M. A.; Giersig, M.; Kotov, N. A.; Liz-Marzán, L. M. Control of Packing Order of Self-Assembled Monolayers of Magnetite Nanoparticles with and without SiO_2 Coating by Microwave Irradiation. *Langmuir* **1998**, *14*, 6430–6435.

30. Finnie, K. R.; Haasch, R.; Nuzzo, R. G. Formation and Patterning of Self-Assembled Monolayers Derived from Long-Chain Organosilicon Amphiphiles and Their Use as Templates in Materials Microfabrication. *Langmuir* **2000**, *16*, 6968–6976.

31. Michel, R.; Lussi, J. W.; Csucs, G.; Reviakine, I.; Danuser, G.; Ketterer, B.; Hubbell, J. A.; Textor, M.; Spencer, N. D. Selective Molecular Assembly Patterning: A New Approach to Micro- and Nanochemical Patterning of Surfaces for Biological Applications. *Langmuir* **2002**, *18*, 3281–3287.

32. Luo, M.-L.; Zhao, J.-Q.; Tang, W.; Pu, C.-S. Hydrophillic Modification of Poly(Ether Sulfone) Ultrafiltration Membrane Surface by Self-Assembly of TiO_2 Nanoparticles. *Appl. Surf. Sci.* **2005**, *249*, 76–84.

33. Murphy, K. L.; Tysoe, W. T.; Bennett, D. W. A Comparative Invesitgation of Aryl Isocyanides Chemisorbed to Palladium and Gold: An ATR-IR Spectroscopic Study. *Langmuir* **2004**, *20*, 1732–1738.

34. Allara, D. L.; Parikh, A. N.; Rondelez, F. Evidence for a Unique Chain Organization in Long Chain Silane Monolayers Deposited on Two Widely Different Solid Substrates. *Langmuir* **1995**, *11*, 2357–2360.

35. Lio, A.; Charych, D. H.; Salmeron, M. Comparative Atomic Force Microscopy Study of the Chain Length Depedence of Fricitional Properties of Alkanethiols on Gold and Alkylsilanes on Mica. *J. Phys. Chem. B* **1997**, *101*, 3800–3805.

36. Bourgeat-Lami, E. Organic-Inorganic Nanostructured Colloids. *J. Nanosci. Nanotech.* **2002**, *2*, 1–24.

37. Gouzman, I.; Dubey, M.; Carolus, M. D.; Schwartz, J.; Bernasek, S. L. Monolayer vs. Multilayer Self-Assembled Alkylphosphonate Films: X-ray Photoelectron Spectroscopy Studies. *Surf. Sci.* **2006**, *600*, 773–781.

38. Jewell, A. D.; Kyran, S. J.; Rabinovich, D.; Sykes, E. C. Gentrly Lifting Gold's Herringbone Recontstrcution: Trimethylphosphine on Au(111). *Phys. Rev. B* **2010**, *82*, 205401.

39. Jewell, A. D.; Kryan, S. J.; Rabinovich, D.; Sykes, E. C. Effect of Head-Group of Head-Group Chemistry on Surface-Mediated Molecular Self-Assembly. *Chemistry* **2012**, *18*, 7169–7178.

40. Huang, F. K.; Horton, R. C.; Myles, D. C.; Garrell, R. L. Selenolates as Alternatives to Thiolates for Self-Assembled Monolayers: A SERS Study. *Langmuir* **1998**, *14*, 4802–4808.

41. Monnell, J. D.; Stapleton, J. J.; Jackiw, J. J.; Dunbar, T.; Reinerth, W. A.; Dirk, S. M.; Tour, J. M.; Allara, D. L.; Weiss, P. S. Ordered Local Domain Structures of Decaneselenolate and Dedecaneselenolate Monolayers on Au{111}. *J. Am. Chem. Soc.* **2011**, *133*, 19422–19431.

42. Hohman, J. N.; Kim, M.; Shupach, B.; Kind, M.; Thomas, J. C.; Terfort, A.; Weiss, P. S. Dynamic Double Lattice of 1-Adamantaneselenolate Self-Assembled Monolayers on Au{111}. *J. Am. Chem. Soc.* **2011**, *133*, 19422–19431.

43. Hohman, J. N.; Thomas, J. C.; Zhao, Y.; Auluck, H.; Kim, M.; Vijselaar, W. J. C.; Kommeren, S.; Terfort, A.; Weiss, P. S. Exchange Reactions between Alkanethiolates and Alkaneselenols on Au{111}. *J. Am. Chem. Soc.* **2014**, *136*, 8110–8121.

44. Smith, R. K.; Lewis, P. A.; Weiss, P. S. Patterning Self-Assembled Monolayers. *Prof. Surf. Sci.* **2004**, *75*, 1–68.

45. Li, J.; Li, X.; Ni, X.; Wang, X.; Li, H.; Leong, K. W. Self-Assembled Supramolecular Hydrogels Formed by Biodegradable PEO-PHB-PEO Triblock Copolymers and Alpha-Cyclodextrin for Controlled Drug Delivery. *Biomaterials* **2006**, *27*, 4132–4140.

46. Uemura, S.; Tanoue, R.; Yilmaz, N.; Ohira, A.; Kunitake, M. Molecular Dynamics in Two-Dimemsional Supramolecular Systems Observed by STM. *Materials* **2010**, *3*, 4252–4276.

47. Dorokhin, D.; Hsu, S. H.; Tomczak, N.; Reinhoudt, D. N.; Huskens, J.; Velders, A. H.; Vancso, G. J. Fabrication and Luminescence of Designer Surface Patterns with Beta-Cyclodextrin Functionalized Quantum Dots via Multivalent Supramolecular Coupling. *ACS Nano* **2010**, *4*, 137–142.

48. Gonzalez-Campo, A.; Hsu, S. H.; Puig, L.; Huskens, J.; Reinhouodt, D. N.; Velders, A. H. Orthogonal Covalent and Noncovalent Functionalization of Cyclodextrin-Alkyne Patterned Surfaces. *J. Am. Chem. Soc.* **2010**, *132*, 11434–11436.

49. Hu, W. S.; Tao, Y. T.; Hsu, Y. J.; Wei, D. H.; Wu, Y. S. Molecular Orientation of Evaporated Pentacene Films on Gold: Alignment Effect of Self-Assembled Monolayers. *Langmuir* **2005**, *21*, 2260–2266.

50. Han, P.; Weiss, P. S. Electronic Substrate-Mediated Interactions. *Surf. Sci. Rep.* **2012**, *67*, 19–81.

51. Clegg, R. S.; Reed, S. M.; Hutchison, J. E. Self-Assembled Monolayers Stabilized by Three-Dimensional Networks of Hydrogen Bonds. *J. Am. Chem. Soc.* **1998**, *120*, 2486–2487.

52. Mao, X.; Wang, Y.; Liu, L.; Niu, L.; Yang, Y.; Wang, C. Molecular-Level Evidence of the Surface-Induced Transformation of Peptide Structures Revealed by Scanning Tunneling Microscopy. *Langmuir* **2009**, *25*, 8849–8853.

53. Nowinski, A. K.; Sun, F.; White, A. D.; Keefe, A. J.; Jiang, S. Sequence, Structure, and Function of Peptide Self-Asssembled Monolayers. *J. Am. Chem. Soc.* **2012**, *134*, 6000–6005.

54. Claridge, S. A.; Thomas, J. C.; Silverman, M. A.; Schwartz, J. J.; Wang, Y.; Wang, C.; Weiss, P. S. Differentiating Amino Acids Residues and Side Chain Orientations in Peptides Using Scanning Tunneling Microscopy. *J. Am. Chem. Soc.* **2013**, *135*, 18528–18535.

55. Yu, M.; Bovet, N.; Satterley, C.; Bengió, S.; Lovelock, K.; Milligan, P.; Jones, R.; Woodruff, D; Dhanak, V. True Nature of an Archetypal Self-Assembly System: Mobile Au-Thiolated Species on Au(111). *Phys. Rev. Lett.* **2006**, *97*, 166102.

56. Mazarello, R.; Cossaro, A.; Verdini, A.; Rosseau, R.; Casalis, L.; Danisman, M.; Floreano, L.; Scandolo. S.; Morgante, A.; Scoles, G. Structure of a CH_3S Monolayer on Au(111) Solved by the Interplay between Molecular Dynamics Calculations and Diffraction Measurements. *Phys. Rev. Lett.* **2007**, *98*, 016102.

57. Cossaro, A.; Mazzarello, R.; Rousseau, R.; Casalis, L.;Verdini, A.; Kohlmeyer, A.; Floreano, L.; Scandolo, S.; Morgante, A.; Klein, M. L.; Scoles, G. X-ray Diffraction and Computation Yiled the Structure of Alkanethiols on Gold(111). *Science* **2008**, *321*, 943–946.

58. Hakkinen, H. The Gold-Sulfur Interface at the Nanoscale. *Nature Chem.* **2012**, *4*, 443–455.

59. Maksymovych, P.; Voznyy, O.; Dougherty, D. B.; Sorescu, D. C.; Yates, J. T. Gold Adatom as a Key Structural Compnonent in Self-Aseembled Monolayers of Organosulfur Molecules on Au(111). *Prof. Surf. Sci.* **2010**, *85*, 206–240.

60. Chaudhuri, A.; Lerotholi, T. J.; Jackson, D. C.; Woodruff, D. P.; Dhanak, V. R. The Local Adsorption Structure of Methylthiolate and Butylthiolate on Au(111): A Photoemission Core-Level Shift Investigation. *Surf. Sci.* **2010**, *604*, 227–234.

61. Otálvaro, D.; Veening, T.; Brocks, G. Self-Assembled Monolayer Induced Au(111) and Ag(111) Reconstructions: Work Functions and Interface Dipole Formation. *J. Phys. Chem. C* **2012**, *116*, 7826–7837.

62. Iski, E. V.; Jewell, A. D.; Tierney, H. L.; Kyriakou, G.; Sykes, E. C. H. Organic Thin Film Induced Substrate Restructuring: An STM Study of the Interaction of Naphtho[2,3-a]pyrene Au(111) Herringbone Reconstruction. *J. Vac. Sci. Tech. A* **2011**, *29*, 040601.

63. Han, P.; Kurland, A. R.; Giordano, A. N.; Nanayakkara, S. U.; Blake, M. M.; Pochas, C. M.; Weiss, P. S. Heads and Tails: Simulaneous Exposed and Buried Interface Imaging in Monolayers. *ACS Nano* **2009**, *3*, 3115–3121.

64. Lou, P.; Bemelmans, N. L.; Pearl, T. P. Unveiling Molecular Adsorption Geometry in Cyclohexanethiolate Self-Assembled Monolayers with Local Barrier Height Imagin. *J. Phys. Chem. C* **2011**, *115*, 17118–17122.

65. Thomas, J. C.; Schwartz, J. J.; Hohman, J. N.; Claridge, S. A.; Auluck, H. S.; Serino, A. C.; Spokoyny, A. M.; Tran, G.; Kelly, K. F.; Mirkin, C. A.; Gilles, J.; Osher, S. J.; Weiss, P. S. Defect-Tolerant Aligned Dipoles within Two-Dimensional Plastic Lattices. *ACS Nano* **2015**, *9*, 4734–4742.

66. Iski, E. V.; El-Kouedi, M.; Calderon, C.; Wang, F.; Bellisario, D. O.; Ye, T.; Sykes, E. C. H. The Extraordinary Stability Imparted to Silver Monolayers by Chloride. *Electrochim. Acta* **2011**, *56*, 1652–1661.

67. Jensen, S. C.; Baber, A. E.; Tierney, H. L.; Sykes, E. C. H. Adsorption, Interaction, and Manipulation of Dibutyl Sulfide on Cu{111}. *ACS Nano* **2007**, *1*, 22–29.

68. Tierney, H. L.; Baber, A. E.; Sykes, E. C. H.; Akimov, A.; Kolomeisky, A. B. Dynamics of Thioether Molecular Rotors: Effects and Surface Interactions and Chain Flexibility. *J. Phys. Chem. C* **2009**, *113*, 10913–10920.

69. Bellisario, D. O.; Jewell, A. D.; Tierney, H. L.; Baber, A. E.; Sykes, E. C. H. Adsorption, Assembly, and Dynamics of Dibutyl Sulfide on Au{111}. *J. Phys. Chem. C* **2010**, *114*, 14583–14589.

70. Tierney, H. L.; Han, J. W.; Jewell, A. D.; Iski, E. V.; Baber, A. E.; Sholl, C. S.; Sykes, E. C. H. Chirality and Rotation of Asymmetric Surface-Bound Thioethers. *J. Phys. Chem. C* **2011**, *115*, 897–901.

71. Monnell, J. D.; Stapleton, J. J.; Dirk, S. M.; Reinerth, W. A.; Tour, J. M.; Allara, D. L.; Weiss, P. S. Relative Conductances of Alkaneselenolate and Alkanethiolate Monolayers on Au{111}. *J. Phys. Chem. B* **2005**, *109*, 20343–20349.

72. de la Llave, E.; Scherlis, D. A. Selenium-Based Self-Assembled Monolayers: the Nature of Adsorbate-Surface Interactions. *Langmuir* **2010**, *26*, 173–178.

73. Szelagowska-Kunstman, K.; Cyganik, P.; Schupbach, B.; Terfort, A. Relative Stability of Thiol and Selenol Based SAMs on Au(111) – Exchange Experiments. *Phys. Chem. Chem. Phys.* **2010**, *12*, 4400–4406.

74. Chaudhari, V.; Kotresh, H. M. N.; Srinivasan, S.; Esaulov, Va. A. Substitutional Self-Assembly of Alkanethiol and Selenol SAMs from a Lying-Down Doubly Tethered Butanedithiol SAM on Gold. *J. Phys. Chem. C* **2011**, *115*, 16518–16523.

75. Choi, J.-S.; Kang, H.-G.; Ito, E.; Hara, M.; Noh, J.-G. Phase Transition of Octaneselenolate Self-Assembled Monolayers on Au(111) Studied by Scanning Tunneling Microscopy. *Bull. Kor. Chem. Soc.* **2011**, *32*, 2623–2627.

76. Prato, M.; Toccafondi, C.; Midecchi, G.; Chaudhari, V.; Harish, M. N. K.; Sampath, S.; Parodi, R.; Esaulov, V. A.; Canepa, M. Mercury Segregation and Diselenide Self-Assembly on Gold. *J. Phys. Chem. C* **2012**, *116*, 2431–2437.

77. Livage, J. The Gel Route to Transition Metal Oxides. *J. Sol. St. Chem.* **1986**, *64*, 322–330.

78. Sanchez, C.; Boissière, C.; Grosso, D.; Laberty, C.; Nicole, L. Design, Synthesis, and Properties of Inorganic and Hybrid Thin Films Having Periodically Organized Nanoporosity. *Chem. Mater.* **2008**, *20*, 682–737.

79. Petrović, Z. e.; Katić, J.; Metikoš-Huković, M.; Dadafarin, H.; Omanovic, S. Modification of a Nitinol Surface by Phosphonate Self-Assembled Monolayers. *J. Electrochem. Soc.* **2011**, *158*, F159–F165.

80. Baber, A. E.; Lawton, T. J.; Sykes, E. C. H. Hydrogen-Bonded Networks in Surface-Bound Methanol. *J. Phys. Chem. C* **2011**, *115*, 9157–9163.

81. Grave, C.; Risko, C.; Shaporenko, A.; Wang, Y.; Nuckolls, C.; Ratner, M. A.; Rampi, M. A.; Zharnikov, M. Charge Transport through Oligoarylene Self-assembled Monolayers: Interplay of Molecular Organization, Metal–Molecule Interactions, and Electronic Structure. *Adv. Funct. Mater.* **2007**, *17*, 3816–3828.

82. Baber, A. E.; Jensen, S. C.; Sykes, E. C. Dipole-Driven Ferroelectric Assembly of Styrene on Au{111}. *J. Am. Chem. Soc.* **2007**, *129*, 6368–6369.

83. Yan, L.; Zheng, Y. B.; Zhao, F.; Li, S.; Gao, X.; Xu, B.; Weiss, P. S.; Zhao, Y. Chemistry and Physics of a Single Atomic Layer: Strategies and Challenges for Functionalization of Graphene and Graphene-Based Materials. *Chem. Soc. Rev.* **2012**, *41*, 97–114.

84. Arakawa, H.; Umemura, K.; Ikai, A. Protein Images Obtained by STM, AFM and TEM. *Nature* **1992**, *358*, 171–173.

85. Mao, X.; Wang, C.; Ma, X.; Zhang, M.; Liu, L.; Zhang, L.; Niu, L.; Zeng, Q.; Yang, Y. Molecular Level Studies on Binding Modes of Labeling Molecules with Polyalanine Peptides. *Nanoscale* **2011**, *3*, 1592–1599.

86. Torres, E.; Blumenau, A. T.; Biedermann, P. U. Steric and Chain Length Effects in the ($\sqrt{3}\times\sqrt{3}$)*R*30° Structures of Alkanethiol Self-Assembled Monolayers on Au(111). *ChemPhysChem* **2011**, *12*, 999–1009.

87. Kumar, A. S.; Ye, T.; Takami, T.; Yu, B. C.; Flatt, A. K.; Tour, J. M.; Weiss, P. S. Reversible Photo-Switching of Single Azobenzene Molecules in Controlled Nanoscale Environments. *Nano Lett.* **2008**, *8*, 1644–1648.

88. Kim, M.; Hohman, J. N.; Serino, A. C.; Weiss, P. S. Structural Manipulation of Hydrogen-Bonding Networks in Amide-Containing Alkanethiolate Monolayers via Electrochemical Processing. *J. Phys. Chem C* **2010**, *114*, 19744–19751.

89. Zheng, Y. B.; Payton, J. L.; Chung, C. H.; Liu, R.; Cheunkar, S.; Pathem, B. K.; Yang, Y.; Jensen, L.; Weiss, P. S. Surface-enhanced Raman Spectroscopy to Probe Reversibly Photoswitchable Azobenzene in Controlled Nanoscale Environments. *Nano Lett.* **2011**, *11*, 3447–3452.

90. Noh, J.; Ito, E.; Hara, M. Self-Assembled Monolayers of Benzenethiol and Benzenemethanethiol on Au(111): Influence of an Alkyl Spacer on the Structure and Thermal Desorption Behavior. *J. Coll. Inter. Sci.* **2010**, *342*, 513–517.

91. Hohman, J. N.; Claridge, S. A.; Kim, M.; Weiss, P. S., Cage Molecules for Self-Assembly. *Mater. Sci. Eng. R* **2010**, *70*, 188–208.

92. Kim, M.; Hohman, J. N.; Morin, E. I.; Daniel, T. A.; Weiss, P. S. Self-Assembled Monolayers of 2-Adamantanethiol on Au{111}: Control of Structure and Displacement. *J. Phys. Chem. A* **2009**, *113*, 3895–3903.

93. Bould, J.; Macháček, J.; Londesborough, M. G.; Macias, R.; Kennedy, J. D.; Bastl, Z.; Rupper, P.; Baše, T. Decaborane Thiols as Building Blocks for Self-Assembled Monolayers on Metal Surfaces. *Inorg. Chem.* **2012**, *51*, 1685–1694.

94. Jobbins, M. M.; Raigoza, A. F.; Kandel, S. A. Adatoms at the Sulfur–Gold Interface in 1-Adamantanethiolate Monolayers, Studied Using Reaction with Hydrogen Atoms and Scanning Tunneling Microscopy. *J. Phys. Chem. C* **2011**, *115*, 25437–25441.

95. Hohman, J. N.; Zhang, P.; Morin, E. I.; Han, P.; Kim, M.; Kurland, A. R.; McClanahan, P. D.; Balema, V. P.; Weiss, P. S. Self-Assembly of Carboranethiol Isomers on Au(111): Intermolecular Interactions Determined by Molecular Dipole Orientations. *ACS Nano* **2009**, *3*, 527–536.

96. Spokoyny, A. M.; Machan, C. W.; Clingerman, D. J.; Rosen, M. S.; Wiester, M. J.; Kennedy, R. D.; Stern, C. L.; Sarjeant, A. A.; Mirkin, C. A. A Coordination Chemistry Dichotomy for Icosahedral Carborane-Based Ligands. *Nature Chem.* **2011**, *3*, 590–596.

97. Clegg, R. S.; Hutchison, J. E. Control of Monolayer Assembly Structure by Hydrogen Bonding Rather Than by Adsorbate−Substrate Templating. *J. Am. Chem. Soc.* **1999**, *121*, 5319–5327.

98. Lewis, P. A.; Smith, R. K.; Kelly, K. F.; Bumm, L. A.; Reed, S. M.; Clegg, R. S.; Gunderson, J. D.; Hutchison, J. E.; Weiss, P. S. The Role of Buried Hydrogen Bonds in Self-Assembled Mixed Composition Thiols on Au{111}. *J. Phys. Chem. B* **2001**, *105*, 10630–10636.

99. Smith, R. K.; Reed, S. M.; Lewis, P. A.; Monnell, J. D.; Clegg, R. S.; Kelly, K. F.; Bumm, L. A.; Hutchison, J. E.; Weiss, P. S. Phase Separation within a Binary Self-Assembled Monolayer on Au{111} Driven by an Amide-Containing Alkanethiol. *J. Phys. Chem. B* **2001**, *105*, 1119–1122.

100. Moore, A. M.; Yeganeh, S.; Yao, Y.; Claridge, S. A.; Tour, J. M.; Ratner, M. A.; Weiss, P. S. Polarizabilities of Adsorbed and Assembled Molecules: Measuring the Conductance through Buried Contacts. *ACS Nano* **2010**, *4*, 7630–7636.

101. Yoon, H. J.; Shapiro, N. D.; Park, K. M.; Thuo, M. M.; Soh, S.; Whitesides, G. M., The Rate of Charge Tunneling through Self-Assembled Monolayers is Insensitive to Many Functional Group Substitutions. *Angew. Chem. Int. Ed. Engl.* **2012**, *51*, 4658–4661.

102. Lawton, T.; Carrasco, J.; Baber, A.; Michaelides, A.; Sykes, E. C. Visualization of Hydrogen Bonding and Associated Chirality in Methanol Hexamers. *Phys. Rev. Lett.* **2011**, *107*, 256101.

103. McGuire, A. F.; Jewell, A. D.; Lawton, T. J.; Murphy, C. J.; Lewis, E. A.; Sykes, E. C. H. Hydrogen Bonding and Chirality in Functionalized Thioether Self-Assembly. *J. Phys. Chem. C* **2012**, *116*, 14992–14997.

104. Wang, H.; He, Y.; Ratner, B. D.; Jiang, S. Modulating Cell Adhesion and Spreading by Control of $FnIII_{7\text{-}10}$ Orientation on Charged Self-Assembled Monolayers (SAMs) of Alkanethiolates. *J. Biomed. Mater. Res. A* **2006**, *77*, 672–678.

105. Patnaik, A.; Setoyama, H.; Ueno, N. Surface/Interface Electronic Structure in C(60) Anchored Aminothiolate Self-Assembled Monolayer: An Approach to Molecular Electronics. *J. Chem. Phys.* **2004**, *120*, 6214–6221.

106. Chambers, R. C.; Inman, C. E.; Hutchison, J. E. Electrochemical Detection of Nanoscale Phase Separation in Binary Self-Assembled Monolayers. *Langmuir* **2005**, *21*, 4615–4621.

107. Carot, M. L.; Macagno, V. A.; Paredes-Olivera, P.; Patrito, E. M. Structure of Mixed Carboxylic Acid Terminated Self-Assembled Monolayers: Experimental and Theoretical Investigation. *J. Phys. Chem. C* **2007**, *111*, 4294–4304.

108. Romaner, L.; Heimel, G.; Zojer, E. Electronic Structure of Thiol-Bonded Self-Assembled Monolayers: Impact of Coverage. *Phys. Rev. B* **2008**, *77*, 045113.

109. Watcharinyanon, S.; Moons, E.; Johansson, L. S. O. Mixed Self-Assembled Monolayers of Ferrocene-Terminated and Unsubstituted Alkanethiols on Gold: Surface Structure and Work Function. *J. Phys. Chem. C* **2009**, *113*, 1972–1979.

110. Yagüe, J. L.; Agulló, N.; Fonder, G.; Delhalle, J.; Mekhalif, Z.; Borrós, S. Thiol versus Selenol SAMs as Nucleation Enhancers and Adhesion Promoters for Plasma Polymerized Pyrrole on Copper Substrates. *Plasma Process. Polym.* **2010**, *7*, 601–609.

111. Cho, J.; Berbil-Bautista, L.; Levy, N.; Poulsen, D.; Frechet, J. M.; Crommie, M. F. Functionalization, Self-Assembly, and Photoswitching Quenching for Azobenzene Derivatives Adsorbed on Au(111). *J. Chem. Phys.* **2010**, *133*, 234707.

112. Lee, S. H.; Lin, W. C.; Chang, C. J.; Huang, C. C.; Liu, C. P.; Kuo, C. H.; Chang, H. Y.; You, Y. W.; Kao, W. L.; Yen, G. J.; Kuo, D. Y.; Kuo, Y. T.; Tsai, M. H.; Shyue, J. J. Effect of the Chemical Composition on the Work Function of Gold Substrates Modified by Binary Self-Assembled Monolayers. *Phys. Chem. Chem. Phy.* **2011**, *13*, 4335–4339.

113. Abendroth, J. M.; Bushuyev, O. S.; Weiss, P. S.; Barrett, C. J. Controlling Motion at the Nanoscale: Rise of the Molecular Machines. *ACS Nano* **2015**, ASAP, DOI: 10.1021/acsnano.5b03367.

114. Saavedra, H. M.; Thompson, C. M.; Hohman, J. N.; Crespi, V. H.; Weiss, P. S. Reversible Lability by In Situ Reaction of Self-Assembled Monolayers. *J. Am. Chem. Soc.* **2009**, *131*, 2252–2259.

115. Vaish, A.; Shuster, M. J.; Cheunkar, S.; Singh, Y. S.; Weiss, P. S.; Andrews, A. M. Native Serotonin Membrane Receptors Recognize 5-Hydroxytryptophan-Functionalized Substrates: Enabling Small-Molecule Recognition. *ACS Chem. Neurosci.* **2010**, *1*, 495–504.

116. Vaish, A.; Liao, W. S.; Shuster, M. J.; Hinds, J. M.; Weiss, P. S.; Andrews, A. M. Thin Gold Film-Assisted Fluorescence Spectroscopy for Biomolecule Sensing. *Anal. Chem.* **2011**, *83*, 7451–7456.

117. Shuster, M. J.; Vaish, A.; Gilbert, M. L.; Martinez-Rivera, M.; Nezarati, R. M.; Weiss, P. S.; Andrews, A. M. Comparison of Oligo(ethylene glycol)Alkanethiols versus *n*-Alkanethiols: Self-Assembly, Insertion, and Functionalization. *J. Phys. Chem. C* **2011**, *115*, 24778–24787.

118. Smith, R. K.; Nanayakkara, S. U.; Woehrle, G. H.; Pearl, T. P.; Blake, M. M.; Hutchison, J. E.; Weiss, P. S. Spectral Diffusion in the Tunneling Spectra of Ligand-Stabilized Undecagold Clusters. *J. Am. Chem. Soc.* **2006**, *128*, 9266–9267.

119. Kim, M.; Hohman, J. N.; Cao, Y.; Houk, K. N.; Ma, H.; Jen, A. K.; Weiss, P. S. Creating Favorable Geometries for Directing Organic Photoreactions in Alkanethiolate Monolayers. *Science* **2011**, *331*, 1312–1315.

120. Donhauser, Z. J.; Mantooth, B. A.; Kelly, K. F.; Bumm, L. A.; Monnell, J. D.; Stapleton, J. J.; Price Jr, D. W.; Rawlett, A. M.; Allara, D. L.; Tour, J. M.; Weiss, P. S. Conductance Switching in Single Molecules through Conformational Changes. *Science* **2001**, *292*, 2303–2307.

121. Lewis, P. A.; Inman, C. E.; Yao, Y.; Tour, J. M.; Hutchison, J. E.; Weiss, P. S. Mediating Stochastic Switching of Single Molecules using Chemical Functionality. *J. Am. Chem. Soc.* **2004**, *126*, 12214–12215.

122. Lewis, P. A.; Inman, C. E.; Maya, F.; Tour, J. M.; Hutchison, J. E.; Weiss, P. S. Molecular Engineering of the Polarity and Interactions of Molecular Electronic Switches. *J. Am. Chem. Soc.* **2005**, *127*, 17421–17426.

123. Moore, A. M.; Dameron, A. A.; Mantooth, B. A.; Smith, R. K.; Fuchs, D. J.; Ciszek, J. W.; Maya, F.; Yao, Y.; Tour, J. M.; Weiss, P. S. Molecular Engineering and Measurements to Test

Hypothesized Mechanisms in Single Molecule Conductance Switching. *J. Am. Chem. Soc.* **2006**, *128*, 1959–1967.

124. Chi, Q.; Zhang, J.; Ulstrup, J. Surface Microscopic Structure and Electrochemical Rectification of a Branched Alkanethiol Self-Assembled Monolayer. *J. Phys. Chem. B* **2006**, *110*, 1102–1106.

125. Cyganik, P.; Buck, M.; Strunskus, T.; Shaporenko, A.; Witte, G.; Zharnikov, M.; Woll, C. Influence of Molecular Structure on Phase Transitions: A Study of Self-Assembled Monolayers of 2-(Aryl)-ethane Thiols. *J. Phys. Chem. C* **2007**, *111*, 16909–16919.

126. Kafer, D.; Witte, G.; Cyganik, P.; Terfort, A.; Woll, C. A Comprehensive Study of Self-Assembled Monolayers of Anthracenethiol on Gold: Solvent Effects, Structure, and Stability. *J. Am. Chem. Soc.* **2006**, *128*, 1723–32.

127. Xu, S.; Liu, G.-Y. Nanometer-Scale Fabrication by Simultaneous Nanoshaving and Molecular Self-Assembly. *Langmuir* **1997**, *13*, 127–129.

128. Bu, D.; Mullen, T. J.; Liu, G. Y. Regulation of Local Structure and Composition of Binary Disulfide and Thiol Self-Assembled Monolayers Using Nanografting. *ACS Nano* **2010**, *4*, 6863–6873.

129. Binnig, G.; Rohrer, H; Gerber, C.; Weibel, E. Surface Studies by Scanning Tunneling Microscopy. *Phys. Rev. Lett.* **1982**, *49*, 57–61.

130. Binnig, G.; Rohrer, H. Nobel Lecture: Scanning Tunneling Microscopy - From Birth to Adolescence, 1986.

131. Binnig, G.; Rohrer, H. Scanning Tunneling Microscopy - From Birth to Adolescence. *Rev. Mod. Phys.* **1987**, *59*, 615–629.

132. Chen, C. J. *Introduction to Scanning Tunneling Microscopy*; Oxford University Press: New York City, 1993.

133. Wiesendanger, R.; Eng, L.; Hidber, H. R.; Oelhafen, P.; Rosenthaler, L.; Staufer, U.; Güntherodt, H. J. Local Tunneling Barrier Height Images Obtained with the Scanning Tunneling Microscope. *Surf. Sci.* **1987**, 189–190, 24–28.

134. Olesen, L.; Brandbyge, M.; Sørensen, M.; Jacobsen, K.; Lægsgaard, E.; Stensgaard, I.; Besenbacher, F. Apparent Barrier Height in Scanning Tunneling Microscopy Revisited. *Phys. Rev. Lett.* **1996**, *76*, 1485–1488.

135. Rusu, P.; Brocks, G. Work Functions of Self-Assembled Monolayers on Metal Surfaces by First-Principles Calculations. *Phys. Rev. B* **2006**, *74*, 073414.

136. Hollander, J. M.; Jolly, W. L. X-ray Photoelectron Spectroscopy. *Acc. Chem. Res.* **1970**, *3*, 193–200.

137. Thomas, J. C.; Boldog, I.; Auluck, H. S.; Bereciartua, P.; Dušek, M.; Macháček, J.; Bastl, Z.; Weiss, P. S.; Baše, T. Self-Assembled *p*-Carborane Analog of *p*-Mercaptobenzoic Acid on Au{111}. *Chem. Mater.* **2015**, *27*, 5425–5435.

138. Wang, Z. L. Transmission Electron Microscopy of Shape-Controlled Nanocrystals and Their Assemblies. *J. Phys. Chem. B* **2000**, *104*, 1153–1175.

139. Stranick, S. J.; Kamna, M. M.; Weiss, P. S. Atomic-Scale Dynamics of a Two-Dimensional Gas-Solid Interface. *Science* **1994**, *266*, 99–102.

140. Ye, T.; Kumar, A. S.; Saha, S.; Takami, T.; Huang, T. J.; Stoddart, J. F.; Weiss, P. S. Changing Stations in Single Bistable Rotaxane Molecules under Electrochemical Control. *ACS Nano* **2010**, *4*, 3697–3701.

CHAPTER 2

Defect-Tolerant Aligned Dipoles within Two-Dimensional Plastic Lattices

2.1 Introduction

Engineering molecular systems with precisely determined positions, orientations, and interactions enables control over chemical reactions[1] with implications for catalysis, nanomaterials engineering, and bio-assembly.[2-7] Molecular dipole alignment has been demonstrated using strong electrostatic fields, collisional forces, and intense laser fields.[8-11] Most alignment characterization methods are ensemble measurements, where local information is lost through averaging.[12-14] The promise of using scanning tunneling microscopy (STM) to resolve chemical state information, at the single-molecule scale, beyond structure, has spurred the development of a plethora of technique extensions, including photon-coupled, alternating current, and microwave-coupled STM.[1,15-22] We employ multimodal STM to visualize molecular alignment of dipole-containing carboranethiolate within self-assembled monolayers (SAMs) at 4 K. We measure local barrier height (LBH) as a function of position across the surface by modulating the tip-surface separation distance (z) around its constant-current (I) topographic imaging value, which is a convolution of both topographic and electronic information. The first harmonic (dI/dz) of the modulated current is mapped as the LBH of the sample, which is related to the local work function.[23-26] This enables simultaneous measurements of the local dipoles and the exposed interface to visualize molecular orientations within simple two-dimensional systems. Here, we observe molecular alignment spanning areas of ~10^3 Å^2, driven by dipole-dipole interactions within SAMs. These long-range interactions, proportional to the inverse cube of the dipole separation ($\propto r^{-3}$) and therefore outside the purview of the Mermin-Wagner theorem,[27,28] support azimuthal molecular ordering. Measurements are recorded using a custom-built, ultrastable microscope.[29] We use STM to determine the interplay between molecular geometry and intermolecular interactions.

Self-assembly provides a convenient platform for the construction of well-defined monomolecular films, with applications ranging from nanotechnology to the life sciences.[30-35] While the more commonly used *n*-alkanethiols in monolayers tilt and have many conformational degrees of freedom that lead to defects, carboranethiols are rigid, three-dimensional carbon-boron-hydrogen cage compounds that adsorb upright and readily form ordered monolayers on gold.[36,37] Since carboranethiols on Au{111} form identical monolayer lattices independent of isomer, they provide simple systems with which to test the effects of intermolecular interactions without varying monolayer structure.[38,39] Motivated by the observation that, at room temperature, carboranethiols with dipole components parallel to the surface outcompete those with dipoles normal to the surface, we sought to observe directly the intermolecular dipole interactions most likely to be responsible for this effect. Conventional STM enables the determination of the positions of individual molecules, but not the orientation nor rotation in azimuthally symmetric systems. Here, carboranethiol isomers contain symmetric backbones and many have significant dipoles, but appear topographically symmetric in STM measurements. As noted above, we inferred that the results of the competitive binding of carboranethiol isomers were due to dipolar interactions, but it was not possible to resolve the orientations of individual symmetric molecules such as carboranethiols until now. We use STM topographic and spectroscopic imaging to measure topography and the spatial dipole orientation, simultaneously, with submolecular resolution. We compare and contrast monolayers of *o*-9-carboranethiolate (**O9**) and *m*-1-carboranethiolate (**M1**); the largest local contribution to charge separation is from the electron-deficient carbon atoms in the *ortho* and *meta* positions, respectively. We then correlate topographic maxima with the tunneling barrier-height extrema to measure the dipole offset within different regions, molecular domains, substrate terraces, and molecules within the SAMs.

Monolayers of carboranethiols and other upright symmetric cage molecules have lattices determined by the projections of the cages on the substrate surface.[37,39-41] Thus, the **O9** and **M1** carboranethiol SAMs have identical lattices. The most common defects in these monolayers are substrate step edges and molecular domain boundaries in which there is a translational (phase) offset of the registry of the lattice of attachment to the substrate.[37,39,40,42,43]

2.2 Results and Discussion

Topographic and LBH modalities are measured simultaneously. We image domains in **O9** monolayers (Figure 2.1 A-C) and compare local molecular dipole orientations across monatomic substrate steps (Figure 2.1 E, F). Local extrema in both modalities are computed within a square pixel window having a width of the approximate nearest neighbor spacing (~7.2 Å). Variations in the tunneling LBH, $\varphi = 0.95(dln(I)/dz)^2$, are related to variations in the local molecular dipole,[44-46] enabling the association of LBH extrema to the substrate dipole signal maxima or minima, while topographic maxima correspond to molecular apexes. The **O9** molecule was designed to contain a large dipole (5.72 D) that is tilted off normal with respect to the underlying substrate surface (see materials and methods for synthesis and appendix A.1 for molecular dipole computation) and we assign LBH minima as the local work function signal minima due to *o*-carbon atoms. Topographic and LBH extrema are overlaid, and the offsets between them are evaluated via block-matching[47,48] to compute correlations between sliding image patches in both bounded modalities within a molecular-sized search window (Figure 2.2). Rose plots are used to depict the dipole offsets from topographic maxima, binned by orientation and magnitude, of multiple domains using image thresholding and masking techniques (Figure 2.3). The analysis of dipole direction across a Au{111} step edge reveals aligned molecular orientations of 154 ± 28° on the

upper terrace and 160 ± 22° on the lower terrace, with respect to the (horizontal, fast-scan direction) image axis of both topography and LBH. Figure 2.4 highlights two groupings of molecules within the same area examined in Figure 2.1, where the local dipole orientations are measured to be 49 ± 5° and 156 ± 28°. Different dipole orientations have been observed in the same multimodal image pairs, but are uncommon. This defect tolerance of dipole alignment with regard to structural domain boundaries and substrate step edges is discussed further below.

We contrast molecular **O9** orientation measurements with those made on SAMs of **M1**, which possess the same lattice structure.[39] Molecular dipoles of **M1** (1.06 D) are smaller in magnitude with the largest component oriented in the plane of the substrate. The LBH minima measured correspond to the electron-deficient carbon atoms at both the 1- and 2-positions within **O9** monolayers and the 1- and 7-carbon atoms within **M1** monolayers. The same analyses, in which topographic maxima and LBH minima are overlaid and correlations are computed, are performed for regions of **M1** SAMs, and orientations are mapped within single atomically flat terraces of gold (Figure 2.5). In Figure 4, three regions are highlighted by inspection, where two are lattice matched with different orientations and the third is a region of local disorder, as confirmed by Fourier analysis of the segmented domains (Figure 2.6). As noted previously, the domain boundaries in complete monolayers of upright symmetric cage molecules are simpler and more difficult to identify than those of the more common alkanethiols and other linear, tilted molecules with conformational degrees of freedom.[39,40] This simplicity is the result of having only rotational and translational lattice offsets between neighboring domains.

In the analyzed regions shown, dipoles are oriented 88 ± 47° with respect to the (horizontal, fast-scan direction) image axis. For both carboranethiol monolayers, defect-tolerant alignment is

observed across both substrate step edges and molecular domain boundaries. This is further demonstrated over 44 h of imaging, where aligned orientations (63 ± 45°) are measured although separated by a monatomic Au{111} substrate step. We observe that, like the molecular structural domain boundaries, the relatively small spatial offset of the substrate step is transited by dipole-dipole interactions, leading to dipole alignment that cross these interfaces.

Correlations are computed using sliding patches taken at the same positions in each image window for each maximum p in the topographic images and each maximum q in the LBH images. We obtain a set of vectors, pq, associated with each dipole. Our analysis shows that the lateral offset measured within **O9** monolayers is 2.0 ± 0.4 Å, as depicted in Figure 1. Correlated local topographic maxima and LBH minima of **M1** SAMs reveal a local offset of 2.3 ± 0.7 Å in Figure 2.5. Across many samples and images ($n_{molecules} > 1000$), **O9** displays an average offset of 1.9 ± 0.5 Å and **M1** shows an average offset of 1.9 ± 0.6 Å. Recently, long-range dipolar interactions of carboranethiol isomers across aqueous media were observed, where molecular dipoles oriented parallel to the surface experience stronger intermolecular interactions that those oriented normal to the surface, likely due to the correlation of lateral surface dipoles.[49] Density functional theory is employed to extrapolate a point dipole that is used to predict alignment.

We apply a simple model to determine the dipole–dipole interaction energies within a SAM and use it to understand the observed data (Figure 2.7). In brief, we define each molecule's dipole interaction energy as the potential energy of its calculated dipole moment in the local electric field it experiences. The in-plane component of the electric field from the tip is insignificant in the tunneling junction; thus, we do not include tip-induced electric field effects in our calculations. This assumption is tested experimentally and confirmed, where molecular orientations remain

fixed in space, independent of scan direction, for over 44 h of imaging at low temperature (Figure 2.8). In our model, the surrounding molecules, assumed to be ideal electric dipoles arranged in a hexagonal lattice, determine the field's strength and direction. Alignment with (against) the field acts to stabilize (change) the dipole orientations. Using this model, we estimate the molecules' interaction energies, and changes in those energies, resulting from dipole reorientations with respect to the surrounding SAM lattice. In order to determine possible stable orientations of molecular dipoles in a SAM, we employ a Monte Carlo method using the Metropolis algorithm[50] and the interaction energies described above. When the temperature is sufficiently low, we find that the system spontaneously evolves toward a state in which the dipoles align along a common direction, as illustrated in Figure 2.9. The favorable dipole alignment energy stabilizes their orientations and promotes the formation and growth of locally ordered regions of molecular dipoles. These results are consistent with the STM topographic and LBH data discussed above and explain the mechanism driving dipole ordering. We expect the transition temperature for the observed molecular alignment occurs between 4 and 293 K, as suggested by our model, but we have neither determined this transition temperature experimentally nor performed temperature-dependent simulations.

Scanning tunneling microscopy can image both molecular overlayers and substrate atoms to make absolute tilt assignments in the case where the molecule-substrate bonds determine the largest dipoles.[26,51] Our measurements, instead, use LBH imaging with molecules possessing a permanent dipole to resolve local orientation within the SAM's chemical environment for the first time. Both topographic and LBH images, 256×256 pixels, are initially corrected for image aberrations, caused by residual drift and non-orthogonalities of the scanner tube during the time allotted for high-resolution data acquisition (~2 h), on a line-by-line basis using a matrix

transformation approach (Figures 2.10 and 2.11). Shear distortions are accounted for in Fourier space, and the corrected images are used in further analyses. Local barrier height images are inverted for clarity and local extrema are overlaid (Figures 2.12 and 2.13); we then connect each topographic maximum to all LBH maxima within a square pixel window as a function size and compare these results to the computed correlations, described above, for both molecular monolayers. In both **O9** and **M1** images shown, the block-matching approach yields the maximum computed correlation, while connecting all extrema in a square pixel window, as a function of size, exhibits increased artifacts. We also compare entropy metrics, quantified in MATLAB (Figures 2.14 and 2.15), within local regions in **O9** monolayers and in **M1** monolayers. When entropy grayscale values are measured in each 9×9 pixel neighborhood, centered at each pixel, mean entropy values in both topographic and LBH image masks contain a large number (256) of accessible values and therefore demonstrate higher image textural contrast in comparison to binary images (with only two possible values) with mean entropy grayscale values near zero.[52] In previous work, near continuous modulation of the metal work function of ~1 eV was attained with controlled mixtures of carboranethiol isomers and these monolayers were shown to be robust with respect to coverage with active organic layers in fabricated devices.[53] Local barrier heights in the figures above show similar modulation of the work function with respect to Au{111}. The analysis and segmentation techniques described here are used to identify the (lattice registry) domains of the carboranethiolates in addition to the dipole orientations within and between domains.[54-56] Data acquisition coupled with new image analysis techniques enable understanding of local snapshots between bounded topographically exposed and dipole interfacial modalities.

2.3 Conclusions and Prospects

This multi-modal imaging procedure permits the measurement of molecular orientations by correlating topographic and LBH images. Carboranethiols are a fruitful system for study, in that both pure **M1** and **O9** form monolayers containing fewer types and number of defects compared to assemblies of linear and/or tilted molecules with conformational and orientational degrees of freedom,[37,39,57-60] and contain a large molecular dipole originating from their rigid cage. Isomeric carborane systems may find immediate application in the fields of molecular machines, dipolar rotors, and functionalized coatings for device frameworks.[49,52,61,62] Scanning tunneling microscopy is able to probe the exposed two-dimensional interface in topographic mode and the corresponding buried dipole interface in LBH mode, simultaneously. We have successfully determined molecular orientation within azimuthally symmetric carboranethiolate monolayers. We have found that dipole alignment crosses domain boundaries and substrate steps. These results are consistent with the preference for adsorption of carboranethiols with dipole components lateral to the surface over those with dipoles normal to the surface observed in competitive adsorption from mixed solutions.[39]

Creating monolayer systems with defect tolerance and precisely determined dipoles enables greater tunability of assemblies with enhanced control of stability through designed interactions. Other single-molecule measurement techniques are hindered by either extreme dilution or specificity, whereas STM can measure the local environment with submolecular resolution and use spectroscopic imaging for chemical identification.[17,61-67] We anticipate that determining and structuring chemical environments with cage-molecule assemblies will be important in creating atomically precise structures in two and three dimensions.

2.4 Materials and Methods

2.4.1 Self-Assembled Monolayer Preparation

Benzene and **M1** were used as received (Sigma-Aldrich, St. Louis, MO). The chemical **O9** was synthesized and characterized in accordance with previously published methods.[43] The Au{111}/mica substrates (Agilent Technology, Tempe, AZ) were hydrogen-flame-annealed prior to SAM formation with 10 passes at a rate of 0.4 Hz. Both SAMs were prepared by immersion into 1 mM solutions in benzene, held at room temperature, for approximately 10 min. Short deposition times were employed to increase the occurrence of local defects and still obtain a well-ordered monolayer. After deposition, each sample was rinsed thoroughly with neat benzene, dried under a stream of ultrahigh purity argon, and then inserted into the UHV chamber for analysis.

2.4.2 Nanoscale Imaging

All STM measurements were performed with a custom-built Besoke-style scanning tunneling microscope held at cryogenic (4 K) and extreme high vacuum ($<10^{-12}$ torr) conditions.[68] Samples were held at a fixed bias (V_{sample} = -0.5 V) and both topographic and LBH modalities were measured in a constant current fashion (I_t = 15 pA). The tunneling-gap distance was oscillated above the microscope feedback loop (~3 kHz) with a sinusoidal amplitude (dz ~ 0.1 Å) and dI/dz was measured with a lock-in technique (Stanford Research Systems SR850 DSP, Sunnyvale, CA). The well-known lattice of atomic Au{111}, held at 4 K, was measured and used to calibrate all images. The measured LBH magnitude may vary in cases where the applied voltage does not exactly equal the voltage across the tunneling junction.[45,69] With this condition in mind, local

barrier height micrographs were calibrated against Au step edge measurements to verify the procedure used (Figure 2.16).

2.4.3 Image Analyses

All STM images were processed and matrix-smoothed with automated routines developed in MATLAB (Mathworks, Natick, MA) to remove any high-frequency noise and intensity spikes that may otherwise impair reliable extrema selection.[26] Images were then skew-corrected and checked in Fourier space to remove any image aberrations due to drift and piezoelectric transducer non-linearities. We denote points p and q as local maxima in topographic and inverted LBH images, respectively. A point p was considered a local maximum if its intensity was greater than that of all surrounding pixels within a molecular-sized neighborhood of radius ws; the same method was used to compute each point q in the LBH image. After the sets of points p and q were obtained, an image patch centered at each p, of the size $[2ps + 1] \times [2ps + 1]$, was then correlated at each pixel against a larger LBH image patch, centered at q, of the size $[2qs + 1] \times [2qs + 1]$. Parameter qs is the size of the next-nearest neighbor spacing, and parameter ps is the size of one molecule. This technique is referred to as block-matching that has established use in the fields of image compression and object recognition.[47,48,70,71] The maximum correlation was chosen for each point p to q, which was then referenced and plotted.

2.4.4 Dipole-Dipole Interaction Energy

We modeled each carboranethiol molecule as an ideal electric dipole moment located at the center of its cage moiety in a hexagonally close-packed array. We estimated a molecule's dipole

interaction energy to be the electric potential energy (U) of the molecule's dipole moment ($\vec{p}$) in the local electric field ($\vec{E}$),

$$U = -\vec{p} \cdot \vec{E}$$

The electric field is the vector sum of the fields produced by the surrounding dipoles,

$$\vec{E} = \sum_i \frac{1}{4\pi\epsilon_0} \frac{3(\vec{p}_i \cdot \hat{r})\hat{r} - \vec{p}_i}{r^3}$$

where r represents the separation distance between the molecule under consideration and its i^{th} neighboring dipole moment ($\vec{p}_i$). The gold substrate also influences the electric field due to the induced charge on the conductor, effectively producing an image dipole beneath the surface for each dipole in the SAM. The dipole interaction strength diminishes as r^{-3}, making more distant dipole moments less significant contributors to the calculated energy. Accordingly, the summation above includes only the neighboring molecular dipoles, and image dipoles, contained within the first four concentric, hexagonal rings surrounding the considered molecule. Finally, we assumed left-right and top-bottom periodicity in our modeled SAM, such that opposite edges of the rectangular molecular lattice coincided, and thus simulated an infinite monolayer.

2.4.5 Monte Carlo Simulations

We used the Metropolis algorithm to determine possible equilibrium orientations of molecular dipole moments within a SAM. Iteratively, the interaction energy of a randomly chosen molecule within a SAM was computed before and after a proposed reorientation. Each reorientation rotated the molecule by a random angle about an axis normal to the substrate, thereby only altering the lateral position and in-plane components of the dipole moment. Depending on the change in energy,

the reorientation was either accepted and preserved in subsequent iterations, or discarded without changing the state of the system. The probability of preserving the change is,

$$\text{Probability}(\%) = 100 \times \begin{cases} 1, \Delta E < 0 \\ e^{-\Delta E / k_B T}, \Delta E \geq 0 \end{cases}$$

where ΔE is the change in the dipole interaction energy due to the reorientation, T is the absolute temperature of the system, and k_B is the Boltzmann constant.

We initialized a model SAM to have no net in-plane polarization (randomized molecular azimuths) and allowed it to evolve through successive iterations. Our simulations predict that, at the low temperatures used experimentally (4 K), both **O9** and **M1** SAMs evolve toward states with regions of locally aligned in-plane molecular dipoles, as shown in the STM data. However, we did not observe spontaneous dipole ordering near room temperature (~293 K) and, furthermore, note the loss of order in a pre-aligned SAM due to random thermal reorientations.

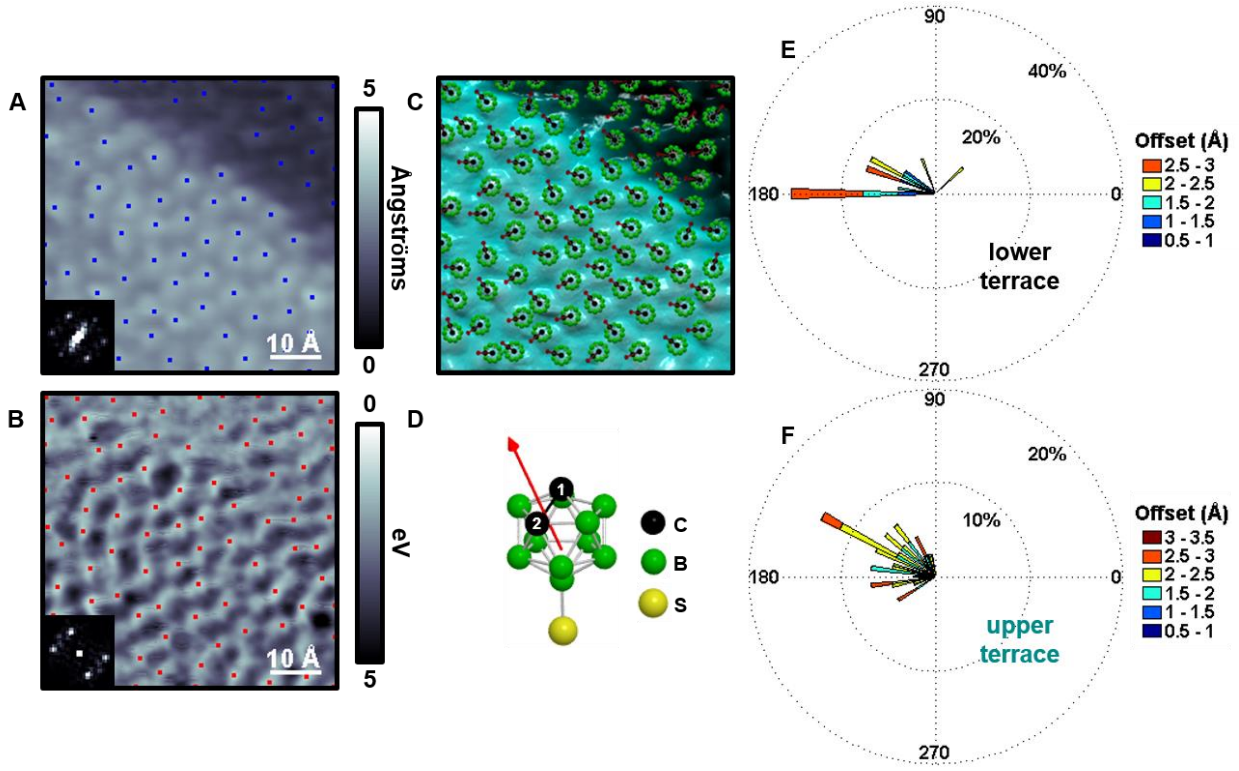

Figure 2.1 (A) Scanning tunneling topograph ($I_{tunneling}$ = 15 pA, V_{sample} = -0.5 V) of *o*-9-carboranethiol (**O9**) on Au{111} along a monatomic substrate step edge with local maxima (blue) depicted. Inset depicts a fast Fourier transform (FFT), corroborating a hexagonally close-packed arrangement with nearest-neighbor spacings of 7.2 ± 0.4 Å. (B) Simultaneously acquired local barrier height (LBH) image, which is inverted to highlight dipole orientations, with computed local maxima (red). Inset depicts a FFT revealing the order seen topographically. (C) Schematic displaying topography and computed molecular orientations. (D) A ball-and-stick model of **O9** that contains a calculated dipole magnitude of 5.72 D, where hydrogen atoms are omitted for clarity. Rose plots (depicting dipole offsets) of the lower terrace (E) and upper terrace (F) that are binned by both magnitude (0.5 Å bins) and orientation (4˚ bins). Angles reported are given with respect to the fast-scan direction, shown as horizontal, in the STM images.

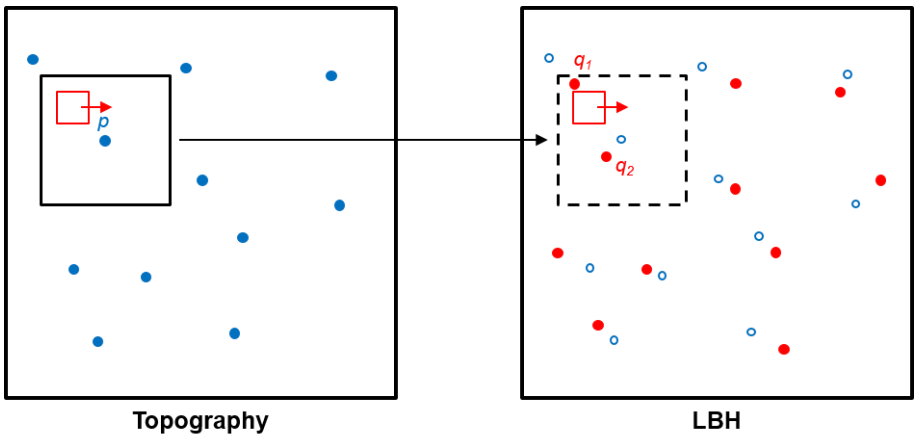

Figure 2.2 With two corresponding sets of local maxima per data set (the blue dots in the topography image and the red dots in the local barrier height, LBH, image), a maximum p from the topography image is selected and we search for its corresponding LBH maximum using a block-matching approach. Since both scanning tunneling microscopy modalities are acquired simultaneously, the two images are bounded, and we can define a search window (the black square in the topography image and dotted black square in the LBH image) centered at p of a given dimension (size of one molecule). Next, we compute the correlation between sliding patches taken at the same position in each image within the search window. Among the LBH maxima candidates (*i.e.*, $q1$ and $q2$) that correspond to p, we choose the one with highest correlation. We perform this procedure for each maximum p in the topographic image and finally compute a set of vectors (dipole positions with respect to molecular maxima) associated with each molecule.

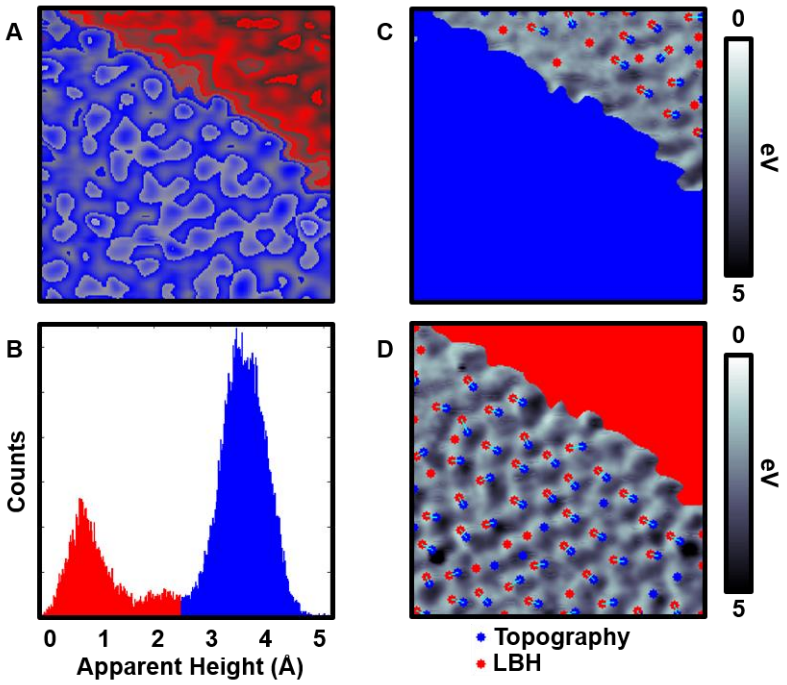

Figure 2.3 We bifurcate the topographic image along a monatomic Au{111} step edge (A) and show the image histogram in B. Here, we separate the upper (blue) and lower (red) terrace in topography based on thresholding and create a mask that is used to segment local barrier height (LBH) images. Topographic and LBH extrema are overlaid for both the lower terrace (C) and upper terrace (D), and correlations are computed. Both C and D show dipole offsets used for the Rose plots in Figure 2.1.

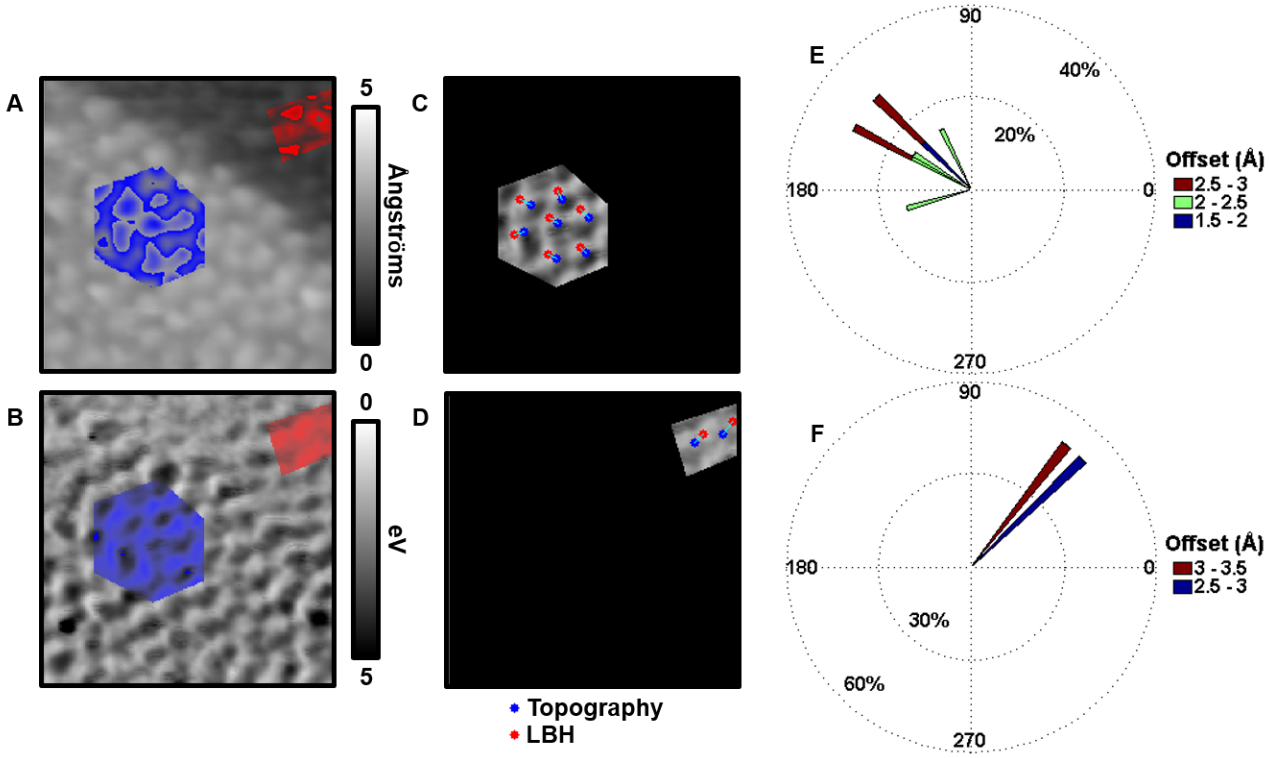

Figure 2.4 (A,B) Two regions are highlighted by inspection in both (A) topography and (B) local barrier height (LBH) images, where each region displays local variation in dipole offsets and orientations within the same image. Masks are created and used to highlight both areas. (C) Topographic maxima and (D) LBH minima are overlaid and correlations are computed. (E,F) Rose plots in each case depict local directionality that is binned by direction (4˚ bins) and magnitude (0.5 Å bins) with respect to the horizontal (fast-scan direction) axis in the images.

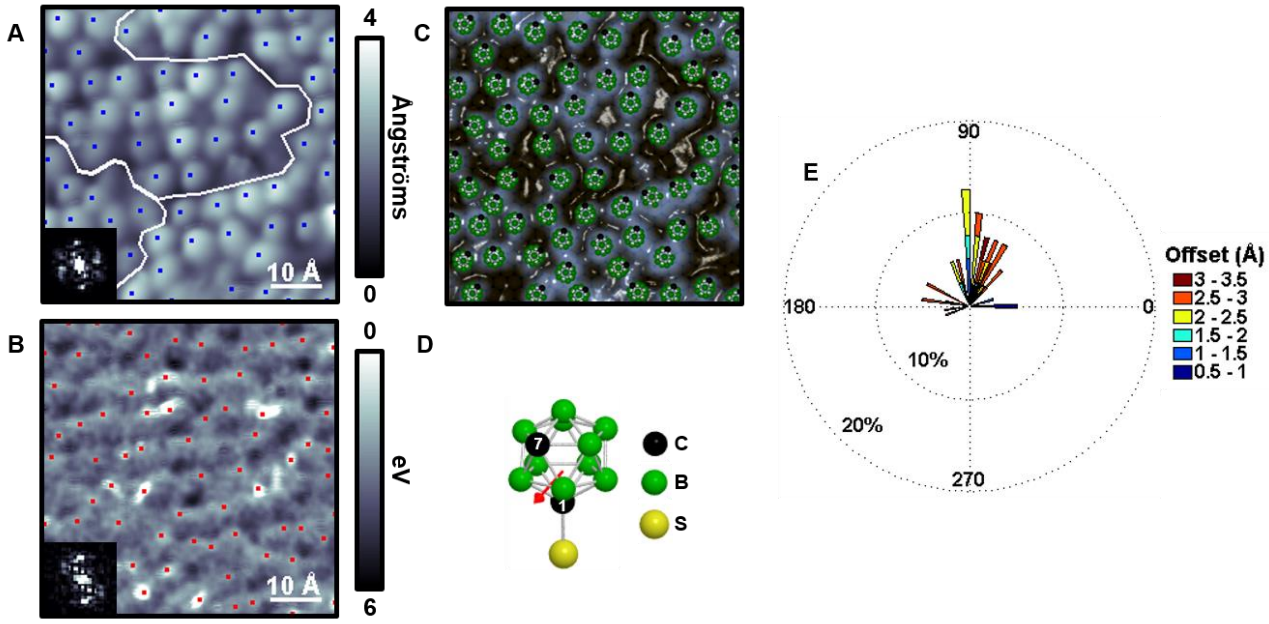

Figure 2.5 (A) Scanning tunneling topograph ($I_{tunneling}$ = 15 pA, V_{sample} = -0.5 V) of *m*-1-carboranethiol (**M1**) on Au{111} on a single Au terrace with lines separating three different regions (see Figure 2.6 for further explanation). Inset depicts the fast Fourier transform, revealing a hexagonally close-packed arrangement with a 7.2 Å nearest-neighbor spacing. Local maxima of both topographic (A) and inverted local barrier height (B) are computed. (C) A schematic displaying molecular position overlaid with topography. (D) A ball-and-stick model of **M1** that contains a dipole (1.06 D) oriented mainly in the plane of the gold substrate, where hydrogen atoms are omitted for clarity. (E) Rose plot of measured dipole vector orientations binned by both magnitude (0.5 Å bins) and orientation (4˚ bins). (See Figure 2.13 for correlation results used in E). Angles reported are given with respect to the fast-scan direction, shown as horizontal, in the STM images.

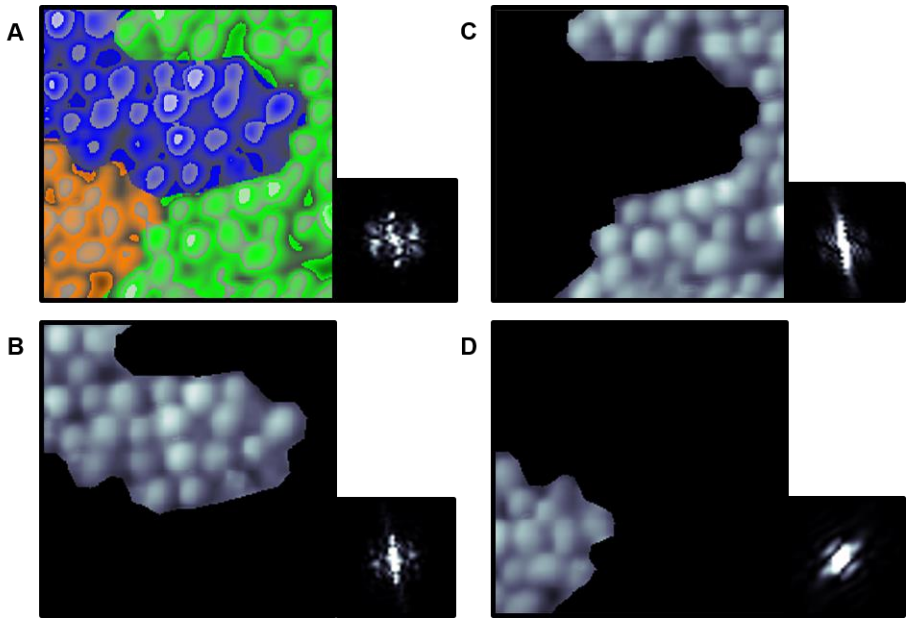

Figure 2.6 (A) The image shown in Figure 2.5 is segmented by inspection to create a mask that is used to separate the image into (B-D) three regions. Each image segment is analyzed in Fourier space, where the remaining areas in C and D are lattice matched with different directions and B is an area of local disorder.

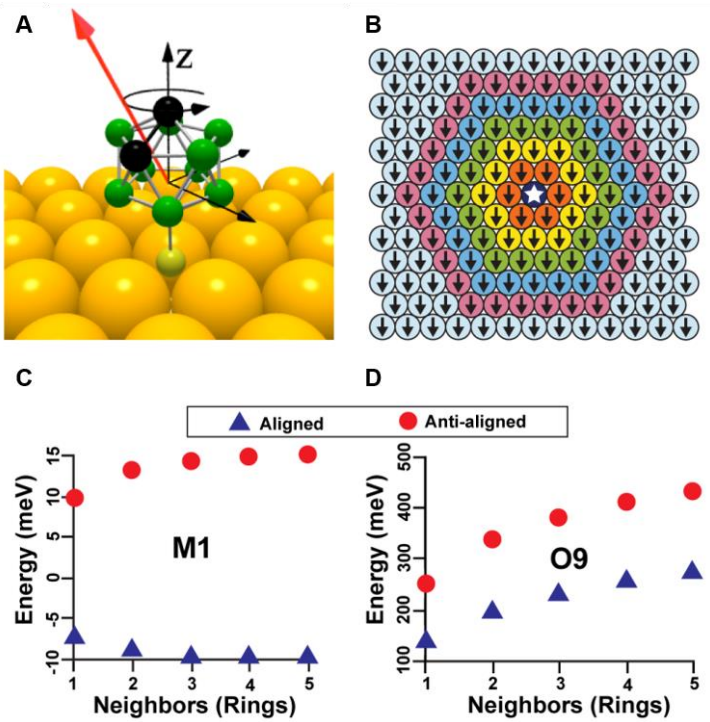

Figure 2.7 Dipole interaction energy. To estimate the dipole interaction energy, we consider carboranethiol molecules standing normal to a gold surface, along the z-axis, as shown in the perspective model (A) of an *o*-9-carboranethiol (**O9**) molecule. Iterations of the Metropolis algorithm affect random rotations about the z-axis, changing the dipole (red arrow) orientation and interaction energy. (B) Representation of a carboranethiol self-assembled monolayer in which each inscribed arrow indicates the in-plane orientation of a molecular dipole. Here, every dipole in the molecular lattice, except that of the central molecule, aligns along the same direction, toward the bottom of the figure. Plots (C) and (D) show the interaction energies of a dipole aligned in the same ("aligned," blue triangles) and opposite ("anti-aligned," red circles) direction as that of its neighbors, in the cases of *m*-1-carboranethiol (**M1**) and **O9** monolayers, respectively. The interaction energy depends on the number of concentric, hexagonal rings of neighboring molecules. In (B), we highlight the first five rings around a central molecule (indicated by an inscribed star)

with the colors orange, yellow, green, blue, and pink. Molecules outside the considered rings do not contribute to the interaction energy.

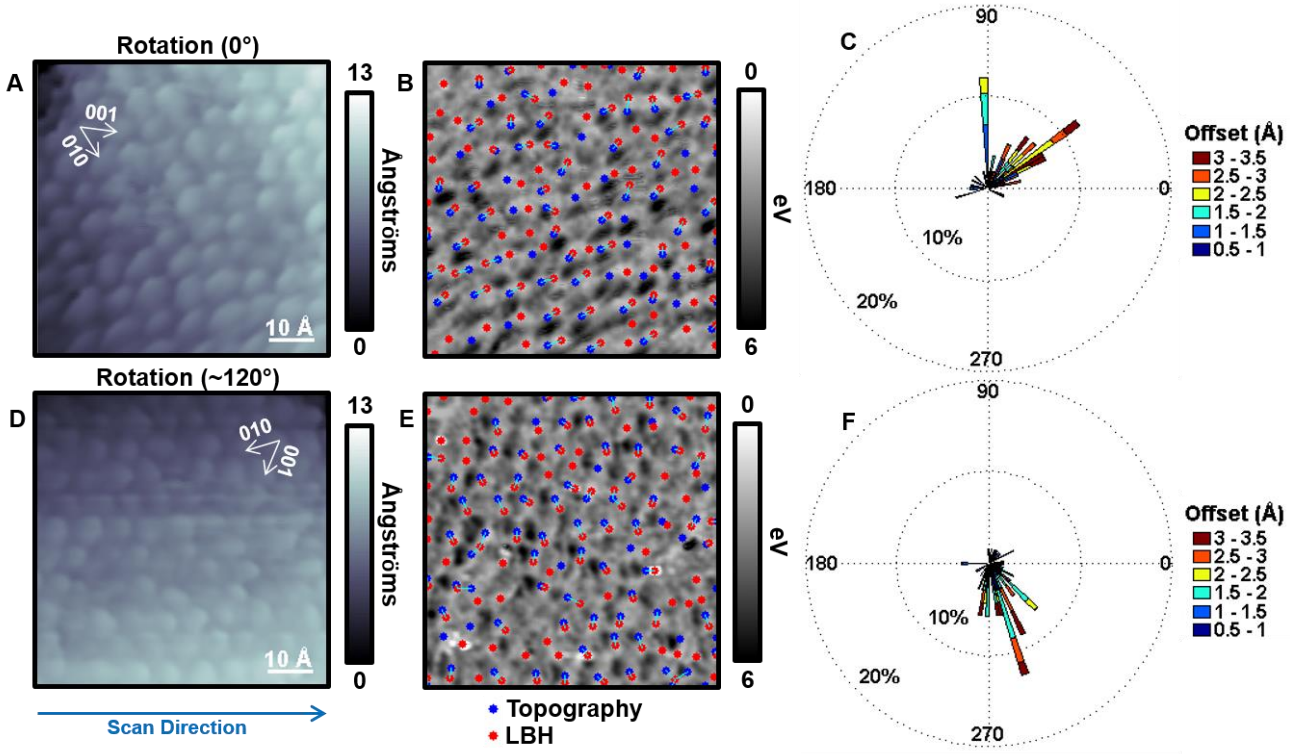

Figure 2.8 Test of the influence of the scanning probe tip electric field during data acquisition by simultaneously acquiring (A) topography ($I_{tunneling}$ = 15 pA, V_{sample} = -0.5 V) and (B) local barrier height (LBH) near a step edge, where topographic maxima and LBH minima are overlaid and correlations are computed. (C) Rose plot shows the local dipole offset in B that is binned by orientation (4˚ bins) and magnitude (0.5 Å bins) with respect to the horizontal (fast-scan direction) axis. (D,E) The scan angle is rotated and both (D) topography and (E) LBH are measured, where correlation procedures are repeated to obtain (F) the Rose plot of dipole orientations. Dipole offsets rotate with scan angle rotation (*i.e.*, remained fixed in space).

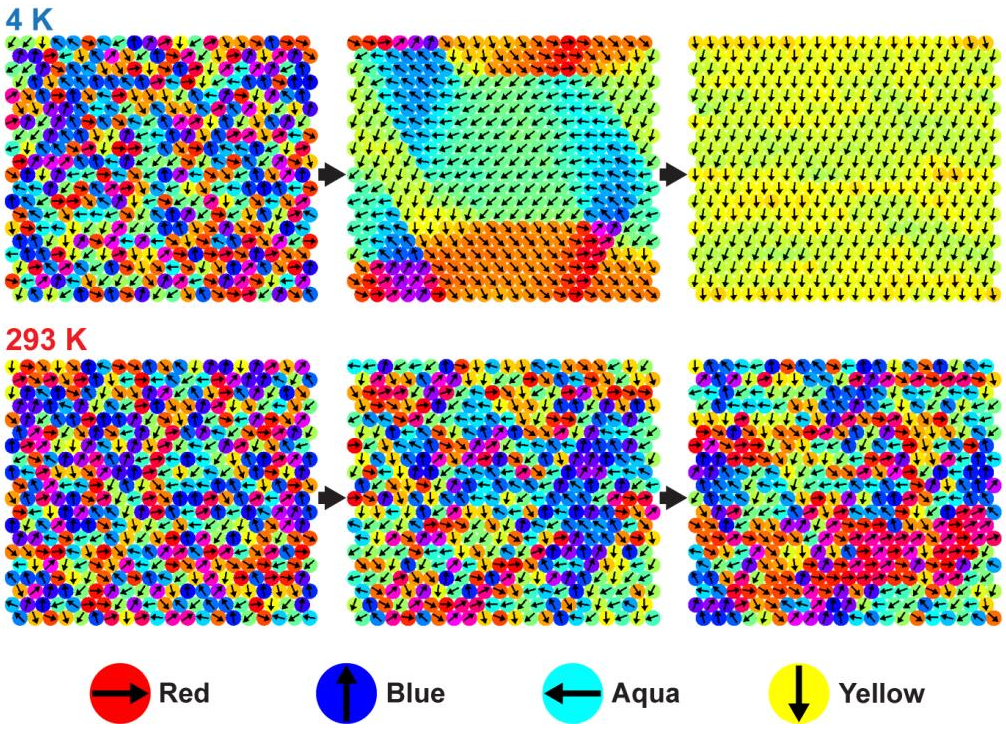

Figure 2.9 Simulated monolayers evolving under the influence of internal dipole fields. We track the orientation of molecular dipoles in a 20×20 molecule region of a self-assembled *o*-9-carboranethiol (**O9)** monolayer. At 4 K (top), the molecular dipoles evolve toward a state in which they align along a common direction. However, we do not observe this trend in simulations at 293 K (bottom); the dipoles remain randomly oriented and no permanent polarization develops. The sequences depict initial (left), intermediate (middle), and final (right) states of the monolayer over the course of 500,000 iterations of a Monte Carlo algorithm. Here, we represent individual **O9** molecules as circles inscribed with an arrow indicating the orientation of the molecule's in-plane dipole moment. The dipole orientation also determines the depicted color of each molecule. Molecules with dipoles oriented toward the top (bottom) of the figure appear blue (yellow), whereas molecules with dipoles oriented left (right) appear aqua (red); intermediate

orientations result in combinations of these colors. Monolayers composed of *m*-1-carboranethiol molecules evolve in a similar way to those of **O9**.

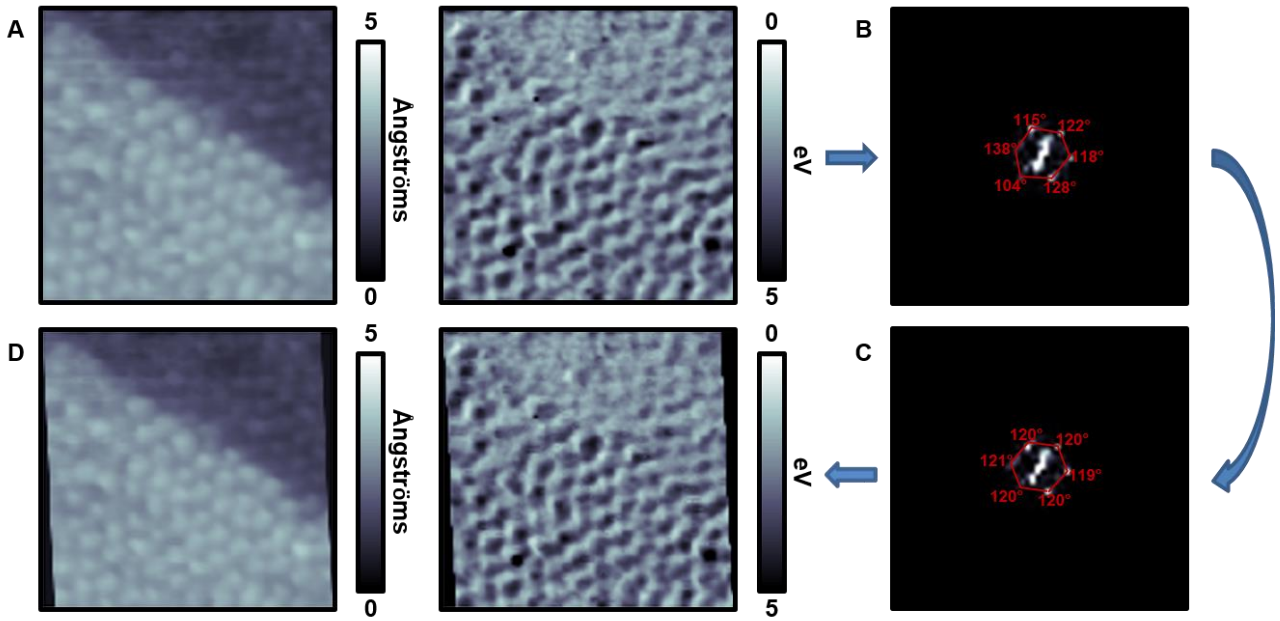

Figure 2.10 (A) (left) Topography and (right) local barrier height (LBH) images of an *o*-9-carboranethiol self-assembled monolayer before image aberration correction. (B) Images are transformed into the Fourier domain, and (C) reciprocal lattice points are symmetrized using the transform matrix, $\begin{pmatrix} 1 & c_1 & 0 \\ c_2 & 1 & 0 \\ 0 & 0 & 1 \end{pmatrix}$, where c_1 and c_2 are the correction factors in the y and x plane, respectively. (D) After optimization, corrected images are displayed and used in further analyses.

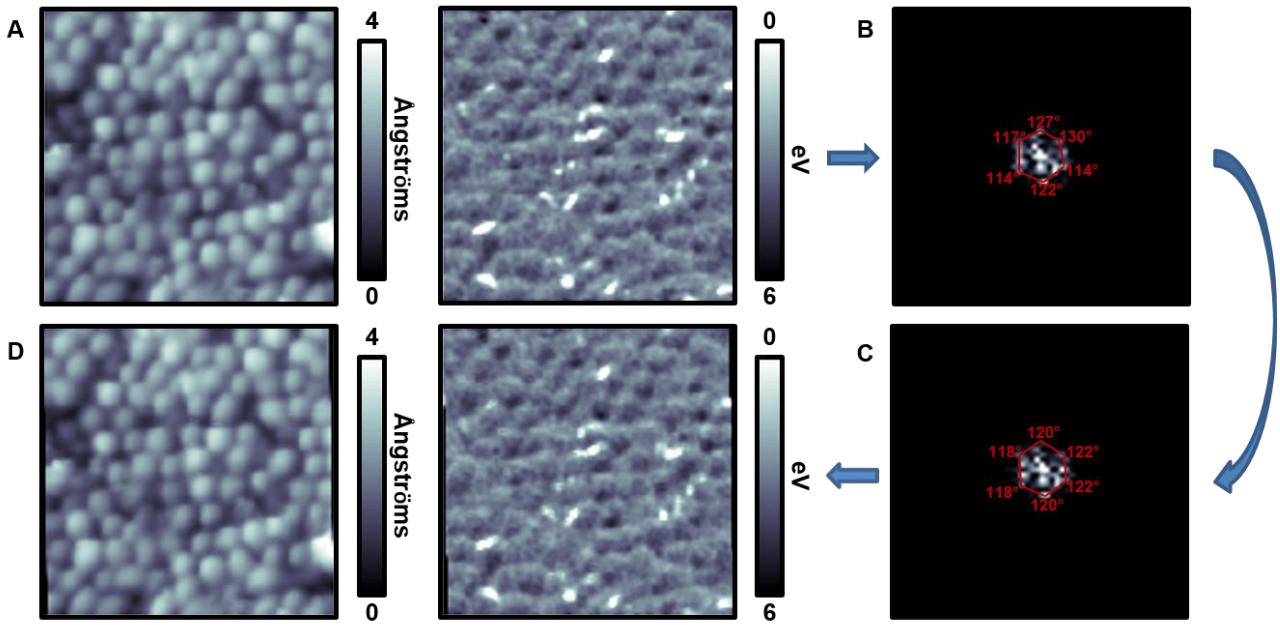

Figure 2.11 (A) (left) Topography and (right) local barrier height images of *m*-1-carboranethiol self-assembled monolayers before image aberration correction. (B) Images are transformed into the Fourier domain, and (C) reciprocal lattice points are symmetrized using the transform matrix shown in the caption to Figure 2.10. (D) After optimization, corrected images are displayed and used in later analyses.

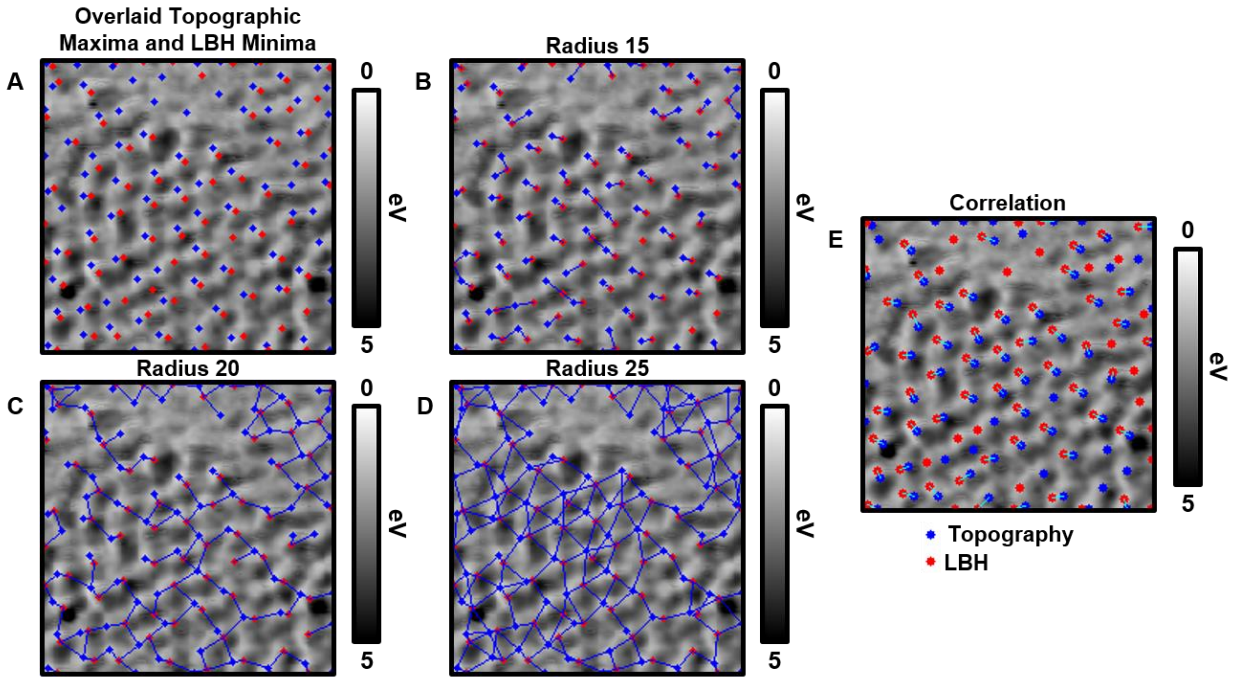

Figure 2.12 (A) Topographic maxima and local barrier height (LBH) minima are overlaid on *o*-9-carboranethiol (**O9**) LBH images for comparison. (B-D) Extrema are first compared by drawing all vectors, pq, within a specified square pixel window [(B) 15, (C) 20, and (D) 25 pixels]. Differences above and below 15-25 pixels are marginal, and all ranges depict many artifacts. (E) A molecular-sized square pixel window is centered at each topographic maximum and correlated within a next-nearest neighbor sized pixel window in the LBH image. The results depicted yield maximum correlated topographic maxima and LBH minima vectors that are then plotted.

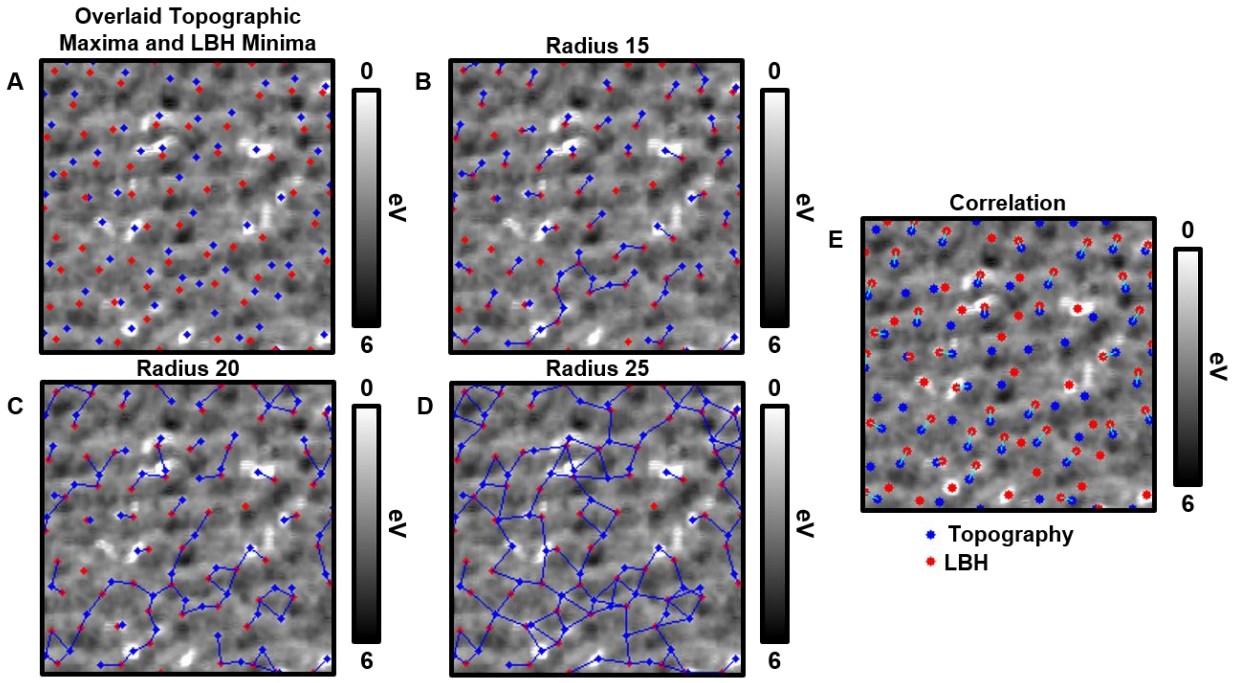

Figure 2.13 (A) Local barrier height (LBH) and topographic maxima are overlaid for *m*-1-carboranethiol monolayers for comparison. (B) Maxima are first compared by drawing all vectors, pq, within a specified pixel radius [(B) 15, (C) 20, and (D) 25 pixels]. Differences above and below a 15-25 square pixel window are negligible. Each increase in window size from 15 pixels to 25 pixels shows increased artifacts. (E) The results shown determine the maximum correlated topographic maxima and LBH minima that are stored and plotted for each molecule.

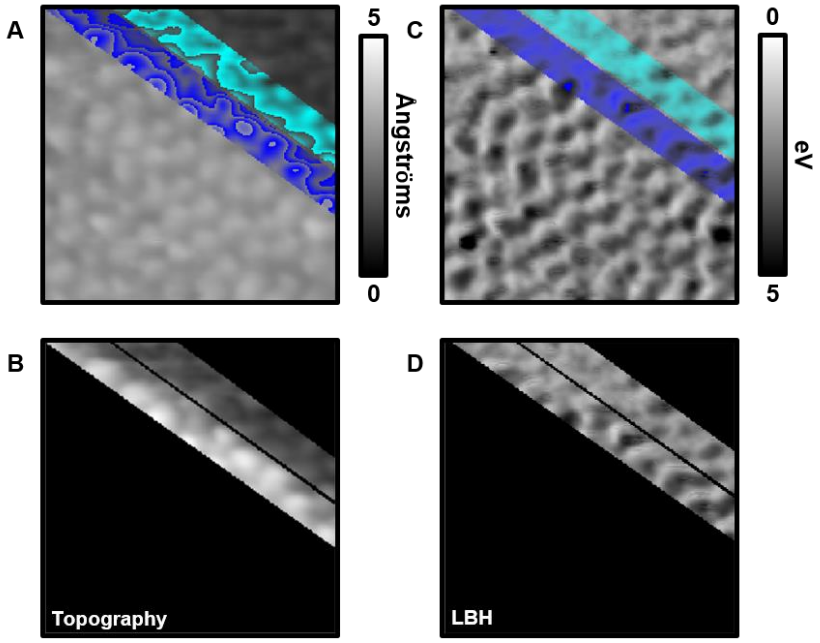

E

Image Mask	Pixel Entropy
Topography (Above Step Edge)	3.75 ± 1.78
Topography (Below Step Edge)	3.74 ± 1.74
LBH (Above Step Edge)	3.97 ± 1.89
LBH (Below Step Edge)	3.87 ± 1.84

$$E = -\sum_i p_i * \log_2 p_i$$

Figure 2.14 Textural differences between the upper and lower terrace of *o*-9-carboranethiol were quantified using MATLAB matrix analysis software. (A,C) Regions around a step edge were selected as shown and (B,D) isolated. Each set of regions was analyzed using entropy filtering that quantifies the number of accessible grayscale states in the intensity values of pixels in a 9×9 pixel neighborhood. Each region is symmetrically padded to eliminate edge effects, and the entropy at the center point is calculated. (E) Results are shown in the table and the equation used is shown below. Regions in both local barrier height (LBH) and topographic mode around the step edge show high textural contrast.

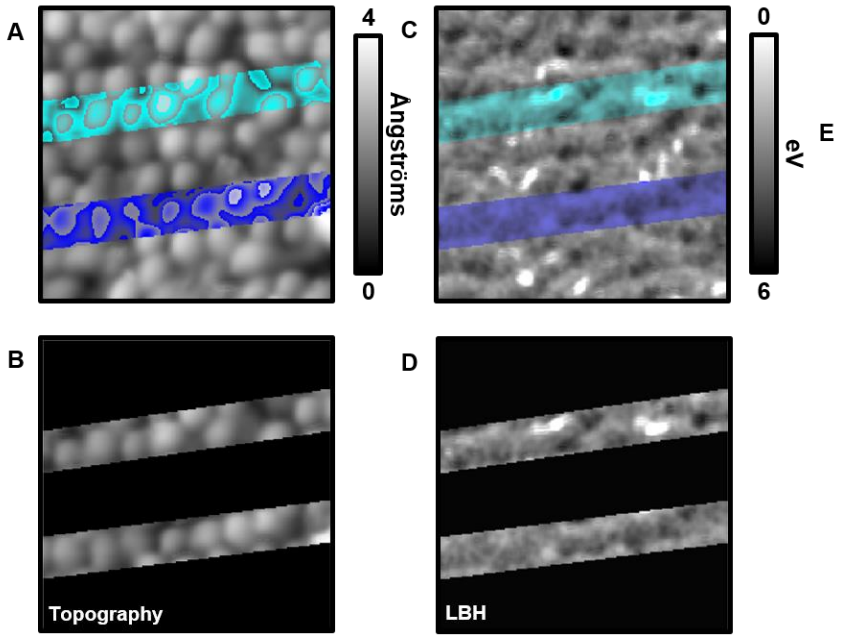

E

Image Mask	Pixel Entropy
Topography (1)	4.14 ± 1.51
Topography (2)	4.23 ± 1.58
LBH (1)	3.84 ± 1.35
LBH (2)	3.99 ± 1.46

Figure 2.15 Textural differences within the same domain of *m*-1-carboranethiol monolayers were quantified using MATLAB matrix analysis software. (A-D) Two regions were specified in both (A) topography and (C) local barrier height (LBH) images and (B,D) isolated by creating masks for the original images. Each set of regions was analyzed in MATLAB. Each region is symmetrically padded to eliminate edge effects, and the entropy at the center point is calculated. (E) Results are tabulated. Within each domain, regions in LBH and topographic modes exhibit high textural contrast.

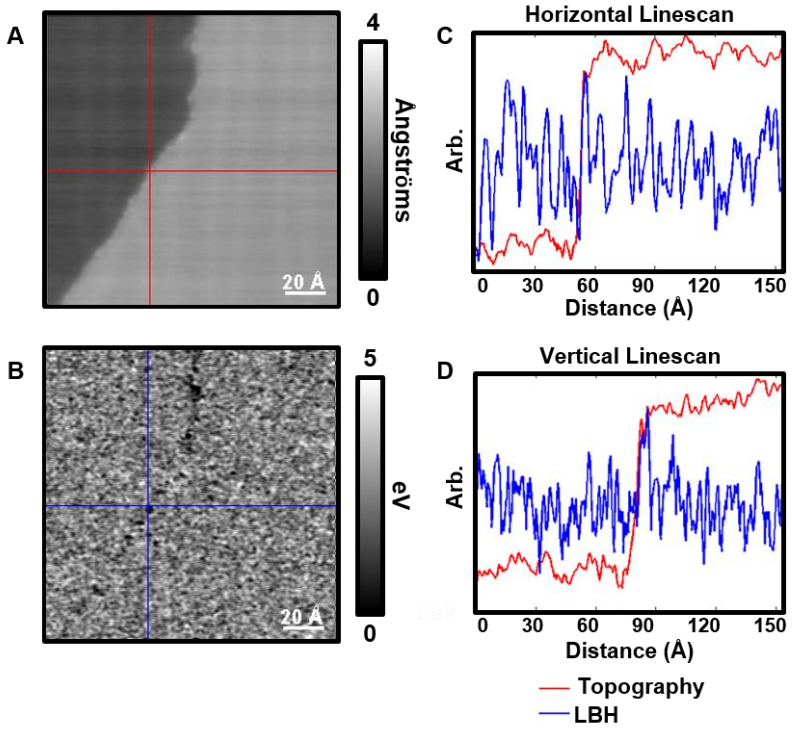

Figure 2.16 (A,B) Calibration images were obtained ($I_{tunneling}$ = 15 pA, V_{sample} = -0.5 V), using the same lock-in parameters in all local barrier height (LBH) measurements, along a single crystal Au{111} step edge simultaneously for both (A) topography and (B) LBH. (C,D) Inset lines in both topography and LBH represent line scans, where the step edge corresponds to a peak in LBH, shown in both the horizontal and vertical directions, thus verifying lock-in parameters.

2.5 References

1. Kim, M.; Hohman, J. N.; Cao, Y.; Houk, K. N.; Ma, H.; Jen, A. K.; Weiss, P. S. Creating Favorable Geometries for Directing Organic Photoreactions in Alkanethiolate Monolayers. *Science* **2011**, *331*, 1312–1315.

2. Jorgensen, W. L.; Swenson, C. J. Optimized Intermolecular Potential Functions for Amides and Peptides. Structure and Properties of Liquid Amides. *J. Am. Chem. Soc.* **1985**, *107*, 569–578.

3. Friedrich, B.; Herschbach, D. Alignment and Trapping of Molecules in Intense Laser Fields. *Phys. Rev. Lett.* **1995**, *74*, 4623–4626.

4. Zhang, Y.; Chang, A.; Cao, J.; Wang, Q.; Kim, W.; Li, Y.; Morris, N.; Yenilmez, E.; Kong, J.; Dai, H. Electric-Field-Directed Growth of Aligned Single-Walled Carbon Nanotubes. *App. Phys. Lett.* **2001**, *79*, 3155–3157.

5. Stapelfeldt, H. Colloquium: Aligning Molecules with Strong Laser Pulses. *Rev. Mod. Phys.* **2003**, *75*, 543–557.

6. Mandal, S. K.; Okawa, Y.; Hasegawa, T.; Aono, M. Rate-Determining Factors in the Chain Polymerization of Molecules Initiated by Local Single-Molecule Excitation. *ACS Nano* **2011**, *5*, 2779–2786.

7. Okawa, Y.; Aono, M. Materials Sciene: Nanoscale Control of Polymerization. *Nature* **2011**, *409*, 683–684.

8. Estler, R. C.; Zare, R. N. Laser-Induced Chemiluminescence: Variation of Reaction Rates with Reagent Approach Geometry. *J. Am. Chem. Soc.* **1978**, *100*, 1323–1324.

9. Loesch, H. J.; Remscheid, A. Brute Force in Molecular Reaction Dynamics: A Novel Technique for Measuring Steric Effects. *J. Chem. Phys.* **1990**, *93*, 4779–4790.

10. Baugh, D. A.; Young Kim, D.; Cho, V. A.; Pipes, L. C.; Petteway, J. C.; Fuglesang, C. D. Production of a Pure, Single Ro-Vibrational Quantum-State Molecular Beam. *Chem. Phys. Lett.* **1994**, *219*, 207–213.

11. Pirani, F.; Cappelletti, D.; Bartolomei, M.; Aquilanti, V.; Scotoni, M.; Vescovi, M.; Ascenzi, D.; Bassi, D. Orientation of Benzene in Supersonic Expansions, Probed by IR-Laser Absorption and by Molecular Beam Scattering. *Phys. Rev. Lett.* **2001**, *86*, 5035–5038.

12. Brooks, P. R.; McKillop, J. S.; Pippin, H. G. Molecular Beam Reaction of K Atoms with Sideways Oriented CF_3I. *Chem. Phys. Lett.* **1979**, *66*, 144–148.

13. Aquilanti, V.; Ascenzi, D.; Cappelletti, D.; Pirani, F. Velocity Dependence of Collisional Alignment of Oxygen Molecules in Gaseous Expansions. *Nature* **1994**, *371*, 399–402.

14. Weida, M. J.; Parmenter, C. S. Aligning Symmetric and Asymmetric Top Molecules *via* Single Photon Excitation. *J. Chem. Phys.* **1997**, *107*, 7138–7147.

15. Berndt, R.; Gaisch, R.; Gimzewski, J. K.; Reihl, B.; Schlittler, R. R.; Schneider, W. D.; Tschudy, M. Photon Emission at Molecular Resolution Induced by a Scanning Tunneling Microscope. *Science* **1993**, *262*, 1425–1427.

16. Stranick, S. J.; Weiss, P. S. Alternating Current Scanning Tunneling Microscopy and Nonlinear Spectroscopy. *J. Phys. Chem.* **1994**, *98*, 1762–1764.

17. McCarty, G. S.; Weiss, P. S. Scanning Probe Studies of Single-Nanostructures. *Chem. Rev.* **1999**, *99*, 1983–1990.

18. Donhauser, Z. J.; Mantooth, B. A.; Kelly, K. F.; Bumm, L. A.; Monnell, J. D.; Stapleton, J. J.; Price, D. W. Jr.; Allara, D. L.; Tour, J. M.; Weiss, P. S. Conductance Switching in Single Molecules through Conformational Changes. *Science* **2001**, *292*, 2303–2307.

19. Wu, S. W.; Ogawa, N.; Ho, W. Atomic-Scale Coupling of Photons to Single-Molecule Junctions. *Science* **2006**, *312*, 1362–1365.

20. Claridge, S. A.; Schwartz, J. J.; Weiss, P. S. Electrons, Photons, and Force: Quantitative Single-Molecule Measurements from Physics to Biology. *ACS Nano* **2011**, *5*, 693–729.

21. Giridharagopal, R.; Zhang, J.; Kelly, K. F. Antenna-Based Microwave Frequency Scanning Tunneling Microscope System. *Rev. Sci. Instrum.* **2011**, *82*, 053710.

22. Bonnell, D. A.; Basov, D. N.; Bode, M.; Diebold, U.; Kalinin, S. V.; Madhavan, V.; Novotny, L.; Salmeron, M.; Schwarz, U. D.; Weiss, P. S. Imaging Physical Phenomena with Local Probes: From Electrons to Photons. *Rev. Mod. Phys.* **2012**, *84*, 1343–1381.

23. Lang, N. D. Apparent Barrier Height in Scanning Tunneling Microscopy. *Phys. Rev. B* **1988**, *37*, 10395–10398.

24. Zheng, X.; Mulcahy, M. E.; Horinek, D.; Galeotti, F.; Magnera, T. F.; Michl, J. Dipolar and Nonpolar Altitudinal Molecular Rotors Mounted on an Au(111) Surface. *J. Am. Chem. Soc.* **2004**, *126*, 4540–4542.

25. Monnell, J. D.; Stapleton, J. J.; Dirk, S. M.; Reinerth, W. A.; Tour, J. M.; Allara, D. L.; Weiss, P. S. Relative Conductances of Alkaneselenolate and Alkanethiolate Monolayers on Au{111}. *J. Phys. Chem. B* **2005**, *109*, 20343–20349.

26. Han, P.; Kurland, A. R.; Giordano, A. N.; Nanayakkara, S. U.; Blake, M. M.; Pochas, C. M.; Weiss, P. S. Heads and Tails: Simultaneous Exposed and Buried Interface Imaging of Monolayers. *ACS Nano* **2009**, *3*, 3115–3121.

27. Mermin, N. D.; Wagner, H. Absence of Ferromagnetism or Antiferromagnetism in One- or Two-Dimensional Isotropic Heisenberg Models. *Phys. Rev. Lett.* **1966**, *17*, 1133–1136.

28. Bruno, P. Absence of Spontaneous Magnetic Order at Nonzero Temperature in One- and Two-Dimensional Heisenberg and XY Systems with Long-Range Interactions. *Phys. Rev. Lett.* **2001**, *87*, 137203.

29. Ferris, J. H.; Kushmerick, J. G.; Johnson, J. A.; Yoshikawa Youngquist, M. G.; Kessinger, R. B.; Kingsbury, H. F.; Weiss, P. S. Design, Operation, and Housing of an Ultrastable, Low Temperature, Ultrahigh Vacuum Scanning Tunneling Microscope. *Rev. Sci. Instrum.* **1998**, *69*, 2691–2695.

30. Ulman, A. Formation and Structure of Self-Assembled Monolayers. *Chem. Rev.* **1996**, *96*, 1533–1554.

31. Smith, R. K.; Lewis, P. A.; Weiss, P. S. Patterning Self-Assembled Monolayers. *Prog. Surf. Sci.* **2004**, *75*, 1–68.

32. Love, J. C.; Estroff, L. A.; Kriebel, J. K.; Nuzzo, R. G.; Whitesides, G. M. Self-Assembled Monolayers of Thiolates on Metals as a Form of Nanotechnology. *Chem. Rev.* **2005**, *105*, 1103–1169.

33. Weiss, P. S. Functional Molecules and Assemblies in Controlled Environments: Formation and Measurements. *Acc. Chem. Res.* **2008**, *41*, 1772–1781.

34. Saavedra, H. M.; Mullen, T. J.; Zhang, P. P.; Dewey, D. C.; Claridge, S. A.; Weiss, P. S. Hybrid Approaches in Nanolithography. *Rep. Prog. Phys.* **2010**, *73*, 036501.

35. Claridge, S. A.; Liao, W. S.; Thomas, J. C.; Zhao, Y.; Cao, H. H.; Cheunkar, S.; Serino, A. C.; Andrews, A. M.; Weiss, P. S. From the Bottom Up: Dimensional Control and Characterization in Molecular Monolayers. *Chem. Soc. Rev.* **2013**, *42*, 2725–2745.

36. Baše, T.; Bastl, Z.; Šlouf, M.; Klementová, M.; Šubrt, J.; Vetushka, A.; Ledinský, M.; Fejfar, A.; Macháček, J.; Carr, M. J.; *et al.* Gold Micrometer Crystals Modified with Carboranethiol Derivatives. *J. Phys. Chem. C* **2008**, *112*, 14446–14455.

37. Hohman, J. N.; Claridge, S. A.; Kim, M.; Weiss, P. S. Cage Molecules for Self-Assembly. *Mater. Sci. Eng. R* **2010**, *70*, 188–208.

38. Baše, T.; Bastl, Z.; Plzák, Z.; Grygar, T.; Plešek, J.; Carr, M. J.; Malina, V.; Šubrt, J.; Boháček, J.; Večerníková, E.; *et al.* Carboranethiol-Modified Gold Surfaces. A Study and Comparison of Modified Cluster and Flat Surfaces. *Langmuir* **2005**, *21*, 7776–7785.

39. Hohman, J. N.; Zhang, P.; Morin, E. I.; Han, P.; Kim, M.; Kurland, A. R.; McClanahan, P. D.; Balema, V. P.; Weiss, P. S. Self-Assembly of Carboranethiol Isomers on Au{111}: Intermolecular Interactions Determined by Molecular Dipole Orientations. *ACS Nano* **2009**, *3*, 527–536.

40. Dameron, A. A.; Charles, L. F.; Weiss, P. S. Structures and Displacement of 1-Adamantanethiol Self-Assembled Monolayers on Au{111}. *J. Am. Chem. Soc.* **2005**, *127*, 8697–8704.

41. Saavedra, H. M.; Barbu, C. M.; Dameron, A. A.; Mullen, T. J.; Crespi, V. H.; Weiss, P. S. 1-Adamantanethiolate Monolayer Displacement Kinetics Follow a Universal Form. *J. Am. Chem. Soc.* **2007**, *129*, 10741–10746.

42. von Wrochem, F.; Scholz, F.; Gao, D.; Nothofer, H.-G.; Yasuda, A.; Wessels, J. M.; Roy, S.; Chen, X.; Michl, J. High-Band-Gap Polycrystalline Monolayers of a 12-Vertex *p*-Carborane on Au(111). *J. Phys. Chem.* **2010**, *1*, 3471–3477.

43. Spokoyny, A. M.; Machan, C. W.; Clingerman, D. J.; Rosen, M. S.; Wiester, M. J.; Kennedy, R. D.; Stern, C. L.; Sarjeant, A. A.; Mirkin, C. A.,A Coordination Chemistry Dichotomy for Icosahedral Carborane-Based Ligands. *Nat. Chem.* **2011**, *3*, 590–596.

44. Wiesendanger, R.; Eng, L.; Hidber, H. R.; Oelhafen, P.; Rosenthaler, L.; Staufer, U.; Güntherodt, H. J. Local Tunneling Barrier Height Images Obtained with the Scanning Tunneling Microscope. *Surf. Sci.* **1987**, *189–190*, 24–28.

45. Olesen, L.; Brandbyge, M.; Sørensen, M.; Jacobsen, K.; Lægsgaard, E.; Stensgaard, I.; Besenbacher, F. Apparent Barrier Height in Scanning Tunneling Microscopy Revisited. *Phys. Rev. Lett.* **1996**, *76*, 1485–1488.

46. Rusu, P.; Brocks, G. Work Functions of Self-Assembled Monolayers on Metal Surfaces by First-Principles Calculations. *Phys. Rev. B* **2006**, *74*, 073414.

47. Jain, J.; Jain, A. Displacement Measurement and Its Application in Interframe Image Coding. *IEEE Trans. Comm.* **1981**, *29*, 1799–1808.

48. Love, N. S.; Kamath, C.,An Empirical Study of Block Matching Techniques for the Detection of Moving Objects. *CASC, LLNL. Livermore* **2006**, 1–36.

49. Kristiansen, K.; Stock, P.; Baimpos, T.; Raman, S.; Harada, J. K.; Israelachvili, J. N.; Valtiner, M. Influence of Molecular Dipole Orientations on Long-Range Exponential Interaction Forces at Hydrophobic Contacts in Aqueous Solutions. *ACS Nano* **2014**, *8*, 10870–10877.

50. Metropolis, N.; Rosenbluth, A. W.; Rosenbluth, M. N.; Teller, A. H.; Teller, E. Equation of State Calculations by Fast Computing Machines. *J. Chem. Phys.* **1953**, *21*, 1087–1092.

51. Pascual, J.; Jackiw, J.; Kelly, K.; Conrad, H.; Rust, H. P.; Weiss, P. S. Local Electronic Structural Effects and Measurements on the Adsorption of Benzene on Ag(110). *Phys. Rev. B* **2000**, *62*, 12632–12635.

52. Claridge, S. A.; Thomas, J. C.; Silverman, M. A.; Schwartz, J. J.; Yang, Y.; Wang, C.; Weiss, P. S. Differentiating Amino Acid Residues and Side Chain Orientations in Peptides Using Scanning Tunneling Microscopy. *J. Am. Chem. Soc.* **2013**, *135*, 18528–18535.

53. Kim, J.; Rim, Y. S.; Liu, Y.; Serino, A. C.; Thomas, J. C.; Chen, H.; Yang, Y.; Weiss, P. S. Interface Control in Organic Electronics Using Mixed Monolayers of Carboranethiol Isomers. *Nano Lett.* **2014**, *14*, 2946–2951.

54. Stranick, S. J.; Parakh, A. N.; Tao, Y.-T.; Allara, D. L.; Weiss, P. S. Phase Separation of Mixed-Composition Self-Assembled Monolayers into Nanometer Scale Molecular Domains. *J. Phys. Chem.* **1994**, *98*, 7636–7646.

55. Smith, R. K.; Reed, S. M.; Monnel, J. D.; Lewis, P. A.; Clegg, R. S.; Kelley, K. F.; Bumm, L. A.; Hutchison, J. E.; Weiss, P. S. Phase Separation within a Binary Self-Assembled Monolayer on Au{111} Driven by an Amide-Containing Alkanethiol. *J. Phys. Chem. B* **2001**, *15*, 1119–1122.

56. Hampton, J. R.; Dameron, A. A.; Weiss, P. S. Double-Ink Dip-Pen Nanolithography Studies Elucidate Molecular Transport. *J. Am. Chem. Soc.* **2006**, *128*, 1648–1653.

57. Nuzzo, R. G.; Dubois, L. H.; Allara, D. L. Fundamental Studies of Microscopic Wetting on Organic-Surfaces. 1. Formation and Structural Characterization of a Self-Consistent Series of Polyfunctional Organic Monolayers. *J. Am. Chem. Soc.* **1990**, *112*, 558–569.

58. Poirier, G. E. Characterization of Organosulfur Molecular Monolayers on Au(111) using Scanning Tunneling Microscopy. *Chem. Rev.* **1997**, *97*, 1117–1127.

59. Dameron, A. A.; Charles, L. F.; Weiss, P. S. Structures and the Displacement of 1-Adamantanethiol Self-Assembled Monolayers on Au{111}. *J. Am. Chem. Soc.* **2005**, *127*, 8697–9704.

60. Kim, M. H.; Hohman, J. N.; Morin, E. I.; Daniel, T. A.; Weiss, P. S. Self-Assembled Monolayers of 2-Adamantanethiol on Au{111}: Control of Structure and Displacement. *J. Phys. Chem. A* **2012**, *113*, 3895–3903.

61. Stipe, B. C.; Rezaei, M. A.; Ho, W. Single-Molecule Vibrational Spectroscopy and Microscopy. *Science* **1998**, *280*, 1732–1735.

62. Khuong, T. A. V.; Nunez, J. E.; Godinez, C. E.; Garcia-Garibay, M. A. Crystalline Molecular Machines: A Quest toward Solid-State Dynamics and Function. *Acc. Chem. Res.* **2006**, *39*, 413-422.

63. Michl, J.; Sykes, C. H. Molecular Rotors and Motors: Recent Advances and Future Challenges. *ACS Nano* **2009**, *3*, 1042-1048.

64. Lee, H. J.; Ho, W. Structural Determination by Single-Molecule Vibrational Spectroscopy and Microscopy: Contrast between Copper and Iron Carbonyls. *Phys. Rev. B* **2000**, *61*, 347–350.

65. Lewis, P. A.; Inman, C. E.; Maya, F.; Tour, J. M.; Hutchison, J. E.; Weiss, P. S. Molecular Engineering of the Polarity and Interactions of Molecular Electronics Switches. *J. Am. Chem. Soc.* **2005**, *127*, 17421–17426.

66. Baber, A. E.; Jensen, S. C.; Sykes, E. C. H. Dipole-Driven Ferroelectric Assembly of Styrene on Au{111}. *J. Am. Chem. Soc.* **2007**, *129*, 6368–6369.

67. Han, P.; Akagi, K.; Canova, F. F.; Mutoh, H.; Shiraki, S.; Iwaya, K.; Weiss, P. S.; Asao, N.; Hitosugi, T. Botton-Up Graphene-Nanoribbon Fabrication Reveals Chiral Edges and Enantioselectivity. *ACS Nano* **2014**, *8*, 9181–9187.

68. Ferris, J. H.; Kushmerick, J. G.; Johnson, J. A.; Yoshikawa Youngquist, M. G.; Kessinger, R. B.; Kingsbury, H. W.; Weiss, P. S. Design, Operation, and Housing of an Ultrastable, Low Temperature, Ultrahigh Vacuum Scanning Tunneling Microscope. *Rev. Sci. Instrum.* **1998**, *69*, 2691–2695.

69. Monnell, J. D.; Stapleton, J. J.; Dirk, S. M.; Reinerth, W. A.; Tour, J. M.; Allara, D. L.; Weiss, P. S. Relative Conductances of Alkaneselenolate and Alkanethiolate Monolayers on Au{111}. *J. Phys. Chem. B* **2005**, *109*, 20343-20349.

70. Chan, M. H.; Yu, Y. B.; Constantinides, A. G. Variable Size Block Matching Motion Compensation with Applications to Video Coding. *IEEE Proc. I* **1990**, *137*, 205–212.

71. Nie, Y.; Ma, K. K. Adaptive Rood Pattern Search for Fast Block-Matching motion estimation. *IEEE Trans. Image Process.* **2002**, *11*, 1442–1449.

CHAPTER 3

Self-Assembled *p*-Carborane Analog of *p*-Mercaptobenzoic Acid on Au{111}

3.1 Introduction

Self-assembled monolayers (SAMs), or *pseudo*-crystalline two-dimensional (2D) interfaces, enable tunable surface properties that find use in nanotechnology and materials development applications.[1,2] Functionalization of molecules, which are used as essential building blocks for SAMs, is a target in efforts to understand and control materials at the nanoscale, and to use individual molecules in the preparation of bottom-up surface assemblies with tailored dimensions, physicochemical properties, and chemical compositions.[3,4] The most common two-dimensional (2D) assemblies comprise organic molecules tethered to gold surfaces via thiol (-SH) / thiolate ($-S^-$) anchoring groups.[5] Recently, in this context, cage molecules have attracted special attention because of their rigid three-dimensional (3D) architectures and extraordinary capacity for structural and chemical modifications.[6-13] Thiolated derivatives of 12-vertex dicarba-*closo*-dodecaboranes of the general formula $(HS)_x$-$C_2B_{10}H_{12-x}$, with their nearly regular icosahedral molecular structures, are representatives of inorganic cluster molecules belonging to this category.[14-16] They have been used as essential components of self-assembled monolayers and have been shown to possess several advantages compared to their organic counterparts, such as higher stability against heating and chemical substitution and pristine monolayer formations that have fewer types and total numbers of defects.[17,18] The latter advantage can be ascribed to the higher axial isotropy of the carborane-based backbones compared to the organic aromatic varieties; this fundamental difference stimulates our research. The large dipole moments in different isomeric carboranethiols enable tunable effective work function modification over a variety of coinage metal substrates.[2,19-21] These robust molecules have also been embedded in functional organic-based SAMs due to their steric properties and wide frontier-orbital energy gaps.[8,22]

Recently, new synthetic strategies for the preparation of the dicarba-*closo*-dodecaborane derivatives substituted at both carbon and boron positions have been proposed as pathways to new precursors and ligands for metal surfaces and coordination compounds.[23-25] These efforts reflect a systematic approach towards forming a library of functionalized carborane cluster compounds with potential use as surface modifiers with new qualities. Our focus is to probe the library of potential carborane-based building blocks in the context of SAMs with importance in supramolecular and materials chemistry through targeted functionalization. These SAM constituents are interesting for ultra-thin film applications, and thus functionalized *p*-isomers become intriguing options for directing nano-architectures from two dimensions into three.[2,7,9,16,26]

In this study, we report on the preparation and characterization of a new cage-thiol with a carboxylic functional group suitable for further chemical modification on exposed self-assembled monolayer surfaces. Our attempt to prepare and to investigate the cluster analogue of *p*-mercaptobenzoic acid (1-HS-4-COOH-C_6H_4) as a modifier of gold surfaces was inspired by recent successes in functionalizing and patterning with *p*-mercaptobenzoic acid itself,[29-31] which has proven to be effective for surface functionalization. The new cage-molecule building block, 1-HS-12-COOH-1,12-$C_2B_{10}H_{10}$ (**A'**), has high axial symmetry, which is another reason for our interest in its use for SAMs. In comparison to the benzene ring of *p*-mercaptobenzoic acid, the larger steric demands of the carborane cage enable greater separations of the carboxylic functional groups in two dimensions. Particularly attractive is the potential use of this new carborane derivative as a functional capping ligand for gold colloidal particles or as a ligand for transition metal complexes. We compare its structure to that of its precursor 1-HS-1,12-$C_2B_{10}H_{11}$ (**A**) as the first step for examination, where single-crystal packing data from X-ray diffraction analysis are discussed and compared to micrographs obtained by scanning tunneling microscopy (STM). The

nature of these two SAM constituents on gold surfaces has been quantified by X-ray photoelectron spectroscopy (XPS) and contact angle measurements that demonstrate the surface wetting characteristics.

3.2 Results and Discussion

Synthesis, nuclear magnetic resonance spectroscopic characterization, and X-ray structural analysis.

1-Mercapto-1,12-dicarba-*closo*-dodecaborane-12-carboxylic acid (**A'**) was synthesized from 1-mercapto-1,12-dicarba-*closo*-dodecaborane (**A**) by lithiation with two equivalents of *n*-BuLi and subsequent reaction with carbon dioxide followed by quenching with an aqueous solution of hydrochloric acid (Figure 3.1).

This new derivative is an inorganic cage analog of *p*-mercaptobenzoic acid. ^{11}B, ^{1}H, and ^{13}C nuclear magnetic resonance (NMR) spectra of the new compound were measured and all resonances were assigned to the respective atoms (Table 3.1). The molecular structure of **A'** was obtained from a single-crystal X-ray diffraction analysis, see Figure 3.2 and Table 3.2. In the NMR data, we may note that the thiol proton chemical shift in **A'** of 3.18 ppm practically does not differ from the value of 3.19 ppm measured in **A**. It demonstrates that the *p*-carborane cage effectively isolates both functional groups.

Single-crystal X-ray diffraction study of **A'** established the positions of all the heavier atoms in the molecules. All cluster hydrogen atoms were apparent in the residual electron-density map after anisotropic refinement of the heavier atoms. After isotropic refinement of all cluster hydrogen atoms, the remaining highest residual electron density peaks revealed the thiol and carboxyl

hydrogen atoms. The thiol hydrogen atoms showed crystallographic disorder that is discussed below.

1,12-Dicarba-*closo*-dodecaborane (1,12-$C_2B_{10}H_{12}$) exhibits contraction along the C···C axis of the molecule and shows the d[C(1)···C(12)] of 3.056(6) Å.[32] This shorter distance compared to the antipodal B···B distances, Ø 3.377(6) Å, which are similar to the d[B(1)···B(12)] of 3.383(2) Å[33] in $[B_{12}H_{12}]^{2-}$, expresses the extent to which the structure deviates from the geometry of a regular icosahedron.

Different substituents attached to the carbon atoms have an additional effect on the C(1)···C(12) distance as a consequence of their electronic influence. The SH group represents an electronegative substituent that pulls electrons from the cluster carbon atoms and causes elongation of the C(1)···C(12) distance. A good example is the structure of 1,12-$(HS)_2$-1,12-$C_2B_{10}H_{10}$ that has been previously investigated using single-crystal X-ray diffraction,[19] gas-phase electron diffraction (GED),[34] and by means of computational analyses.[19,34] Table 3.3 shows two mutually related cluster parameters: the C(1)···C(12) distance and the angle α that are both defined in Figure 3.2. The molecule of **A'** exhibits the d[C(1)···C(12)] of 3.091(3) Å, which is slightly shorter than the d[C(1)···C(12)] of 3.107(3) Å in 1,12-$(HS)_2$-1,12-$C_2B_{10}H_{10}$. The COOH functional group elongates the C(1)···C(12) distance less than the SH group. Since neither the molecule **A'** nor **A** has perfect D_{5d} symmetry; the parameter α represents the average value. We distinguish in Table 3.3 between angle α_{COOH} and α_{SH} reflecting whether the value belongs to the pentagonal pyramid close to the SH or COOH group. Similarly, two angles (α_{SH} and α_H) are distinguished for the calculated structure of **A**, which has an SH group attached to only one of the carbon atoms,

while the other bears hydrogen as in the unsubstituted 1,12-dicarba-*closo*-dodecaborane, 1,12-$C_2B_{10}H_{12}$.

Additional analyses of the interatomic distances in both **A** and **A'**, such as B-B connections, show that the cluster does not exhibit any other significant changes due to the presence of the thiol (-SH) or carboxyl (-COOH) substituents than those reported above. With respect to these findings the cluster architecture can be more precisely described as a bi-capped pentagonal antiprism.

The supramolecular structure of **A'**, as it appears in the single crystal, is depicted in Figure 3.3. It consists of molecular pairs bound in the typical dimeric $R_2^2(8)$ association pattern[35] of carboxylic acids with the O·(H)··O interatomic distance of 2.647 Å. In contrast, the thiol groups facing each other form a zig-zag arranged -$(SH)_n$- chain, along the lattice vector a, with the S·(H)··S interatomic distances between 4.002 and 4.057 Å. The hydrogen atoms within the -$(SH)_n$- chains are crystallographically disordered (Figure 3.4). The isomer **A'** is soluble in most polar as well as nonpolar organic solvents, and it is worth noting that these molecules might exist, especially in aprotic solvents, in the form of the non-dissociated dimers.

In the direction along the -$(SH)_n$- chain, perpendicular to the C(1)···C(12) axis of the molecules, the cages are arranged in rows with nearest-neighbor distances of 6.635 Å. Figure 3.5 shows space-filling and schematic drawings of this row with COOH groups on top, which illustrate how close this nearest intermolecular distance is compared to the intermolecular distance in a SAM.

Another important note is the alignment of the COOH groups that are, in a crystal structure, involved in strong hydrogen-bonding interactions between two COOH groups and contribute significantly to the crystal packing forces. This hydrogen bond does not occur in a SAM.

Independent computational investigation of the COOH group conformations were done using MP2/6-31+G* calculations. Two conformations were investigated and the –COOH rotational barrier was assessed. Computational data show almost free rotation of the COOH group, which may contribute to difficulties in obtaining molecular resolution with STM (vide infra). The distance between two molecules on a flat surface precludes any significant direct lateral hydrogen-bonding interactions between the COOH groups. Figure 3.6 shows a schematic of two potential conformations denoted as 0° and 180° according to the B-C-C=O torsion angle. The difference between the alignment of COOH groups in the crystal structure and the computational analyses is attributed to almost free rotation of the COOH groups, assessed from the energy barrier, and to the effect of crystal packing forces.

In the computationally optimized geometries of 1-(S-)-12-COOH-1,12-$C_2B_{10}H_{10}$, the SH hydrogen atom was removed intentionally for reasons of simplicity. The conformation with the doubly bonded oxygen of the carboxyl group over a B-B connection line and its hydroxyl over a boron atom (conformation 180°) is the most stable one, while the opposite (conformation 0°), with the doubly bonded oxygen over a boron and the hydroxyl over a B-B connection line, has the highest energy.

The barrier of the carboxyl rotation is nevertheless small, 0.00345 eV at the HF/6-31+G* level, that becomes 0.00149 eV with zero-point correction, and 0.00210 eV at the MP2/6-31+G* level (without zero-point correction). At the laboratory temperature of 20 °C, it is significantly smaller than the thermal energy (kT = 0.0253 eV) that is expected to lead to essentially unrestricted rotation. These computational results are summarized in the Supporting Information (Table 3.4).

The packing of molecules in single crystals as well as different structural aspects of the molecule itself offer an opportunity for comparison with the packing in a self-assembled monolayer on Au{111}.

Scanning Tunneling Microscopy.

We first imaged 2D lattices of **A** on Au{111}/mica with molecular resolution under ambient conditions and used this lattice as a backbone to trap islands of **A'** in mixed (1:10, **A'**:**A**) deposited SAMs. Single-component SAMs of **A'** were difficult to visualize with molecular resolution under ambient conditions due to strongly hydrophilic COOH functional groups that rotate almost freely around the five-fold symmetry axis of the *p*-carborane cage and the capability for water adsorption.

We use STM as a tool to probe the exposed interfaces of conductive thin films with molecular precision.[36,37] Constant-current mode imaging was used to acquire data that represent a convolution of topography and electronic structure.[38,39] Homogenous monolayers of **A** on Au{111} form into two-phase hexagonally close-packed arrays with a 7.2 ± 0.5 Å nearest neighbor spacings (Figures 3.7 and 3.8), consistent with our earlier measurements of SAMs of simple carboranethiols on Au{111}.[18] This spacing is greater than the closest arrangement observed in the crystal structure (Figure 3.5). Possible unit cell structures include $(\sqrt{97}\times\sqrt{97})R15.30°$, (5×5), $(\sqrt{57}\times\sqrt{57})R6.59°$, and $(\sqrt{7}\times\sqrt{7})R19.12°$ which have nearest-neighbor spacings of 7.09, 7.2, 7.25, and 7.62 Å, respectively. Measured SAMs may compete between any of the above structures; incommensurate lattices are also possible.[40,41]

Simple calculations of a 2D array of **A**, used to estimate the steric demands of the cage moiety, predict nearest-neighbor intermolecular distances of 7.26 Å (Figure 3.9), which best fits the $(\sqrt{57}\times\sqrt{57})R6.59°$ unit cell structure.

The five-fold symmetry of the *para*-carborane cage precludes the calculated lattice constants from being the same. Two phases that differ in apparent height ($dz_{apparent} = 1.0 \pm 0.3$ Å) were measured. We attribute the lower apparent height features to thiolate-bound moieties and the more protruding apparent height features to thiol moieties. Local analyses across different areas and samples ($n_{samples} > 3$) exhibits an average coverage of 5.1 ± 1.4% of the thiol-bound moiety and a 95 ± 3% average coverage of the thiolate-bound moiety (Figure 3.10), indicating that the thiolate bound state is preferred and dominant. In this regard, it is important to note that previous STM investigations of the isomeric 1-HS-1,7-$C_2B_{10}H_{11}$ showed only the thiolate-bound state.[18] This mixed composition SAM proved useful in promoting sparse **A'** monolayer formation. Scanning tunneling micrographs of co-deposited SAMs show distributed islands of **A'**, where the lattice of the **A** backbone is confirmed and **A'** is resolved in apparent height. Hydrogen bonding among the molecules of **A'** in solution may play a major role in its 2D packing, due to intermolecular forces, and thus the formation of island aggregates. Scanning tunneling micrographs show a difference in apparent height of 1.2 ± 0.2 Å, under the conditions used, where the carboxyl moiety is topographically more protruding (Figure 3.11). Local ordering of the **A** backbone, with minimal defects surrounding **A'** patches, suggests the **A'** moieties have adopted the same nearest neighbor spacing as the backbone monolayer of ~7.2 Å, as has been observed in other SAMs.[37] This system may find use in the preparation of patterned substrates with chemically functionalized island targets dispersed within monolayer matrices.[1,16,30,42-51]

X-ray photoelectron spectroscopy.

X-ray photoelectron spectroscopy (XPS) was used to investigate the adsorption of both derivatives, **A** and **A'**, on Au{111} surfaces further. The respective data are summarized in Tables 3.5 and 3.6. Good agreement between the measured and nominal stoichiometries of the molecules was observed.

The XPS data provide important information about the form in which the molecules are adsorbed on gold surfaces (**A** SAM and **A'** SAM). Of particular use in this respect are the binding energy (BE) values of S 2p electrons summarized in Table 3.6.

Both derivatives **A** and **A'** self-assembled on Au{111} show comparable spectra in the S 2p region with sulfur atoms in two oxidation states and the amount of the second component ranging from 12% to 39% (Figure 3.12). The COOH group does not show any evident influence on how these two derivatives adsorb on the surface.

This observation corresponds to practically identical S-H proton chemical shifts in ^{1}H NMR spectra of both **A** and **A'** (Table 3.1). The measured BE value of S $2p_{3/2}$ electrons at ~162.0 eV is comparable to the value reported in the literature[52-54] for alkanethiolates on planar gold surfaces. The second sulfur species with the S $2p_{3/2}$ electrons at ~164 eV can be assigned to a free thiol (-SH) group.[52-54] Observations of sulfur atoms in both states can be rationally explained by a fraction of molecules being adsorbed on the Au{111} surface without SH bond scission. The BE value of the second component assigned to the thiol moiety interacting with a Au{111} surface, ~164.0 eV, is close to 163.7 eV, which was reported previously for a free SH group in 1,12-$(HS)_2$-1,12-$C_2B_{10}H_{10}$.[19] This small, reproducible difference can be understood by the

interaction of the lone pair electrons pairs of sulfur of the non-dissociated SH group with a gold surface, which reduces the electron density on the S atom and thus shifts the BE of S $2p_{3/2}$ electrons to a slightly higher value. We note that we do not have information from the STM images nor the XPS data on any possible reorganization of Au substrate atoms. Evidence for Au adatom and so-called staple structures have been observed in a number of studies of alkanethiols, alkaneselenols, and related molecules on Au{111} and on nanoparticle surfaces.[10,37,55-60] Heating the SAM of **A'** on Au{111} up to 350 °C in the X-ray photoelectron spectrometer led to the disappearance of the (protonated) sulfur with the binding energy value of ~164.0 eV, and was accompanied by a corresponding decrease of the surface concentration of carborane molecules and an increase of the signal from the gold substrate (Tables 3.5 and 3.6). This result points to the (expected) higher thermal stability of the thiolate form of the molecules in the SAM.

By this means, one can tune the ratio of thiolate and thiol molecules on the surface. This observation is consistent with the STM analyses of the SAMs prepared at higher temperatures, which exhibit lower surface fractions of the features that we attribute to the adsorbed thiol (*i.e.*, protonated) moiety. Thus, temperature provides a means for controlling the surface ratio of these species both on deposition and via subsequent processing. The former provides a complete monolayer whereas later heating is expected to allow access to the substrate and thus to open up space for further deposition.[31]

An alternative preparation of the SAMs is from their constituent vapors (in this report referred to as gas phase, GP, adsorption).[61,62] This strategy usually leads to less carbon contamination than deposition from solution as the surface is not exposed to solvent. While the spectra of S 2p photoelectrons were in good agreement for both **A** and **A'** SAMs, the surface exposed to the former

derivative shows higher coverage, presumably because of the higher volatility of **A** compared to **A'**. In Table 3.5, the atomic concentration of Au is included as a relative measure of surface coverage.

The spectra of C 1s photoelectrons were fit by three components of the same width with binding energies 284.6, 286.0, and 288.8 eV, which can be assigned to carbon atoms in C-C, C-H (first component), C-B with contribution of C-O (second component), and COO (third component) bonds. As expected, the third component was not present for the adsorbed molecules of **A**. The samples were prepared and transferred under ambient conditions and consequently some amount of carbonaceous contamination was present on their surfaces.

Dynamic contact angles.

The measurements of dynamic contact angles provide macroscopic characterization of modified surfaces and information about the hydrophilic/hydrophobic surface character.[7,63] Au{111} surfaces modified with derivatives **A** and **A'** show advancing and receding wetting angle values of 87.5 (0.3)° and 76.8 (0.2)° for SAMs of **A**, respectively, and 30.0 (0.1)° and 24.8 (0.1)° for SAMs of **A'**, respectively. The measured values are significantly different and demonstrate the hydrophilic character of SAMs of **A'** compared to those of **A**. The hydrophilic character of SAMs of **A'** is an expected result of the introduction of the exposed COOH functional groups. This result is also consistent with the expected orientations of the molecules on gold surfaces, *i.e.*, with the thiol/thiolate groups anchor the molecules to the substrate; the carboxylic functional groups interact only weakly with the underlying gold surface and are at the exposed surface. Moreover, both derivatives **A** and **A'** exhibit features in the S 2p region of the XP spectra and it is therefore

unlikely that the second sulfur species, observed at 164.0 eV, would result from the adsorption of **A'** via its carboxylic group.

Acid-base titration of selected carboranethiol derivatives.

The adsorption of **A** and **A'** on Au{111} shows co-existing thiolate- and thiol-bound moieties. This phenomenon has not been observed with closely related species - isomeric to **A** - studied previously with XPS (1-HS-1,2-$C_2B_{10}H_{11}$)[17] and STM (1-HS-1,7-$C_2B_{10}H_{11}$).[18] Therefore, the acidity of the SH group, which is influenced by decreasing electron-accepting properties of the carboranyl backbone in the order from *ortho* through *meta* to *para* isomers, is further analyzed as an intrinsic property of the molecule, determining the thiol (-SH) / thiolate ($-S^-$) adsorption scheme. All derivatives were titrated with aqueous solution of sodium hydroxide and the titration curves are shown with the respective pK_a values in Figure 3.13. The results show that the derivative **A'** is a diprotic acid. Dissociation of the COOH group prior to the SH group is in accord with the acidity constant order, and corresponds to our computational results at the CC2/def2-TZVP level of theory. Comparisons of **A** (1-HS-1,12-$C_2B_{10}H_{11}$) with its positional isomers derived from *ortho*-dicarba-*closo*-dodecaborane, 1-HS-1,2-$C_2B_{10}H_{11}$, and *meta*-dicarba-*closo*-dodecaborane, 1-HS-1,7-$C_2B_{10}H_{11}$, shows a trend of increasing SH group acidic character from *para*- through *meta*- to *ortho*-carborane, which is generally expected and confirmed by measured acidity constants. These results are in good agreement with previously published constants[64] and also are consistent with our computational results, presented in Figure 3.14. Of the three isomers, **A** (1-HS-1,12-$C_2B_{10}H_{11}$) exhibits the greatest energy difference between its protonated and de-protonated form, which corresponds to the weakest acidic character observed in the titration experiments. In comparison, the isomer 1-HS-1,2-$C_2B_{10}H_{11}$ dissociates more easily, shows the

smallest energy difference between its protonated and deprotonated forms, and has been previously reported to exhibit only the thiolate species in acquired X-ray photoelectron spectra.[17] A similar trend is observed with the isomer 1-HS-1,7-$C_2B_{10}H_{11}$ that has been previously reported to show only one apparent height in STM images.

3.3 Conclusions and Prospects

A new bifunctional cage molecule, derived from 12-vertex *p*-carborane, for SAMs was synthesized and thoroughly characterized using structural and spectroscopic methods. This new building block has greater steric demands and higher axial symmetry compared to its planar organic analogue, *p*-mercaptobenzoic acid. As a constituent of SAMs on Au{111}, these bulkier molecules arrange into a hexagonal, close-packed array with the nearest-neighbor distance of 7.2 ± 0.5 Å. In single crystals, the molecules assemble into close-packed rows with nearest-neighbor distances of only 6.635 Å. Such tight packing cannot be effectively achieved in a 2D arrangement because no regular 2D periodic pattern can follow the five-fold symmetry axis of the *p*-carborane cage. Both steric demands and axial symmetry, therefore, influence packing on Au{111} surfaces. A mixed SAM of the new constituent and its non-carboxylated analogue shows that this system can be used to prepare pristine monolayers with separated islands of additional functional groups on top, which can be used in targeted surface patterning. The interactions of the new molecule with gold surfaces were investigated by XPS, which shows that the molecules adsorb preferably as thiolates, but a small fraction of bound thiol moieties has also been observed. This result is consistent with previous studies of mono-thiolated *o*- and *m*-carboranes[17-19] which both dissociate more easily than mono-thiolated *p*-carborane. The presence of a carboxylic

functional group on top of the *p*-carborane is shown to have a negligible effect on the interactions between the SH group and the substrate surfaces.

In comparison with its organic analog, *p*-mercaptobenzoic acid, **A'** produces SAMs with several interesting properties, mainly resulting from the fact that carborane cages provide more rigid and larger lattice spacings than alkyl or aryl substituents.[7] A large nearest-neighbor spacing and free carboxyl rotation may be further exploited in SAM-modified gold electrodes, where certain proteins exhibit optimal voltammetric responses in mixed alkanethiolate and hydroxyl-terminated alkanethiolate SAM-modified electrodes.[64] Similar modification on the *m*- and *o*- isomers would enable increased backbone interaction strengths primed for surface functionalization.[65] These observations complement the results obtained recently with similar *p*-carborane derivatives used as building blocks for metal-organic frameworks.[41,49] Combinations of both kinds of carborane-based building blocks provide bases for grafting porous 3D structures such as *p*-carboranylcarboxylate metal-organic frameworks.

3.4 Materials and Methods

3.4.1 Chemical Procedures

1-HS-1,12-$C_2B_{10}H_{11}$ (**A**) was prepared according to the literature[66,67] and its purity was checked by gas chromatography with mass spectrometric detection (GC-MS) and by ^{11}B and ^{1}H NMR spectroscopy. Nuclear magnetic resonance spectroscopy was performed at room temperature on a Varian MercuryPlus at 400 MHz using standard techniques and procedures. Acid-base titrations were done according to the procedure reported previously.[68] Dichloromethane (obtained in p.a. grade from Penta a.s., Czech Republic) was additionally dried over anhydrous K_2CO_3 for several

weeks and freshly distilled prior to use. Monoglyme (1,2-dimethoxyethane) and *n*-BuLi (2.5 M solution in hexanes) were both purchased from Sigma-Aldrich. Monoglyme was additionally dried with sodium in the presence of benzophenone (99.8%, purchased from Sigma-Aldrich) and freshly distilled before experiments. Benzene and other solvents for STM experiments were purchased from Sigma-Aldrich and used as received. The NMR spectra were measured in CD_3OD (99.8% D) as received from Eurisotop.

3.4.2 Synthesis of 1-(HS)-12-(COOH)-1,12-$C_2B_{10}H_{10}$

1,12-Dicarba-*closo*-dodecaborane-1-thiol, **A**, (1.058 g, 6 mmol) was placed in a dry, Ar-purged 500 ml flask and dissolved in 180 ml of dry and freshly distilled monoglyme. While cooling the reaction mixture in an ice-water bath, 9.6 ml of 2.5 M *n*-BuLi solution in hexanes (24 mmol) was slowly added over a ~10 min period. The cooling bath was removed shortly after the addition of *n*-BuLi and the white suspension was stirred for an additional 1.5 h at room temperature. Afterwards, carbon dioxide was bubbled through the stirred slurry for approximately 3 h (stream of ~1-5 L/h) and the reaction mixture was additionally stirred overnight. The solvent was evaporated to dryness under reduced pressure and 60 ml of distilled water were added that yielded a colorless, slightly turbid solution that was acidified with a 10% aqueous solution of HCl (pH ~2). The precipitated solid was filtered off, washed generously with distilled water, and dried over $CaCl_2$ in an evacuated desiccator. The crude product, 1.132 g, was sublimed ($5\text{-}15\times10^{-2}$ Torr, T = 100-125 °C) and yielded 0.96 g (73%) of a pure white solid product. Single crystals, suitable for X-ray diffraction analysis, were obtained by slow sublimation in a glass ampoule sealed under reduced pressure (~0.1 Torr) and stored at ~40-60 °C. The product is soluble in organic solvents such as ethanol, methanol, diethyl ether, chloroform, and hexane. The NMR

data with peak assignments are provided in Table 3.1. Single-crystal X-ray diffraction analysis is discussed. The sublimed product was further characterized by mass spectrometry using a Thermo-Finnigan LCQ-Fleet Ion Trap instrument with electrospray (ESI) ionisation in the negative ion mode. ESI-MS *m/z*: 440.14 (100%, $[2M-H]^-$), calcd. 440.30 for $B_{20}C_6H_{23}O_4S_2$; 220.18 (5%, $[M-H]^-$), calcd. 220.14 for $B_{10}C_3H_{11}O_2S_1$; 175.17 (5%, $[M-COOH]^-$), calcd. 175.16 for $B_{10}C_2H_{11}S_1$; 461.08 (4%, $[2M-H+Na]^-$), calcd. 461.29 for $B_{20}C_6H_{23}O_4Na_1S_2$. Both experimental and calculated isotopic distribution envelopes are shown in Figures 3.15-3.18 in the supporting information. Melting point: 197-198 °C, melting was accompanied by turning brown due to decomposition. Elemental analysis, Found: C, 16.34; B, 49.04; S, 14.59; H, 5.47; Calculated for $B_{10}C_3H_{12}O_2S$: C, 16.36; B, 49.07; S, 14.55; H, 5.49. Infrared spectra of both **A'** and **A** (measured in KBr pellets) are presented in Figure 3.19.

3.4.3 Self-Assembled Monolayer Preparation

A and **A'** SAMs were deposited either from solution or from the vapor phase. For solution deposition, 0.5 mmol of **A** or **A'** were dissolved in 5 mL of freshly distilled CH_2Cl_2 (dried with CaH_2) and applied to Au{111} substrates. For spectroscopic measurements of solution-deposited SAMs, two forms of gold substrates were used: Au films comprising a 200-nm thick, evaporation-deposited gold film with ~2 nm of a Cr interlayer on a glass wafer (11 mm × 11 mm) purchased from Arrandee, Germany, and Au micrometer single crystals[19] deposited from an ethanol suspension on a quartz plate and cleaned by multiple cycles of 30 min exposure in a UV-ozone cleaner (Novascan 4" PSD standard system) and subsequent H_2-flame annealing. The substrates were immersed in the respective solutions of **A** or **A'** for 1 h, then quickly removed and immediately, before their surfaces could dry, immersed in a beaker with freshly

distilled CH_2Cl_2 used for washing. This procedure was followed by additional rinsing with an excess of CH_2Cl_2 and drying in a gaseous stream of Ar.

Adsorption experiments from the gas phase were conducted on Platypus template stripped gold films (Platypus, USA). Freshly stripped gold films were exposed to vapors of either **A** or **A'** in a closed vial at room temperature.

For STM, both pure and co-deposited **A** and (1:10) **A'**:**A** SAMs for STM imaging were fabricated via solution deposition onto commercially available Au{111}/mica substrates (Agilent, Santa Clara, CA). The Au/mica substrates were annealed with 10 passes of a hydrogen flame (0.5 Hz) and placed into a capped vial with 1 mL of a 1 mM solution of either **A** or **A'**:**A** (1:10) in benzene. Each sample was heated at 78 °C in a Barnstead Thermolyne 1400 furnace (ThermoFisher Scientific, Waltham, MA) for 24 h. Subsequently, samples were cleaned with neat benzene and dried with a stream of nitrogen gas before loading into the custom-built ambient microscope.

3.4.4 Crystallography

Crystals suitable for single-crystal X-ray crystallography were obtained by slow sublimation in a sealed ampoule over a few weeks. The data were measured at 120 K with up to 0.87 Å resolution on an Agilent diffractometer Xcalibur using mirror-collimated Cu K_α radiation (Gemini ultra Cu) from a sealed X-ray tube, and CCD detector Atlas. Data processing was made using program CrysAlis PRO, with empirical absorption correction. Structures were solved by charge flipping with Superflip[69] and refined with Jana2006, http://jana.fzu.cz (Structure Determination Software Programs, Institute of Physics, Prague, Czech Republic).[70] The sample was a twin rotated by 180°

around the reciprocal axis c*. This twinning operation generated overlaps of some diffraction spots; the overlaps were detected by the data processing program CrysAlis PRO and encoded to the reflection file in a form of the so-called hklf5 format. Using this format, the partial overlaps due to twinning could be taken into the account by the refinement program Jana2006. This considerably improved the sensitivity of the refinement of hydrogen atom positions.

All hydrogen atoms appeared in difference Fourier maps. Hydrogen atoms attached to boron were constrained to have the same B-H distance while hydrogen atoms attached to oxygen of carboxyl were refined with constrained O-H distances of 0.82 Å. The difference Fourier maps also revealed disorder of the thiol hydrogen, which occupied two positions, both suitable for forming S-H···S hydrogen bonds. In the refinement, the occupancy of these disordered positions was fixed to 0.5 and the distances S-H as well as the angles C-S-H were restrained to be the same. The isotropic displacement parameters of hydrogen atoms were constrained as a 1.2 multiple of the equivalent isotropic displacement parameter of their parent atoms. ORTEP-3 was used to prepare Figure 3.2.[71] Other Figures were made in Mercury. Selected collection and refinement data are listed in Table 3.2 together with the CCDC number. Supplementary crystallographic data can be also obtained free of charge via http://www.ccdc.cam.ac.uk/conts/retrieving.html.

3.4.5 Scanning Tunneling Microscopy

All STM measurements were performed in air using a custom beetle-style microscope and a platinum/iridium probe tips (80:20).[7,72] The well-known lattice of the 1-dodecanethiolate SAM on Au{111} was used to calibrate piezoelectric scanners, and these calibrations were subsequently checked against the expected spacings of SAMs of **A**. Samples were held within a -1 to -0.1 V bias

range, and 256 × 256 pixel images were collected in constant-current mode at a tunneling current of 100 pA.

3.4.6 X-ray Photoelectron Spectroscopy

Self-assembled monolayers of **A** and **A'** were measured using an ESCA310 (Scienta, Sweden) electron spectrometer equipped with a hemispherical electron analyzer operated in a fixed transmission mode. Monochromatic Al K_α radiation was used for electron excitation. The spectrometer was calibrated to the Au $4f_{7/2}$ peak at 84.0 eV. The spectra were recorded at room temperature. The energy spectra of the emitted Au 4*f*, C 1*s*, B 1*s*, and S 2*p* photoelectrons were measured. The electron detection angle was 45^o with respect to the macroscopic sample surface. The pressure of residual gases in the analyzer chamber during spectra acquisition was 2×10^{-9} mbar. The accuracy of the measured binding energies was ±0.1 eV. The spectra were fit after subtraction of the Shirley background[73] using Gaussian-Lorentzian line shape and non-linear least-squares algorithms. The fitting of S 2p profiles was made subject to the constraints of the constant spin-orbit splitting 1.18 eV and the constant S $2p_{3/2}$: S $2p_{1/2}$ branching ratio 2:1.[74] Quantification of the elemental concentrations was accomplished by correcting photoelectron peak intensities for their cross-sections[75] and analyzer transmission function. In the calculations, homogeneous compositions of the analyzed layer of the samples measured was assumed. The typical error of the quantitative analysis by XPS is ~10%.[76]

3.4.7 Water Contact-Angle Measurements

Contact angle measurements for carboranethiolate SAMs on Au/Si were performed using a custom-built goniometer. It is based on InfiniStix (Hitachi Ltd., Tokyo, Japan)

0.50× magnification, 94 mm focal length CCD camera. Droplets are created and manipulated using a 0.5 mL Luer Lock syringe (Cole-Palmer, Vernon Hills, IL) and a 30 gauge needle. For data acquisition and contact angle measurements, FTA 1000 B software, produced by First Ten Angstroms, Inc. (Portsmouith, VA), was used.

Contact angle data were collected using a dynamic sessile drop method, where a sample is placed near the tip of the needle. A drop of deionized H_2O (2 μL) is deposited on the sample and the needle is carefully positioned in the center of the drop without deforming its shape. Drop size is then increased to 6 μL and a photograph is obtained which provides the advancing contact angle. Drop volume is then increased to 8 μL and then reduced to 6 μL. Another photograph is obtained, resulting in the receding contact angle. All these measurements were collected on an automated system with photographs collected at 60 frames per sec for seven cycles. Reported values are an average of measurements on 3 samples with 5 drops per sample.

3.4.8 Computational Modeling

The geometries of the molecules and anions were calculated using the open-source quantum chemical package NWChem[77] with the help of the Gabedit GUI.[78] The C_S symmetry of the principal rotamers was used. First, the geometries were optimized at the Hartree-Fock level in Pople's 6-31+G* basis that contains polarization as well as diffuse functions at all non-hydrogen atoms, the analytical Hessian of the optimized structure was calculated, and frequency analysis performed. The number of imaginary frequencies was used to determine whether the structure is a minimum or a transition state. Finally, the geometries were further optimized at the level of the second order Møller-Plesset perturbation theory using the same basis functions set. For 1-S-12-COOH-1,12-$C_2B_{10}H_{10}$(-), conformation analysis was performed. For other species studied,

possible rotamers of their carboxyl or thiol groups were tested, and the most stable conformers selected.

The surface packing was modeled as a simple 2D periodic array of molecules, omitting their interactions with the metal surface. The structure was calculated within the approximations of density functional theory with plane wave basis sets using the Abinit package.[79,80] The third dimension for the 2D cell was fixed at 30 Å, while the two dimensions of interest were set to 7.2 Å, at an angle of 60°, and optimized along with the molecular geometry. The general gradient approximation exchange-correlation functional of Perdew, Burke, and Ernzerhof was used, and the atoms were described by the projector-augmented waves approximation with the atomic data downloaded from the Abinit web.[81] The plane-wave basis was cut off at the energy of 15 Ha, for the double grid cutoff 50 Ha was applied. The 3×3×1 Monkhorst-Pack k-point grid was automatically generated so as not to produce erroneous contributions to the Fourier transform of real space vectors shorter than 50 Å (see Figures 3.20 and 3.21).

3.4.9 Mass Spectrometry

Mass spectrometry measurements were performed on a Thermo Scientific LCQ Fleet Ion Trap instrument using electrospray (ESI) ionization with helium (5.0 Messer) as a collision gas in the ion trap. The sample was dissolved in acetonitrile (concentration ~100 ng/ml) were introduced through a fused-silica sample tube of 0.100 mm (internal diameter) × 0.19 mm (outer diameter) to the ion source from a Hamilton syringe using infusion at 15 μL/min, source voltage 5.47 kV, tube lens voltage -44.71 V, capillary voltage -23.06 V, capillary temperature 165.01 °C, and N_2 (isolated from air in NitroGen N1118LA, Peak Scientific) as a nebulizing sheath gas (flow rate 14.97 p.d.u.). Only negative ions of the respective molecular peaks were detected.

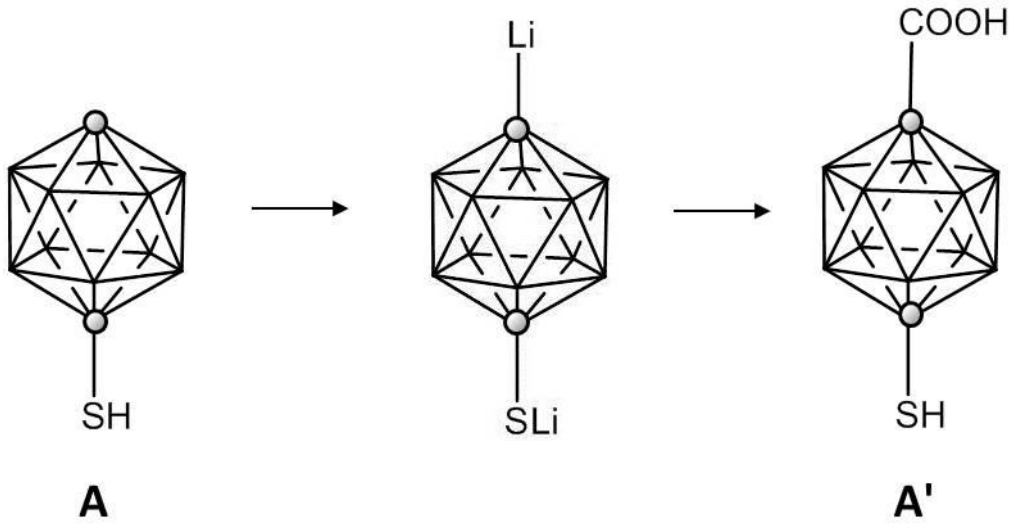

Figure 3.1 Synthesis of 1-SH-12-COOH-1,12-$C_2B_{10}H_{10}$ (**A'**) starting from the parental 1-SH-1,12-$C_2B_{10}H_{11}$ precursor (**A**).

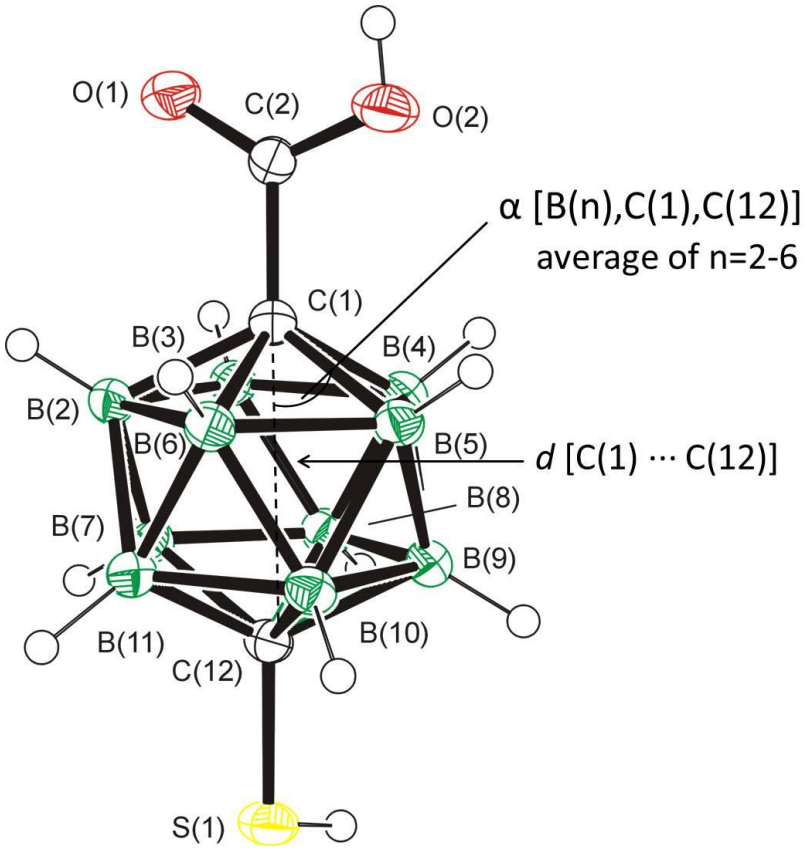

Figure 3.2 Crystallographically determined molecular structure of 1-(HS)-12-(COOH)-1,12-$C_2B_{10}H_{10}$ (**A'**).

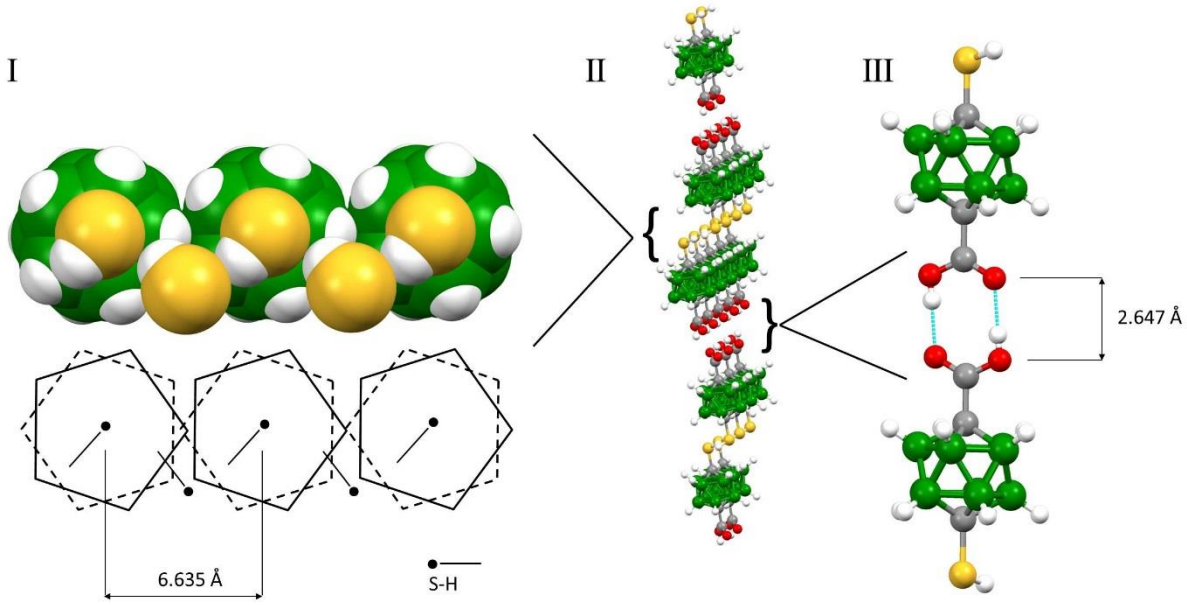

Figure 3.3 I Space-filling (top) and schematic (bottom) view of **A'** along the C(1)···C(12) axis of the molecule with the -$(SH)_n$- chain on top. The molecules are further associated in 2D sheets (**II**) through the dimeric $R_2^2(8)$ association pattern of carboxylic acids (**III**) with the O···O interatomic distance of 2.647 Å.

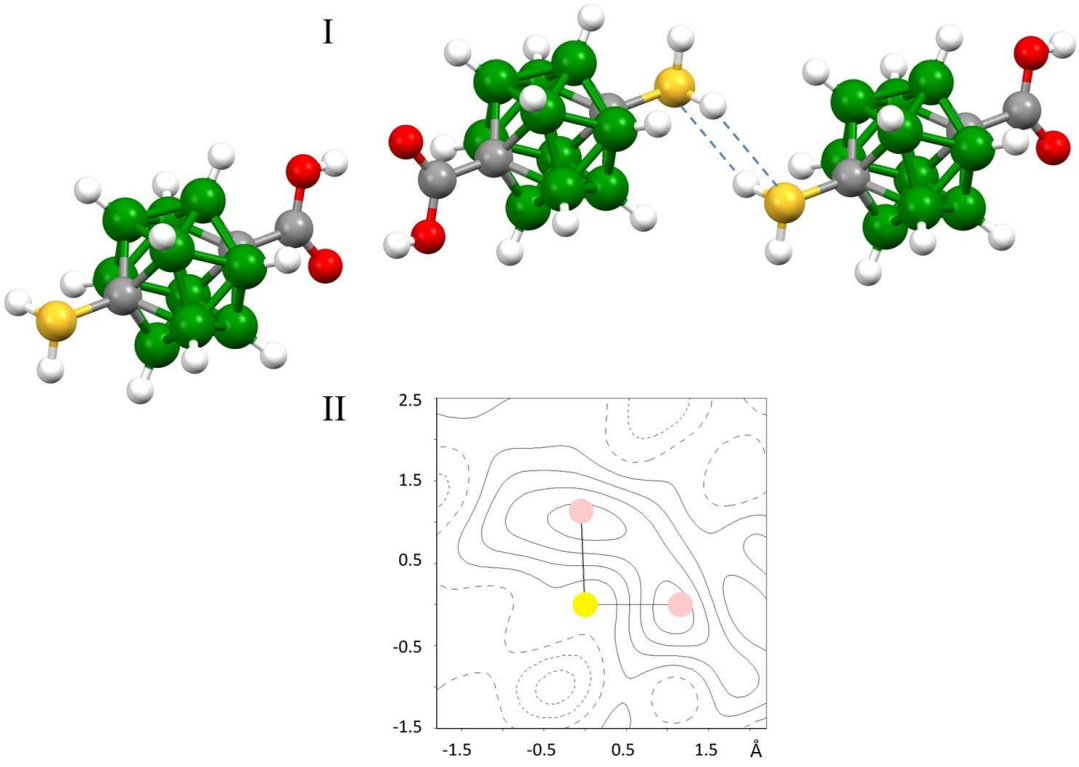

Figure 3.4 A sketch of the crystallographic disorder of the SH hydrogen atoms in **A'** (**I**) with the difference Fourier map (**II**) showing a section defined by H-S-H plane, merging the electron density 0.25 Å above and below the plane. Contour step is 0.05 $e^{-}Å^{-3}$; distances are given in Å.

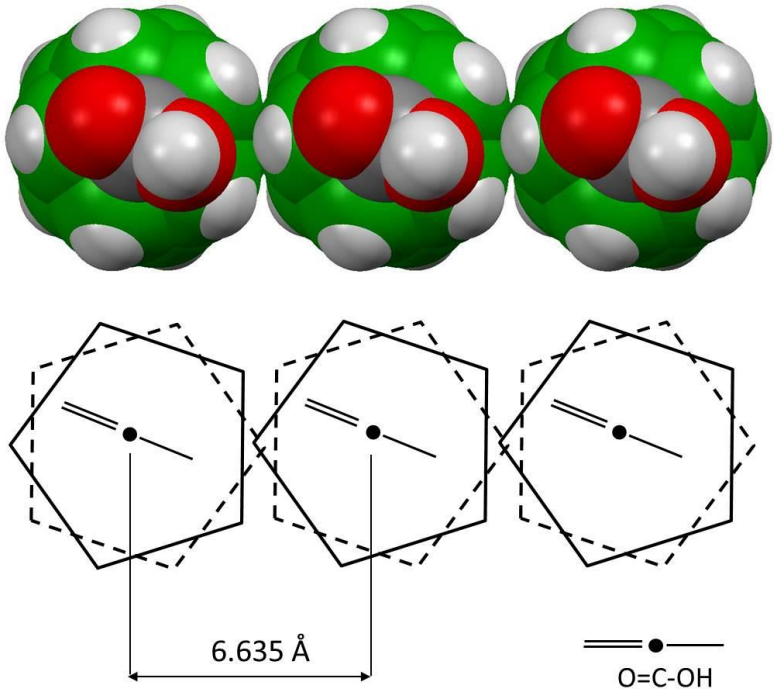

Figure 3.5 Space-filling (top) and schematic (bottom) drawings of a part of the crystallographic structure of **A'** (viewed along the C(1)···C(12) vectors of the molecular structure, with COOH groups on top) illustrating the closest packing of the molecules in a single crystal.

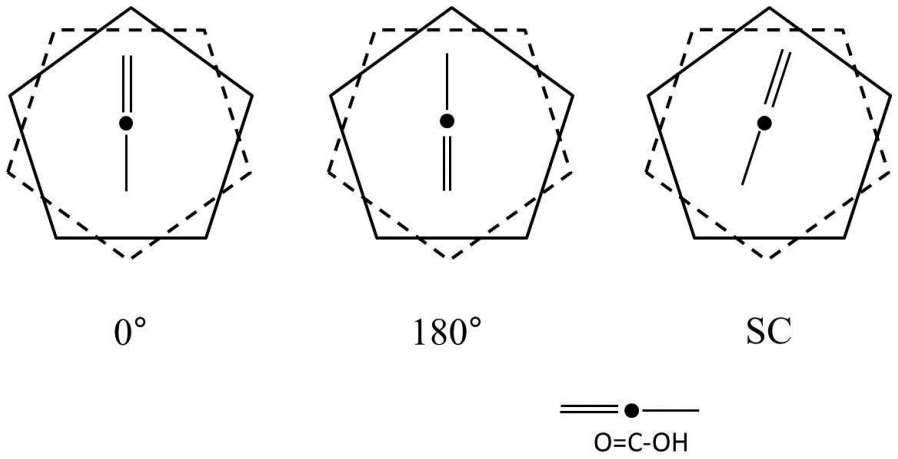

Figure 3.6 A schematic representation of two computationally optimized -COOH conformations (0° and 180°) and the conformation observed in single crystals (SC). The black dot in the middle indicates the position of a COOH carbon atom. The double line represents the doubly bonded oxygen and the single line represents hydroxyl part of the carboxylic group.

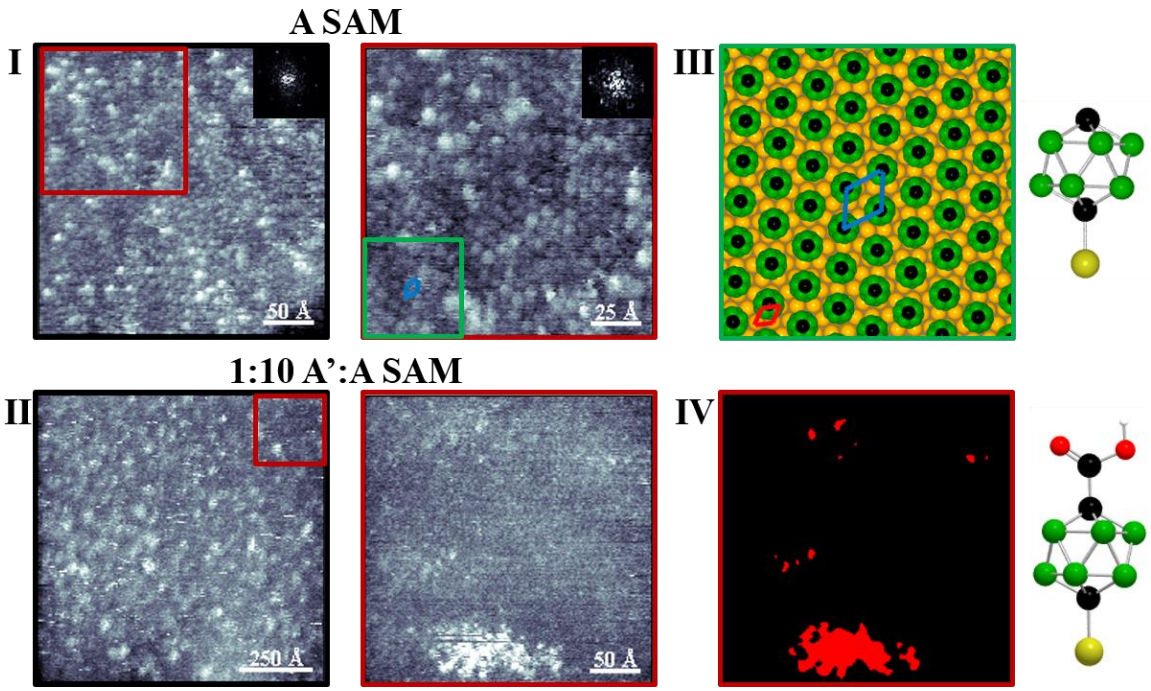

Figure 3.7 I Scanning tunneling micrographs ($I_{tunneling}$ = 100 pA, V_{sample} = -0.1 V) of **A** at 280 Å × 280 Å and 140 Å × 140 Å. Each inset depicts a Fourier transform showing a hexagonally close-packed array with nearest-neighbor spacings of 7.2 ± 0.5 Å. **II** A structural schematic depicting the observed lattice (blue lines indicate nearest neighbors) with respect to the underlying (1×1) unit cell (red rhombus) of the unreconstructed Au{111} substrate. **III** Scanning tunneling micrographs ($I_{tunneling}$ = 100 pA, V_{sample} = -1.0 V) of a co-deposited (1:10, **A'**:**A**) SAM, at both 940 Å × 940 Å and 280 Å × 280 Å scan sizes. **IV** Thresholding enables the isolation of **A'** regions that are highlighted in red.

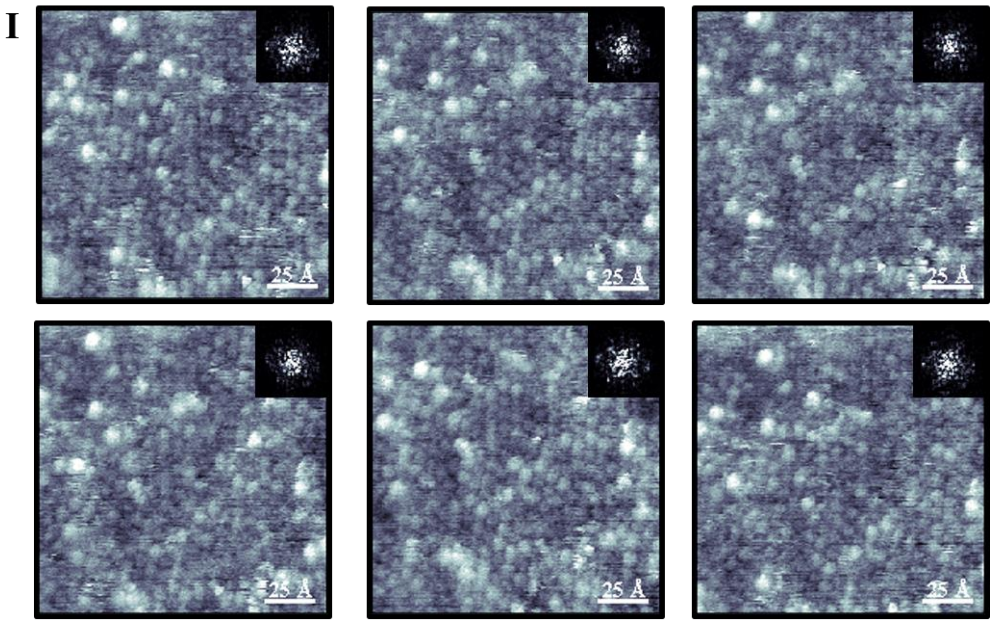

Figure 3.8 Compilation of scanning tunneling micrographs, which measure hexagonally close-packed arrays of **A** on Au{111}/mica. Both the thiol- (higher intensity) and thiolate- (lower intensity) bound moieties are resolved, and show average nearest neighbor distances of 7.2 ± 0.5 Å. Each image inset depicts a Fourier transform used to obtain lattice spacings.

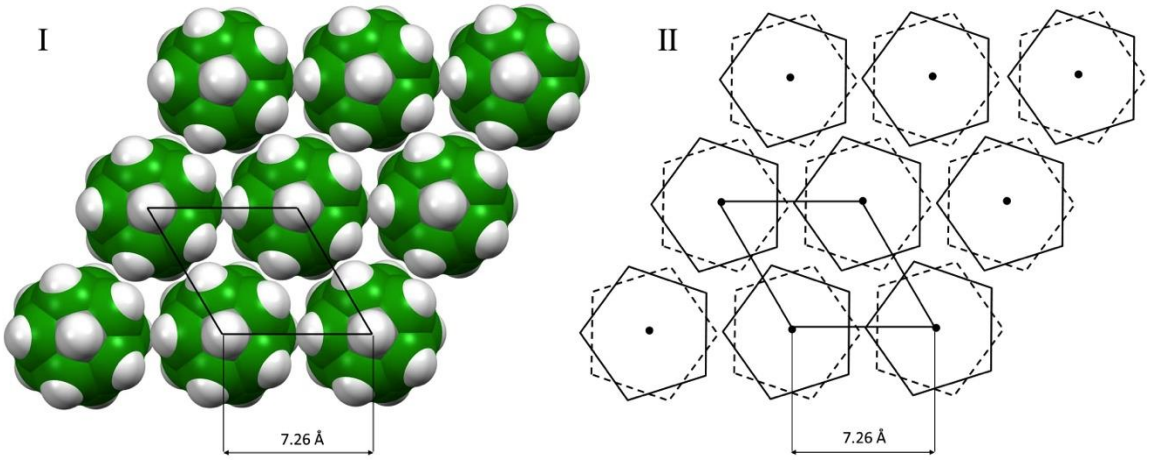

Figure 3.9 Calculated (using density functional theory) 2D array of molecules **A** showing a close-packed structure with the lattice parameters 7.26 Å × 7.27 Å (α = 60.07°). Space-filling (**I**) and schematic (**II**) representations.

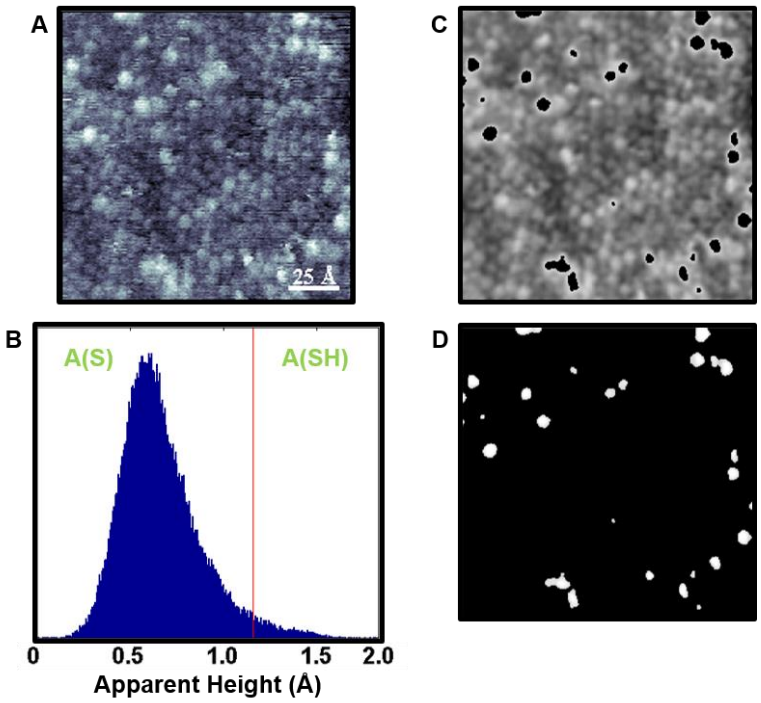

Figure 3.10 (A) Scanning tunneling micrograph of **A** deposited on a Au{111}/mica substrate with a corresponding apparent height histogram (B). The micrograph is thresholded by separating pixels that differ in average apparent height. Masking techniques, performed in Matlab, enable regions of **A** bound as thiols and thiolates to be separated and analyzed independently (C and D, respectively). The summed average percent of **A** (bound as thiolate) is 95% (5% **A**, bound as thiol), which suggests that cleaved hydrogen-sulfur surface bonding is energetically favorable in comparison to the non-cleaved bonding scheme.

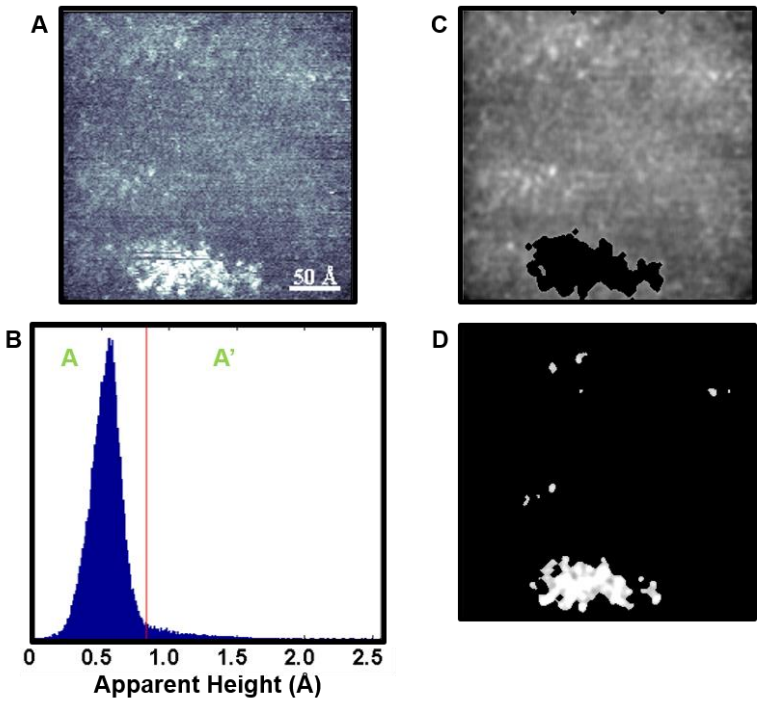

Figure 3.11 (A) Scanning tunneling micrograph of a 1:10 (**A'**:**A**) solution deposited self-assembled monolayer, with measured coverages consistent with deposited ratios, on an Au{111}/mica substrate with a corresponding apparent height histogram (B). The micrograph is thresholded by apparent height differences. Masking techniques, performed in Matlab, enable regions of **A** and **A'** to be separated and analyzed independently (C and D, respectively). The **A'** moiety displays a larger apparent height of 1.2 ± 0.2 Å due to protruding carboxyl groups.

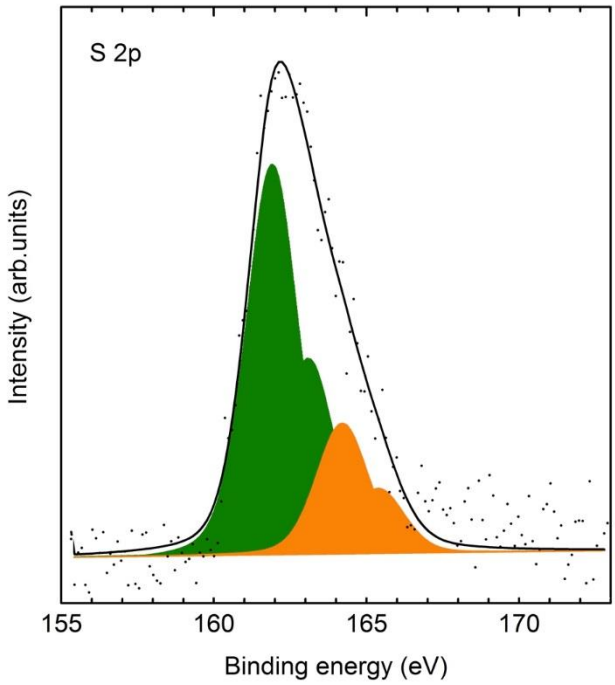

Figure 3.12 X-ray photoelectron spectrum of S 2p photoelectrons fit to indicate the contributions of both the thiolate (green) and the thiol (yellow) bound moieties of A' on Au{111} (background subtracted).

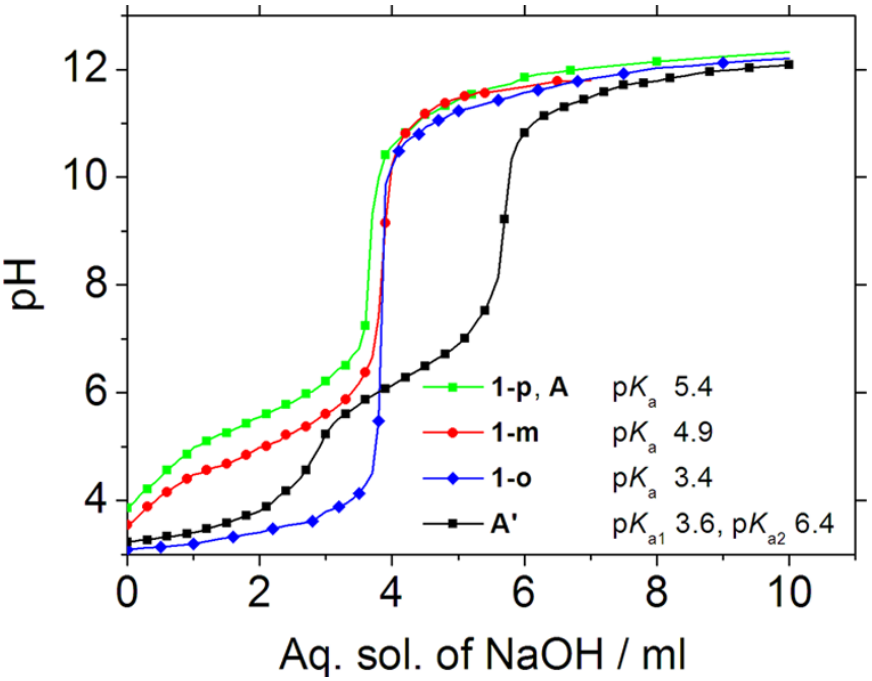

Figure 3.13 Acid-base titration curves of 1-HS-1,2-$C_2B_{10}H_{11}$ (**1-o**), 1-HS-1,7-$C_2B_{10}H_{11}$ (**1-m**), 1-HS-1,12-$C_2B_{10}H_{11}$ (**1-p**, **A**), and 1-HS-12-COOH-1,12-$C_2B_{10}H_{10}$ (**A'**).

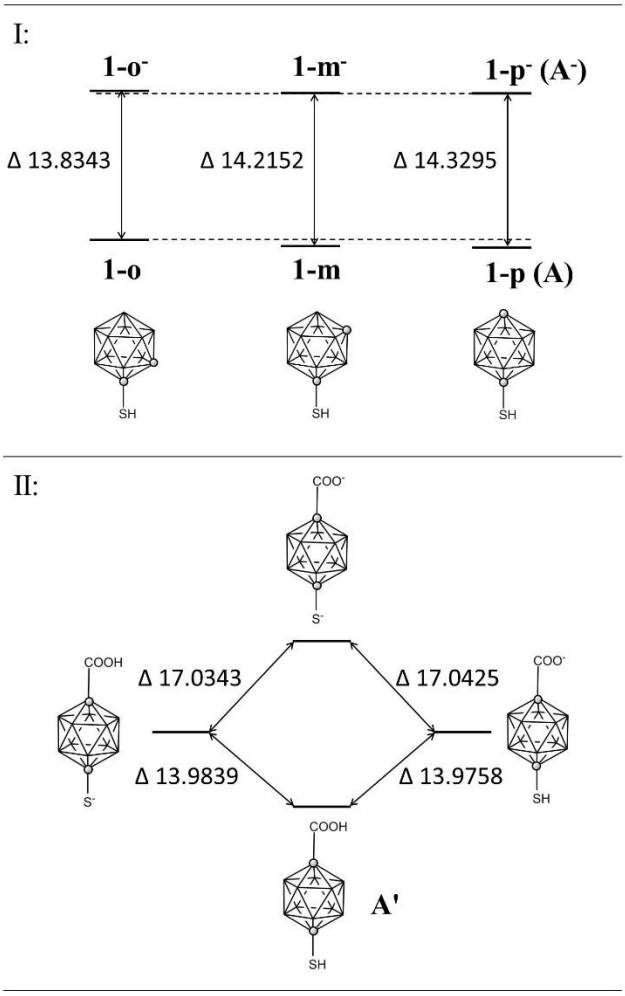

Figure 3.14 I: Relative energies of 1-HS-1,2-$C_2B_{10}H_{11}$ (**1-o**), 1-HS-1,7-$C_2B_{10}H_{11}$ (**1-m**), 1-HS-1,12-$C_2B_{10}H_{11}$ (**1-p**, **A**), and their respective deprotonated forms (**1-o-**, **1-m-**and **1-p-**). II: Relative energies of 1-HS-12-COOH-1,12-$C_2B_{10}H_{10}$ (**A'**) and its deprotonated forms. Schematic representations of the respective molecules are shown without hydrogen atoms in their vertices for clarity. The positions of carbon atoms in the skeletons are marked with circles. All values are in eV.

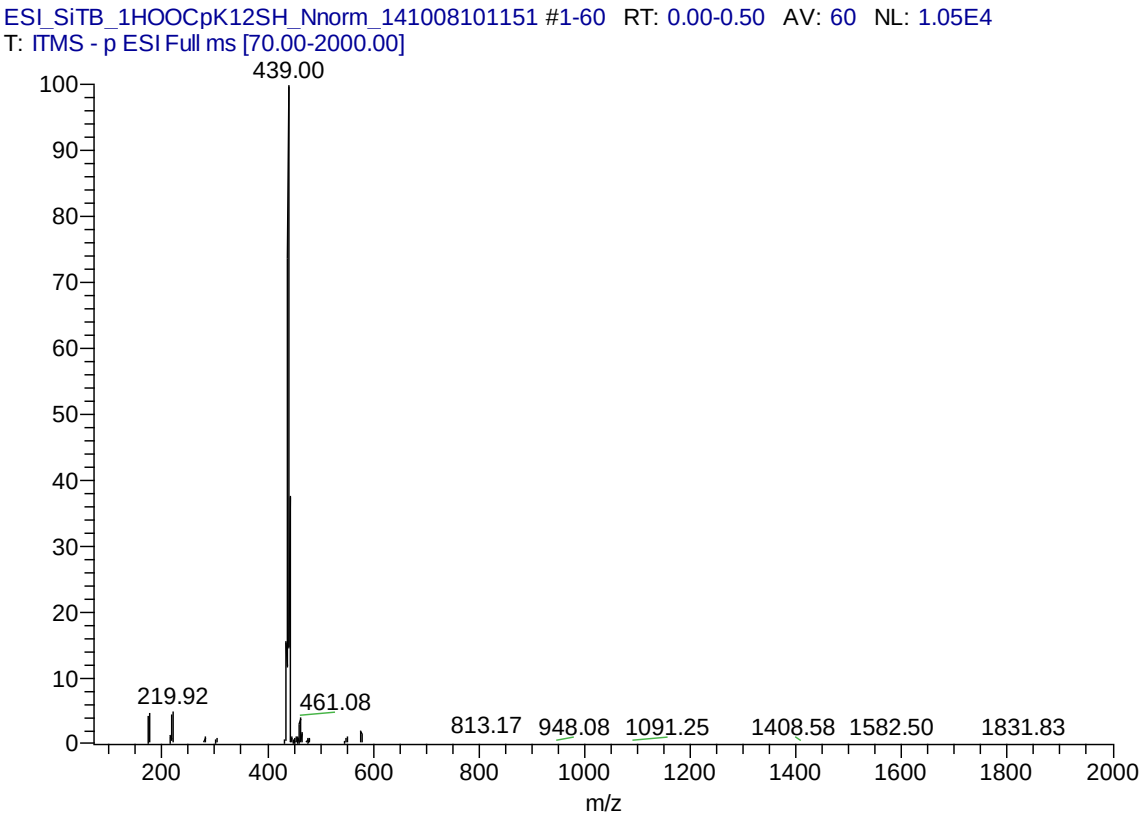

Figure 3.15 Mass spectrum of **A'**. (The peak at 461.08 can be assigned to $[2M-H]^-$ with one Na atom.)

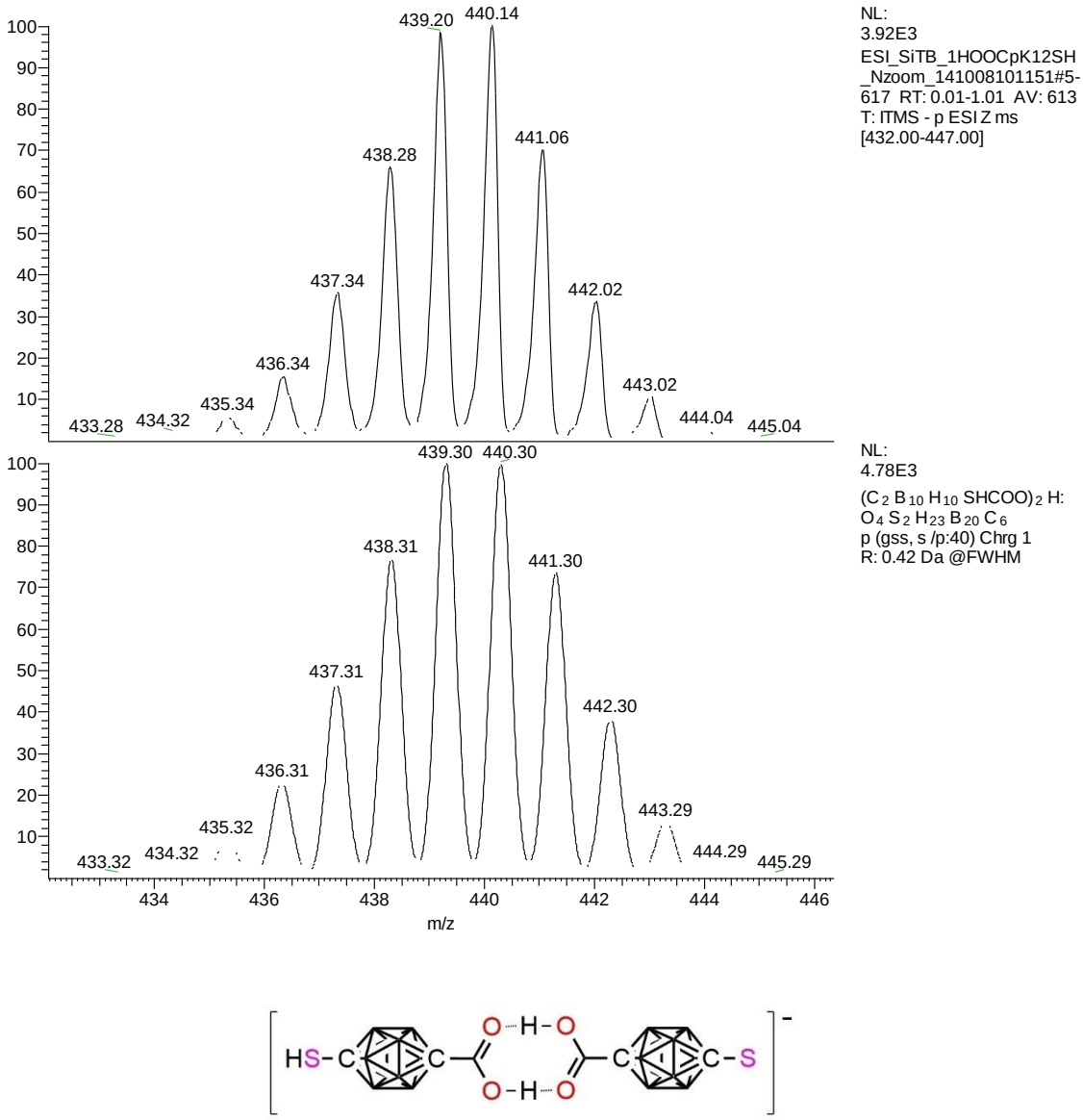

Figure 3.16 (Top) Measured and (bottom) calculated isotopic distribution envelopes for molecular masses corresponding to $[2M-H]^-$, M: $C_3B_{10}H_{12}S_1O_2$. A possible structure is depicted below the spectra.

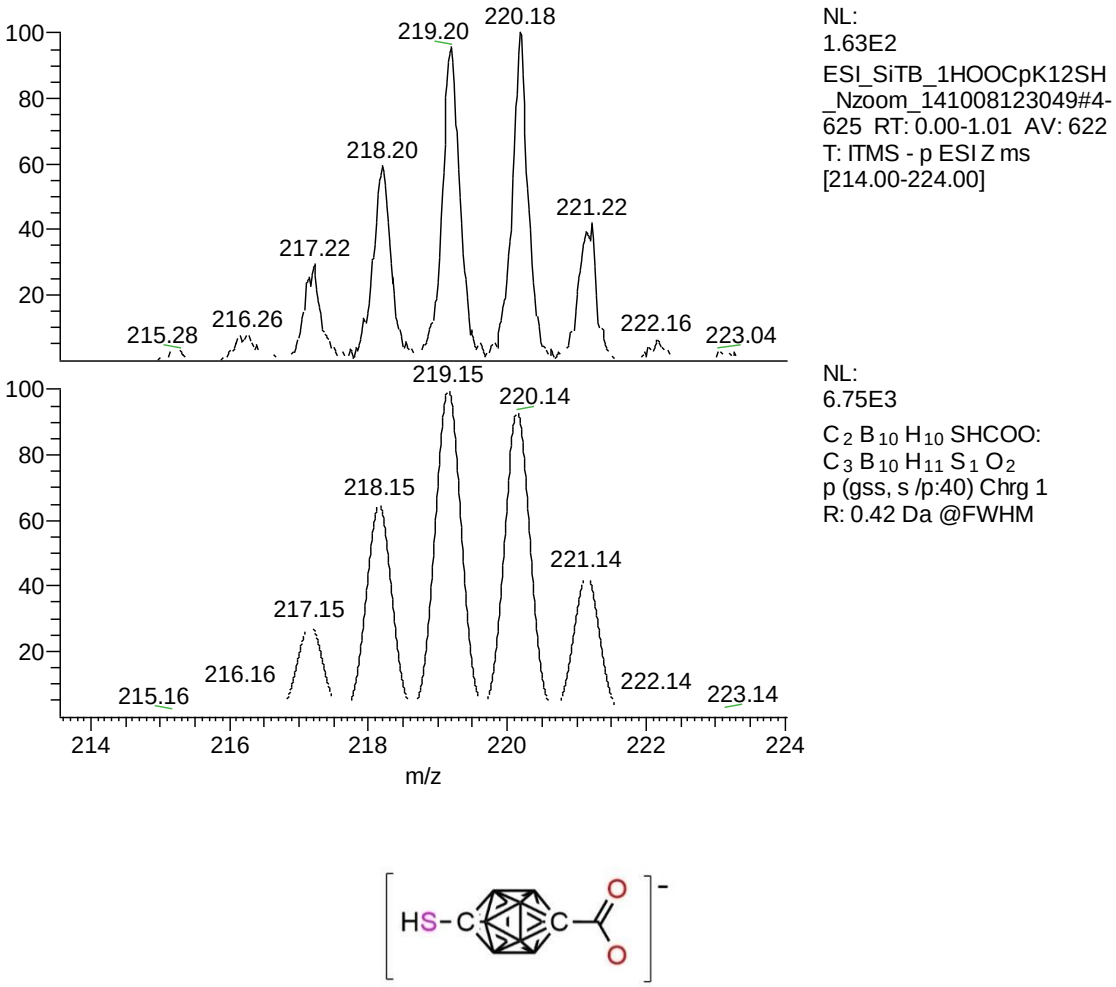

Figure 3.17 (Top) Measured and (bottom) calculated isotopic distribution envelopes for molecular masses corresponding to $[M-H]^-$, M: $C_3B_{10}H_{12}S_1O_2$. A possible structure is depicted below the spectra.

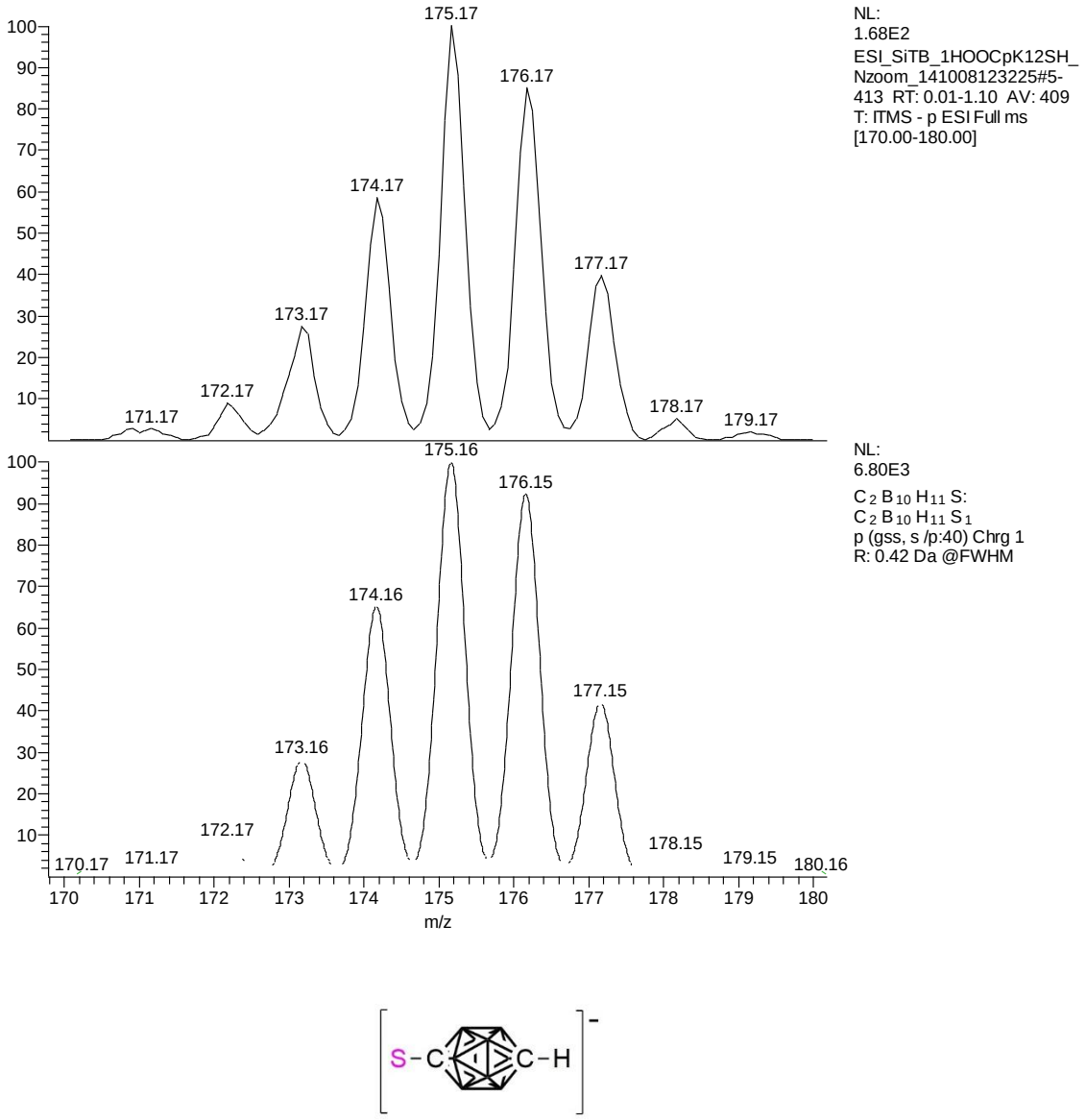

Figure 3.18 (Top) Measured and (bottom) calculated isotopic distribution envelopes for molecular masses corresponding to $[M\text{-}COOH]^-$, M: $C_3B_{10}H_{12}S_1O_2$. A possible structure is depicted below the spectra.

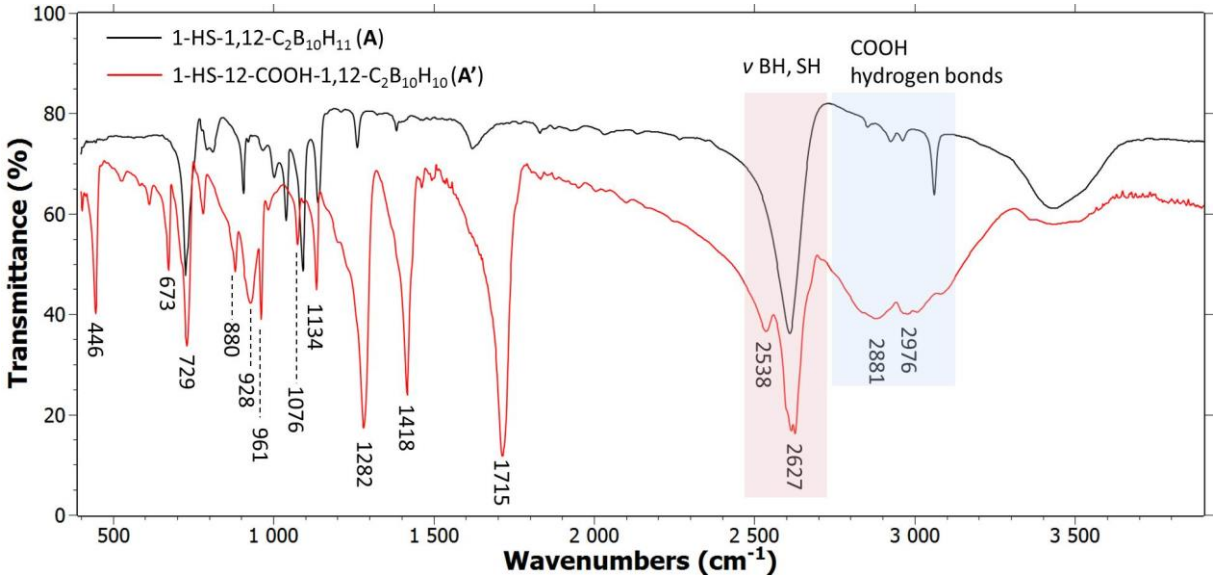

Figure 3.19 The infrared spectrum of **A'** (red curve) measured in KBr pellet using Nicolet Avatar. The spectrum of **A** (black curve) is shown for comparison.

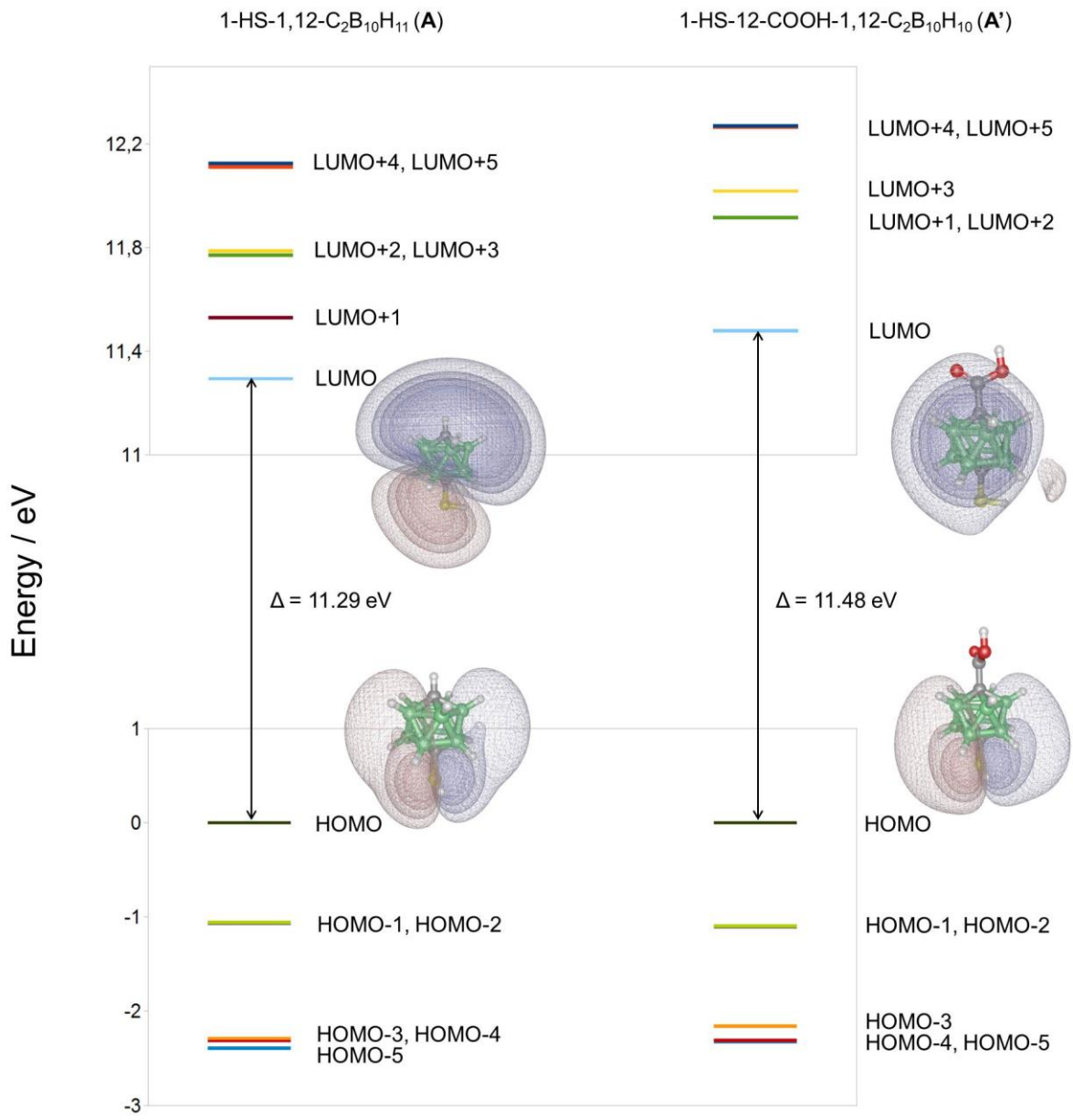

Figure 3.20 Energy diagrams of **A** and **A'**. The orbitals are depicted by a series of surfaces of constant probability density that form envelopes containing the space of consecutively 80, 90, 95, and 99% probability of the electron presence. The surfaces belonging to the positive parts of the orbitals are colored in hues of blue, those of the negative ones in hues of red.

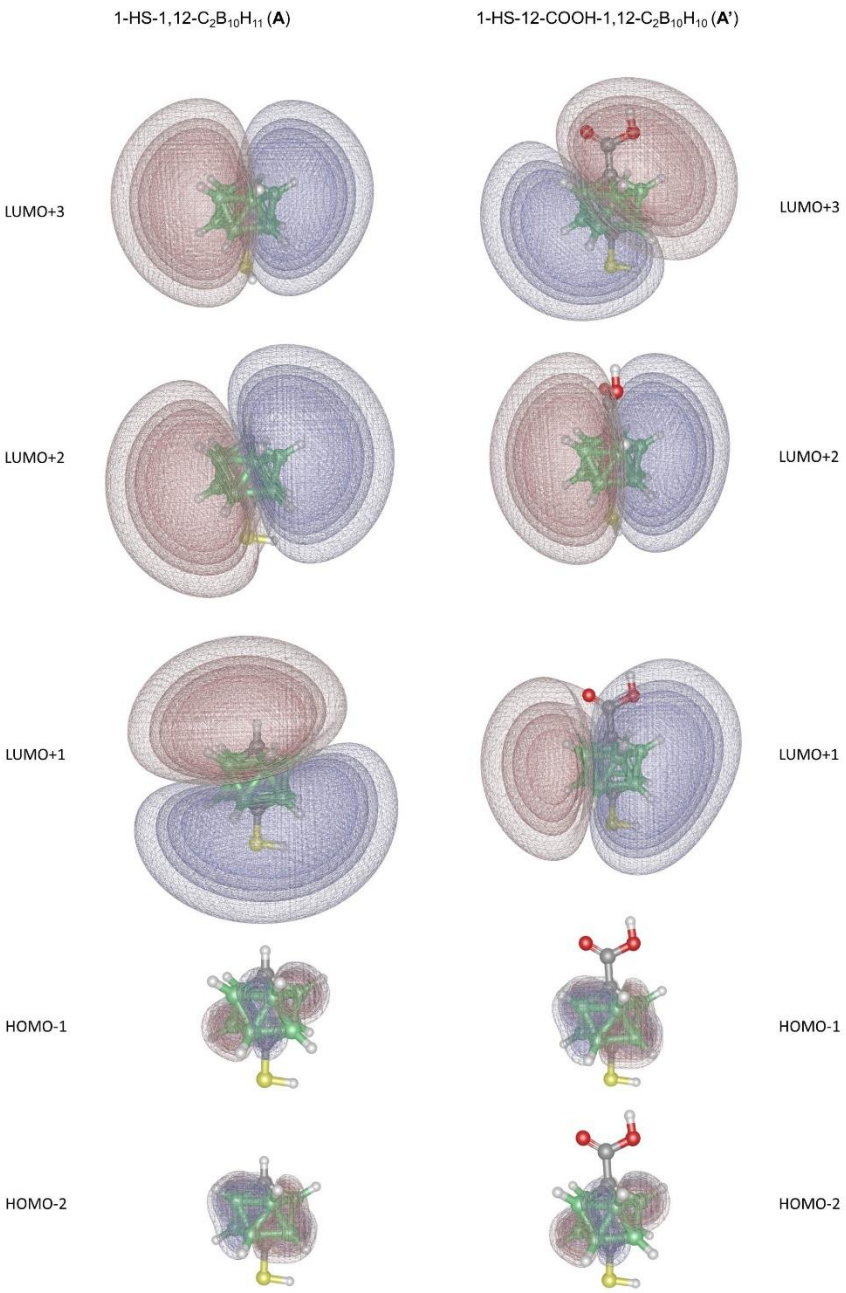

Figure 3.21 Further orbitals (HOMO-1, HOMO-2, LUMO+1, LUMO+2 and LUMO+3) of **A** and **A'.** The orbitals are depicted by a series of surfaces of constant probability density that form envelopes containing the space of consecutively 80, 90, 95, and 99% probability of the electron

presence. The surfaces belonging to the positive parts of the orbital are colored in hues of blue, those of the negative ones in hues of red.

A'				A		
Assign.	δ ^{11}B	δ ^{1}H	δ ^{13}C	δ ^{11}B	δ ^{1}H	δ ^{13}C
1			74.07			74.56
2-6	-11.25	2.41		-10.22	2.45	
7-11	-13.20	2.47		-14.09	2.19	
12			72.69		3.14	58.30
S-H (1)		3.18			3.19	
COO-H (12)		3.74[a]	163.21			

Table 3.1 Measured ^{11}B, ^{13}C, and ^{1}H NMR chemical shift data for compounds 1-HS-12-COOH-1,12-$C_2B_{10}H_{10}$ (A') and 1-HS-1,12-$C_2B_{10}H_{11}$ (A) in CD_3OD solution at 300 K. [a]The respective proton appears as a broad band.

[a]	A'
CCDC	1028174
Formula	$C_3H_{12}B_{10}O_2S$
M	220.30
crystal system	Triclinic
space group	P -1
a/Å	6.6353(3)
b/Å	7.1464(4)
c/Å	13.7788(7)
α/deg	79.537(5)
β/deg	84.127(4)
γ/deg	62.494(5)
V/Å^3	569.75(6)
D_{calc}/g·cm^{-3}	1.284
F_{000}	224.0
μ mm^{-1}	2.201
GooF	1.78
R1 (I > 3σ(I))	0.0418(2670)
wR2 (all data)	0.1067 (3742)
$\rho_{max\ and\ min}$/e$^-$ Å^{-3}	0.27, -0.29

Table 3.2 Crystallographic collection and refinement data.

	α / °	d[C(1)···C(12)] / Å
A'	62.4(1)$^{sc,\ \alpha\ (COOH)}$ 62.2(1)$^{sc,\ \alpha\ (SH)}$ 62.43$^{comp,\ \alpha\ (COOH)}$ 62.15$^{comp,\ \alpha\ (SH)}$	3.091(3)^{sc} 3.077^{comp}
A	62.18$^{comp,\ \alpha\ (SH)}$ 62.74$^{comp,\ \alpha\ (H)}$	3.067^{comp}
1,12-$(HS)_2$-1,12-$C_2B_{10}H_{10}$	62.0(1)^{sc,19} 62.15^{comp,19}	3.107(3)^{sc,19} 3.091^{comp,19}
1,12-$C_2B_{10}H_{12}$	62.8(2)^{sc,32}	3.056(6)^{sc,32}
$[B_{12}H_{12}]^{2-}$	58.3(1)^{sc,33}	3.383(2)^{sc,33,a}

Table 3.3 Selected cluster geometry parameters for compounds 1-HS-12-COOH-1,12-$C_2B_{10}H_{10}$ (A'), 1-HS-1,12-$C_2B_{10}H_{11}$ (A), and for comparison also 1,12-$(HS)_2$-1,12-$C_2B_{10}H_{10}$, 1,12-$C_2B_{10}H_{12}$, and $[B_{12}H_{12}]^{2-}$. ^{sc}Data from an X-ray structural analysis of a single crystal, ^{comp}Computational data, ^{a}d[B(1)···B(12)].

	A' (-)	
B-C-C=O torsion	180°	0°
E(HF)	-24877.2294	-24877.2260
ΔE(HF)	0.0000	0.0034
N(imag)	0	1
ZP corr.	5.2173	5.2154
Ecorr(HF)	-909.0040	-909.0058
ΔEcorr(HF)	0.0000	0.0018
E(MP2)	-24928.6243	-24928.6222
ΔE(MP2)	0.0000	0.0022

Table 3.4 Conformational analysis of 1-S-12-COOH-1,12-$C_2B_{10}H_{10}$ (-), **A'** (-). All energy values are in eV.

Sample	S	$C_{CB(CO)}$	$^{a}C_{CH,CC}$	C_{CO}	Au	O
A						
Au {111}^{s}	1.1	2.0	1.4	~0	20.0	0.9
Au {111}^{gp}	1.1	2.0	2.7	0.6	10.8	1.4
A'						
Au {111}^{s}	1.0	2.7	2.5	1.2	10.7	4.5
350 °C	1.2	3.8	7.4	0.8	29.0	-
Au {111}^{gp}	1.2	2.4	5.4	1.0	28.0	2.3

Table 3.5 Atomic concentrations of elements on Au surfaces modified with A and A' compounds relative to the concentration of boron atoms (=10) as determined from XPS analyses assuming homogeneous samples (Au is included as a relative measure of the surface coverage by the adsorbed species; higher Au signals indicate lower carborane coverages). ^{s}Adsorption from solution; ^{gp}adsorption from the gas phase; ^{a}adventitious carbonaceous contamination.

Sample	S $2p_{3/2}$	B 1s	C 1s
		A	
Au {111}^{s}	162.1 (2.0) 164.0 (2.0)	189.1 (1.9)	284.4 (2.1) 285.9 (2.1)
Au {111}^{gp}	162.5 (2.2) 164.6 (2.2)	189.1 (1.9)	284.6 (2.2) 286.2 (2.2) 289.0 (2.2)
		A'	
Au {111}^{s}	162.2 (1.8) 164.0 (1.8)	189.2 (2.1)	284.7 (2.2) 286.1 (2.2) 288.8 (2.2)
350 °C	162.4 (2.5)	189.7 (2.2)	284.5 (2.4) 286.0 (2.4) 288.7 (2.4)
Au {111}^{gp}	161.9 (2.2) 164.1 (2.2)	189.1 (1.9)	284.5 (2.2) 286.1 (2.2) 289.0 (2.2)

Table 3.6 Measured core-level binding energies and FWHM[a] (parenthesis) for Au films modified with 1-HS-1,12-$C_2B_{10}H_{11}$ (A) and 1-HS-12-COOH-1,12-$C_2B_{10}H_{10}$ (A'). The binding energy of Au $4f_{7/2}$ is 84.0 eV for all samples. All values are in eV. [a]Full width at half maximum; [s]adsorption from solution; [v]adsorption from the gas phase.

3.5 References

1. Smith, R. K.; Lewis, P. A.; Weiss, P. S. Patterning Self-Assembled Monolayers. *Prog. Surf. Sci.* **2004**, *75*, 1–68.

2. Kim, J.; Rim, Y. S.; Liu, Y.; Serino, A. C.; Thomas, J. C.; Chen, H.; Yang, Y.; Weiss, P. S. Interface Control in Organic Electronics Using Mixed Monolayers of Carboranethiol Isomers. *Nano Lett.* **2014**, *14*, 2946–2951.

3. Love, J. C.; Estroff, L. A.; Kriebel, J. K.; Nuzzo, R. G.; Whitesides, G. M. Self-Assembled Monolayers of Thiolates on Metals as a Form of Nanotechnology. *Chem. Rev.* **2005**, *105*, 1103–1169.

4. Gooding, J. J.; Ciampi, S. The Molecular Level Modification of Surfaces: From Self-Assembled Monolayers to Complex Molecular Assemblies. *Chem. Soc. Rev.* **2011**, *40*, 2704–2718.

5. Ulman, A. Formation and Structure of Self-Assembled Monolayers. *Chem. Rev.* **1996**, *96*, 1533–1554.

6. Fujii, S.; Akiba, U.; Fujihira, M. Geometry for Self-Assembling of Spherical Hydrocarbon Cages with Methane Thiolates on Au(111). *J. Am. Chem. Soc.* **2002**, *124*, 13629–13635.

7. Hohman, J. N.; Claridge, S. A.; Kim, M.; Weiss, P. S. Cage Molecules for Self-Assembly. *Mat. Sci. Eng. R* **2010**, *70*, 188–208.

8. von Wrochem, F.; Scholz, F.; Gao, D.; Nothofer, H.-G.; Yasuda, A.; Wessels, J. M.; Roy, S.; Chen, X.; Michl, J. High-Band-Gap Polycrystalline Monolayers of a 12-Vertex *p*-Carborane on Au(111). *J. Phys. Chem. Lett.* **2010**, *1*, 3471–3477.

9. Hohman, J. N.; Kim, M.; Shüpback, B.; Kind, M.; Thomas, J. C.; Terfort, A.; Weiss, P. S. Dynamic Double Lattice of 1-Adamantaneselenolate Self-Assembled Monolayers on Au{111}. *J. Am. Chem. Soc.* **2011**, *133*, 19422–19431.

10. Spokoyny, A. M.; Machan, C. W.; Clingerman, D. J.; Rosen, M. S.; Wiester, M. J.; Kennedy, R. D.; Stern, C. L.; Sargeant, A. A.; Mirkin, C. A. A Coordination Chemistry Dichotomy for Icosahedral Carborane-Based Ligands. *Nature Chem.* **2011**, *3*, 590–596.

11. Katano, S.; Kim, Y.; Kitagawa, T.; Kawai, M. Tailoring Electronic States of a Single Molecule using Adamantane-Based Molecular Tripods. *Phys. Chem. Chem. Phys.* **2013**, *15*, 14229–14233.

12. Wann, D. A.; Lane, P. D.; Robertson, H. E.; Baše, T.; Hnyk, D. The Gaseous Structure of *closo*-9,12-(SH)(2)-1,2-$C_2B_{10}H_{10}$, A Modifier of Gold Surfaces, as Determined using Electron Diffraction and Computational Methods. *Dalton Trans.* **2013**, *42*, 12015–12019.

13. Grimes, R. N. Carboranes in the Chemist's Toolbox. *Dalton Trans.* **2015**, *44*, 5939–5956.

14. Yeager, L. J.; Saeki, F.; Shelley, K.; Hawthorne, M. F.; Garrell, R. A New Class of Self-Assembled Monolayers: *closo*-$B_{12}H_{11}S_3$- on Gold. *J. Am. Chem. Soc.* **1998**, *120*, 9961–9962.

15. Scholz, F.; Nothofer, H.-G.; Wessels, J. M.; Nelles, G.; von Wrochem, F.; Roy, S.; Chen, X.; Michl, J. Permethylated 12-Vertex p-Carborane Self-Assembled Monolayers. *J. Phys. Chem. C* **2011**, *115*, 22998–23007.

16. Claridge, S. A.; Liao, W. S.; Thomas, J. C.; Cao, H.; Cheunkar, S.; Serino, A. C.; Andrews, A. M.; Weiss, P. S. From the Bottom Up: Dimensional Control and Characterization in Molecular Monolayers. *Chem. Soc. Rev.* **2013**, *42*, 2725–2745.

17. Baše, T.; Bastl, Z.; Plzák, Z.; Grygar, T.; Plešek, J.; Carr, M. J.; Malina, V.; Šubrt, J.; Boháček, J.; Večerníková, E.; Kříž, O. Carboranethiol-Modified Gold Surfaces. A Study and Comparison of Modified Cluster and Flat Surfaces. *Langmuir* **2005**, *21*, 7776–7785.

18. Hohman, J. N.; Zhang, P. P.; Morin, E. I.; Han, P.; Kim, M.; Kurland, A. R.; McClanahan, P. D.; Balema, V. P.; Weiss, P. S. Self-Assembly of Carboranethiol Isomers on Au{111}: Intermolecular Interactions Determined by Molecular Dipole Orientations. *ACS Nano* **2009**, *3*, 527–536.

19. Baše, T.; Bastl, Z.; Šlouf, M.; Klementová, M.; Šubrt, J.; Vetushka, A.; Ledinský, M.; Fejfar, A.; Macháček, J.; Carr, M. J.; Londesborough, M. G. S. Gold Micrometer Crystals Modified with Carboranethiol Derivatives. *J. Phys. Chem. C* **2008**, *112*, 14446–14455.

20. Baše, T.; Bastl, Z.; Hávranek, V.; Lang, K.; Bould, J.; Londesborough, M. G. S.; Macháček, J.; Plešek, J. Carborane-Thiol-Silver Interactions. A Comparative Study of the Molecular Protection of Silver Surfaces. *Surf. Coat. Technol.* **2010**, *204*, 2639–2646.

21. Lübben, J. F.; Baše, T.; Rupper, P.; Künniger, T.; Macháček, J.; Guimond, S. Tuning the Surface Potential of Ag Surfaces by Chemisorption of Oppositely-Oriented Thiolated Carborane Dipoles. *J. Colloid Interface Sci.* **2011**, *354*, 168–174.

22. Ito, M.; Wei, T. X.; Chen, P.-L.; Akiyama, H.; Matsumoto, M.; Tamada, K.; Yamamoto, Y. A Novel Method for Creation of Free Volume in a One-Component Self-Assembled Monolayer. Dramatic Size Effect of *p*-Carborane. *J. Mater. Chem.* **2005**, *15*, 478–483.

23. Langecker, J.; Fejfarová, K.; Dušek, M.; Rentsch, D.; Baše, T. Carbon-Substituted 9,12-dimercapto-1,2-dicarba-*closo*-Dodecaboranes via a 9,12-bis(methoxy-methylthio)-1,2-dicarba-*closo*-Dodecaborane Precursor. *Polyhedron* **2012**, *45*, 144–151.

24. Frank, R.; Boehnke, S.; Aliev, A.; Hey-Hawkins, E. From *o*-Carbaborane-9-thiol towards New Building Blocks. *Polyhedron* **2012**, *39*, 9–13.

25. Kabytaev, K. Z.; Everett, T. A.; Safronov, A. V.; Sevryugina, Y. V.; Jalisatgi, S. S.; Hawthorne, M. F. B-Mercaptocarboranes: A New Synthetic Route. *Eur. J. Inorg. Chem.* **2013**, 2488–2491.

26. Weiss, P. S. Functional Molecules and Assemblies in Controlled Environments: Formation and Measurements. *Acc. Chem. Res.* **2008**, ***41***, 1772–1781.

27. Ackerson, C. J.; Jadzinsky, P. D.; Kornberg, R. D. Thiolate Ligands for Synthesis of Water-Soluble Gold Clusters. *J. Am. Chem. Soc.* **2005**, *127*, 6550–6551.

28. Jadzinsky, P. D.; Calero, G.; Ackerson, C. J.; Bushnell, D. A.; Kornberg, R. D. Structure of a Thiol Monolayer-Protected Gold Nanoparticle at 1.1 Angstrom Resolution. *Science* **2007**, *318*, 430–433.

29. Walter, M.; Akola, J.; Lopez-Acevedo, O.; Jadzinsky, P. D.; Calero, G.; Ackerson, C. J.; Whetten, R. L.; Grönbeck, H.; Häkkinen, H. A Unified View of Ligand-Protected Gold Clusters as Superatom Complexes. *Proc. Natl. Acad. Sci.* **2008**, *105*, 9157–9162.

30. Saavedra, H. M.; Thompson, C. M.; Hohman, J. N.; Crespi, V. H.; Weiss, P. S. Reversible Lability by in Situ Reaction of Self-Assembled Monolayers. *J. Am. Chem. Soc.* **2009**, *131*, 2252–2259.

31. Saavedra, H. M.; Mullen, T. J.; Zhang, P. P.; Dewey, D. C.; Claridge, S. A.; Weiss, P. S. Hybrid Strategies in Nanolithography. *Rep. Prog. Phys.* **2010**, ***73***, 036501.

32. Davidson, M. G.; Hibbert, T. G.; Howard, J. A. K.; Mackinnon, A.; Wade, K. Definitive Crystal Structures of Ortho-, Meta- and Para-Carboranes: Supramolecular Structures Directed Solely by C-H···O Hydrogen Bonding to HMPA (HMPA = hexamethylphosphoramide). *Chem. Commun.* **1996**, *19*, 2285–2286.

33. Tiritiris, I.; Schleid, T. Z. The dodecahydro-*closo*-Dodecaborates $M_2[B_{12}H_{12}]$ of the Heavy Alkali Metals ($M = K^+$, Rb^+, NH_4^+, Cs^+) and their Formal Iodide Adducts $M_3I[B_{12}H_{12}]$ ($MI{\times}M_2[B_{12}H_{12}]$). *Anorg. Allg. Chem.* **2003**, *629*, 1390–1402.

34. Hnyk, D.; Holub, J.; Hofmann, M.; Schleyer, P. v. R.; Robertson, H. E.; Rankin, D. W. H. Synthesis and Molecular Structure of 1,12-dicarba-*closo*-Dodecaborane(12)-1,12-dithiol, 1,12-(SH)(2)-1,12-$C_2B_{10}H_{10}$, in the Gaseous Phase, Determined by Electron Diffraction and *Ab Initio* Calculations; Geometrical Consequences of Three-Dimensional Aromaticity in Carboranes 1,12-X-2-1,12-$C_2B_{10}H_{10}$. *J. Chem. Soc.*, *Dalton Trans*. **2000**, 4617–4622.

35. Bernstein, J.; Davis, R. E.; Shimoni, L.; Chang, N.-L. Patterns in Hydrogen Bonding: Functionality and Graph Set Analysis in Crystals. *Angew. Chem. Int. Ed. Eng.* **1995**, *34*, 1555–1573.

36. Claridge, S. A.; Schwartz, J. J.; Weiss, P. S. Electrons, Photons, and Force: Quantitative Single-Molecule Measurements from Physics to Biology. *ACS Nano* **2011**, *5*, 693–729.

37. Hohman, J. N.; Thomas, J. C.; Zhao, Y.; Auluck, H.; Kim, M.; Vijselaar, W. J. C.; Kommeran, S.; Terfort, A.; Weiss, P. S. Exchange Reactions between Alkanethiolates and Alkaneselenols on Au{111}. *J. Am. Chem. Soc.* **2014**, *136*, 8110–8121.

38. Han, P.; Kurland, A. R.; Giordano, A. N.; Nanayakkara, S. U.; Blake, M. M.; Pochas, C. M.; Weiss, P. S. Heads and Tails: Simultaneous Exposed and Buried Interface Imaging of Monolayers. *ACS Nano* **2009**, *3*, 3115–3121.

39. Claridge, S. A.; Thomas, J. C.; Silverman, M. A.; Schwartz, J. J.; Yang, Y.; Wang, C.; Weiss, P. S. Differentiating Amino Acid Residues and Side Chain Orientations in Peptides Using Scanning Tunneling Microscopy. *J. Am. Chem. Soc.* **2013**, *135*, 18528–18535.

40. Fujii, S.; Akiba, U.; Fujihira, M. Geometry for Self-Assembling of Spherical Hydrocarbon Cages with Methane Thiolates on Au(111). *J. Am. Chem. Soc.* **2002**, *124*, 13629–13635.

41. Farha, O.; Spokoyny, A. M.; Mulfort, K. L.; Hawthorne, M. F.; Mirkin, C. A.; Hupp, J. T. Synthesis and Hydrogen Sorption Properties of Carborane Based Metal-Organic Framework Materials. *J. Am. Chem. Soc.* **2007**, *129*, 12680–12681.

42. Stranick, S. J.; Parikh, A. N.; Tao, Y.-T.; Allara, D. L.; Weiss, P. S. Phase-Separation of Mixed-Composition Self-Assembled Monolayers into Nanometer-Scale Molecular Domains. *J. Phys. Chem.* **1994**, *98*, 7636–7646.

43. Weck, M.; Jackiw, J. J.; Rossi, R. R.; Weiss, P. S.; Grubbs, R. H. Ring-Opening Metathesis Polymerization from Surfaces. *J. Am. Chem. Soc.* **1999**, *121*, 4088–4089.

44. Liu, G.-Y.; Xu, S.; Qian, Y. Nanofabrication of Self-Assembled Monolayers using Scanning Probe Lithography. *Acc. Chem. Res.* **2000**, *33*, 457–466.

45. Zhang, H.; Li, Z.; Mirkin, C. A. Dip-Pen Nanolithography-Based Methodology for Preparing Arrays of Nanostructures Functionalized with Oligonucleotides. *Adv. Mater.* **2002**, 14, 1472–1473.

46. Srinivasan, C.; Mullen, T. J.; Hohman, J. N.; Anderson, M. E.; Dameron, A. A.; Andrews, A. M.; Dickey, E. C.; Horn, M. W.; Weiss, P. S. Scanning Electron Microscopy of Nanoscale Chemical Patterns. *ACS Nano* **2007**, *1*, 191–201.

47. Mullen, T. J.; Srinivasan, C.; Hohman, J. N.; Gillmor, S. D.; Shuster, M. J.; Horn, M. W.; Andrews, A. M.; Weiss, P. S. Microcontact Insertion Printing. *Appl. Phys. Lett.* **2007**, *90*, 063114.

48. Shuster, M. J.; Vaish, A.; Szapacs, M. E.; Anderson, M. E.; Weiss, P. S.; Andrews, A. M. Biospecific Recognition of Tethered Small Molecules Diluted in Self-Assembled Monolayers. *Adv. Mater.* **2008**, *20*, 164–167.

49. Spokoyny, A. M.; Kim, D.; Sumrein, A.; Mirkin, C. A. Infinite Coordination Polymer Nano- and Microparticle Structures. *Chem. Soc. Rev.* **2009**, *38,* 1218–1227.

50. Liao, W.-S.; Cheunkar, S.; Cao, H.; Bednar, H.; Weiss, P. S.; Andrews, A. M. Subtractive Patterning via Chemical Lift-Off Lithography. *Science* **2012**, *337*, 1517–1521.

51. Zheng, Y. B.; Pathem, B. K.; Hohman, J. N.; Thomas, J. C.; Kim, M. H.; Weiss, P. S. Photoresponsive Molecules in Well-Defined Nanoscale Environments. *Adv. Mater.* **2013**, ***25***, 302–312.

52. Castner, D. G.; Hinds, K.; Grainger, D. W. X-ray Photoelectron Spectroscopy Sulfur 2p Study of Organic Thiol and Disulfide Binding Interactions with Gold Surfaces. *Langmuir* **1996**, *12*, 5083–5086.

53. Duwez, A.-S. Exploiting Electron Spectroscopies to Probe the Structure and Organization of Self-Assembled Monolayers: A Review. *J. Electron Spectrosc. Relat. Phenom.* **2004**, *134*, 97–138.

54. Penza, E.; Cortés, E.; Corthey, G.; Carro, P.; Vericat, C.; Fonticelli, M. H.; Benítez, G.; Rubert, A. A.; Salvarezza, R. C. The Chemistry of the Sulfur-Gold Interface: In Search of a Unified Model. *Acc. Chem. Res.* **2012**, *45*, 1183–1192.

55. Yu, M.; Bovet, N.; Satterley, C. J.; Bengió, S.; Lovelock, K. R. J.; Milligan, P. K.; Jones, R. G.; Woodruff, D. P.; Dhanak, V. True Nature of an Archetypal Self-Assembly System: Mobile Au-Thiolate Species on Au(111). *Phys. Rev. Lett.* **2006**, 97, 166102.

56. Maksymovych, P.; Sorescu, D. C.; Yates, J. T., Jr. Gold-Adatom-Mediated Bonding in Self-Assembled Short-Chain Alkanethiolate Species on the Au(111) Surface. *Phys. Rev. Lett.* **2006**, *97*, 146103.

57. Moore, A. M.; Mantooth, B. A.; Donhauser, Z. J.; Yao, Y.; Tour, J. M.; Weiss, P. S. Real-Time Measurements of Conductance Switching and Motion of Single Oligo(phenylene ethynylene) Molecules. *J. Am. Chem. Soc.* **2007**, *129*, 10352–10353.

58. Jadzinsky, P. D.; Calero, G.; Ackerson, C. J.; Bushnell, D. A.; Kornberg, R. D. Structure of a Thiol Monolayer-Protected Gold Nanoparticle at 1.1 Angstrom Resolution. *Science* **2007**, *19*, 430–433.

59. Maksymovych, P.; Voznyy, O.; Dougherty, D. B.; Sorescu, D. C.; Yates, J. T., Jr. Gold Adatom as a Key Structural Component in Self-Assembled Monolayers of Organosulfur Molecules on Au(111). *Prog. Surf. Sci.* **2010**, *85*, 206–240.

60. Vericat, C.; Vela, M. E.; Benitez, G.; Carro, P.; Salvarezza, R. C. Self-Assembled Monolayers of Thiols and Dithiols on Gold: New Challenges for a Well-Known System. *Chem. Soc. Rev.* **2010**, *39*, 1805–1834.

61. Poirier, G. E. Characterization of Organosulfur Molecular Monolayers on Au(111) using Scanning Tunneling Microscopy. *Chem. Rev.* **1997**, *97*, 1117–1127.

62. Donhauser, Z. J.; Price, Jr. D. W.; Tour, J. M.; Weiss, P. S. Control of Alkanethiolate Monolayer Structure using Vapor-Phase Annealing. *J. Am. Chem. Soc.* **2003**, *125*, 11462–11463.

63. Vaish, A; Shuster, M. J.; Cheunkar, S.; Weiss, P. S.; Andrews, A. M. Tuning Stamp Surface Energy for Soft Lithography of Polar Molecules to Fabricate Bioactive Small-Molecule Microarrays. *Small* **2011**, *7*, 1471–1479.

64. Fujita, K.; Nakamura, N..; Ohno, H.; Leigh, B. S.; Niki, K.; Gray, H. B.; Richards, J. H. Mimicking Protein-Protein Electron Transfer: Voltammetry of *Pseudomonas aeruginosa* Azurin and the Thermus Thermophilus Cu-A Domain at Omega-Derivatized Self-Assembled-Monolayer Gold Electrodes. *J. Am. Chem. Soc.* **2004**, 126, 13954–13961.

65. Thomas, J. C.; Schwartz, J. J.; Hohman, J. N.; Claridge, S. A.; Auluck, H. S.; Serino, A. C.; Spokoyny, A. M.; Tran, G.; Kelly, K. F.; Mirkin, C. A.; Gilles, J.; Osher, S. J.; Weiss, P. S. Defect-Tolerant Aligned Dipoles within Two-Dimensional Plastic Lattices. *ACS Nano* **2015**, 9, 4734–4742.

66. Plešek, J.; Heřmánek, S. Experimental Evaluation of Charge-Distribution on Particular Skeletal Atoms in Icosahedral Carboranes by Means of HS-Derivatives. *Collect. Czech. Chem. Commun.* **1979**, *44*, 24–33.

67. Plešek, J.; Heřmánek, S. Syntheses and Properties of Substituted Icosahedral Carborane Thiols. *Collect. Czech. Chem. Commun.* **1981**, *46*, 687–692.

68. Baše, T.; Bastl, Z.; Havránek, V.; Macháček, J.; Langecker, J.; Malina, V. Carboranedithiols: Building Blocks for Self-Assembled Monolayers on Copper Surfaces. *Langmuir* **2012**, *28*, 12518–12526.

69. Palatinus, L.; Chapuis, G. SUPERFLIP - A Computer Program for the Solution of Crystal Structures by Charge Flipping in Arbitrary Dimensions. *J. Appl. Crystallogr.* **2007**, *40*, 786–790.

70. Petříček, V.; Dušek, M.; Palatinus, L. Crystallographic Computing System JANA2006: General Features. *Z. Kristallogr.* **2014**, *229*, 345–352.

71. Farrugia, L. J. *ORTEP*-3 for Windows - A Version of *ORTEP*-III with a Graphical User Interface (GUI). *J. Appl. Crystallogr.* **1997**, *30*, 565–565.

72. Bumm, L. A.; Arnold, J. J.; Charles, L. F.; Dunbar, T. D.; Allara, D. L.; Weiss, P. S. Directed Self-Assembly to Create Molecular Terraces with Molecularly Sharp Boundaries in Organic Monolayers. *J. Am Chem. Soc.* **1999**, *121*, 8017–8021.

73. Shirley, D. A. High-Resolution X-ray Photoemission Spectrum of Valence Bands of Gold. *Phys. Rev. B* **1972**, *5*, 4709–4714.

74. Moulder, J. F.; Stickle, W. F.; Sobol, P. E.; Bomben, K. D.; *Handbook of X-ray Photoelectron Spectroscopy*, Perkin-Elmer Corp, Eden Prairie, MN, 1992, 60.

75. Scofield, J. H. Hartree-Slater Subshell Photoionization Cross-Sections at 1254 and 1487 eV. *J. Electron Spectrosc. Relat. Phenom.* **1976**, *8*, 129–137.

76. Briggs, D.; Grant, J. T. (ed.) Surface Analysis by Auger and X-Ray Photoelectron Spectroscopy, IM Publications and SurfaceSpectra Ltd., Cromwell Press, Trowbridge 2003, 326.

77. Valiev, M.; Bylaska, E. J.; Govind, N.; Kowalski, K.; Straatsma, T. P.; Van Dam, H. J. J.; Wang, D.; Nieplocha, J.; Apra, E.; Windus, T. L.; de Jong, W. A. NWChem: A Comprehensive and Scalable Open-Source Solution for Large Scale Molecular Simulations. *Comp. Phys. Commun.* **2010**, *181*, 1477–1489.

78. Allouche, A.-R. Gabedit – A Graphical User Interface for Computational Chemistry Softwares. *J. Comp. Chem.* **2011**, 32, 174–182.

79. *ABINIT*; Université Catholique de Louvain, Corning Incorporated, Université de Liège, Commissariat à l'Energie Atomique, Mitsubishi Chemical Corp., Ecole Polytechnique Palaiseau, and other contributors. http://www.abinit.org

80. Gonze, X.; Amadon, B.; Anglade, P.-M.; Beuken, J.-M.; Bottin, F.; Boulanger, P.; Bruneval, F.; Caliste, D.; Caracas, R.; Cote, M.; Deutsch, T.; Genovese, L.; Ghosez, P.; Giantomassi, M.; Goedecker, S.; Hamann, D. R.; Hermet, P.; Jollet, F.; Jomard, G.; Leroux, S.; Mancini, M.; Mazevet, S.; Oliveira, M. J. T.; Onida, G.; Pouillon, Y.; Rangel, T.; Rignanese, G.-M.; Sangalli, D.; Shaltaf, R.; Torrent, M.; Verstraete, M. J.; Zerah, G.; Zwanziger, J. W. ABINIT: First-Principles Approach to Material and Nanosystem Properties. Comput. Phys. Commun. **2009**, 180, 2582–2615.

81. PAW dataset for Abinit — ABINIT http://www.abinit.org/downloads/PAW2 (accessed Jan, 2014).

CHAPTER 4

Acid-Base Control of Valency within Carboranedithiol Self-Assembled Monolayers:

Molecules Do the Can-Can

4.1 Introduction

Self-assembled monolayer (SAM) formation is driven by a combination of substrate-molecule interactions, molecule-molecule interactions, and molecule-environment interactions.[1-3] The most commonly studied SAMs, *n*-alkanethiolates on Au{111} contain a single thiol group available for substrate binding and have a linear backbone, resulting in numerous defects that originate from *gauche* defects in the alkyl chains, different alkyl tilt orientations, translational and rotational lattice registry offsets, and defects due to the underlying substrate.[1,4-8] Monolayers formed from dialkyl disulfides result in identical assemblies as the Au surface cleaves the S-S bond.[9,10] In contrast, in carboranethiol SAMs, the molecules do not tilt nor can they conformationally relax; thus, there are fewer and simpler defects in comparison to SAMs composed of *n*-alkanethiols.[10-15] Interactions between carboranethiol molecules at the exposed interface have been demonstrated, where carboranethiol isomers with dipoles oriented parallel to the surface exhibit long-range attractive interactions due to dipole alignment.[16] This phenomenon was previously demonstrated by competitive adsorption, where carboranethiol isomers with larger in-plane dipole components outcompeted those with greater out-of-plane components.[17] Mixed assemblies of carboranethiol isomers can be used to tailor the effective metal work function of noble metal surfaces while not changing the wetting properties of the overlying polymers and thus not changing their morphologies.[13] These interactions have been observed at the single-molecule scale, where correlations between simultaneously acquired topographic and local barrier height (LBH) images enabled the observation of single-molecule orientations within SAM matrices and demonstrated defect-tolerant dipole alignment.[14] The surfactants 9,12-carboranedithiol (**9O12**) and 1,2-carboranedithiol (**1O2**) have been shown to be stable isomers, to functionalize noble metal surfaces, and to modify effective metal work functions due to oppositely oriented dipoles

originating from the carborane backbone.[18-23] Here, both isomers of carboranedithiol studied (**1O2** and **9O12**) promote formations with higher densities of sulfur-surface coverage and fewer defects due to rigid, nearly spherical backbones.

Typical SAM formation from thiols is governed by a simple acid-base reaction, where an acidic thiol group (SH) is deprotonated to a thiolate (S^-) on reactive surfaces.[4,24] As noted above, disulfides can form SAMs by having the surface reduce and cleave the disulfide bonds, again leading to adsorbed thiolates.[9,10] Adsorbed thiolates form stable bonds to Au surfaces (~50 kcal/mol), with higher binding energy than the typical Au-Au bond.[3,25,26] Adsorbed thiols have also been measured in low concentrations within SAMs, composed of *p*-carboranethiol, on Au.[15] This ease of formation coupled with tunable defect formations contributes towards thin films with controllable intermolecular interactions and modifiable surface-mediated effects that can be used to place and to direct single molecules and supramolecular assemblies into controlled environments.[2,3,10,11,27] Acid-base chemistry, at the interface, has shown broad importance in surface wettability, colloid and emulsion stability, biological signal transduction and membrane assembly, and in catalysis.[28-31] We sought to manipulate and to control the valency, the molecule-substrate bond density, and subsequent monolayer formation using different isomers of carboranedithiol on Au surfaces, which have the potential for one *or* two bonds to the substrate per molecule. Both **1O2** and **9O12** are stable in their respective dithiol and dianion states, where **1O2** is a stronger acid compared to **9O12**.[23] The acid-base properties inherent in homogenous monolayers composed of either **1O2** or **9O12** can be used as a means of control.

Kitagawa and coworkers have assembled adamantanetrithiol on Au{111} and have found trivalent interactions that resulted in small clusters of chiral structures on the surface.[32] In earlier,

unpublished work, we found that it is important to take into account both bond angles and substrate access in forming multivalent molecule-substrate interactions.[33] The lessons learned from those studies resulted in the inclusion of flexible linkers in attaching caltrops and other molecules to surfaces.[34-37]

Control of thin film properties of both exposed and buried interfaces has broad implications, *e.g.*, for molecular devices and lithographic patterning.[3,25,27,29,38,39] Isomers of *o*-carboranedithiols serve as ideal test candidates for tests of binding, valency, and surface bond density, where singly bound (monovalent) modes produce monolayers with lower thiolate-Au bond densities in comparison to doubly bound (divalent) modes. We demonstrate, with a variety of surface-sensitive techniques, that homogenous monolayers composed of either **1O2** or **9O12** show two distinct binding states, which are susceptible to manipulation by controlled pH conditions, in solution, prior to and during deposition *via* exposure to acidic or basic solution, and retain identical nearest-neighbor spacings throughout processing.

4.2 Results and Discussion

Scanning tunneling microscopy (STM) is able to probe the topographic landscape of surfaces with sub-Ångström precision.[7,40-43] We assembled and measured monolayers composed of either **1O2** or **9O12** on Au{111}/mica and recorded, in each homogenous SAM, two distinct binding states that differ in apparent height (Figure 4.1). Results indicated a bimodal distribution, with tunable coverages, of both singly bound (monovalent) and doubly bound (divalent) states. Self-assembled monolayers formed of **1O2** from a neutral solution show a 21 ± 8% coverage of the singly bound (higher intensity) binding mode and, correspondingly, a 79 ± 8% coverage of the dual bound (lower intensity) mode. These modes are differentiated as described below. Conversely,

monolayers composed of **9O12** show a strong monovalent preference (98 ± 1%) in comparison to the divalent mode (2 ± 1%). Images can be segmented by apparent height in topographic images by applying a grayscale threshold value that is used to compute binding concentrations in image binaries (Figure 4.2). Monovalent modes in **1O2** monolayers are higher in apparent height (1.5 ± 0.3 Å) in contrast to the divalent mode, and the monovalent modes in **9O12** SAMs are lower in apparent height (0.4 ± 0.2 Å) in comparison with the divalent mode. The aggregation of phase domains in SAMs composed of **1O2** strongly suggests intermolecular interactions between singly bound molecules, which possess a larger in-plane dipole component due to binding geometry. The reported dipole for **1O2** and **9O12** is 3.7 D and 5.5 D, respectively.[21] This component is nominally along the surface normal if both thiols are bound, however, the singly bound state contains a ~30˚ tilt that yields a parallel component (~1.8 D for **1O2** and ~2.8 D for **9O12**). This dipole component results in increased intermolecular interactions between neighboring singly bound adsorbates and, thus, permits phase separation. This is confirmed in samples of each monolayer and further enables binding assignments; SAMs composed of **1O2** demonstrate aggregation between higher intensity protrusions, and, in SAMs composed of **9O12**, higher intensity protrusions are localized and not phase aggregated. Both isomers form into hexagonally close-packed monolayers with nearest-neighbor spacings of 7.6 ± 0.5 Å. This formation is best explained by a $(\sqrt{7}\times\sqrt{7})R19.12^{\circ}$ superstructure that is predicted to be stable for thiols on Au{111} surfaces.[44] Both isomers form into monolayers with the same spacing and surface structures, however, each contain different concentrations of monovalent and divalent modes. Next, we tested each binding state by coupling STM with scanning tunneling spectroscopy (STS) to monitor both the topographic and local work function interfaces.

Multi-modal STM, which can simultaneously record the topographic landscape and the dipolar interface, can be used to extract molecular tilt information and molecular orientations in azimuthally symmetric systems.[7,14,45-48] Topographic and local barrier height maxima are computed within a defined radial vector (the size of one molecule) and correlations are computed *via* block-matching,[49,50] to match symmetric molecular apexes with dipolar extrema.[7,14] Here, local maxima (inverted minima) within SAMs composed of **9O12** can be locally attributed to carbons at the 1- and 2- positions within the cage. Conversely, local maxima within SAMs composed of **1O2** can be attributed to local dipolar offset within the boron cage. Correlated topographic maxima to LBH extrema values, shown in Rose plots (Figure 4.3), detail that greater protrusions in SAMs composed of **1O2** possess a larger offset (3.8 ± 1.0 Å) than lesser protrusions (2.2 ± 0.6 Å). In SAMs composed of **9O12**, greater protrusions show slightly smaller offsets (1.9 ± 0.3 Å) in comparison to lesser protrusions (2.6 ± 0.6 Å). Orientations in each homogenous monolayer (283 ± 39˚ in **1O2** SAMs, 150 ± 33˚ in **9O12** SAMs with respect to the fast-scan direction, shown as horizontal in displayed images) suggest charge-separation stabilization and relative dipolar alignment across each two-dimensional landscape. These are consistent with our binding model (monovalent and divalent modes) in each homogenous monolayer. Since each binding state maintains the same nearest-neighbor spacings, the percent sulfur bound to the Au substrate can be tuned up to a factor of two if binding can be manipulated. Motivated by the fact that the each isomer is stable in their dithiol and dithiolate states,[21] we modify the pH to deposit either the dithiol or the dithiolate. In chemical lift-off lithography,[25,26] the amount sulfur bound to Au may affect the amount and structure of lifted-off Au from the surface. Controlling the sulfur-surface density would enable tunable amounts of surface-bound Au available for patterning.

We imaged the resulting assemblies of each carboranedithiol in both basic (2:1 NaOH:carboranedithiol) and acidic conditions (1:1 HCl:carboranedithiol) with STM. Upon deposition under basic conditions, a majority switch is achieved that is attributed to deposition of the molecular dianion (dithiolate) state. Scanning tunneling micrographs depict a concentration change of each phase, and show predominance of the divalent mode in monolayers fabricated under basic conditions (Figure 4.4). Images are segmented by apparent height to compute percent coverage (Figure 4.5). The divalent mode is dominant in each homogenous monolayer (98 ± 2% for **1O2**, 99 ± 1% for **9O12**) under basic conditions. The relative apparent height difference between each **9O12** binding state is larger under basic deposition conditions (1.1 ± 0.2 Å) and smaller in the neutral deposition case (0.4 ± 0.2 Å). This distinct contrast change is recorded within monolayers composed of **9O12**, where divalent species appear more intense in apparent height under neutral conditions and lower in apparent height under basic conditions. On the contrary, relative apparent heights between binding states, in SAMs composed of **1O2**, remain consistent in both basic and neutral deposition conditions (1.5 ± 0.3 Å). This apparent height difference enables us to conclude that a dithiol species exists, in SAMs composed of **9O12**, under neutral conditions. Deposition under basic conditions enables the predominate formation of a dithiolate species. The existence of adsorbed carboranethiol has been seen in the literature previously,[15] which provides further justification for measured binding assignments that are fully detailed in Figure 4.6. We also performed deposition experiments in acidic conditions and measureed resulting monolayer formations.

Saturating carboranedithiol solutions with excess protons, prior to deposition, enables slightly higher concentrations of monovalent (thiol/thiolate) molecules, in comparison to their counterparts deposited from neutral solutions. Figure 4.7 depicts the topographic environment after acidic

deposition, where an increase in greater protrusions in SAMs composed of **1O2** show a somewhat higher concentration of monovalent (thiol/thiolate) molecules, however, SAMs composed of **9O12** show no change within a proton-rich environment and retain the original binding motif (98 ± 1%). Images that are segmented by apparent height highlight a larger percentage of monovalent molecules (31 ± 3%) in SAMs composed of **1O2** that is further shown in Figure 4.8. In summary, SAMs composed of divalent **1O2** or **9O12** (basic conditions) enable higher sulfur-surface coverage, where SAMs composed of monovalent **9O12** (neutral or acidic conditions) permit lower sulfur-surface coverage simply due to the controllable binding nature within structurally-equivalent isomeric monolayers.

In order to monitor the integrity of SAM formation in each modified environment, we used both X-ray photoelectron spectroscopy (XPS) and Fourier transform infrared (FTIR) spectroscopy to track ensemble characteristics. All measured XPS values, FTIR values, and modeled values are detailed in Table 4.1 and Table 4.2, where each monolayer shows the presence of sulfur and similar B-H vibrational characteristics under all conditions measured with STM. Characteristic orbital energy peaks of each atomic species within the monolayer can be measured with XPS. Here, we confirmed prior XPS measurements in both monolayers deposited under neutral conditions, where sulfur 2p orbital peaks show similar eV shifts compared to previously reported values.[18] To further verify monolayer integrity, we also measured each monolayer after pH manipulation (Figures 4.9 and 4.10). Values reported here for XPS not only show the retention of sulfur 2p energy values, but also confirm the lack of any Cl^- or Na^+ presence within each monolayer after pH variation. Using FTIR, we specifically tracked the B-H vibrational stretch, which is around 2600 cm^{-1} and characteristic for carboranes.[17,51] Measured SAMs composed of **1O2** show similar vibrational characteristics under all conditions, however, SAMs composed of **9O12** reveal a significant peak

decrease centered at 2593 cm^{-1} and a peak loss at 2559 cm^{-1} (Figures 4.11 and 4.12), which is attributed to a majority monovalent to divalent switch in SAMs composed of **9O12** under deposition in the presence of NaOH. Each experiment was repeated numerous times (n > 3), and enables a comparative means to track functional control at both the local and ensemble scales. Vibrational peaks are also modeled in the gas-phase using density functional theory. We attribute measured peaks in SAMs composed of **1O2** to a convolution of B-H stretches at all vertices of the icosahedral cage. In SAMs composed of **9O12**, a triplet is measured with FTIR that is also modeled (Table 4.2), where we can assign peaks centered around 2559 cm^{-1} to the 8 and 10 vertices, peaks at 2595 cm^{-1} to the 4 and 7 vertices, and peaks at 2633 cm^{-1} to a convolution of vibrational excitations at the 3, 6, 4, 5, 7, and 11 vertices. The peak decrease at 2595 cm^{-1} and loss at 2559 cm^{-1} are consistent with our assignments and peak quenching due to structural reconfiguration upon basic conditions, where the loss of stretches at the 4, 7, 8, and 10 vertices is due to surface dipole selection.

We are able to use both STM and STS that is further coupled with ensemble methodologies to confirm majority binding control within monolayers composed of bifunctional carboranedithiols. This deposition switch can be monitored by apparent height in STM, dipole offsets in simultaneous STM and LBH measurements, infrared spectroscopy, and X-ray photoelectron spectroscopy.

4.3 Conclusions and Prospects

Creating thin films with switchable substrate-molecule bond strengths while preserving lattice constants enables new explorations of this important interface and adds to the repertoire of controllable interactions at surface-molecule, molecule-molecule, and molecule-environment interfaces. By simply varying the head group, molecular backbone, or the tail group, an

extraordinary amount control is attainable.[1-3,6,8,11] Cage molecules, especially carboranethiols, exhibit unique properties and provide a unique test bed for exploring individual aspects of self-assembly, such as dipole interactions, molecular orientations, electron transfer, surface polarity, and now valency.[3,11,13-15,52] Here, bifunctional carboranedithiols assemble into well-ordered monolayers on Au surfaces with two distinct binding modes that are confirmed by STM, STS, FTIR, and XPS.

Control of valency is fundamental in the fields of chemistry, nanoscience, and biology. We detail the manipulation of either a monovalent or divalent modality within SAMs composed of different isomeric carboranedithiols, which retain their two-dimensional structural characteristics in controlled pH environments. With this level of control, we are able to dictate surface-atom-molecule stoichiometry with simple acid-base chemistry. This phenomenon is unique to multifunctional surfactants. We anticipate using these and related systems to explore the effects of valency on surface patterning[25,26,29,30] and dynamics.[53,54]

4.4 Materials and Methods

4.4.1 Monolayer Preparation

The chemicals **1O2** and **9O12** were synthesized and characterized in accordance with previously published methods.[18,21] Ethanol was used as received (Sigma-Aldrich, St. Louis, MO). The Au{111}/mica substrates (Agilent Technology, Tempe, AZ) were hydrogen-flame-annealed prior to SAM formation with 10 passes at a rate of 0.4 Hz. Both unmodified SAMs were prepared by immersion into 1 mM ethanolic solutions and held at room temperature for approximately 24 h. Short deposition times (1 h), in acidic or basic solutions, were employed to decrease the possibility

of molecular degradation. After deposition, each sample was rinsed thoroughly with neat ethanol and dried under a stream of ultrahigh purity argon for atleast three cycles.

Since carboranes have been reported to be reactive and to degrade upon exposure to concentrated base or acid,[55] we use dilute concentrations of acid and base to prevent side reactions. Hydrochloric acid (12 M) and NaOH pellets were used as received (Sigma-Aldrich, St. Louis, MO). Acidic solutions were prepared by mixing 0.5 mL of 2 mM HCl in EtOH and 0.5 mL of 2 mM **1O2** or **9O12** in EtOH in a gasketed v-vial. Basic solutions were prepared by mixing 0.5 mL of 4 mM NaOH in EtOH and 0.5 mL of 2 mM **1O2** or **9O12** in EtOH. Monolayers were prepared by immersing flame-annealed Au{111}/mica substrates into modified solutions for 1 h. Larger ratios of both acid (2:1) and base (4:1) were tested, however, no differences were found.

4.4.2 Imaging

All STM measurements were performed in either a custom-built Besoke-style scanning tunneling microscope held in ambient conditions or a custom-built Besoke-style scanning tunneling microscope held at cryogenic (4 K) and extreme high vacuum ($<10^{-12}$ torr) conditions.[56,57] Samples were held at a fixed bias (V_{sample} = -0.5 V) and both topographic and LBH modalities were measured in a constant current fashion (I_t = 15 pA). The tunneling-gap distance was oscillated above the microscope feedback loop (~3 kHz) with a sinusoidal amplitude (dz ~ 0.1 Å) and dI/dz was measured with a lock-in technique (Stanford Research Systems SR850 DSP, Sunnyvale, CA). The well-known lattice of atomic Au{111}, held at 4 K, was measured and used to calibrate all low temperature images, and the known lattice within SAMs of 1-dodecanethiolate were used to calibrate all images obtained at room temperature.

4.4.3 Image Analyses

All STM images were processed with automated routines developed in MATLAB (Mathworks, Natick, MA) to remove high-frequency noise and intensity spikes that may impair reliable interpretation.[7] Local maxima (minima) for both topography and local barrier height images were chosen as the highest (lowest) intensity pixel within a defined radial vector (the size of one molecule). Dipole offsets were computed using a block-matching approach,[14,49,50] where topographic image patches (size of one molecule) were correlated against larger local barrier height image patches (size of the nearest-neighbor spacing) to obtain a set of points (*p* and *q*) that were referenced and plotted. Correlated values (shown in Figure 4.3) were compared against connecting all points within a defined pixel radius, as a function of size, where correlation yielded the least artifacts (Figures 4.13 and 4.14). Grayscale threshold values were chosen based on apparent height differences to produce binary image highlights, which were further used to obtain percent coverages.

4.4.4 Infrared Spectroscopy

All infrared spectra were collected with a Nicolet 6700 FTIR spectrometer (Thermo Electron Corp., Waltam, MA) that was equipped with a mercury-cadmium-telluride detector, held at liquid nitrogen temperatures, and a Seagull variable-angle reflection accessory (Harrick Scientific, Inc., Ossinging, NY). Water and carbon dioxide were removed from the spectrometer by an FTIR purge gas generator (Parker-Balston, Cleveland, OH). A grazing incidence reflection angle (82˚ with respect to the surface normal) with p-polarized light, a mirror speed of 1.27 cm/s, and a resolution of 2 cm^{-1}. Spectra were averaged over 5120 scans and normalized against spectra of perdeuterated *n*-dodecanethiolate monolayers on Au{111}.

4.4.5 X-ray Photoelectron Spectroscopy

All XPS spectra were collected with an AXIS Ultra DLD instrument (Kratos Analytical Inc., Chestnut Ridge, NY). A monochromatic Al Kα X-ray source (20 mA, 15 kV) with a 200 μm circular spot size that was held at ultrahigh vacuum (10^{-9} torr) were used for all measurements. Spectra were acquired at a pass energy of 160 eV for survey spectra and 20 eV for high resolution spectra of S 2p, C 1s, B 1s, and Au 4f regions that used a 200 ms dwell time. Different numbers of scans were carried out depending on the amount required for high resolution spectra, which ranged from 20 scans for C 1s to 75 scans for S 2p. Binding energies were calibrated to the Au 4f peak at 83.98 eV.[58] Spectra were fit using CasaXPS software with Gaussian-Lorentzian lineshapes after Shirley background subtraction. Sulfur regions were fitted by a doublet structure with a 1.18 eV spin-orbit splitting and a defined intensity ratio ($2p_{3/2}$:$2p_{1/2,}$ 2:1).

4.4.6 Computational Modeling

Quantum chemistry calculations were performed by the NWChem[59] package. The geometries were optimized and vibrational frequencies[60] calculated by the means of the density functional theory with the hybrid exchange–correlation functional PBE0.[61-64] Jensen's double–zeta basis PC-1[65] was used. The translations and rotations were projected out of the nuclear hessian using the standard Eckart algorithm.[66] The calculated frequencies and normal vibrational modes were examined with the help of the visualization program Gabedit.[67] The vibrational spectra were simulated with Gabedit by simple application of lorentzian line shape of uniform arbitrary half width 5 cm^{-1}.

The plane-wave density functional theory (PW-DFT) code, Quantum Espresso[68] (*QEspresso*), was employed for geometric optimization of the surface mounted 1,2-carboranedithiols (Figure 4.15), protonated and unprotonated. Both the singly bound (-1.51 eV) and the dual bound (-2.83 eV) where shown to be favorable binding modalities. Spin-unrestricted calculations, utilizing the set of scalar-relativistic ultra-soft pseudo potentials using the PBE functional,[69,70] were carried out. To examine certain findings in greater detail, some simulations were reproduced that included London dispersion, using the default parameters in *QEspresso*. The latter case is of interest as it was shown by others[71] to lead to good agreement between theory and experiment for other gold-supported molecules.

The gold slab was modeled as a 4×4×6 unit cell of pristine gold. Having experimentally validated the cleanliness of the gold surfaces, simulations of defected surfaces were not included. A small unit-cell of bulk gold was optimized and then extended to the desired cell size, the bottom three layers of the cell were held fixed and the system optimized yielding the pristine surface used for further simulations. A vacuum gap of about 12 Å between the highest atom of the supported carborane molecule and the repeated image of the slab's bottom layer ensured the results would be insensitive to any spurious effects due to the enforcement of periodic boundary conditions. Large kinetic energy cut-offs of 435 eV and 4,352 eV were applied to the wavefunctions and charge density, respectively. A 4×4×1 Monkhorst-Pack k-point grid allowed for the numerical solution of Hamiltonian and overlap matrix elements; shifts on or off the Γ-point along k_z, resulted in negligible changes to the energy (below the level of 0.002 eV).

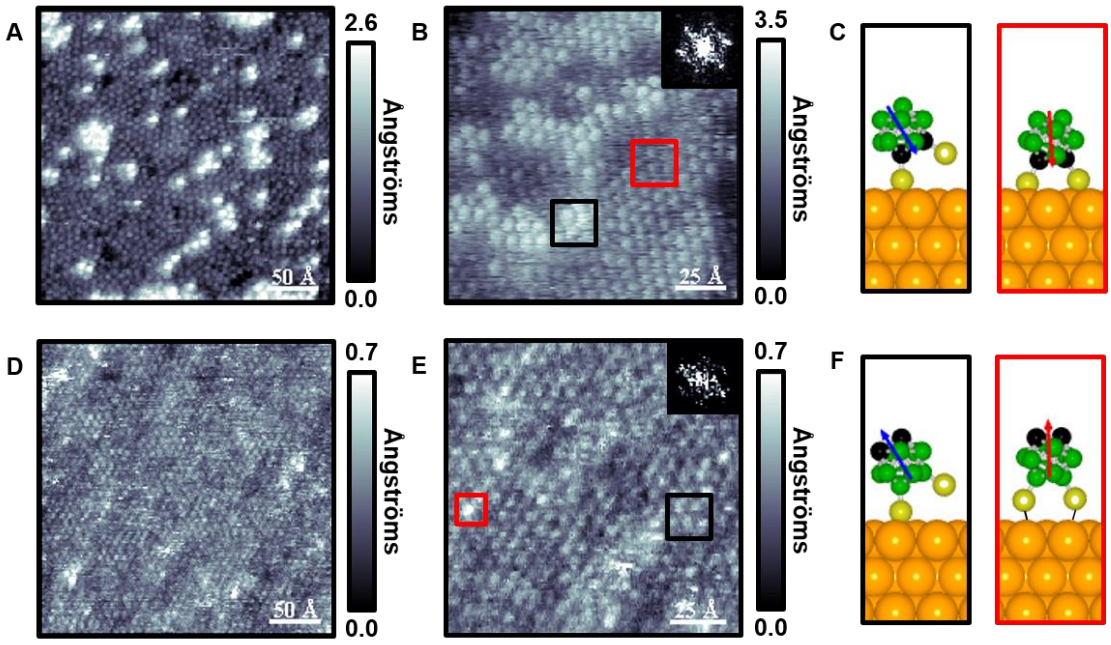

Figure 4.1 (A,B) Scanning tunneling topographs ($I_{tunneling}$ = 100 pA, V_{sample} = -0.1 V) of 1,2-$(HS)_2$-1,2-$C_2B_{10}H_{10}$ (**1O2**) on Au{111}/mica at two different image sizes. Inset depicts a fast Fourier transform (FFT) that corroborates a hexagonally close-packed arrangement with a nearest-neighbor spacing of 7.6 ± 0.5 Å, and two distinct binding states are highlighted in red and black. (C) Binding modes are shown in a schematic, where **1O2** assembles into both monovalent (black) and divalent (red) modes. (D,E) Scanning tunneling topographs ($I_{tunneling}$ = 100 pA, V_{sample} = -0.1 V) of 9,12-$(HS)_2$-1,2-$C_2B_{10}H_{10}$ (**9O12**) on Au{111}/mica at different resolutions. Inset depicts a FFT showing a hexagonally close-packed arrangement with the same spacing as **1O2**. The two binding states are highlighted in red and black. (F) Binding modes for **9O12** are depicted schematically, where both monovalent (black) and divalent (red) modes are present.

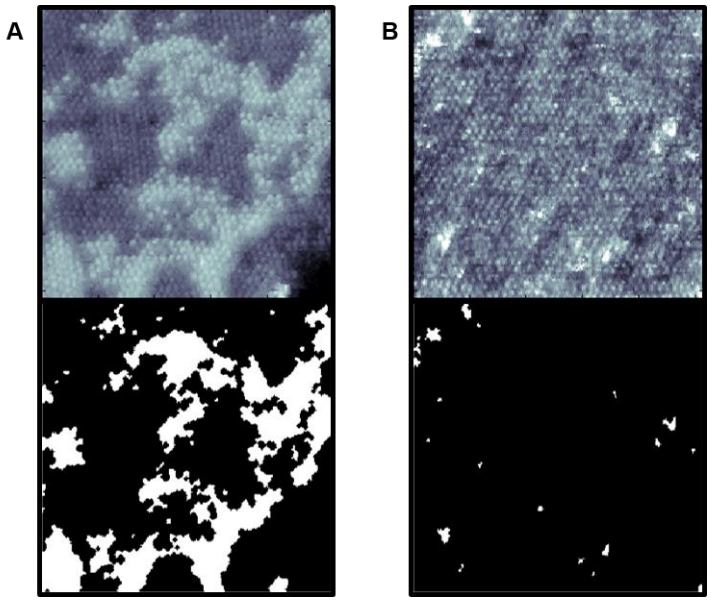

Figure 4.2 (A) Scanning tunneling topographs ($I_{tunneling}$ = 100 pA, V_{sample} = -0.1 V) of 1,2-$(HS)_2$-1,2-$C_2B_{10}H_{10}$ (**1O2**) on Au{111}/mica, that was segmented by apparent height to highlight areas of different binding (GrayScaleThreshold = 0.75). (B) Scanning tunneling topograph ($I_{tunneling}$ = 100 pA, V_{sample} = -0.1 V) of 9,12-$(HS)_2$-1,2-$C_2B_{10}H_{10}$ (**9O12**) on Au{111}/mica that was segmented by apparent height to highlight binding mode concentrations (GrayScaleThreshold = 0.99).

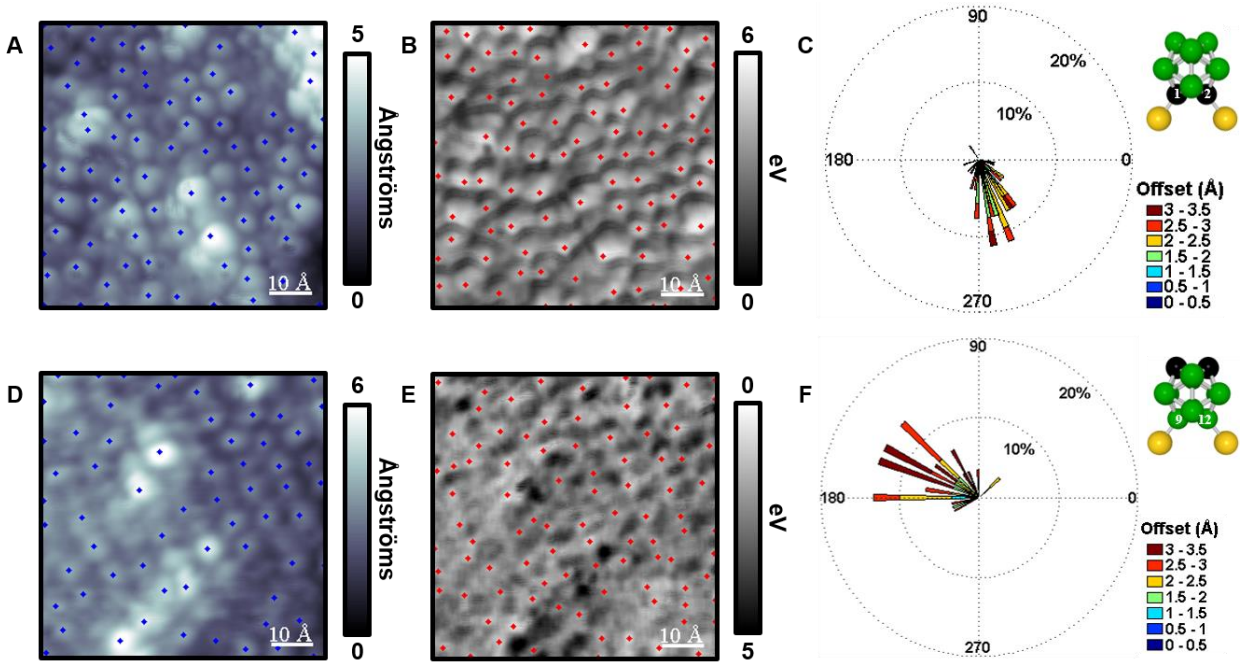

Figure 4.3 (A) Scanning tunneling topograph, in ultrastable conditions, ($I_{tunneling}$ = 15 pA, V_{sample} = -0.5 V) of 1,2-$(HS)_2$-1,2-$C_2B_{10}H_{10}$ (**1O2**) on Au{111} with local maxima (blue) depicted. (B) Simultaneously acquired local barrier height (LBH) image, with correlated topographic maxima (blue) to LBH maxima (red). (C) Rose plot (depicting dipole offsets in B) that is binned by both magnitude (0.5 Å bins) and orientation (4˚ bins), and a ball-and-stick model of **1O2** showing thiol positions. (D) Scanning tunneling topograph ($I_{tunneling}$ = 15 pA, V_{sample} = -0.5 V) of 9,12-$(HS)_2$-1,2-$C_2B_{10}H_{10}$ (**9O12**) on Au{111} with local maxima (blue) depicted. (E) Simultaneously acquired LBH map, with correlated topographic maxima (blue) to LBH maxima (red). (F) Rose plot (depicting dipole offsets in E) that is binned by both magnitude (0.5 Å bins) and orientation (4˚ bins), and a ball-and-stick model of **9O12**.

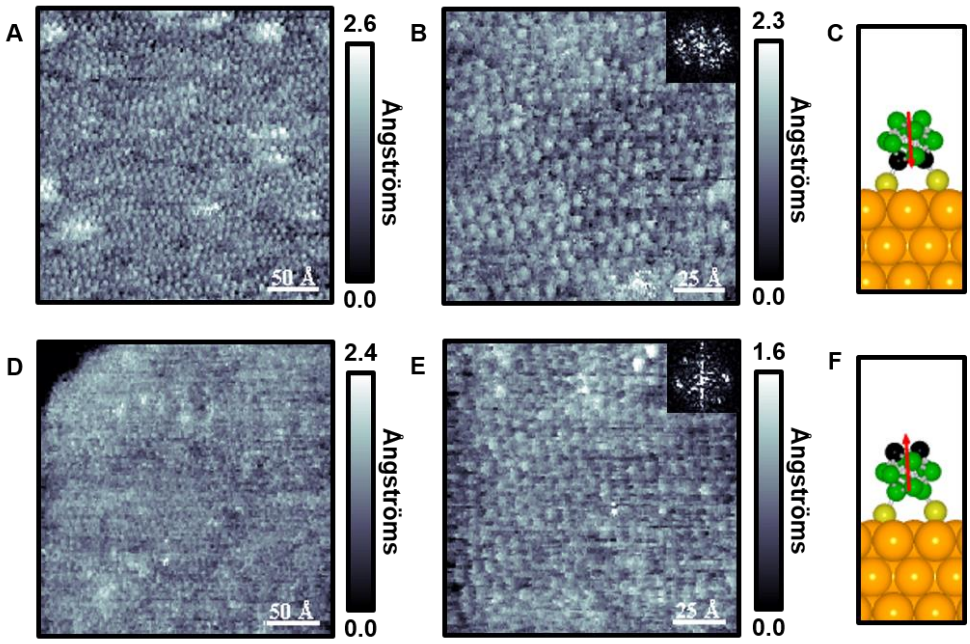

Figure 4.4 (A,B) Scanning tunneling topographs ($I_{tunneling}$ = 100 pA, V_{sample} = -0.1 V) of 1,2-$(HS)_2$-1,2-$C_2B_{10}H_{10}$ (**1O2**) on Au{111}/mica at two different image sizes under basic deposition conditions (2:1, NaOH:**1O2**). Inset depicts a fast Fourier transform (FFT) that shows a hexagonally close-packed arrangement with the same nearest-neighbor spacing as in Figure 4.1. (C) A majority switch to the divalent mode is achieved and depicted schematically. (D,E) Scanning tunneling topographs ($I_{tunneling}$ = 100 pA, V_{sample} = -0.1 V) of 9,12-$(HS)_2$-1,2-$C_2B_{10}H_{10}$ (**9O12**) on Au{111}/mica at different resolutions after basic deposition (2:1, NaOH:**9O12**). Inset depicts a FFT showing the same arrangement and spacing as **1O2**. (F) A divalent global switch is accomplished and shown schematically.

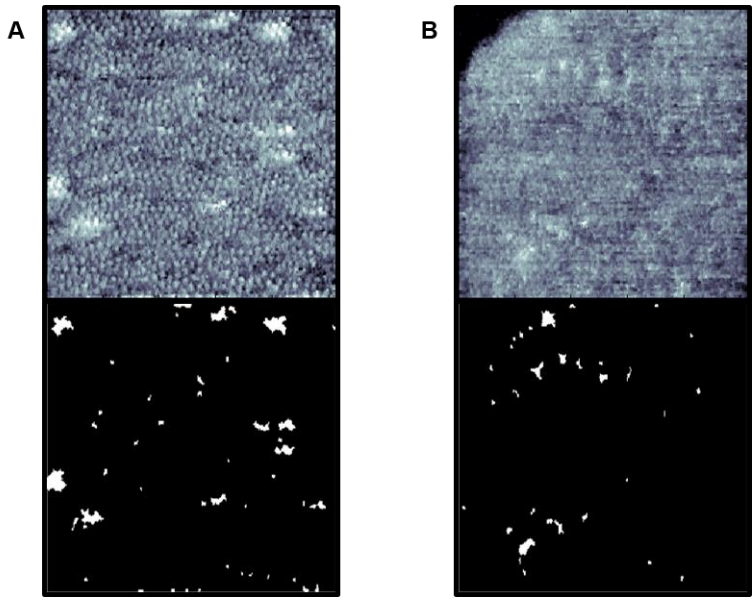

Figure 4.5 (A) Scanning tunneling topograph ($I_{tunneling}$ = 100 pA, V_{sample} = -0.1 V) of 1,2-$(HS)_2$-1,2-$C_2B_{10}H_{10}$ (**1O2**) on Au{111}/mica after deposition in basic conditions that is segmented by apparent height to highlight binding mode density (GrayScaleThreshold = 0.975). (B) Scanning tunneling topograph ($I_{tunneling}$ = 100 pA, V_{sample} = -0.1 V) of 9,12-$(HS)_2$-1,2-$C_2B_{10}H_{10}$ (**9O12**) on Au{111}/mica deposited under basic conditions that is segmented by apparent height to highlight molecular binding mode concentrations (GrayScaleThreshold = 0.982).

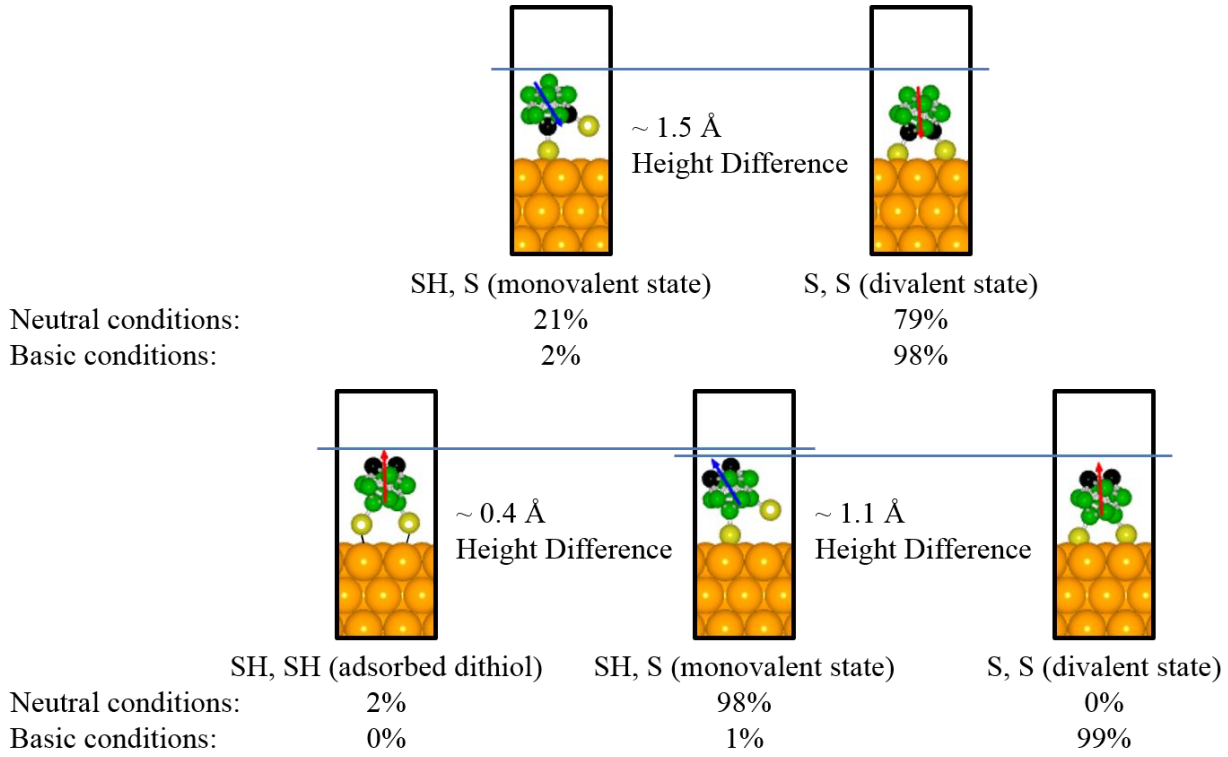

Figure 4.6. Binding assignments that are measured by scanning tunneling microscopy and scanning tunneling spectroscopy (STS). Self-assembled monolayers composed of 1,2-$(HS)_2$-1,2-$C_2B_{10}H_{10}$ form into a thiol/thiolate state and a dithiolate state that differ in apparent height. Monolayers composed of 9,12-$(HS)_2$-1,2-$C_2B_{10}H_{10}$ form into an adsorbed dithiol state and a thiol/thiolate state, under neutral conditions, that differ in measured apparent height. These binding modes also match STS measurements shown in Figure 4.3, where bivalent modes exhibit lower offsets in comparison to monovalent modes. Upon deposition under basic conditions, a majority dithiolate switch is recorded for both isomers, shown by topographic imaging.

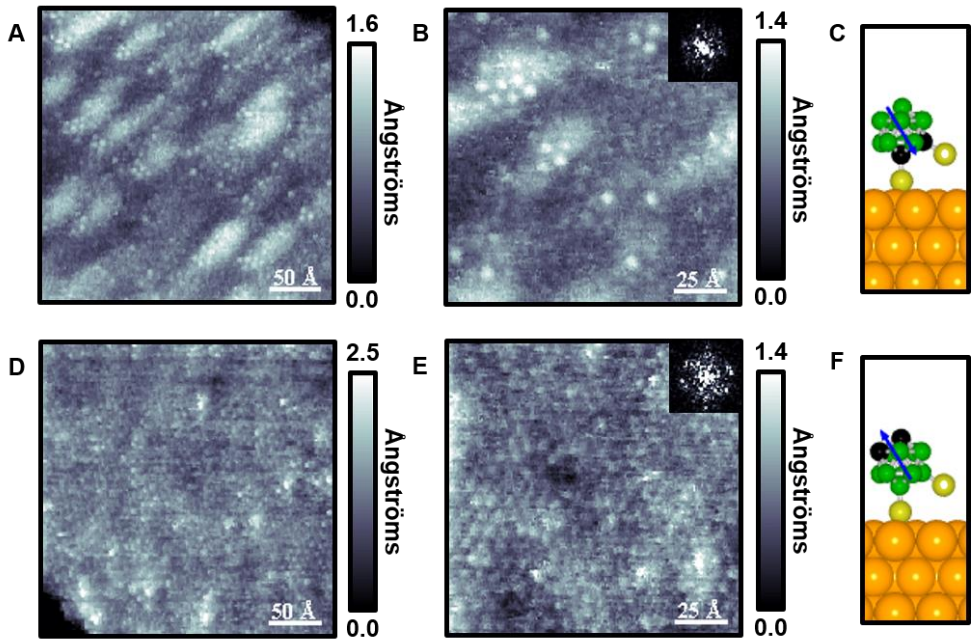

Figure 4.7 (A,B) Scanning tunneling topographs ($I_{tunneling}$ = 100 pA, V_{sample} = -0.1 V) of 1,2-$(HS)_2$-1,2-$C_2B_{10}H_{10}$ (**1O2**) on Au{111}/mica at two different image sizes under acidic deposition conditions (1:1, HCl:**1O2**). Inset depicts a fast Fourier transform (FFT) that shows a hexagonally close-packed arrangement with the same nearest-neighbor spacings measured in both basic and neutral conditions. (C) A minority push to the monovalent mode is achieved and depicted schematically. (D,E) Scanning tunneling topographs ($I_{tunneling}$ = 100 pA, V_{sample} = -0.1 V) of 9,12-$(HS)_2$-1,2-$C_2B_{10}H_{10}$ (**9O12**) on Au{111}/mica at different resolutions after acidic deposition (1:1, HCl:**9O12**). Inset depicts a FFT showing the same arrangement and spacing as in neutral conditions. (F) As monolayers composed of **9O12** are already predominately monovalent, no change is measured, in comparison to neutral deposition conditions, for this system that is depicted schematically.

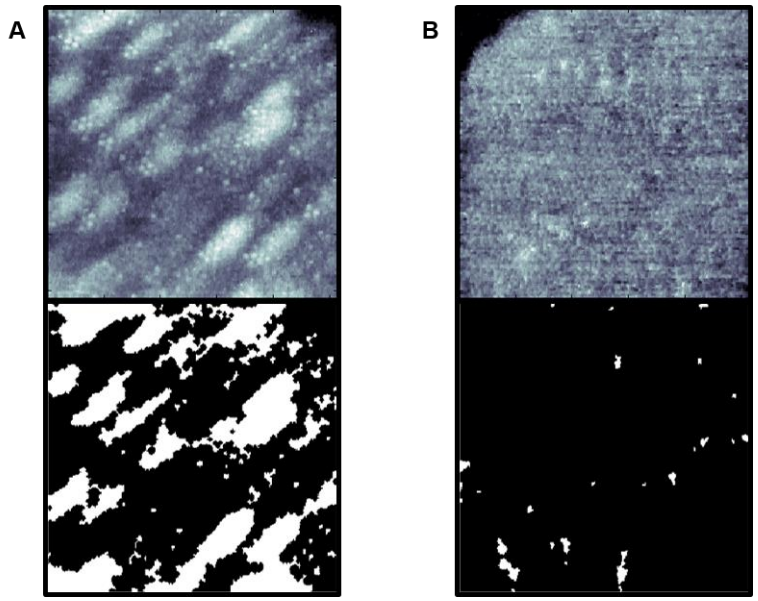

Figure 4.8 (A) Scanning tunneling topograph ($I_{tunneling}$ = 100 pA, V_{sample} = -0.1 V) of 1,2-$(HS)_2$-1,2-$C_2B_{10}H_{10}$ (**1O2**) on Au{111}/mica after deposition under acidic conditions that is segmented by apparent height to highlight binding mode density (GrayScaleThreshold = 0.69). (B) Scanning tunneling topograph ($I_{tunneling}$ = 100 pA, V_{sample} = -0.1 V) of 9,12-$(HS)_2$-1,2-$C_2B_{10}H_{10}$ (**9O12**) on Au{111}/mica deposited under acidic conditions that is segmented by apparent height to highlight binding mode concentrations (GrayScaleThreshold = 0.985).

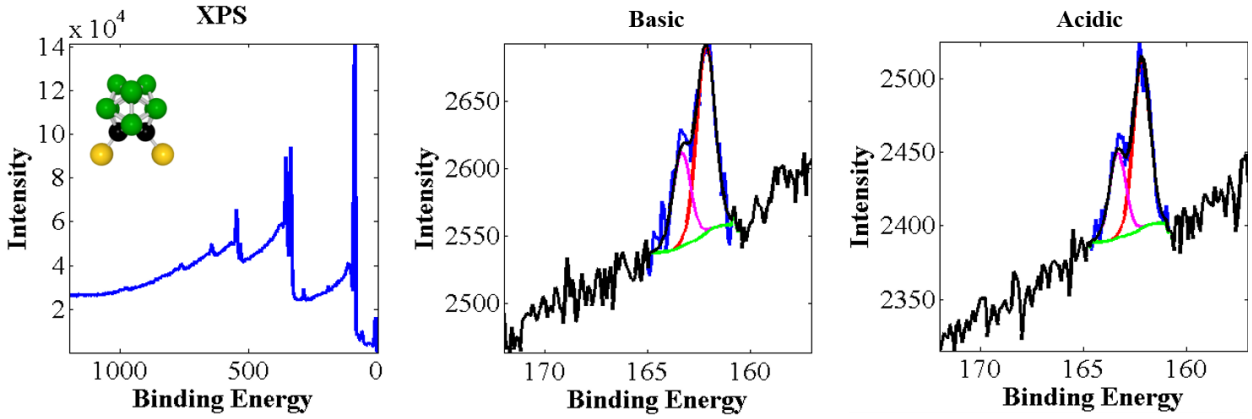

Figure 4.9 X-ray photoelectron spectra of 1,2-$(HS)_2$-1,2-$C_2B_{10}H_{10}$ on Au on Si{100} that shows the full sweep under neutral conditions, and high resolution scans of the S 2p area. Binding energies are consistent and confirm monolayer integrity under all conditions reported.

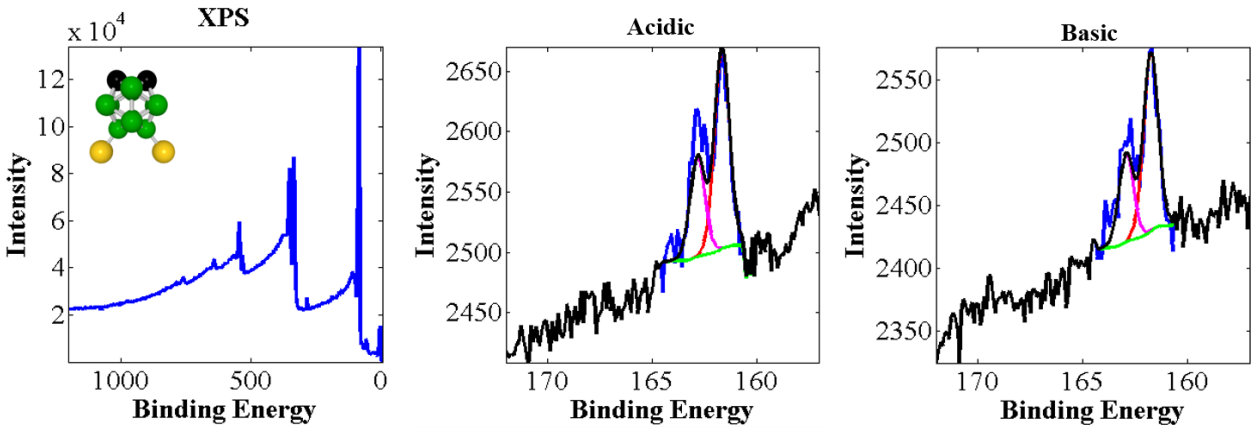

Figure 4.10 X-ray photoelectron spectra of 9,12-$(HS)_2$-1,2-$C_2B_{10}H_{10}$ on Au on Si{100} that shows the full sweep under neutral conditions and high resolution scans of the S 2p area under both basic and acidic conditions. Binding energies under all conditions remain consistent and confirm monolayer integrity.

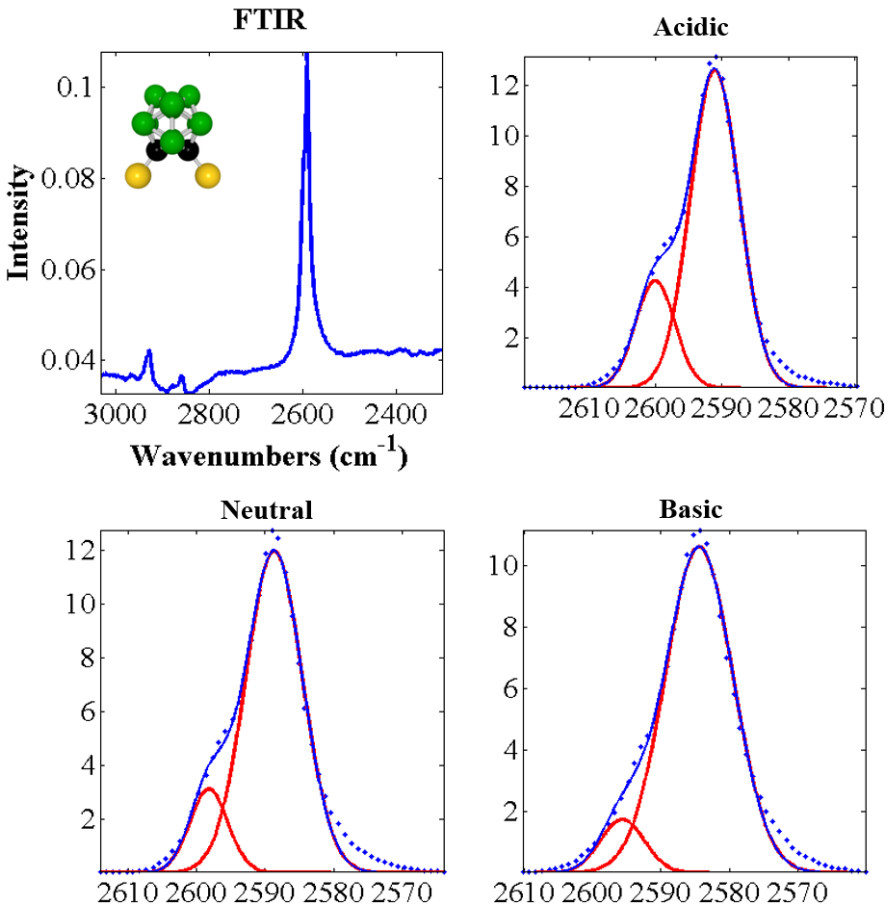

Figure 4.11 Infrared spectroscopy that highlights the B-H region for 1,2-$(HS)_2$-1,2-$C_2B_{10}H_{10}$ on Au on Si{100} under all conditions reported. Here, B-H intensity remains nominally consistent throughout. Peaks and assignments are detailed in Table 4.2.

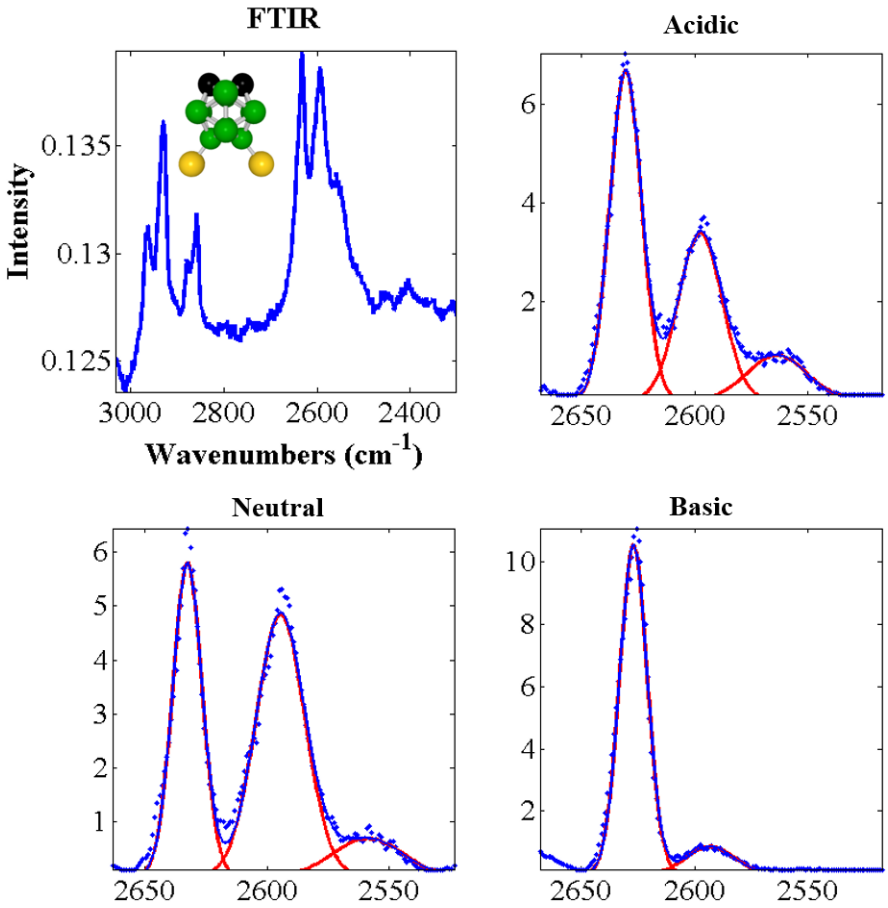

Figure 4.12 Infrared spectroscopy that highlights the B-H region for 9,12-$(HS)_2$-1,2-$C_2B_{10}H_{10}$ (**9O12**)on Au on Si{100} under conditions reported. Peaks centered at 2600 cm^{-1} is reduced under acidic conditions, which is likely due to small-scale degradation. This peak, however, is significantly decreased under basic conditions, which we attribute to the bivalent nature of SAMs formed under Peaks centered at 2550 cm^{-1} show a slight increase under acidic conditions, and a complete disappearance under basic conditions. Peaks and assignments are further detailed in Table 4.2.

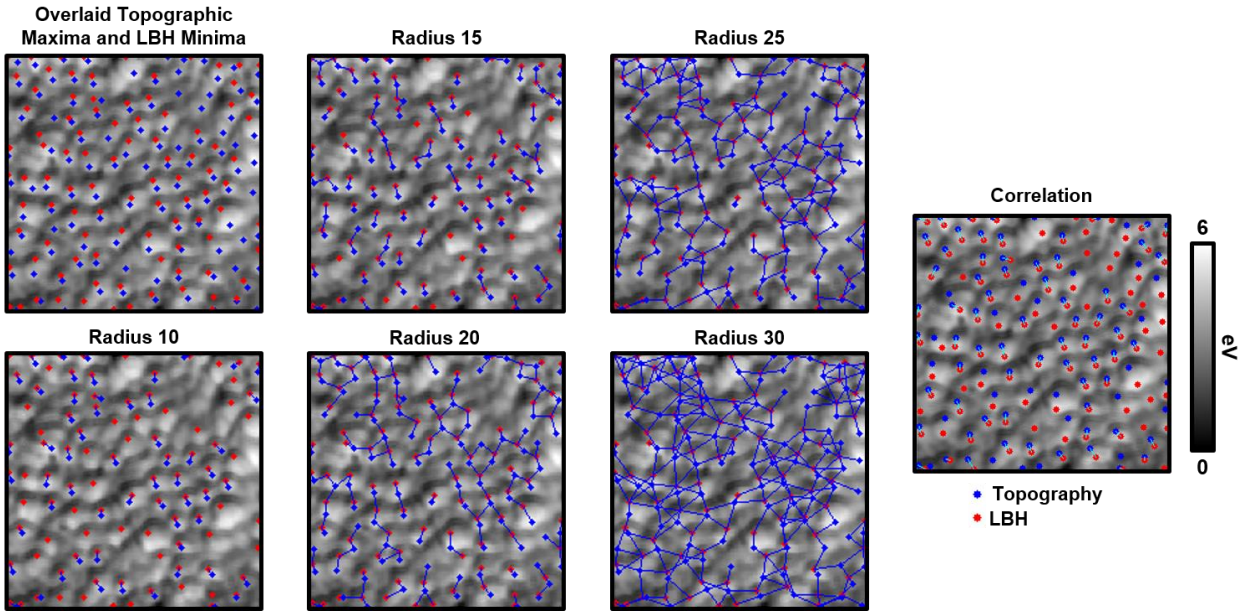

Figure 4.13 Scanning tunneling local barrier images ($I_{tunneling}$ = 15 pA, V_{sample} = -0.5 V) of 1,2-$(HS)_2$-1,2-$C_2B_{10}H_{10}$ (**1O2**) on Au{111}/mica with overlaid topographic and local barrier height maxima. We connect all topographic maxima to all local barrier height maxima within a defined radial vector and compare with results obtained through block-matching.

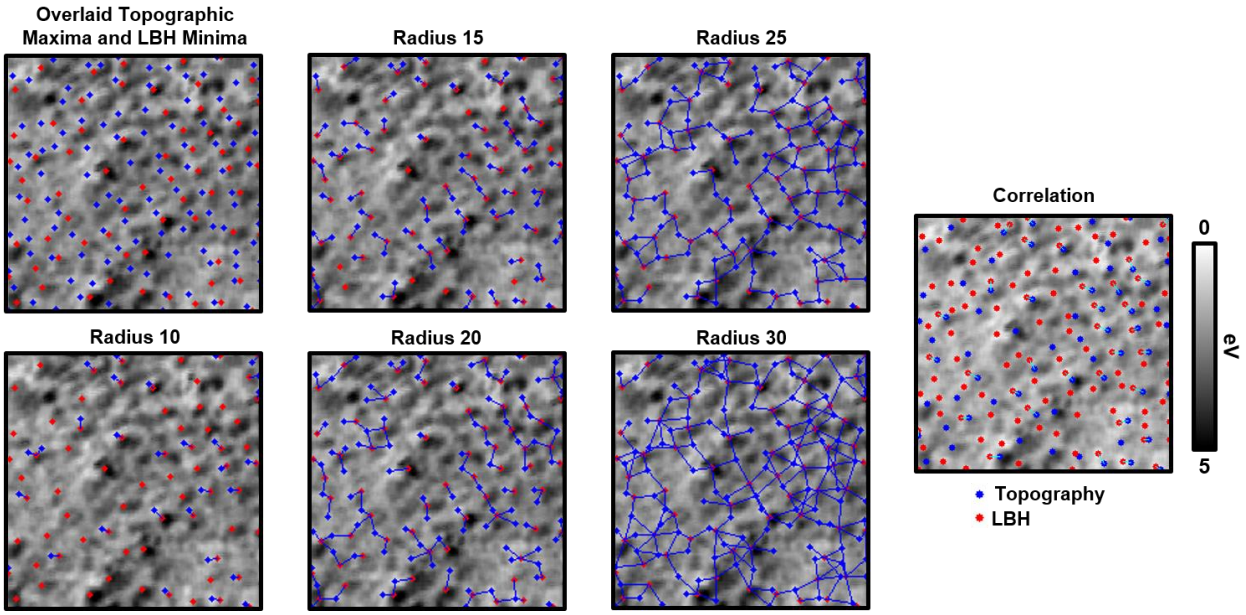

Figure 4.14 Scanning tunneling local barrier images ($I_{tunneling}$ = 15 pA, V_{sample} = -0.5 V) of 9,12-$(HS)_2$-1,2-$C_2B_{10}H_{10}$ (**9O12**) on Au{111}/mica with overlaid topographic and local barrier height maxima (inverted to highlight dipole minima). We connect all topographic maxima to all local barrier height maxima within a defined radial vector and compare with correlated results.

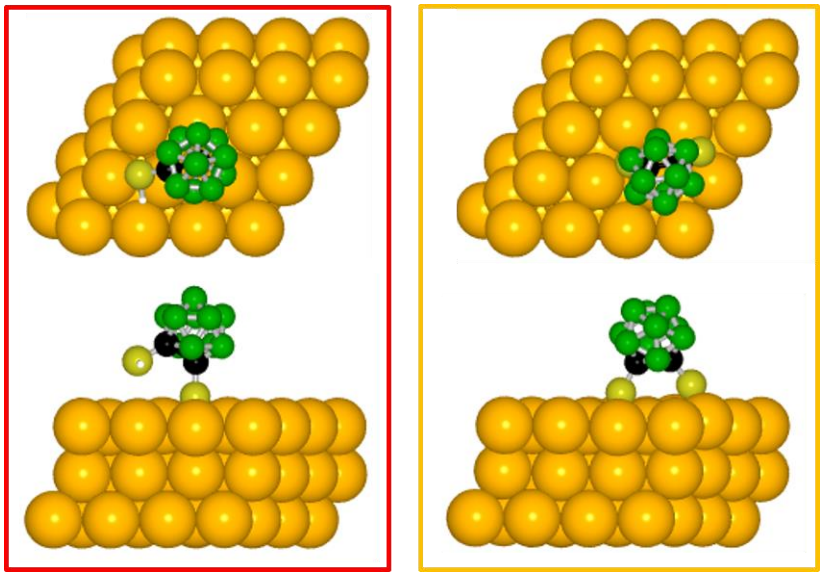

Figure 4.15 Optimized binding geometries for 1,2-carboranedithiolate on Au{111}. Binding energies were calculated ($E_{binding} = E_{system} - E_{molecule} - E_{substrate}$) for both the singly bound (red, -1.51 eV) and the dual bound (yellow, -2.83 eV).

	1O2 n	**9O12 n**	**1O2 b**	**9O12 b**	**1O2 a**	**9O12 a**
Au 4f	84.0 eV	84.0 eV	84.0 eV	84.0 eV	84.0 eV	84.0 eV
B 1s	189.0 eV	189.0 eV	189.0 eV	189.0 eV	189.0 eV	189.0 eV
S 2p	162.2 eV	161.7 eV	162.2 eV	161.7 eV	162.2 eV	161.7 eV
C 1s	285.0 eV	285.0 eV	285.0 eV	285.0 eV	285.0 eV	285.0 eV
Na 1s	-	-	-	-	-	-
Cl 2p	-	-	-	-	-	-
B-H (FTIR)	2589 cm^{-1} 2598 cm^{-1}	2559 cm^{-1} 2595 cm^{-1} 2633 cm^{-1}	2584 cm^{-1} 2596 cm^{-1}	2593 cm^{-1} 2627 cm^{-1}	2600 cm^{-1} 2591 cm^{-1}	2564 cm^{-1} 2598 cm^{-1} 2630 cm^{-1}

Table 4.1 A summary of all X-ray photoelectron spectroscopy energy shifts and Fourier transform spectroscopy frequency values in the B-H region (row). Columns are titled with 1,2-$(HS)_2$-1,2-$C_2B_{10}H_{10}$ (**1O2**) or 9,12-$(HS)_2$-1,2-$C_2B_{10}H_{10}$ (**9O12**) and labeled with neutral (n), basic (b), or acidic (a) deposition conditions.

	1O2	9O12
B-H Measured by FTIR	2589 cm^{-1} 2598 cm^{-1}	2559 cm^{-1} 2595 cm^{-1} 2633 cm^{-1}
Modeled B-H Frequencies (Vertices)	2600 cm^{-1} (7,5) 2597 cm^{-1} (4,11) 2594 cm^{-1} (5,7) 2592 cm^{-1} and 2591 cm^{-1} (3,4,5,6,7,11) 2579 cm^{-1} (8,9,10,12) 2572 cm^{-1} (8,10) 2571 cm^{-1} (9,12)	2633 cm^{-1} and 2631 cm^{-1} (3,6) 2619 cm^{-1} (4,5,7,11) 2610 cm^{-1} (4) 2608 cm^{-1} (7) 2589 cm^{-1} (8) 2587 cm^{-1} (10)

Table 4.2 A compilation of all B-H stretches measured with infrared spectroscopy in neutral conditions along with their simulated values and cage vertex assignments.

4.5 References

1. Love, J. C.; Estroff, L. A.; Kriebel, J. K.; Nuzzo, R. G.; Whitesides, G. M. Self-Assembled Monolayers of Thiolates on Metals as a Form of Nanotechnology. *Chem. Rev.* **2005,** *105*, 1103–1170.

2. Weiss, P. S. Functional Molecules and Assemblies in Controlled Environments: Formation and Measurements. *Acc. Chem. Res.* **2008,** *41*, 1772–1781.

3. Claridge, S. A.; Liao, W. S.; Thomas, J. C.; Zhao, Y.; Cao, H. H.; Cheunkar, S.; Serino, A. C.; Andrews, A. M.; Weiss, P. S. From the Bottom Up: Dimensional Control and Characterization in Molecular Monolayers. *Chem. Soc. Rev.* **2013,** *42*, 2725–2745.

4. Ulman, A. Formation and Structure of Self-Assembled Monolayers. *Chem. Rev.* **1996,** *96*, 1533–1554.

5. Poirier, G. E. Characterization of Organosulfur Molecular Monolayers on Au(111) using Scanning Tunneling Microscopy. *Chem. Rev.* **1997,** *97*, 1117–1128.

6. Smith, R. K.; Lewis, P. A.; Weiss, P. S. Patterning Self-Assembled Monolayers. *Prog. Surf. Sci.* **2004,** *75*, 1–68.

7. Han, P.; Kurland, A. R.; Giordano, A. N.; Nanayakkara, S. U.; Blake, M. M.; Pochas, C. M.; Weiss, P. S. Heads and Tails: Simultaneous Exposed and Buried Interface Imaging of Monolayers. *ACS Nano* **2009,** *3*, 3115–3121.

8. Hohman, J. N.; Thomas, J. C.; Zhao, Y.; Auluck, H.; Kim, M.; Vijselaar, W.; Kommeren, S.; Terfort, A.; Weiss, P. S. Exchange Reactions between Alkanethiolates and Alkaneselenols on Au{111}. *J. Am. Chem. Soc.* **2014,** *136*, 8110–8121.

9. Nuzzo, R. G.; Allara, D. L. Adsorption of Bifunctional Organic Disulfides on Gold Surfaces. *J. Am. Chem. Soc.* **1983**, *105*, 4481–4483.

10. Kim, M.; Hohman, J. N.; Cao, Y.; Houk, K. N.; Ma, H.; Jen, A. K.; Weiss, P. S. Creating Favorable Geometries for Directing Organic Photoreactions in Alkanethiolate Monolayers. *Science* **2011,** *331*, 1312–1315.

11. Hohman, J. N.; Claridge, S. A.; Kim, M.; Weiss, P. S. Cage Molecules for Self-Assembly. *Mater. Sci. Eng. R* **2010,** *70*, 188–208.

12. Spokoyny, A. M.; Machan, C. W.; Clingerman, D. J.; Rosen, M. S.; Wiester, M. J.; Kennedy, R. D.; Stern, C. L.; Sarjeant, A. A.; Mirkin, C. A. A Coordination Chemistry Dichotomy for Icosahedral Carborane-Based Ligands. *Nat. Chem.* **2011,** *3*, 590–596.

13. Kim, J.; Rim, Y. S.; Liu, Y.; Serino, A. C.; Thomas, J. C.; Chen, H.; Yang, Y.; Weiss, P. S. Interface Control in Organic Electronics Using Mixed Monolayers of Carboranethiol Isomers. *Nano Lett.* **2014,** *14*, 2946–2951.

14. Thomas, J. C.; Schwartz, J. J.; Hohman, J. N.; Claridge, S. A.; Auluck, H. S.; Serino, A. C.; Spokoyny, A. M.; Tran, G.; Kelly, K. F.; Mirkin, C. A.; Gilles, J.; Osher, S. J.; Weiss, P. S. Defect-Tolerant Aligned Dipoles within Two-Dimensional Plastic Lattices. *ACS Nano* **2015,** *9*, 4734–4742.

15. Thomas, J. C.; Boldog, I.; Auluck, H. S.; Bereciartua, P.; Dušek, M.; Macháček, J.; Bastl, Z.; Weiss, P. S.; Baše, T. Self-Assembled *p*-Carborane Analog of *p*-Mercaptobenzoic acid on Au{111}. *Chem. Mater.* **2015**, *27*, 5425–5435.

16. Kristiansen, K.; Stock, P.; Baimpos, T.; Raman, S.; Harada, J. K.; Israelachvili, J. N.; Valtiner, M. Influence of Molecular Dipole Orientations on Long-Range Exponential Interaction Forces at Hydrophobic Contacts in Aqueous Solutions. *ACS Nano* **2014,** *8*, 10870–10877.

17. Hohman, J. N.; Zhang, P.; Morin, E. I.; Han, P.; Kim, M.; Kurland, A. R.; McClanahan, P. D.; Balema, V. P.; Weiss, P. S. Self-Assembly of Carboranethiol Isomers on Au{111}: Intermolecular Interactions Determined by Molecular Dipole Orientations. *ACS Nano* **2009,** *3*, 527–536.

18. Baše, T.; Bastl, Z.; Plzák, Z.; Grygar, T.; Plešek, J.; Carr, M.; Malina, V.; Šubrt, J.; Boháček, J.; Večerníková, E.; Kříž, O. Carboranethiol-Modified Gold Surfaces. A Study and Comparison of Modified Cluster and Flat Surfaces. *Langmuir* **2005,** *21*, 7776–7785.

19. Baše, T.; Bastl, Z.; Šlouf, M.; Klementová, M.; Šubrt, J.; Vetushka, A.; Ledinský, M.; Fejfar, A.; Macháček, J.; Carr, M. J.; Londesborough, M. G. S. Gold Micrometer Crystals Modified with Carboranethiol Derivatives. *J. Phys. Chem. C* **2008,** *112*, 14446–14455.

20. Baše, T.; Bastl, Z.; Havránek, V.; Lang, K.; Bould, J.; Londesborough, M. G. S.; Macháček, J.; Plešek, J. Carborane-Thiol-Silver Interactions. A Comparative Study of the Molecular Protection of Silver Surfaces. *Surf. Coat. Tech.* **2010,** *204*, 2639–2646.

21. Lübben, J. F.; Baše, T.; Rupper, P.; Künniger, T.; Macháček, J.; Guimond, S. Tuning the Surface Potential of Ag Surfaces by Chemisorption of Oppositely-Oriented Thiolated Carborane Dipoles. *J. Colloid Interface Sci.* **2011,** *354*, 168–174.

22. Langecker, J.; Fejfarová, K.; Dušek, M.; Rentsch, D.; Baše, T. Carbon-Substituted 9,12-Dimercapto-1,2-Dicarba-*closo*-Dodecaboranes via a 9,12-Bis(Methoxy-Methylthio)-1,2-Dicarba-*closo*-Dodecaborane Precursor. *Polyhedron* **2012,** *45*, 144–151.

23. Baše, T.; Bastl, Z.; Havránek, V.; Macháček, J.; Langecker, J.; Malina, V. Carboranedithiols: Building Blocks for Self-Assembled Monolayers on Copper Surfaces. *Langmuir* **2012,** *28*, 12518–12526.

24. Nuzzo, R. G.; Dubois, L. H.; Allara, D. L. Fundamental Studies of Microscopic Wetting on Organic-Surfaces. 1. Formation and Structural Characterization of a Self-Consistent Series of Polyfunctional Organic Monolayers. *J. Am. Chem. Soc.* **1990,** *112*, 558–569.

25. Liao, W. S.; Cheunkar, S.; Cao, H. H.; Bednar, H. R.; Weiss, P. S.; Andrews, A. M. Subractive Patterning via Chemical Lift-off Lithography. *Science* **2012,** *337*, 1517–1521.

26. Kim, J.; Rim, Y. S.; Chen, H.; Cao, H. H.; Nakatsuka, N.; Hinton, H. L.; Zhao, C.; Andrews. A. M.; Yang, Y.; Weiss, P. S. Fabrication of High-Performance Ultrathin In_2O_3 Film Field-Effect Transistors and Biosensors Using Chemical Lift-Off Lithography. *ACS Nano* **2015,** *9*, 4572–4582.

27. Zheng, Y. B.; Pathem, B. K.; Hohman, J. N.; Thomas, J. C.; Kim, M.; Weiss, P. S. Photoresponsive Molecules in Well-Defined Nanoscale Environments. *Adv. Mater.* **2013,** *25*, 302–312.

28. He, H.-X.; Huang, W.; Zhang, H.; Li, Q. G.; Li, S. F. Y.; Liu, Z. F. Demonstration of High-Resolution Capability of Chemical Force Titration via Study of Acid/Base Properties of a Patterned Self-Assembled Monolayer. *Langmuir* **2000,** *16*, 517–521.

29. Saavedra, H. M.; Thompson, C. M.; Hohman, J. N.; Crespi, V. H.; Weiss, P. S. Reversible Lability by in Situ Reaction of Self-Assembled Monolayers. *J. Am. Chem. Soc.* **2009,** *131*, 2252–2259.

30. Saavedra, H. M.; Mullen, T. J.; Zhang, P.; Dewey, D. C.; Claridge, S. A.; Weiss, P. S. Hybrid Strategies in Nanolithography. *Rep. Prog. Phys.* **2010,** *73*, 036501–036600.

31. Saadi, F. H.; Carim, A. I.; Verlage, E.; Hemminger, J. C.; Lewis, N. S.; Soriaga, M. P. CoP as an Acid-Stable Active Electrocatalyst for the Hydrogen-Evolution Reaction: Electrochemical Synthesis, Interfacial Characterization and Performance Evaluation. *J. Phys. Chem. C* **2014,** *118*, 29294–29300.

32. Katano, S.; Kim, Y.; Matsubara, H.; Kitagawa, T.; Kawai, M. Hierarchical Chiral Framework Based on a Rigid Adamantane Tripod on Au(111). *J. Am. Chem. Soc.* **2007**, *129*, 2511–2515.

33. Hatzor, A.; McCarty, G. S.; D'Onofrio, T. G.; Fuchs, D. J.; Allara, D. L.; Tour, J. M.; Weiss, P. S. STM Imaging and Spectroscopy of Caltrops on Au{111}. Unpublished work.

34. Yao, Y.; Tour, J. M. Facile Convergent Route to Molecular Caltrops. *J. Org. Chem.* **1999**, *64*, 1968–1971.

35. Jian, H.; Tour, J. M. En Route to Surface-Bound Electric Field-Driven Molecular Motors. *J. Org. Chem.* **2003**, *68*, 5091–5103.

36. van Delden, R. A.; ter Wiel, M. K. J.; Pollard, M. M.; Vicario, J.; Koumura, N.; Feringa, B. L. Unidirectional Molecular Motor on a Gold Surface. *Nature* **2005**, *437*, 1337–1340.

37. Ye, T.; Kumar, A. S.; Saha, S.; Takami, T.; Huang, T. J.; Stoddart, J. F.; Weiss, P. S. Changing Stations in Single Bistable Rotaxane Molecules under Electrochemical Control. *ACS Nano* **2010**, *4*, 3697–3701.

38. Donhauser, Z. J.; Mantooth, B. A.; Kelly, K. F.; Bumm, L. A.; Monnell, J. D.; Stapleton, J. J.; Price, D. W. Jr.; Rawlett, A. M.; Allara, D. L.; Tour, J. M.; Weiss, P. S. Conductance Switching in Single Molecules through Conformational Changes. *Science* **2001,** *292*, 2303–2307.

39. Lewis, P. A.; Inman, C. E.; Maya, F.; Tour, J. M.; Hutchison, J. E.; Weiss, P. S. Molecular Engineering of the Polarity and Interactions of Molecular Electronics Switches. *J. Am. Chem. Soc.* **2005,** *127*, 17421–17426.

40. Tersoff, J.; Hamann, D. R. Theory and Application for the Scanning Tunneling Microscope. *Phys. Rev. Lett.* **1998**, *50*, 1998–2001.

41. McCarty, G. S.; Weiss, P. S. Scanning Probe Studies of Single Nanostructures. *Chem. Rev.* **1999,** *99*, 1983–1990.

42. Claridge, S. A.; Schwartz, J. J.; Weiss, P. S. Electrons, Photons, and Force: Quantitative Single-Molecule Measurements from Physics to Biology. *ACS Nano* **2011,** *5*, 693–729.

43. Bonnell, D. A.; Basov, D. N.; Bode, M.; Diebold, U.; Kalinin, S. V.; Madhavan, V.; Novotny, L.; Salmeron, M.; Schwarz, U. D.; Weiss, P. S. Imaging Physical Phenomena with Local Probes: From Electrons to Photons. *Rev. Mod. Phys.* **2012,** *84*, 1343–1381.

44. Fujii, S.; Akiba, U.; Fujihira, M. Geometry for Self-Assembling of Spherical Hydrocarbon Cages with Methane Thiolates on Au(111). *J. Am. Chem. Soc.* **2002,** *124*, 13629–13635.

45. Wiesendanger, R.; Eng, L.; Hidber, H. R.; Oelhafen, P.; Rosenthaler, L.; Staufer, U.; Güntherodt, H. J. Local Tunneling Barrier Height Images Obtained with the Scanning Tunneling Microscope. *Surf. Sci.* **1987,** *189–190*, 24–28.

46. Olesen, L.; Brandbyge, M.; Sørensen, M. R.; Jacobsen, K. W.; Lægsgaard, E.; Stensgaard, I.; Besenbacher, F. Apparent Barrier Height in Scanning Tunneling Microscopy Revisited. *Phys. Rev. Lett.* **1996,** *76*, 1485–1488.

47. Lang, N. D. Apparent Barrier Height in Scanning Tunneling Microscopy. *Phys. Rev. B* **1988,** *37*, 10395–10398.

48. Monnell, J. D.; Stapleton, J. J.; Dirk, S. M.; Reinerth, W. A.; Tour, J. M.; Allara, D. L.; Weiss, P. S. Relative Conductances of Alkaneselenolate and Alkanethiolate Monolayers on Au{111}. *J. Phys. Chem. B* **2005,** *109*, 20343–20349.

49. Jain, J.; Jain, A. Displacement Measurement and Its Application in Interframe Image Coding. *IEEE Trans. Comm.* **1981,** *29*, 1799–1808.

50. Love, N. S.; Kamath, C. An Empirical Study of Block Matching Techniques for the Detection of Moving Objects. *CASC, LLNL. Livermore* **2006**, 1–36.

51. Leites, L. A. Vibrational Spectroscopy of Carboranes and Parent Boranes and its Capabilities in Carborane Chemistry. *Chem. Rev.* **1992,** *92*, 279–323.

52. Shimizu, T. K.; Jung, J.; Otani, T.; Han, Y.-K.; Kawai, M.; Kim Y. Two-Dimensional Superstructure Formation of Fluorinated Fullerene on Au(111): A Scanning Tunneling Microscopy Study. *ACS Nano* **2012**, *6*, 2679–2685.

53. Stranick, S. J.; Parikh, A. N.; Allara, D. L.; Weiss, P. S. A New Mechanism for Surface Diffusion: Motion of a Substrate-Adsorbate Complex. *J. Phys. Chem.* **1994**, *98*, 11136–11142.

54. Poirier, G. E.; Tarlov, M. J. Molecular Ordering and Gold Migration Observed in Butanethiol Self-Assembled Monolayers using Scanning Tunneling Micrscopy. *J. Phys. Chem.* **1995**, *99*, 10966–10970.

55. Wiesboeck, R. A.; Hawthorne, M. F. Dicarbaundecaborane(13) and Derivatives. *J. Am. Chem. Soc.* **1964,** *86*, 1642–1643.

56. Bumm, L. A.; Arnold, J. J.; Charles, L. F.; Dunbar, T. D.; Allara, D. L.; Weiss, P. S. Directed Self-Assembly to Create Molecular Terraces with Molecularly Sharp Boundaries in Organic Monolayers. *J. Am. Chem. Soc.* **1999,** *121*, 8017–8021.

57. Ferris, J. H.; Kushmerick, J. G.; Johnson, J. A.; Yoshikawa Youngquist, M. G.; Kessinger, R. B.; Kingsbury, H. F.; Weiss, P. S. Design, Operation, and Housing of an Ultrastable, Low Temperature, Ultrahigh Vacuum Scanning Tunneling Microscope. *Rev. Sci. Instrum.* **1998,** *69*, 2691–2695.

58. Moulder, J. F. *Handbook of X-ray Photoelectron Spectroscopy: A Reference book of Standard Spectra for Idenfication and Interpretation of XPS Data*; Perkin-Elmer Corporation, Physical Electronics Division: Eden Prairie, MN, 1992.

59. Valiev, M.; Bylaska, E. J.; Govind, N.; Kowalski, K.; Straatsma, T. P.; Van Dam, H. J. J.; Wang, D.; Nieplocha, J.; Apra, E.; Windus, T. L.; de Jong, W.A. NWChem: A Comprehensive and Scalable Open-Source Solution for Large Scale Molecular Simulations. *Computer Physics Communications* **2010**, *181*, 1477–1489.

60. Johnson, B. G.; Fisch, M. J. An Implementation of Analytic Second Derivatives of the Gradient-Corrected Density Functional Energy. *J. Chem. Phys.* **1994**, *100*, 7429–7442.

61. Adamo, C.; Barone, V. Toward Reliable Density Functional Methods without Adjustable Parameters: The PBE0 Model. *J. Chem. Phys.* **1999**, *110*, 6158.

62. Adamo, C.; Barone, V. Inexpensive and Accurate Predictions of Optical Excitations in Transition-Metal Complexes: The TDDFT/PBE0 Route. *Theor. Chem. Acc.* **2000**, *105*, 169–172.

63. Adamo, C.; Barone, V. Physically Motivated Density Functionals with Improved Performances: The Modified Perdew–Burke–Ernzerhof Model. *J. Chem. Phys.* **2002**, *116*, 5933.

64. Adamo, C.; Scuseria, G. E.; Barone, V. Accurate Excitation Energies from Time-Dependent Density Functional Theory: Assessing the PBE0 Model. *J. Chem. Phys.* **1999**, *111*, 2889.

65. Jensen, F. Unifying General and Segmented Contracted Basis Sets. Segmented Polarization Consistent Basis Sets. *J. Chem. Theory Comput.* **2014**, *10*, 1074–1085.

66. Eckart, C. Some Studies Concerning Rotating Axes and Polyatomic Molecules. *Phys. Rev.* **1935**, *47*, 552–558.

67. Allouche, A.-R. Gabedit—A Graphical User Interface for Computational Chemistry Softwares. *J. Comput. Chem.* **2011**, *32*, 174–182.

68. Giannozzi, P.; Baroni, S.; Bonini, N.; Calandra, M.; Car, R.; Cavazzoni, C.; Ceresoli, D.; Chiarottie, G. L.; Cococcioni, M.; Dabo, I.; Corso, A. D.; de Gironcoli, S.; Fabris, S.; Fratesi, G.; Gebauer, R.; Gerstmann, U.; Gougoussis, C.; Kokalj, A.; Lazzeri, M.; Martin-Samos, L.; Marzari, N.; Mauri, F.; Mazzarello, R.; Paolini, S.; Pasquarello, A.; Paulatto, L.; Sbraccia, C.; Scandolo, S.; Sclauzero, G.; Seitsonen, A. P.; Smogunov, A.; Umari, P.; Wenzcovitch, R. M. Quantum Espresso: A Modular and Open-Source Software Project for Quantum Simulations of Materials. *J. Phys.: Condens. Matter.* **2009**, *21*, 395502.

69. Perdew, J. P.; Burke, K.; Ernzerhof, M. Generalized Gradient Approximation Made Simple. *Phys. Rev. Lett.* **1996**, *77*, 3865–3868.

70. Perdew, J. P.; Burke, K.; Ernzerhof, M. Generalized Gradient Approximation Made Simple [Phys. Rev. Lett. 77, 3865 (1996)]. *Phys. Rev. Lett.* **1997**, *78*, 1396–3868.

71. Anderson, M. P. Density Functional Theory with Modified Dispersion Correction for Metals Applied to Self-Assembled Monolayers of Thiols on Au(111). *J. Theory Chem.* **2013**, 327839.

CHAPTER 5

Holey Graphene as a Weed Barrier for Molecules

5.1 Introduction

The extraordinary electronic, thermal, and mechanical properties of graphene have been elaborated and exploited.[1] Graphene's high carrier mobility and ambipolarity make it a potentially powerful component in electronic systems.[2] An equally intriguing aspect of graphene is its capacity to act as an impermeable or semipermeable membrane; Bunch *et al.* demonstrated the impermeability of graphene to helium through the inflation of a "nanoballoon".[3,4] Graphene can also act as an effective barrier to oxidation of metal surfaces under certain conditions.[5-7] The purposeful introduction of pores into graphene tunes this permeability by allowing certain molecules to pass through while others are inhibited. This use of graphene has led to proposals as varied as desalination and DNA sequencing.[8-12] Here, we demonstrate and explore the use of "holey" graphene as a molecular barrier by applying it to adsorption and self-assembly.

Self-assembly provides a convenient route towards the bottom-up placement of single molecules with applications ranging from nanotechnology to biology.[13-16] Molecules for self-assembly typically comprise an attaching head group, an interacting backbone, and a functional tail group. The head group binds the molecule to a substrate, backbone intermolecular interactions lead to crystalline packing (through design), and the exposed terminal functional group can tune interfacial chemical properties between the substrate and its environment.[17] Molecular monolayers enable controllable surface functionalization and can be used to isolate and to study individual molecules.[18-20] Self-assembly is made even more powerful when combined with patterning. Currently, patterning of self-assembled monolayers (SAMs) is achieved through conventional, soft, or hybrid lithographies that are limited by the conflicting requirements of feature resolution and large-scale fabrication, where manufacturing cost and assembly time each

play key roles.[21-25] Inspired by the approach of Battaglini *et al.*, we pattern SAMs by masking the surface with an inert material.[26] We find that graphene can function as such a mask, as it is a material with relatively inert chemistry[27] and functions as an impermeable barrier against other molecules. Our choice was also influenced by the number of techniques that enable the introduction of nanoscale pores of arbitrary size and location to graphene, including both electron-beam bombardment and chemical approaches.[28-34] These techniques will ultimately provide flexibility in pattern shape and scale.

5.2 Results and Discussion

The process we developed for producing spatially patterned monolayers on Au{111} using a graphene mesh is shown schematically in Figure 5.1. We fabricate "holey" graphene by depositing graphene on a SiO_2 substrate,[35-37] then evaporate a thin layer of Au (2 nm) onto the exposed graphene layer. Subsequent annealing forms surface-bound Au nanoparticles. The Au nanoparticles catalyze oxidation of the graphene by oxygen in the air, thereby forming pores. The Au nanoparticles are then etched via brief immersion into an etchant solution (see materials and methods for details). A thin protecting layer of poly(methyl methacrylate) (PMMA) is added to facilitate transfer, and the "holey" graphene is transferred onto a Au{111} substrate. The protecting layer is removed and samples are ready for characterization. Further annealing at 100 ˚C removes any excess solvent, and the covered Au{111} substrate is thereby primed for molecular deposition. We confirm the fabrication of porous graphene by transmission electron microscopy (TEM), where TEM images show a graphene mesh with randomly distributed holes; measured holes have an average diameter of 37 ± 8 Å (Figure 5.2 and Figure 5.3). Images also depict cracks in the graphene induced by the transfer and annealing processes. Graphene is known to retain the surface

morphology of the substrate on which it was synthesized even when attached to the PMMA overlayer.[38] When transferred to the final substrate, this morphology results in gaps between the graphene and the substrate that can cause folding and cracking when the PMMA is removed. Further, water caught between the graphene and the substrate can leave gaps between the graphene and substrate upon drying that lead to folds, thereby appearing like graphite in images.[38] After the mesh is successfully transferred to Au{111} and annealed, we use scanning tunneling microscopy (STM) to probe the local environment.

The scanning tunneling microscope provides a window into the nanoscopic world, where constant-current imaging measures a convolution of electronic and topographic structure as a function of position across surfaces.[39-41] Measurements are recorded on a custom-built, ultrastable microscope held at ambient temperature and pressure.[42] Scanning tunneling micrographs before annealing are shown in Figure 5.4, where we note a large depression (pore) in the center of the image that is surrounded by other pores filled with residual solvent from the transfer step. Annealing removes the solvent within the pores. The annealed graphene-gold surface is shown in Figure 5.5, where images depict porous graphene with hole diameters that match TEM measurements. The surrounding graphene Moiré pattern shows a sixfold symmetry with a nearest-neighbor distance of 5.0 ± 0.5 Å, which is in good agreement with the predicted and energetically favorable (2×2) superstructure for graphene on a Au{111} substrate.[43]

The structure of graphene on Au{111} is difficult to predict and likely to be locally varied, where measured superlattices are highly influenced by both the underlying Au substrate and the detailed structure of the STM tip.[35,44] With this caveat in mind, acquired STM images confirm a single transferred layer of holey graphene with exposed Au regions, where image differences were

quantified in real and Fourier space. Thresholding and masking techniques, performed in MATLAB, enable gold and graphene regions to be segmented and compared (Figure 5.6). In STM images, under the conditions used, graphene layers are 2.1 ± 1.1 Å more protruding in apparent height compared to exposed Au regions. The same sample is then exposed to an ethanolic vapor solution of the self-assembling cage molecule 1-adamantanethiol (1AD) and subsequently imaged.

The diamondoid 1AD is ideal for an initial patterning test, in that it is commercially available, forms well-ordered monolayers with few defects (due to limited degrees of freedom), and has a well-defined structure.[45-48] Scanning tunneling micrographs recorded after deposition show islands of molecular protrusions consistent with the diameters of the pores (Figure 5.7). Nearest-neighbor distances within measured molecular protrusions (7.2 ± 1.1 Å) are near previously recorded distances of 1AD on Au{111} (6.9 ± 0.4 Å) (Figure 5.8).[45,49] The areas surrounding the islands proved difficult to resolve, however, there were small, well-resolved areas bearing molecular features that were analyzed (Figure 5.9). Several of these areas topographically resemble the graphene overlayer imaged prior to 1AD deposition. The average nearest-neighbor spacings of these areas is (5.0 ± 1.1 Å), consistent with the graphene overlayer. The difference in nearest-neighbor spacings provides evidence of separate molecular domains brought about due to the graphene masking effect against the deposition of 1AD. Graphene regions show a different apparent height than 1AD islands and can be segmented (Figure 5.10), where 1AD patches differ by 1.1 ± 0.5 Å in the z-direction under the STM imaging conditions used. Measured spacings, both in the lateral and surface normal (apparent height) directions, and consistent hole diameters confirm the blocking effect of the graphene layer. The same samples are then annealed again to test if molecular desorption can be achieved, and thus if the bare surface in the pores of the graphene mask can be regenerated.

Scanning tunneling topographs before and after this second anneal, to 250 ˚C, are shown in Figure 5.11, where evidence of molecular desorption is obtained.[16,50,51] Once filled holes are now empty and the hexagonal spacing of 5.0 ± 0.5 Å is recovered outside graphene pores. We confirm desorption by topographic imaging, where the exposed areas within the mask are destructively regenerated and thus prepared for further molecular deposition steps (Figure 5.12). We note that non-destructive methods such as displacement techniques can also be applied, since 1AD has been shown to be labile upon exposure via solution, vapor, or contact to more strongly bound self-assembling molecules.[47,48]

5.3 Conclusions and Prospects

The graphene mask approach embodies a wholly different set of strengths and weaknesses than photolithographic and soft-lithography approaches.[22,24] Patterning is achieved with electron-beam and chemical methods, surpassing the diffraction limit of photolithographic methods and placing it in league with scanning probe lithography in feature size. The graphene mask, akin to the PDMS stamp and unlike the scanning probe lithography techniques, is reusable, and can cover large areas. Our approach permits control over the pattern, overcoming a major limitation of Battaglini's approach, though it is not removable and thus cannot be backfilled. The value of graphene as a mask is further enhanced by its thermal stability, making it resilient to high-temperature fabrication processes.[59] Importantly for SAMs, thermal stability implies that the integrity of the graphene should not be compromised when annealing the masked substrate to remove adsorbates and thereby to regenerate the mask.

Our results show that graphene can serve as a barrier to adsorption and open up a plethora of future patterning experiments. Since graphene pores can be readily manufactured, masks can be

used with a wide variety adsorbates with implications ranging from constructing well-defined nanoarchitectures to pattern biosensors sequentially.

5.4 Materials and Methods

5.4.1 Holey Graphene Sample Preparation

Graphene was synthesized on a 25-mm-thick copper foil (99.8%, Alfa Aesar, Ward Hill, MA) that was treated with hydrochloric acid/deionized water (1:10) (36.5-38.0%, Sigma-Aldrich, St. Louis, MO) for 30 min and rinsed by isopropyl alcohol (99.8%, Sigma-Aldrich, St. Louis, MO) for 10 min. After drying under an N_2 stream, the copper foil was loaded into the chemical vapor deposition (CVD) furnace (1-inch tube diameter; Lindbergh/Blue M, Thermo Scientific, Waltham, MA). The system was pumped down to a vacuum of 10 mTorr in 30 min and refilled with 300 sccm H_2/Ar flow (25 sccm/475 sccm) and heated to 1040 ˚C within 25 min. Next, diluted methane and Ar were introduced into the CVD system for graphene growth at 1040 ˚C for 90 min (500 ppm methane in Ar, 35 sccm) with H_2/Ar (25 sccm/440 sccm). All process gases were supplied by Airgas, Inc (Burbank, CA).

Graphene was grown on both sides of the copper foil, and one side of the graphene/copper surface was spin-coated with poly(methyl methacrylate) (PMMA; 495 PMMA C_2, MicroChem, Newton, MA) and baked at 140 ˚C for 5 min. The other side of the copper foil was exposed to O_2 plasma for 1 min to remove the graphene. After that, the Cu foil was etched away using copper etchant (ferric chloride, Transene), resulting in a free-standing PMMA/graphene membrane floating on the surface of the etchant bath. The PMMA/graphene film was washed with HCl/deionized H_2O (1:10) and deionized water several times, and then transferred onto a 300-nm-

thick SiO_2 substrate. After air-drying, the PMMA was dissolved by acetone and the substrate was rinsed with isopropyl alcohol to yield a graphene film on the substrate.

A 2-nm-thick gold film was deposited using thermal evaporation onto the graphene/SiO_2 substrate. After annealing at 350 ˚C for 15 min, gold nanoparticles were found on the substrate. The holey graphene is oxidized by exposure to oxygen in the ambient air, with gold nanoparticles acting as the catalyst. The gold nanoparticles were removed by gold etchant (KI/I_2 solution, Sigma-Aldrich, St. Louis, MO) and washed with isopropyl alcohol and deionized water. The graphene/SiO_2 was again spin-coated with PMMA, and the SiO_2 substrate was etched away using a buffered oxide etch. The PMMA-coated holey graphene was washed in deionized water and transferred to a deionized water bath. A H_2 flame-annealed (at a rate of 1 Hz, 10 passes) Au{111}/mica substrate (Agilent, Santa Clara, CA) was then used to scoop the PMMA-coated graphene from the water bath. The PMMA/graphene/Au substrate was allowed to air dry overnight, and then the PMMA was dissolved in acetone and the graphene/Au substrate was washed with isopropyl alcohol.

5.4.2 Transmission Electron Microscopy

The morphology and structure of the graphene were characterized with field emission high-resolution transmission electron microscopy (TEM; FEI Titan S/TEM), typically with an accelerating voltage at an accelerating voltage of 300 kV. The diffraction patterns were collected with accelerating voltages of 300 kV to assess whether the beam energy played a role in graphene surface changes. Specimens for TEM analysis were prepared by the same as the process of graphene transfer onto 200 mesh formvar/copper grids purchased from Ted Pella, Inc. (Redding, CA).

5.4.3 Scanning Tunneling Microscope Sample Preparation

Holey graphene was deposited onto flame annealed, commercially available Au{111} on mica substrates. Samples were imaged and then subsequently annealed at 100 ˚C for a period of 24 h in a gasketed glass v-vial (Wheaton, Millville, NJ). Samples were heated in a chamber of a Barstead Thermolyne 1400 furnace (ThermoFischer Scientific, Waltham, MA). Samples were taken out and imaged with the scanning tunneling microscope, then placed back into a clean v-vial above a solution of 1 mM commercially available 1-adamantanethiol (Sigma-Aldrich, St. Louis, MO) in ethanol for vapor deposition. Vials were placed back into a preheated furnace at 78 ˚C for a period of 24 h. Inserted 1-adamantanethiolate holey graphene samples were taken out for STM imaging. After sufficient experiments were performed, samples were placed back into a preheated furnace at 250 ˚C for a period of 24 h for molecular desorption. Samples were then taken out for subsequent imaging and desorption confirmation.

5.4.4 Imaging

All STM measurements were performed in air using a custom beetle-style scanning tunneling microscope and a platinum/iridium tip (80:20).[42] The known lattice of 1-dodecanethiolate SAMs on Au{111} was used to calibrate the piezoelectric scanners. The sample was held between -1 V to -0.1 V bias range, and 256 × 256 pixel images were collected, at varying size, in constant-current mode with a tunneling current ranging from 2 to 80 pA. There is a strong tip dependence for imaging cage molecules, as reported previously.[60]

5.4.5 Image Analyses

All STM images were initially processed with automated routines developed in MATLAB (Mathworks, Natick, MA) to remove any high-frequency noise and intensity spikes that may otherwise impair reliable segmentation.[40] Images used to obtain nearest-neighbor spacings were resized to account for drift at room temperature. Transmission electron microscopy images were thresholded to segment both graphene holes and the graphene layer that was used to create a binary mask, where the average diameter of the holes was computed. The nearest-neighbor spacing of graphene was computed in Fourier space for the pre-1-adamantanethiol deposition and post-annealing experiments. The spacings of assembled 1-adamantanethiol and the surrounding graphene were determined by fitting the centers of the molecules using a binary mask generated through thresholding and the Regionprops function in Matlab. Values obtained by Fourier analysis and Regionprops fitting on the same image were compared to ensure that results were similar. Apparent height was also used for image segmentation and to determine separation distances in the z-direction.

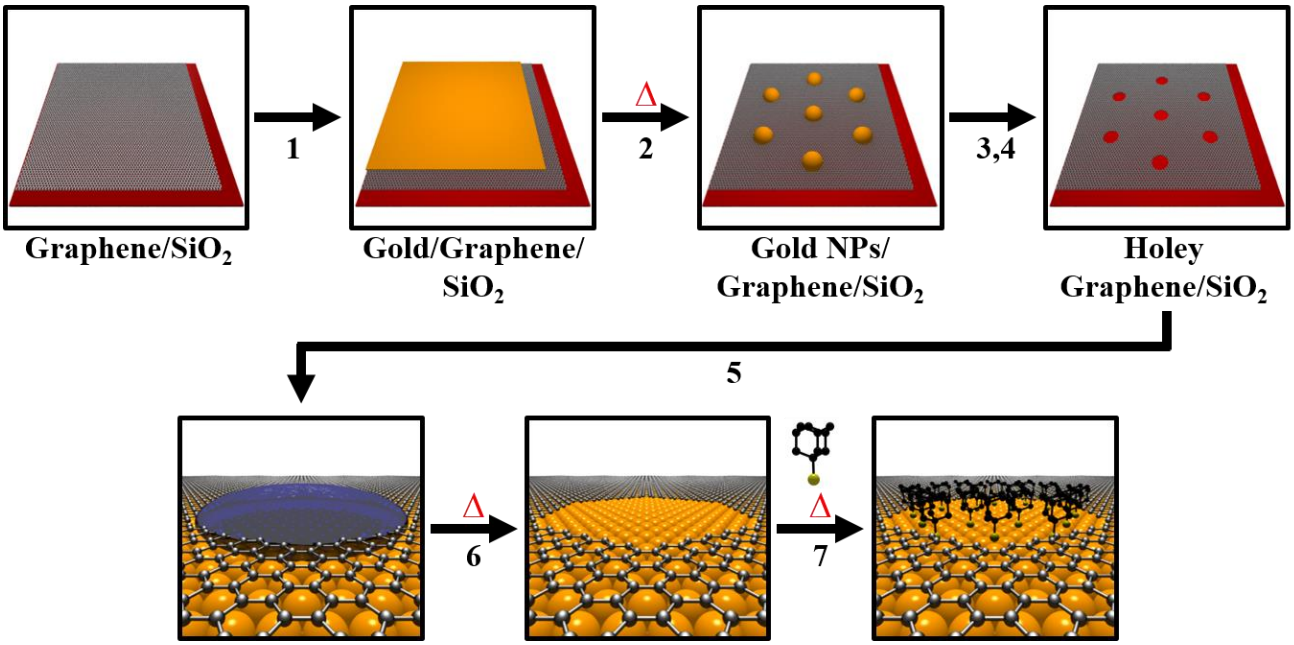

Figure 5.1 Process for producing spatially patterned monolayers on Au{111} using a graphene mesh. From a monolayer sheet of graphene on a SiO_2 substrate, (1) 2 nm of Au is deposited and (2) then annealed for 15 min at 350 ˚C. (3) The Au is etched (KI/I_2, solution) for 30 sec and (4) washed in DI water for 30 sec. (5) "Holey" graphene is then transferred to a Au{111}/mica substrate and (6) annealed at 100 ˚C for 24 h. (7) The same substrate is then exposed to a vapor solution of 1-adamantanethiol (1AD) at 78 ˚C for 24 h for deposition.

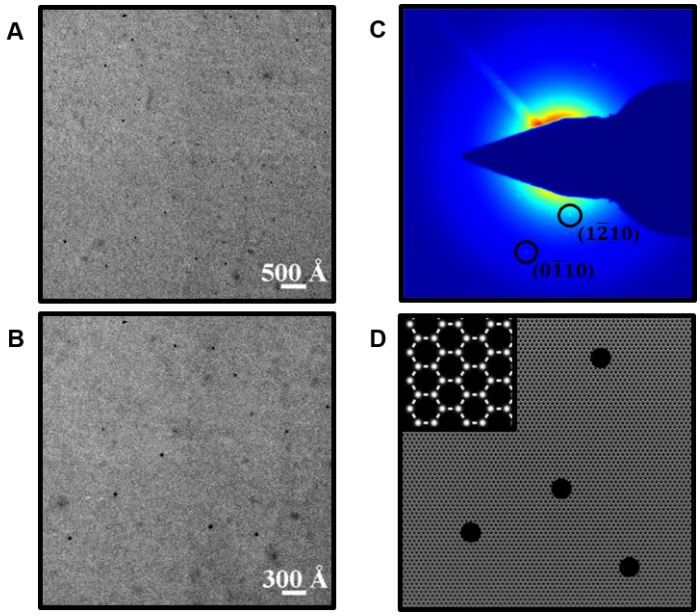

Figure 5.2 (A, B) "Holey" graphene measured with transmission electron microscopy (TEM) supported on a 200 mesh formvar/copper grid. Each image was acquired at an accelerating voltage of 300 kV using a FEI Titan microscope. Holes measured with TEM are 37 ± 8 Å in diameter and are randomly distributed across the graphene layer. (C) A diffraction image of B is shown, where the hexagonal pattern of graphene is observed. (D) Schematic that depicts "holey" graphene with randomly distributed holes and an inset showing a graphene layer.

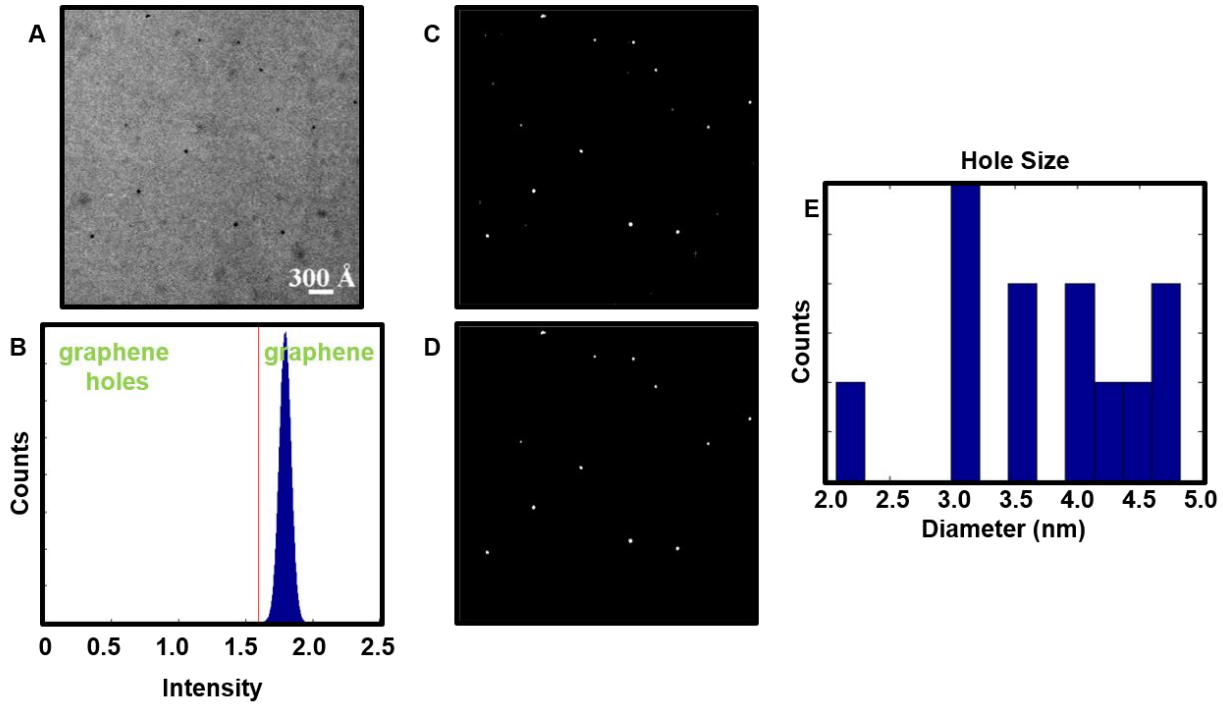

Figure 5.3 (A) Original transmission electron microscopy image from Figure 5.2 before segmentation. (B) An image histogram of the data in A showing the intensity threshold cut off used to create an image binary. (C) Resulting binary mask, where graphene holes are separated from the graphene layer. (D) Small outlier artifacts in the image binary are removed. (E) The diameters of the remaining holes are displayed in a bar graph, binned by diameter (10 Å bin width); we measure an average 37 ± 8 Å hole size.

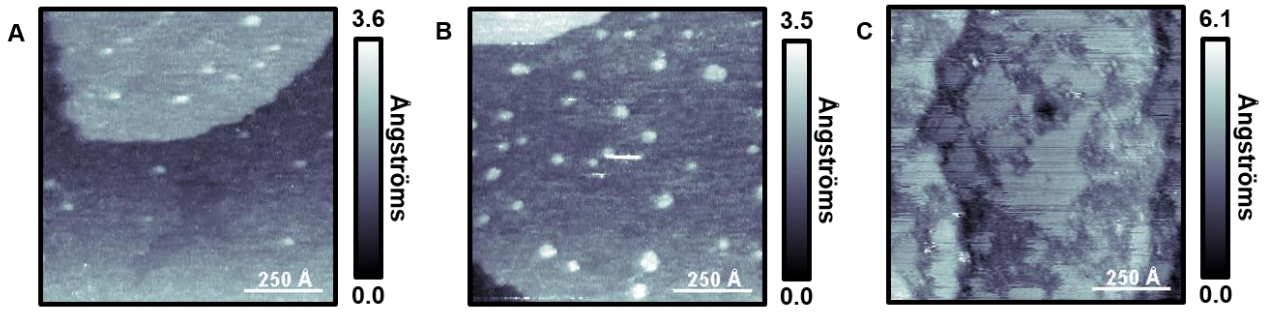

Figure 5.4 (A,B) Scanning tunneling micrographs ($I_{tunneling}$ = 3 pA, V_{sample} = -1.0 V) of "holey" graphene on Au{111}/mica directly after deposition from solution of water and acetone. Images show protrusions and depressions, displayed as brighter and dimmer, respectively. We attribute the higher protrusions as solvent that has not desorbed from the holes, and depressions as holes (without solvent) within the graphene overlayer. (C) After annealing at 100 ˚C for 24 h, all solvent is evaporated and only the depressions (holes) remain.

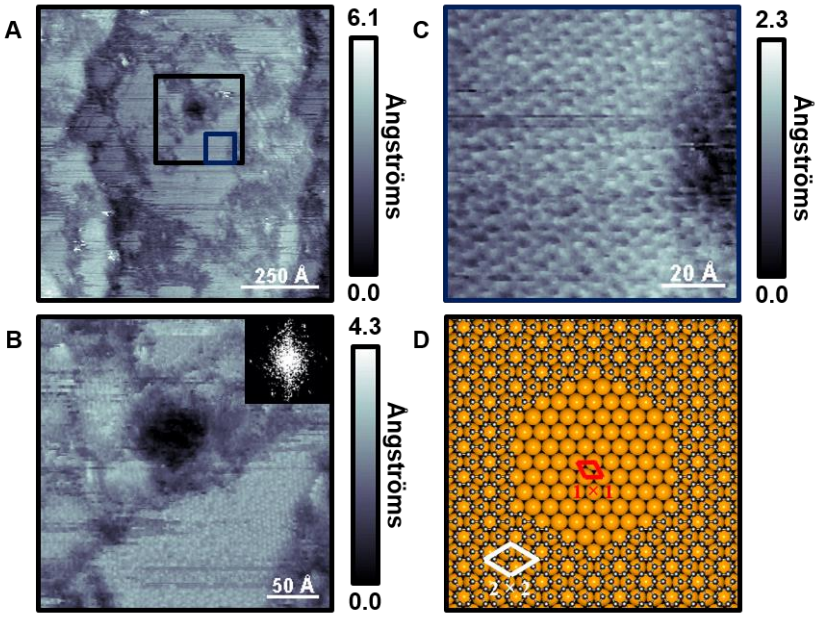

Figure 5.5 (A) Scanning tunneling micrograph ($I_{tunneling}$ = 3 pA, V_{sample} = -1.0 V) of "holey" graphene on Au{111}/mica along two monoatomic step edges after annealing at 100 ˚C for 24 h. (B) Higher resolution of the larger box in A. (C) Higher resolution image of the smaller box in (A). Insets in B and C show fast Fourier transforms, where graphene displays a hexagonal nearest-neighbor spacing of 5.0 ± 0.5 Å. (D) A schematic showing a pore in graphene exposing the underlying Au{111} substrate that further depicts the measured (2 × 2) Moiré superstructure of graphene on Au.

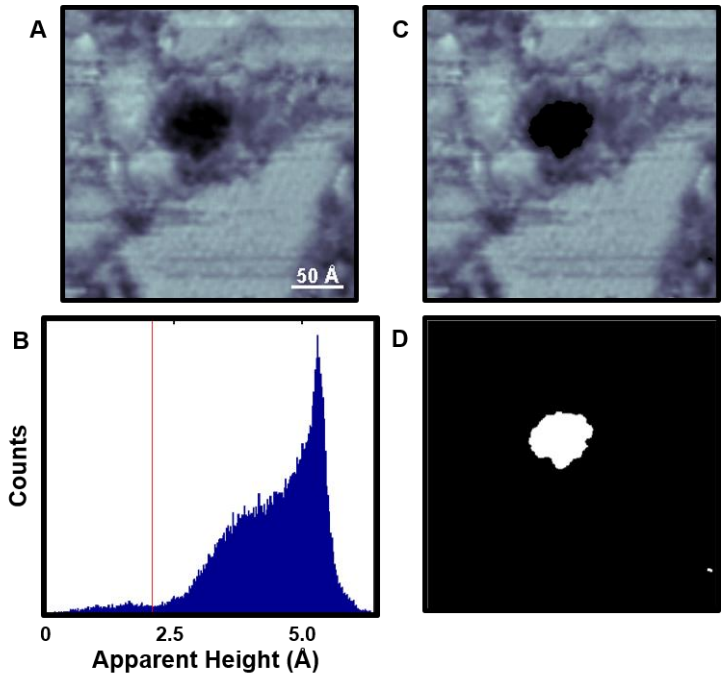

Figure 5.6 (A) Scanning tunneling micrograph ($I_{tunneling}$ = 3 pA, V_{sample} = -1.0 V) of "holey" graphene on Au{111}/mica with (B) a corresponding apparent height histogram. Masking techniques, performed in MATLAB, enable "holey" regions and graphene regions to be isolated and analyzed independently. (C) The image in A is segmented by apparent height. The graphene layer is 2.1 ± 1.2 Å higher in average apparent height compared to (D) the exposed Au region.

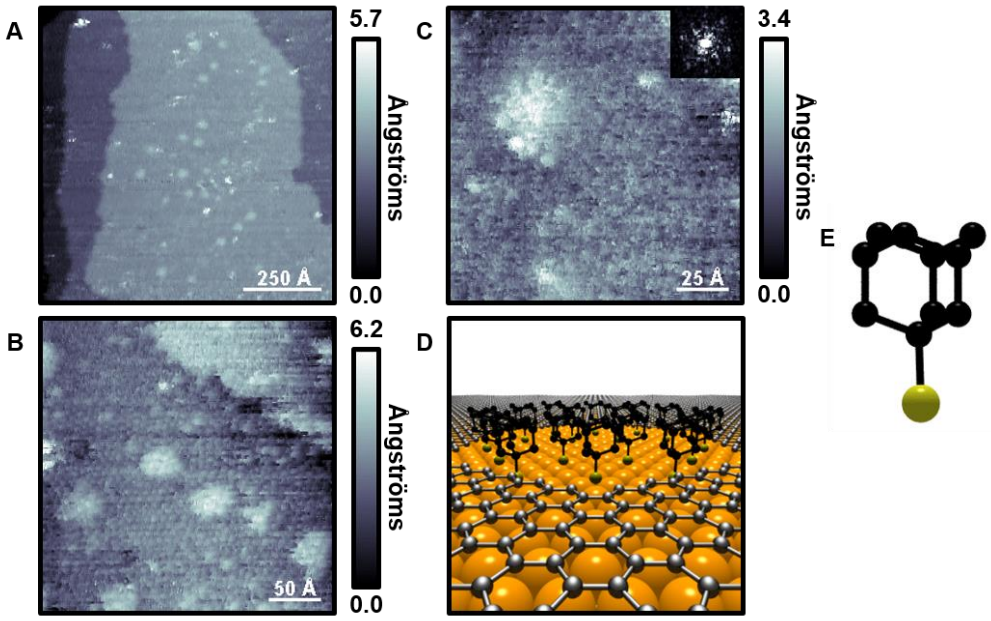

Figure 5.7 (A) Scanning tunneling micrograph ($I_{tunneling}$ = 3 pA, V_{sample} = -1.0 V) of "holey" graphene on Au{111}/mica after exposure to a vapor solution of 1-adamantanethiol (1AD) in ethanol. (B, C) Two regions where 1AD has assembled on Au{111} within the confines of the pores of the holey graphene. (C, inset) A fast Fourier transform shows local order of both the self-assembled molecules in the pores and the graphene overlayer with nearest-neighbor spacings of 7.2 ± 1.1 Å and 5.0 ± 1.1 Å, respectively. (D) A schematic of the arrangement in (C) where the graphene pore is filled with assembled 1AD. (E) Ball-and-stick model of the 1AD molecule with hydrogens not shown, for clarity.

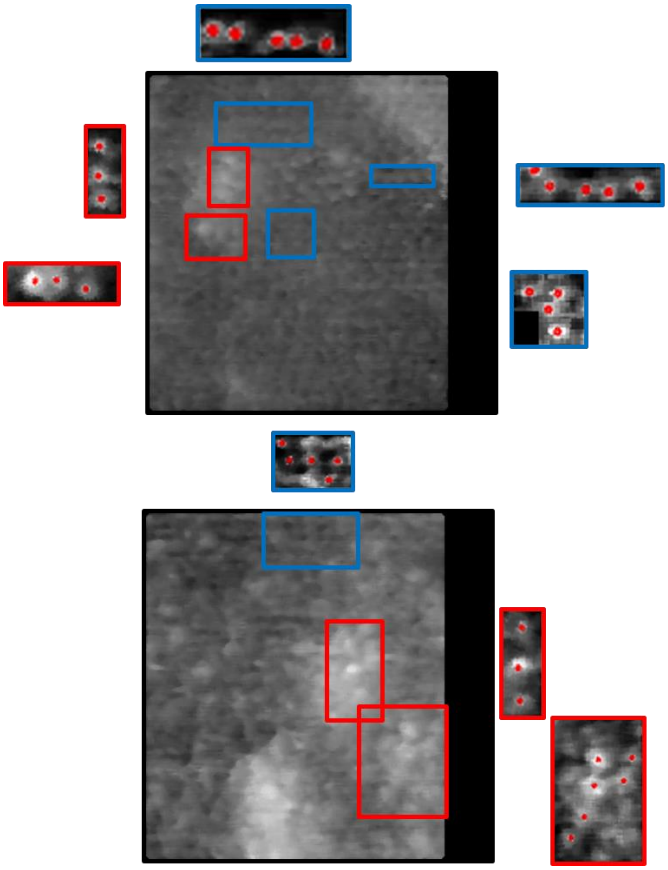

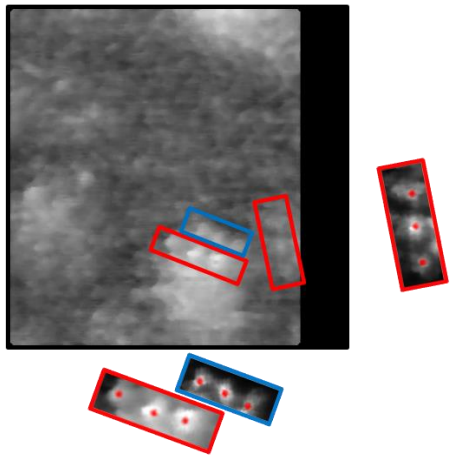

	Lattice Constant (A)	Number of Pairs
1AD	7.2 ± 1.1 Å	17
Graphene	5.0 ± 1.1 Å	19

Figure 5.8 Scanning tunneling micrographs ($I_{tunneling}$ = 3 pA, V_{sample} = -1.0 V) of "holey" graphene filled with 1-adamantanethiolate (1AD) on Au{111}/mica, where the spacing between adjacent 1AD molecules and graphene atoms is recorded. Images of the molecules were first smoothed and then analyzed using the Regionprops function in Matlab in the molecular regions highlighted. The inserted molecular layer shows an average spacing (across multiple images) of 7.2 ± 1.1 Å, while the graphene mask shows an average spacing of 5.0 ± 1.1 Å.

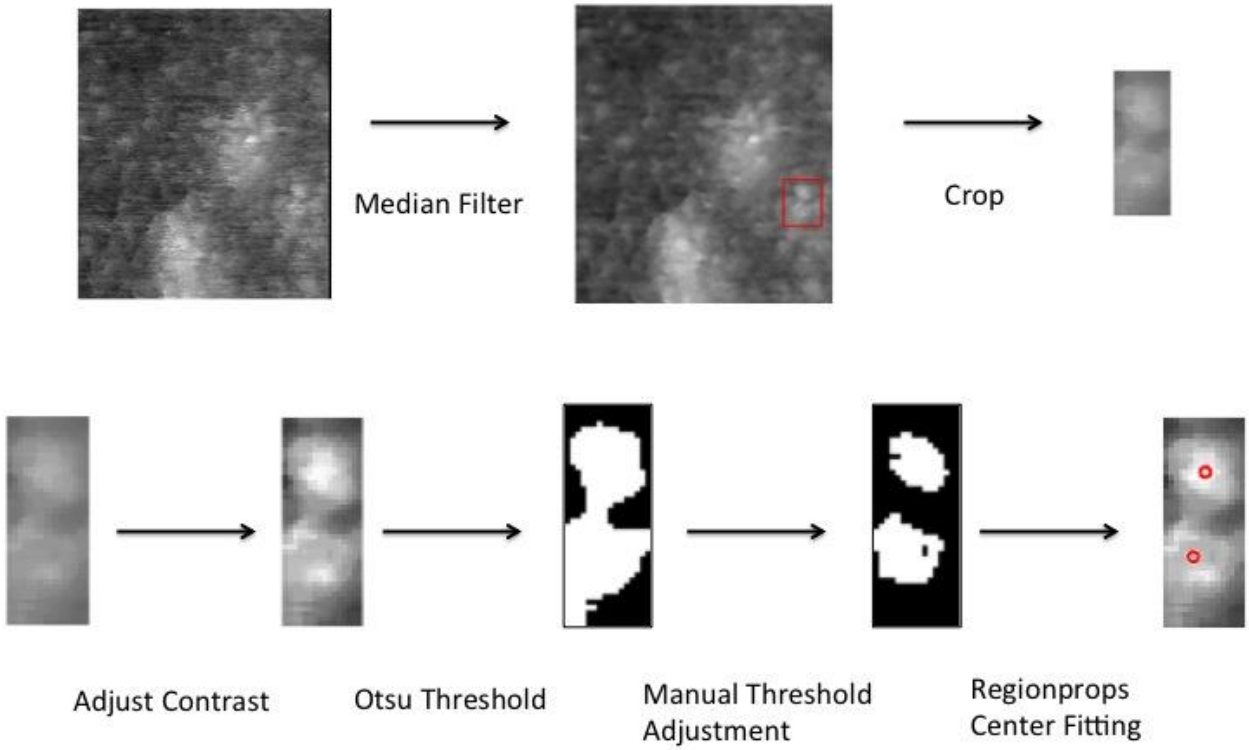

Figure 5.9 Molecule-Fitting Methodology. To determine nearest-neighbor spacings between molecules post-1AD deposition, molecules were fit using the Regionprops function in Matlab. A median filter is applied to remove intensity spikes, and then the region of interest is cropped for analysis. The contrast of the cropped image is enhanced, and then the image is thresholded using the Otsu cutoff. The cutoff was increased until sufficient segmentation was achieved. The average adjustment was 0.16 where images were set to a grayscale. Finally, the center of each segmented molecule was determined. The locations of these centers were used to calculate nearest-neighbor distances. Fittings were also performed on regions that were analyzed in Fourier space to crosscheck results.

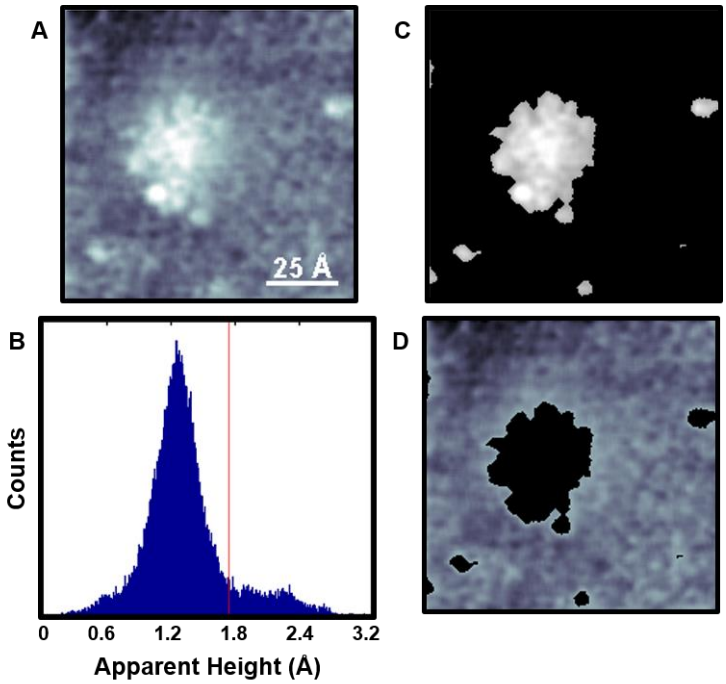

Figure 5.10 (A) Scanning tunneling micrograph ($I_{tunneling}$ = 3 pA, V_{sample} = -1.0 V) of "holey" graphene filled with 1-adamantanethiolate on Au{111}/mica with (B) a corresponding apparent height histogram. Masking techniques, performed in MATLAB, enable filled regions and bare graphene regions to be isolated and analyzed independently. (C,D) The image in A is segmented by apparent height and displayed. A 1-admantanethiolate patch appears on average 1.1 ± 0.5 Å than the graphene layer.

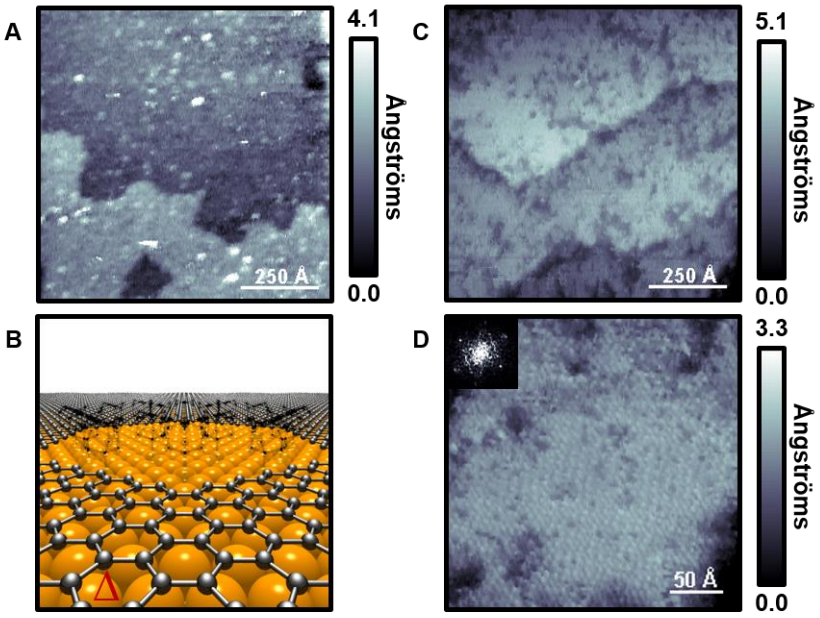

Figure 5.11 (A) Scanning tunneling micrograph ($I_{tunneling}$ = 3 pA, V_{sample} = -1.0 V) of "holey" graphene with the 2D pores filled with assembled 1-adamantanethiol on Au{111}/mica. (B) Annealing at 250 ˚C for 24 h removes adsorbates from the pores, as shown schematically. (C, D) Scanning tunneling micrographs ($I_{tunneling}$ = 3 pA, V_{sample} = -1.0 V) of the same sample after complete molecular desorption, recorded at two different resolutions, as indicated. (D, inset) A fast Fourier transform shows the recovered hexagonal spacing (5.0 ± 0.5 Å) measured previously.

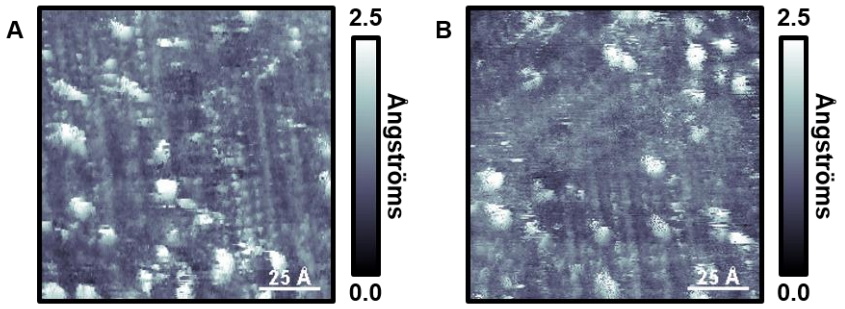

Figure 5.12 (A, B) Scanning tunneling micrographs ($I_{tunneling}$ = 3 pA, V_{sample} = -1.0 V) of "holey" graphene on Au{111}/mica after a second 1-adamantanethiolate vapor deposition for 24 h. Each sample was regenerated, prior to the second deposition step, by annealing at 250 ˚C. Images depict 1AD molecules within a "holey" graphene framework.

5.5 References

1. Novoselov, K. S.; Geim, A. K.; Morozov, S. V.; Jiang, D.; Zhang, Y.; Dubonos, S. V.; Grigorieva, I. V.; Firsov, A. A. Electric Field Effect in Atomically Thin Carbon Films. *Science* **2004**, *306*, 666–669.

2. Allen, M. J.; Tung, V. C.; Kaner, R. B. Honeycomb Carbon: A Review of Graphene. *Chem. Rev.* **2010**, *110*, 132–145.

3. Bunch, J. S.; Verbridge, S. S.; Alden, J. S.; van der Zande, A. M.; Parpia, J. M.; Craighead, H. G.; McEuen, P. L. Impermeable Atomic Membranes from Graphene Sheets. *Nano Lett.* **2008**, *8*, 2458–2462.

4. Berry, V. Impermeability of Graphene and its Applications. *Carbon* **2013**, *62*, 1–10.

5. Prasai, D.; Tuberquia, J. C.; Harl, R. R.; Jennings, G. K.; Bolotin, K. I. Graphene: Corrosion-Inhibiting Coating. *ACS Nano* **2012**, *6*, 1102–1108.

6. Nilsson, L.; Andersen, M.; Balog, R.; Lægsgaard, E.; Hofmann, P.; Besenbacher, F.; Hammer, B.; Stensgaard, I.; Hornekær, L. Graphene Coatings: Probing the Limits of the One Atom Thick Protection Layer. *ACS Nano* **2012**, *6*, 10258–10266.

7. Schriver, M.; Regan, W.; Gannett, W. J.; Zaniewski, A. M.; Crommie, M. F.; Zettl, A. Graphene as a Long-Term Metal Oxidation Barrier: Worse Than Nothing. *ACS Nano* **2013**, *7*, 5763–5768.

8. Schneider, G. F.; Kowalczyk, S. W.; Calado, V. E.; Pandraud, G.; Zandbergen, H. W.; Vandersypen, L. M. K.; Dekker, C. DNA Translocation through Graphene Nanopores. *Nano Lett.* **2010**, *10*, 3163–3167.

9. Siwy, Z. S.; Davenport, M. Nanopores: Graphene Opens up to DNA. *Nature Nano.* **2010**, *5*, 697–698.

10. Merchant, C. A.; Healy, K.; Wanunu, M.; Ray, V.; Peterman, N.; Bartel, J.; Fischbein, M. D.; Venta, K.; Luo, Z.; Johnson, A. T. C.; Drndić, M. DNA Translocation through Graphene Nanopores. *Nano Lett.* **2010**, *10*, 2915–2921.

11. Cohen-Tanugi, D.; Grossman, J. C. Water Desalination across Nanoporous Graphene. *Nano Lett.* **2012**, *12*, 3602–3608.

12. Russo, P.; Hu, A.; Compagnini, G. Synthesis, Properties and Potential Applications of Porous Graphene: A Review. *Nano-Micro Lett.* **2013**, *5*, 260–273.

13. Ulman, A. Formation and Structure of Self-Assembled Monolayers. *Chem. Rev.* **1996**, *96*, 1533–1554.

14. Poirier, G. E. Characterization of Organosulfur Molecular Monolayers on Au(111) using Scanning Tunneling Microscopy. *Chem. Rev.* **1997**, *97*, 1117–1127.

15. Smith, R. K.; Lewis, P. A.; Weiss, P. S. Patterning Self-Assembled Monolayers. *Prog. Surf. Sci.* **2004**, *75*, 1–68.

16. Love, J. C.; Estroff, L. A.; Kriebel, J. K.; Nuzzo, R. G.; Whitesides, G. M. Self-Assembled Monolayers of Thiolates on Metals as a Form of Nanotechnology. *Chem. Rev.* **2005**, *105*, 1103–1169.

17. Claridge, S. A.; Liao, W. -S.; Thomas, J. C.; Zhao, Y.; Cao, H. H.; Cheunkar, S.; Serino, A. C.; Andrews, A. M.; Weiss, P. S. From the Bottom Up: Dimensional Control and Characterization in Molecular Monolayers. *Chem. Soc. Rev.* **2013**, *42*, 2725–2745.

18. Donhauser, Z. J.; Mantooth, B. A.; Kelly, K. F.; Bumm, L. A.; Monnell, J. D.; Stapleton, J. J.; Price, D. W., Jr.; Rawlett, A. M.; Allara, D. L.; Tour, J. M.; Weiss, P. S. Conductance Switching in Single Molecules through Conformational Changes. *Science* **2001**, *292*, 2303–2307.

19. Shuster, M. J.; Vaish, A.; Szapacs, M. E.; Anderson, M. E.; Weiss, P. S.; Andrews, A. M. Biospecific Recognition of Tethered Small Molecules Diluted in Self-Assembled Monolayers. *Adv. Mater.* **2008**, *20*, 164–167.

20. Weiss, P. S. Functional Molecules and Assemblies in Controlled Environments: Formation and Measurements. *Acc. Chem. Res.* **2008**, *41*, 1772–1781.

21. Gates, B. D.; Xu, Q.; Stewart, M.; Ryan, D.; Willson, C. G.; Whitesides, G. M. New Approaches to Nanofabrication: Molding, Printing, and Other Techniques. *Chem. Rev.* **2005**, *105*, 1171–1196.

22. Srinivasan, C.; Mullen, T. J.; Hohman, J. N.; Anderson, M. E.; Dameron, A. A.; Andrews, A. M.; Dickey, E. C.; Horn, M. W.; Weiss, P. S. Scanning Electron Microscopy of Nanoscale Chemical Patterns. *ACS Nano* **2007**, *1*, 191–201.

23. Willson, C. G.; Roman, B. J. The Future of Lithography: SEMATECH Litho Forum 2008. *ACS Nano* **2008**, *2*, 1323–1328.

24. Saavedra, H. M.; Mullen, T. J.; Zhang, P. ; Dewey, D. C.; Claridge, S. A.; Weiss, P. S. Hybrid Approaches in Nanolithography. *Rep. Prog. Phys.* **2010**, *73*, 036501.

25. Liao, W.-S.; Cheunkar, S.; Cao, H. H.; Bednar, H. R.; Weiss, P. S.; Andrews, A. M. Subtractive Patterning via Chemical Lift-Off Lithography. *Science* **2012**, *337*, 1517–1521.

26. Battaglini, N.; Qin, Z.; Campiglio, P.; Repain, V.; Chacon, C.; Rousset, S.; Lang, P. Directed Growth of Mixed Self-Assembled Monolayers on a Nanostructured Template: A Step Toward the Patterning of Functional Molecular Domains. *Langmuir* **2012**, *28*, 15095–15105.

27. Yan, L.; Zheng, Y. B.; Zhao, F.; Li, S.; Gao, X.; Xu, B.; Weiss, P. S.; Zhao, Y. Chemistry and Physics of a Single Atomic Layer: Strategies and Challenges for Functionalization of Graphene and Graphene-Based Materials. *Chem. Soc. Rev.* **2012**, *41*, 97–114.

28. Fischbein, M. D.; Drndić, M. Electron Beam Nanosculpting of Suspended Graphene Sheets. *Appl. Phys. Lett.* **2008**, *93*, 113107.

29. Bai, J.; Zhong, X.; Jiang, S.; Huang, Y.; Duan, X. Graphene Nanomesh. *Nature Nano.* **2010**, *5*, 190–194.

30. Song, B.; Schneider, G. F.; Xu, Q.; Pandraud, G.; Dekker, C.; Zandbergen, H. Atomic-Scale Electron-Beam Sculpting of Near-Defect-Free Graphene Nanostructures. *Nano Lett.* **2011**, *11*, 2247–2250.

31. Liu, J.; Cai, H.; Yu, X.; Zhang, K.; Li, X.; Li, J.; Pan, N.; Shi, Q.; Luo, Y.; Wang, X. Fabrication of Graphene Nanomesh and Improved Chemical Enhancement for Raman Spectroscopy. *J. Phys. Chem. C* **2012**, *116*, 15741–15746.

32. Radich, J. G.; Kamat, P. V. Making Graphene 'Holey'. Gold-Nanoparticle-Mediated Hydroxyl Radical Attack on Reduced Graphene Oxide. *ACS Nano* **2013**, *7*, 5546–5557.

33. Xu, Q.; Wu, M.-Y.; Schneider, G. F.; Houben, L.; Malladi, S. K.; Dekker, C.; Yucelen, E.; Dunin-Borkowski, R. E.; Zandbergen, H. W. Controllable Atomic Scale Patterning of Freestanding Monolayer Graphene at Elevated Temperature. *ACS Nano* **2013**, *7*, 1566–1572.

34. Han, X.; Funk, M. R.; Shen, F.; Chen, Y.-C.; Li, Y.; Campbell, C. J.; Dai, J.; Yang, X.; Kim, J.-W.; Liao, Y.; Connell, J. W.; Barone, V.; Chen, Z.; Lin, Y.; Hu, L. Scalable Holey Graphene Synthesis and Dense Electrode Fabrication toward High-Performance Ultracapacitors. *ACS Nano* **2014**, *8*, 8255–8265.

35. Ishigami, M.; Chen, J. H.; Cullen, W. G.; Fuhrer, M. S.; Williams, E. D. Atomic Structure of Graphene on SiO_2. *Nano Lett.* **2007**, *7*, 1643–1648.

36. Liao, L.; Bai, J.; Cheng, R.; Lin, Y.-C.; Jiang, S.; Huang, Y.; Duan, X. Top-Gated Graphene Nanoribbon Transistors with Ultrathin High-k Dielectrics. *Nano Lett.* **2010**, *10*, 1917–1921.

37. Liao, L.; Bai, J.; Qu, Y.; Huang, Y.; Duan, X. Single-Layer Graphene on Al_2O_3/Si Substrate: Better Contrast and Higher Performance of Graphene Transistors. *Nanotech.* **2010**, *21*, 015705.

38. Liang, X.; Sperling, B. A.; Calizo, I.; Cheng, G.; Hacker, C. A.; Zhang, Q.; Obeng, Y.; Yan, K.; Peng, H.; Li, Q.; Zhu, X.; Yuan, H.; Walker, A. R. H.; Liu, Z.; Peng, L.-M.; Richter, C. A. Toward Clean and Crackless Transfer of Graphene. *ACS Nano* **2011**, *5*, 9144–9153.

39. Monnell, J. D.; Stapleton, J. J.; Dirk, S. M.; Reinerth, W. A.; Tour, J. M.; Allara, D. L.; Weiss, P. S. Relative Conductances of Alkaneselenolate and Alkanethiolate Monolayers on Au{111}. *J. Phys. Chem. B* **2005**, *109*, 20343–20349.

40. Han, P.; Kurland, A. R.; Giordano, A. N.; Nanayakkara, S. U.; Blake, M. M.; Pochas, C. M.; Weiss, P. S. Heads and Tails: Simultaneous Exposed and Buried Interface Imaging of Monolayers. *ACS Nano* **2009**, *3*, 3115–3121.

41. Claridge, S. A.; Schwartz, J. J.; Weiss, P. S. Electrons, Photons, and Force: Quantitative Single-Molecule Measurements from Physics to Biology. *ACS Nano* **2011**, *5*, 693–729.

42. Bumm, L. A.; Arnold, J. J.; Charles, L. F.; Dunbar, T. D.; Allara, D. L.; Weiss, P. S. Directed Self-Assembly to Create Molecular Terraces with Molecularly Sharp Boundaries in Organic Monolayers. *J. Am. Chem. Soc.* **1999**, *121*, 8017–8021.

43. Khomyakov, P. A.; Giovannetti, G.; Rusu, P. C.; Brocks, G.; van den Brink, J.; Kelly, P. J. First-Principles Study of the Interaction and Charge Transfer Between Graphene and Metals. *Phys. Rev. B* **2009**, *79*, 1954525.

44. Wofford, J. M.; Starodub, E.; Walter, A. L.; Nie, S.; Bostwick, A.; Bartelt, N. C.; Thürmer, K.; Rotenberg, E.; McCarty, K. F.; Dubon, O. D. Extraordinary Epitaxial Alignment of Graphene Islands on Au(111). *New J. Phys.* **2012**, *14*, 053008.

45. Dameron, A. A.; Charles, L. F.; Weiss, P. S. Structures and the Displacement of 1-Adamantanethiol Self-Assembled Monolayers on Au{111}. *J. Am. Chem. Soc.* **2005**, *127*, 8697–8704.

46. Mullen, T. J.; Dameron, A. A.; Saavedra, H. M.; Williams, M. E.; Weiss, P. S. Dynamics of Solution Displacement in 1-Adamantanethiolate Self-Assembled Monolayers. *J. Phys. Chem. C* **2007**, *111*, 6740–6746.

47. Dameron, A. A.; Mullen, T. J.; Hengstebeck, R. W.; Saavedra, H. M.; Weiss, P. S. Origins of Displacement in 1-Adamantanethiolate Self-Assembled Monolayers. *J. Phys. Chem. C* **2007**, *111*, 6747–6752.

48. Saavedra, H. M.; Barbu, C. M.; Dameron, A. A.; Mullen, T. J.; Crespi, V. H.; Weiss, P. S. 1-Adamantanethiolate Monolayer Displacement Kinetics Follow a Universal Form. *J. Am. Chem. Soc.* **2007**, *129*, 10741–10746.

49. Fujii, S.; Akiba, U.; Fujihira, M. Geometry for Self-Assembling of Spherical Hydrocarbon Cages with Methane Thiolates on Au(111). *J. Am. Chem. Soc.* **2002**, *124*, 13629–13625.

50. Kondoh, H.; Kodama, C.; Nozoye, H. Structure-Dependent Change of Desorption Species from n-Alkanethiol Monolayers Adsorbed on Au(111): Desorption of Thiolate Radicals from Low-Density Structures. *J. Phys. Chem. B* **1998**, *102*, 2310–2312.

51. Kondoh, H.; Kodama, C.; Sumida, H.; Nozoye, H. Molecular Processes of Adsorption and Desorption of Alkanethiol Monolayers on Au(111). *J. Chem. Phys.* **1999**, *111*, 1175–1184.

52. Gao, L.; Ren, W.; Xu, H.; Jin, L.; Wang, Z.; Ma, T.; Ma, L.-P.; Zhang, Z.; Fu, Q.; Peng, L.-M.; Bao, X.; Cheng, H.-M. Repeated Growth and Bubbling Transfer of Graphene with Milimetre-Size Single-Crystal Grains Using Platinum. *Nature Comm.* **2012**, *3*, 699.

53. Suk, J. W.; Kitt, A.; Magnuson, C. W.; Hao, Y.; Ahmed, S.; An, J.; Swan, A. K.; Goldberg, B. B.; Ruoff, R. S. Transfer of CVD-Grown Monolayer Graphene onto Arbitrary Substrates. *ACS Nano* **2011**, *5*, 6916–6924.

54. Kang, J.; Hwang, S.; Kim, J. H.; Kim, M. H.; Ryu, J.; Seo, S. J.; Hong, B. H.; Kim, M. K.; Choi, J.-B. Efficient Transfer of Large-Area Graphene Films onto Rigid Substrates by Hot Pressing. *ACS Nano* **2012**, *6*, 5360–5365.

55. Chen, X.-D.; Liu, Z.-B.; Zheng, C.-Y.; Xing, F.; Yan, X.-Q.; Chen, Y.; Tian, J.-G. High-Quality and Efficient Transfer of Large-Area Graphene Films onto Different Substrates. *Carbon* **2013**, *56*, 271–278.

56. Müllen, K. Evolution of Graphene Molecules: Structural and Functional Complexity as Driving Forces behind Nanoscience. *ACS Nano* **2014**, *8*, 6531–6541.

57. Han, P.; Akagi, K.; Canova, F. F.; Mutoh, H.; Shiraki, S.; Iwaya, K.; Weiss, P. S.; Asao, N.; Hitosugi, T. Bottom-Up Graphene-Nanoribbon Fabrication Reveals Chiral Edges and Enantioselectivity. *ACS Nano* **2014**, *8*, 9181–9187.

58. Narita, A.; Verzhbitskiy, I. A.; Frederickx, W.; Mali, K. S.; Jensen, S. A.; Hansen, M. R.; Bonn, M.; De Feyter, S.; Casiraghi, C.; Feng, X.; Müllen, K. Bottom-Up Synthesis of Liquid-Phase-Processable Graphene Nanoribbons with Near-Infrared Absorption. *ACS Nano* **2014**, *8,* 11622–11630.

59. Leong, W. S.; Nai, C. T.; Thong, J. T. L. What Does Annealing Do to Metal-Graphene Contacts? *Nano Lett.* **2014**, *14*, 3840–3847.

60. Hohman, J. N.; Zhang, P.; Morin, E. I.; Han, P.; Kim, M.; Kurland, A. K.; McClanahan, P. D.; Balema, V. P.; Weiss, P. S. Self-Assembly of Carboranethiol Isomers on Au{111}: Intermolecular Interactions Determined by Molecular Dipole Orientations. *ACS Nano* **2009**, 3, 527–536.

CHAPTER 6

Mapping Buried Hydrogen Bonding Networks

6.1 Introduction

Nanotechnology is inherently dependent upon the interactions between molecules and atoms, where bottom-up assembly aims to control single chemical units, linear arrays, two-dimensional thin films, and three-dimensional architectures by tuning and controlling chemical interactions at all scales. Self-assembled monolayers (SAMs), where surfactants spontaneously order on a substrate from disordered systems, enable the placement and direction of single molecules and supramolecular assemblies on surfaces.[1-4] Monolayers can be tuned through a variety of different interactions, where increasing intermolecular interactions becomes a pathway to create robust, adjustable, and even precise formations. To this end, self-assembly has found use in molecular coatings, substrate electronic property modification, processable biosensors, and other areas.[5-7] Scanning tunneling microscopy (STM) is able to record and to leverage sparse details, in that single-component information can be differentiated and compared to ensemble measurements and individual molecules and features are typically oversampled. Prompted by the analytical power and resolution of STM, a number efforts have focused on developing multi-modal spectroscopic imaging capabilities.[8-15] Monolayers composed of 3-mercapto-*N*-nonylpropionamide (1ATC9) have been extensively studied; however, the buried hydrogen-bonding network presumed responsible for the stability and directionality of these systems has not previously been visualized;[16-23] indeed, it has been long-standing challenge to measure buried chemical functionality with molecular and submolecular resolution.[10,24-29] Using 1ATC9 monolayers as a model system, we have measured buried hydrogen-bonding networks within single-component amide-containing SAMs and visualized bonding previously hidden from conventional scanning probe techniques.

Many single-molecule techniques remain hindered by either extreme dilution or lack of specificity, whereas STM is able to resolve chemical state information at the single-molecule and atomic levels.[10,22,24-27,30,31] Rastering an atomically sharp tip across a conductive substrate enables the acquisition of apparent height information, where the measured data are convolutions of electronic and topographic structure. Upon applying an AC modulation to the tunneling-gap distance, the local surface work function can be accessed with sub-Ångström precision.[29,32,33] This technique has been previously employed to measure the tilt of dual component alkanethiolate monolayers, where local extrema were related to the largest buried dipole (Au-S bond) and topographic maxima were related to molecular apexes.[28] In symmetric cage molecule, carboranethiolate, monolayers, topographic and local barrier height modalities were correlated to reveal single-molecule orientations and dipolar alignment within homogenous monolayers.[29] Motivated by these recent technical advances in imaging and image analysis, we sought to resolve single hydrogen bonds and the subsequently formed buried networks within monolayers of 1ATC9.

Amide and hydrogen bonds are of fundamental importance to biological functionality, peptide-sheet formation, and in the formation of protein structure.[34-39] The precise interplay between single- and supramolecular constructs and bulk functionality remains one of the elusive and quintessential aspects that structural biologists have yet to understand, where a concert of techniques and methodologies have been developed to address this problem. Charge separation within the amide bond has been extensively studied and shown to vary with different chemical substituents with bonding enthalpies ranging from 2 to 65 kcal/mol, but is typically much greater than van der Waals interactions (5 kcal/mol).[35] This bond is near the order of the Au-S bond (~50 kcal/mol) that is greater than the typical Au-Au bond (~44 kcal/mol),[40] possesses a large

dipole moment (~3.7 D for amide bonds and 1-2 D for Au-S bonds),[41,42] and helps to explain why different tilt orientations, in monolayers composed of 1ATC9, would reflect a convolution of the bond dipole.[4] Intermolecular interactions permit favorable hydrogen-bonding interactions between the dipoles in the net positively charged N-H and net negatively charged oxygen species within a large number of systems. In terms of molecular self-assembly, the presence of amide groups within monolayers composed of 1ATC9 enables increased molecular interplay between nearest neighbors and the formation of stable, protective ultra-thin coatings.[43] Electrochemical measurements, performed by Clegg *et al.*, confirmed that electron transfer (ET) was indeed kinetically limited, providing evidence that neither analyte permeation nor analyte pinhole diffusion played a significant role and thus ET was primarily due to electronic coupling between chains. Infrared spectroscopy measurements also showed that amide-containing SAMs of varied chain length were extensively ordered with C=O and N-H bonds nearly parallel to the substrate plane.[18] We used buried amide-based hydrogen-bonding networks to encapsulate liquid-metal nanoparticles and to prevent oxidation.[43] With significant ensemble evidence of buried networks, it becomes sufficiently feasible to probe the local work function within this system directly.

6.2 Results and Discussion

The two tilt-phases of 1ATC9 can be conventionally distinguished by apparent height using STM in topographic mode, however, scanning tunneling spectroscopy (STS) is able to access both topographic and buried information in local barrier height mode to enable more precise structural determination identification. We use a custom-built scanning tunneling microscope held at low temperature (4 K) and ultrahigh vacuum ($\leq 10^{-12}$ torr).[44] Topographic images depict the expected $(\sqrt{3}\times\sqrt{3})R30°$ superstructure, however, we observe contrast reversal, under the conditions reported,

in comparison to measurements recorded at room temperature.[19,23] This reversal is consistent with stronger electronic influences, rather than topographic features, at cryogenic temperatures, which has been reported in peptide assemblies.[34] Images show a distinct structural dependence in LBH mode, where the tilted structure (18˚) (Figure 6.1 1), with respect to the underlying substrate normal, shows a local barrier height contrast difference compared to the normally oriented (0˚) structure (Figure 6.2 2) and can be segmented by conventional image thresholding (Figure 6.3 S1). The ability to distinguish each structure by respective LBH permits segmentation and the relative determination of individual alkyl chain segment tilts and orientations within molecules. We controllably assembled our samples to form predominantly the 18˚ structure through high-temperature annealing, as determined by Kim *et al.* previously, but can still measure small areas of the 0˚ structure.[23]

Analyses within areas composed of the 18˚ structure are able to retrieve both molecular tilts, when compared with previous ensemble results, and one-dimensional (1D) hydrogen-bonding networks that is detailed in Figure 6.1 1. To determine tilts and solid angles, we measured all distances within a defined radial range and orientation to compute both lateral offsets, azimuthal orientations, and tilts, with respect to the surface normal. This information and the directional criteria used are presented in Table 6.1 S1, where the polar angles determined are, within error, consistent with previous results.[16,23] Little prior information has been available on azimuthal orientations. Applying a work function cut-off threshold to LBH images, to form an image binary, highlights the 1D orientations of hydrogen bonds, where the LBH data obtained contain contributions from both the buried Au-S and amide dipoles. Here, 1D variations may be attributed to local differences in amide bond orientation, which are predominantly in one direction. These buried domains span areas of tens to hundreds of nanometers, and cross structural domains and

disordered regions, as measured via STM topographic imaging (Figure 6.2 2). We compare analyses obtained by two-dimensional variational mode decomposition (2DVMD) to straightforward thresholded images (Figure 6.4 S2). Variational mode decomposition builds upon empirical mode decomposition, which is used to detect and to decompose images into principal modes, with non-recursive methods that are fully adaptive.[45,46] A mode, in this context, is based on an intrinsic mode function that meets two conditions: the number of extrema and the number of zero crossings differ at most by one, and the mean values of the local maxima and local minima envelopes are zero.[47] The thresholded image binary retains all principal modes, where 2DVMD succeeds in decomposing each mode into different crystalline directions and enables full image reconstruction. We show all principal modes (Figure 6.5 S3) obtained that are, again, verified by summing each mode into the reconstructed, original signal shown in Figure 6.2B 2B. The $< 111 >$ direction is emphasized, which distinguishes a buried region of disorder that is underrepresented, where the same area is strongly represented in the $< 11\bar{1} >$ direction. Thus, we are able to determine that hydrogen bonds cross the topographic domains featured in Figure 6.2A.

In the normally oriented phase, we used a block-matching approach to compare molecular apexes with dipolar extrema, where image patches (the size of one molecule) are correlated within larger LBH image patches (the size of nearest and next-nearest neighbors) to compute molecular orientations and the polar and azimuthal tilt angles of the *segments* of the molecular chains on each side of the amide functionality.[29,48,49] A randomly oriented lateral distance of 1.3 ± 0.4 Å was recorded that represents a near normal tilt (Figure 6.6 3), where nanoscale fluctuations can be understood by increased amide-amide interactions and an imperfect backbone structure formed after assembly.[18] We also measured all possible maxima offsets within a given radius and orientation (Table 6.2), where correlation yields the largest number of vector offsets. We have

successfully measured the local landscape of both the buried Au-S bonds and the buried hydrogen-bonding networks using STM coupled with spectroscopic imaging.

6.3 Conclusions and Prospects

Our measurements confirm long-range interactions between amide-containing SAM units, and provide a new avenue to monitor and to characterize buried functionality within a 2D matrix. Correlations and comparative analyses reveal both the hydrogen-bonding networks and the molecular orientations (tilts) of parts of each 1ATC9 molecule. As hydrogen bonding is critical in biomolecular and supramolecular assembly, we foresee widespread applicability of elucidating important structures and interactions with this method.[4,34,38]

Scanning tunneling microscopy is capable of resolving exquisite single-component chemical state information beyond ensemble structures.[13,29,50,51] Networks of buried hydrogen bonds have been resolved and span areas of tens to hundreds of square nanometers.

6.4 Materials and Methods

6.4.1 Monolayer Preparation

The chemicals 3-mercapto-*N*-nonylpropionamide and neat benzene (Sigma-Aldrich, St. Louis, MO) were used as received. The Au{111} on mica substrates (Agilent Technology, Tempe, AZ) were hydrogen-flame-annealed prior to SAM formation with 10 passes at a rate of 0.4 Hz. Substrates were immersed into 1 mM solutions in benzene and held at 70 ˚C for 24 hours. Each sample was removed from solution and cleaned by 3 cycles of rinsing with neat benzene and blown dry with nitrogen gas. The samples were immediately placed into the vacuum chamber, and placed in the cyrostat after sufficient vacuum was reached.

6.4.2 Imaging

All STM measurements were performed in ultrastable (10^{-12} torr, 4 K) conditions using a custom beetle-style scanning tunneling microscope and a platinum/iridium tip (80:20).[44] The known atomic spacing of Au{111} was used to calibrate all piezoelectric scanners. The sample was held at a fix bias (V_{sample} = -0.5 V) and both topographic and LBH modalities were measured in a constant current fashion (I_t = 15 pA) at 256 × 256 pixel resolution. The tunneling-gap distance was modulated at a frequency about the STM feedback loop bandwidth (~3 kHz) with a sinusoidal amplitude (dz ~ 0.1 Å) and dI/dz was recorded with a lock-in amplifier (Stanford Research Systems SR850 DSP, Sunnyvale, CA). Local barrier height micrographs were calibrated against a Au step edge, under the caveat that the LBH magnitude may vary in cases where the applied voltage may not always equal the voltage across the tunneling junction.[29,31]

6.4.3 Imaging Analyses

All STM images were initially processed with automated routines developed in MATLAB (Mathworks, Natick, MA) to remove any high-frequency noise and intensity spikes that may otherwise impair reliable segmentation.[28,29] We define local maxima in topographic [p] and LBH images [q] if its intensity was greater than that of all surrounding pixels within a molecular-sized window. For the normally oriented (0˚) phase, each set of local maxima was obtained for both simultaneously acquired images, and a topographic image patch centered at each maxima point was correlated at each pixel against a larger LBH image patch; the size of one molecule and nearest-neighbor spacing, respectively. The maximum correlation was chosen for each maxima point, which was then referenced and plotted.[29,48,49] Image thresholds and masks were obtained with known processes in MATLAB. For the tilted (18˚) phase, all maxima [p q] were connected

within a defined radial range and orientation, and then referenced and tabulated. Variational mode decomposition results were obtained with previously published MATLAB script.[45,46] Local barrier image histograms shown in Figure 6.3 were fit against two Gaussian curves, and the peak to peak energy distance was referenced.

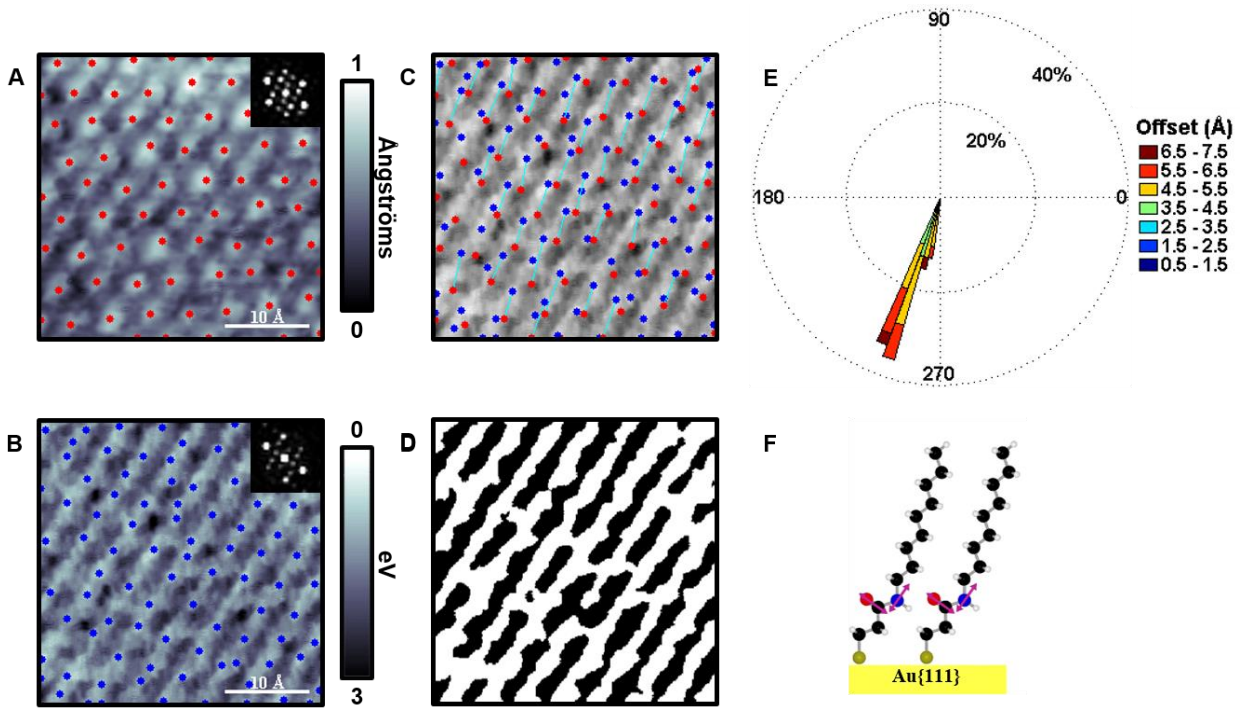

Figure 6.1 (A,B) Scanning tunneling microscope topographic image ($I_{tunneling}$ = 15 pA, V_{sample} = -0.5 V) and simultaneously acquired local barrier height (LBH) map over an area of the more tilted (18˚) structure of 3-mercapto-*N*-nonylpropionamide (1ATC9), with respect to the underlying Au{111} surface. The local maxima of both topography (red) and inverted LBH (blue) in B are computed. Insets depict fast Fourier transforms showing the expected topographic hexagonal nearest-neighbor spacing, which is also maintained within LBH images. (C) All maxima were connected within a defined radial range and orientation; best fit molecular orientations show the expected polar tilt angles. (D) Thresholded image binary of B, which highlights the 1D linear networks of hydrogen bonds. (E) Rose plot (depicting fitted maximum offsets) that are binned by both magnitude (0.5 Å bins) and orientation (4˚ bins). (F) A ball-and-stick model of 1ATC9 showing a polar chain tilt of 18˚ (for the molecular segment above the amide) and amide bonds nearly parallel to the substrate.

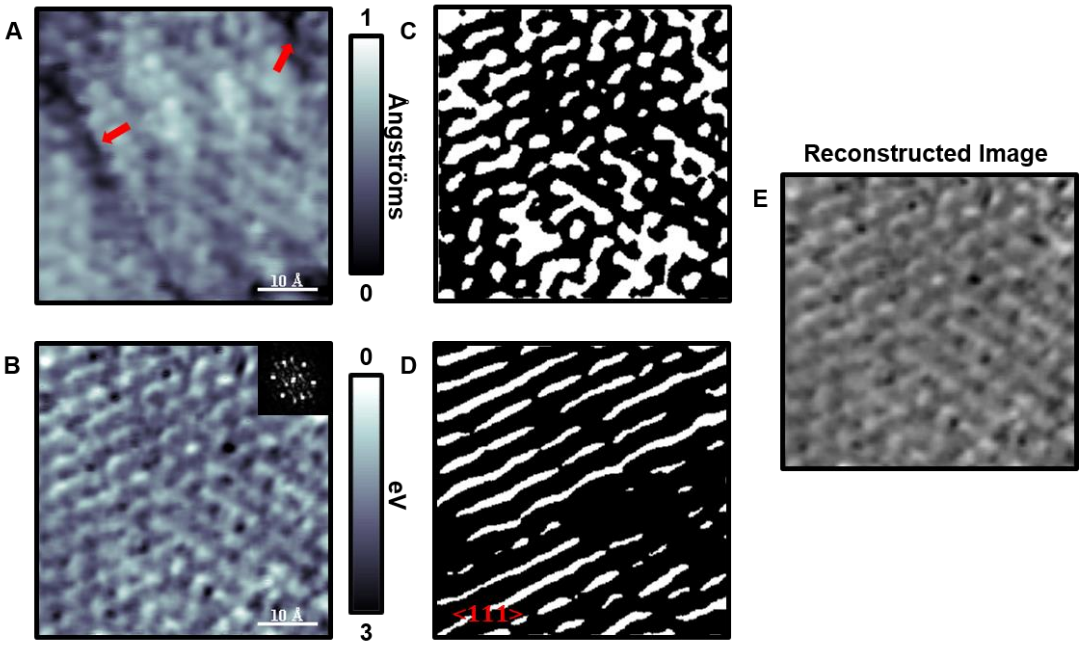

Figure 6.2 (A) Scanning tunneling micrograph ($I_{tunneling}$ = 15 pA, V_{sample} = -0.5 V) of three domains of a self-assembled monolayer of 3-mercapto-*N*-nonylpropionamide (1ATC9), where a lattice registry offset domain and an area of topographic disorder are highlighted by red arrows. (B) Simultaneously acquired local barrier height map of the same area measured in A. Inset depicts a fast Fourier transform of B, which is used for image decomposition. (C) Thresholded image binary of B. (D) Results obtained by two-dimensional variational mode decomposition of the <111> directional mode, where amide bonds cross each topographic domain highlighted in A, and a buried region of local disorder is depicted in the middle-right part of the image. (E) Reconstructed image of all deconstructed modes that tests the employed methodology (see Supplemental Figure 6.5 for all deconstructed modes).

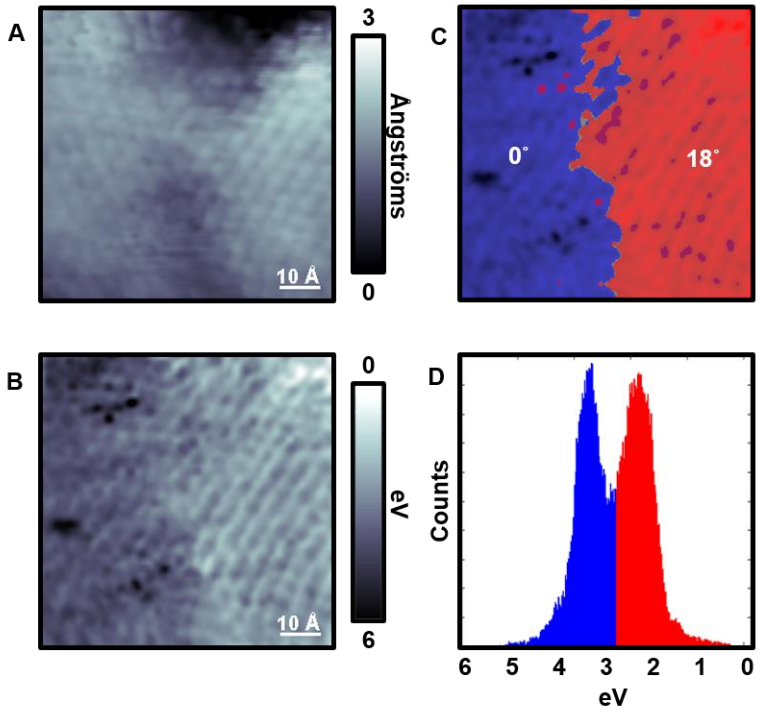

Figure 6.3 (A) Scanning tunneling micrograph of 3-mercapto-N-nonylpropionamide on Au{111} along a tilt domain ($I_{tunneling}$ = 15 pA, V_{sample} = -0.5 V). (B) Simultaneously acquired local barrier height (LBH) image of A. (C) We separate the upper (red) and lower (blue) domain boundary in LBH based on relative work function differences. (D) Image histogram of C showing the energy cut-off used that was also fitted with two Gaussian curves to solve for peak-to-peak image contrast differences.

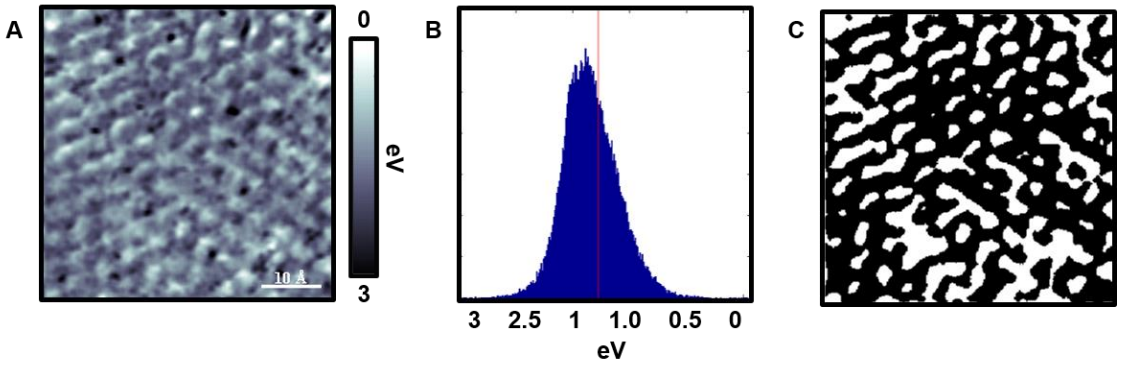

Figure 6.4 (A) Local barrier height image ($I_{tunneling}$ = 15 pA, V_{sample} = -0.5 V) of the results shown in Figure 4. (B) Image histogram showing the energy cut-off (red line) that was used to create an image binary. (C) Thresholded image binary of A.

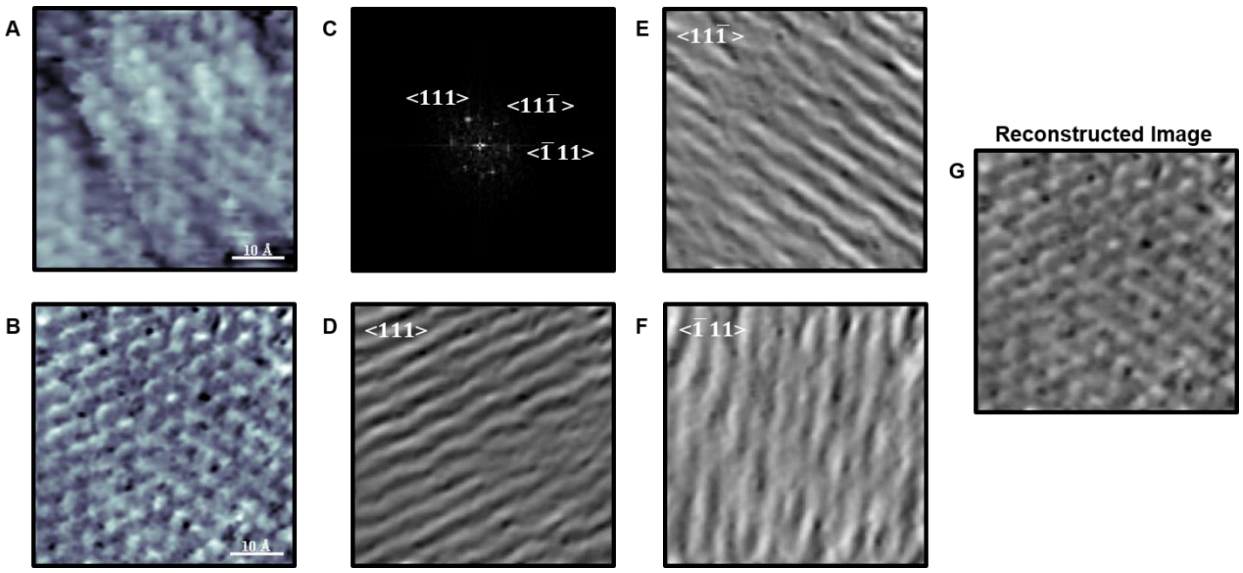

Figure 6.5 (A) Scanning tunneling micrograph ($I_{tunneling}$ = 15 pA, V_{sample} = -0.5 V) of a zoomed out area of the amide-containing self-assembled monolayer. (B) Simultaneously acquired local barrier height map of A. (C) Fast Fourier transform of B, where all of the directional image modes were chosen as initialization points. (D,E,F) Results obtained by two-dimensional variational mode decomposition all directional modes that were converged upon with a tolerance value of 10^{-6}. (G) Reconstructed image of all deconstructed modes that validates the employed methodology, where the image difference between B and G is near zero.

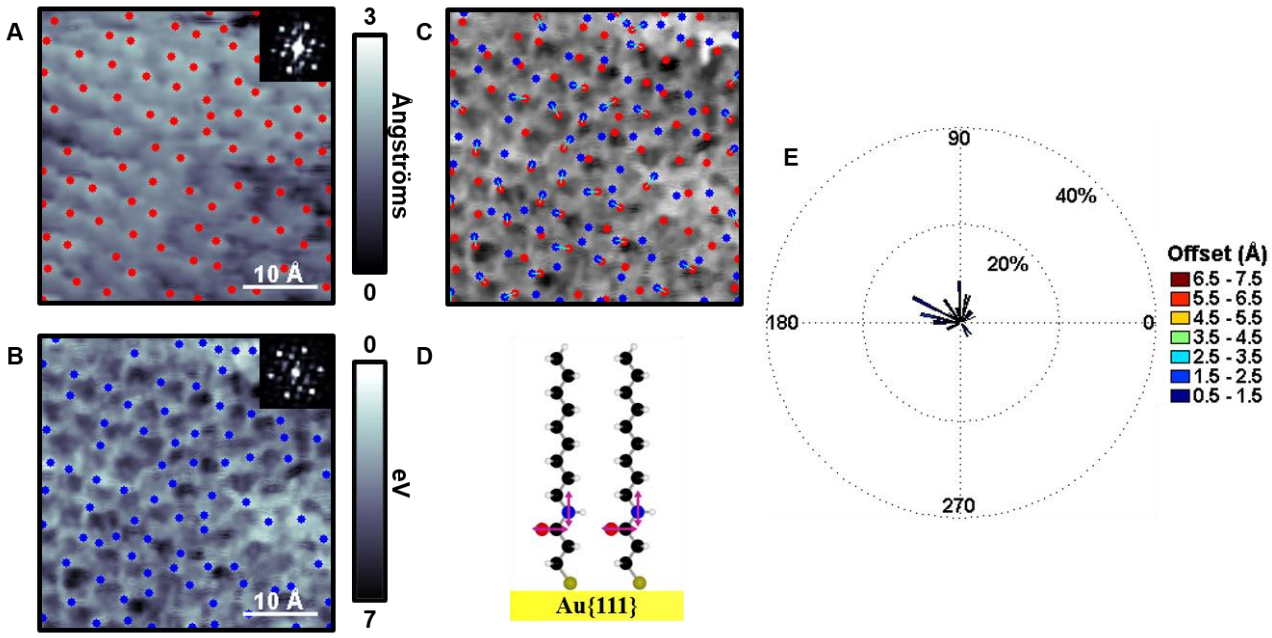

Figure 6.6 (A) Scanning tunneling microscope topographic image ($I_{tunneling}$ = 15 pA, V_{sample} = -0.5 V) and (B) simultaneously acquired local barrier height (LBH) map over the normally oriented (0˚) structure, with respect to the underlying Au{111} substrate, within monolayers of 3-mercapto-*N*-nonylpropionamide (1ATC9). Local maxima in both topography (red) in A and inverted LBH (blue) in B are computed. Insets depict fast Fourier transforms of both topography and LBH images. (C) Computed molecular orientations overlaid onto the LBH map. (D) A ball-and-stick model of 1ATC9 normally oriented on a Au substrate. (E) Rose plot of measured vector orientations binned by both magnitude (0.5 Å bins) and orientation (4˚ bins), which indicates that the molecules are oriented near normal.

Directions	δ(Å)	α(°)	θ(°)
a	4.4 ± 0.7	190 ± 5	15 ± 3
b	5.1 ± 0.7	252 ± 4	18 ± 3
c	5.9 ± 0.4	312 ± 5	20 ± 2
d	6.9 ± 0.7	1 ± 5	25 ± 3
e	6.7 ± 1.1	47 ± 4	24 ± 4
f	3.8 ± 0.6	120 ± 5	13 ± 2
g	8.5 ± 0.7	120 ± 4	30 ± 3
h	7.8 ± 0.8	149 ± 4	28 ± 3
i	8.8 ± 0.4	175 ± 2	32 ± 2
j	8.2 ± 1.0	212 ± 3	30 ± 4
k	9.3 ± 1.1	243 ± 2	34 ± 5
l	9.7 ± 0.9	272 ± 3	36 ± 4
m	9.4 ± 1.7	302 ± 3	35 ± 7
n	10.1 ± 0.6	330 ± 4	38 ± 2
o	7.9 ± 1.4	1 ± 3	29 ± 6
p	11.6 ± 0.8	28 ± 3	45 ± 4
q	11.1 ± 0.9	50 ± 3	42 ± 4
r	6.6 ± 1.0	89 ± 3	23 ± 4

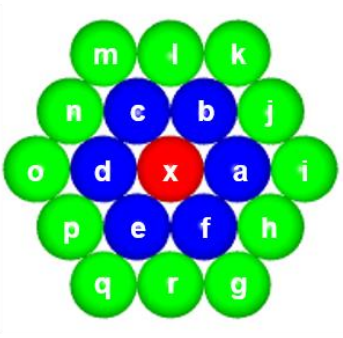

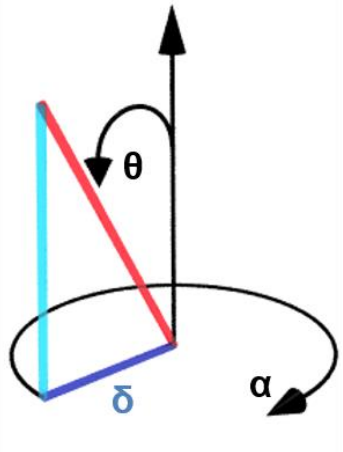

Table 6.1 Measured δ, α, and θ values for the image shown in Figure 6.1. The red box highlights the assigned molecular orientations. The directional coordinate system is shown, with nearest-neighbors in blue and next-nearest neighbors in green. Orientations are defined by three values, where δ is the surface projection of the shift between S head groups and methyl termini of a single 3-mercapto-*N*-nonylpropionamide molecule, α is the azimuthal angle with respect to the horizontal, fast-scan direction, and θ is the polar tilt.

Directions	δ(Å)	α(°)	θ(°)
a	4.8 ± 1.0	161 ± 5	16 ± 4
b	5.0 ± 1.0	230 ± 5	17 ± 4
c	5.8 ± 0.9	290 ± 6	20 ± 4
d	5.7 ± 0.8	338 ± 5	20 ± 3
e	5.3 ± 1.0	33 ± 5	19 ± 4
f	4.5± 0.6	92 ± 5	15 ± 3

Table 6.2 Measured δ, α, and θ values for the image shown in Figure 6.6 within the nearest-neighbor spacing.

6.5 References

1. Ulman, A. Formation and Structure of Self-Assembled Monolayers. *Chem. Rev.* **1996,** *96*, 1533–1554.

2. Love, J. C.; Estroff, L. A.; Kriebel, J. K.; Nuzzo, R. G.; Whitesides, G. M. Self-Assembled Monolayers of Thiolates on Metals as a Form of Nanotechnology. *Chem. Rev.* **2005,** *105*, 1103–1170.

3. Weiss, P. S. Functional Molecules and Assemblies in Controlled Environments: Formation and Measurements. *Acc. Chem. Res.* **2008,** *41*, 1772–1781.

4. Claridge, S. A.; Liao, W.-S.; Thomas, J. C.; Zhao, Y.; Cao, H. H.; Cheunkar, S.; Serino, A. C.; Andrews, A. M.; Weiss, P. S. From the Bottom Up: Dimensional Control and Characterization in Molecular Monolayers. *Chem. Soc. Rev.* **2013,** *42*, 2725–2745.

5. Vericat, C.; Vela, M. E.; Benitez, G.; Carro, P.; Salvarezza, R. C. Self-Assembled Monolayers of Thiols and Dithiols on Gold: New Challenges for a Well-Known System. *Chem. Soc. Rev.* **2010,** *39*, 1805–1834.

6. Kim, J.; Rim, Y. S.; Liu, Y.; Serino, A. C.; Thomas, J. C.; Chen, H.; Yang, Y.; Weiss, P. S. Interface Control in Organic Electronics Using Mixed Monolayers of Carboranethiol Isomers. *Nano Lett.* **2014,** *14*, 2946–2951.

7. Kim, J.; Rim, Y. S.; Chen, H.; Cao, H. H.; Nakatsuka, N.; Hinton, H. L.; Zhao, C.; Andrews, A. M.; Yang, Y.; Weiss, P. S. Fabrication of High-Performance Ultrathin In_2O_3 Film Field-Effect Transistors and Biosensors Using Chemical Lift-Off Lithography. *ACS Nano* **2015,** *9*, 4572–4582.

8. Berndt, R.; Gaisch, R.; Gimzewski, J. K.; Reihl, B.; Schlittler, R. R.; Schneider, W. D.; Tschudy, M. Photon Emission at Molecular Resolution Induced by a Scanning Tunneling Microscope. *Science* **1993,** *262*, 1425–1427.

9. Stranick, S. J.; Weiss, P. S. Alternating Current Scanning Tunneling Microscopy and Nonlinear Spectroscopy. *J. Phys. Chem.* **1994,** *98*, 1762–1764.

10. McCarty, G. S.; Weiss, P. S. Scanning Probe Studies of Single Nanostructures. *Chem. Rev.* **1999,** *99*, 1983–1990.

11. Donhauser, Z. J.; Mantooth, B. A.; Kelly, K. F.; Bumm, L. A.; Monnell, J. D.; Stapleton, J. J.; Price Jr., D. W.; Rawlett, A. M.; Allara, D. L.; Tour, J. M.; Weiss, P. S. Conductance Switching in Single Molecules through Conformational Changes. *Science* **2001,** *292*, 2303–2307.

12. Wu, S. W.; Ogawa, N.; Ho, W. Atomic-Scale Coupling of Photons to Single-Molecule Junctions. *Science* **2006,** *312*, 1362–1365.

13. Claridge, S. A.; Schwartz, J. J.; Weiss, P. S. Electrons, Photons, and Force: Quantitative Single-Molecule Measurements from Physics to Biology. *ACS Nano* **2011,** *5*, 693–729.

14. Kim, M.; Hohman, J. N.; Cao, Y.; Houk, K. N.; Ma, H.; Jen, A. K.-Y.; Weiss, P. S. Creating Favorable Geometries for Directing Organic Photoreactions in Alkanethiolate Monolayers. *Science* **2011,** *331*, 1312–1315.

15. Bonnell, D. A.; Basov, D. N.; Bode, M.; Diebold, U.; Kalinin, S. V.; Madhavan, V.; Novotny, L.; Salmeron, M.; Schwarz, U. D.; Weiss, P. S. Imaging Physical Phenomena with Local Probes: From Electrons to Photons. *Rev. Mod. Phys.* **2012,** *84*, 1343–1381.

16. Tam-Chang, S.-W.; Biebuyck, H. A.; Whitesides, G. M.; Jeon, N.; Nuzzo, R. G. Self-Assembled Monolayers on Gold Generated from Alkanethiols with the Structure $RNHCOCH_2SH$. *Langmuir* **1995,** *11*, 4371–4382.

17. Clegg, R. S.; Reed, S. M.; Hutchison, J. E. Self-Assembled Monolayers Stabilized by Three-Dimensional Networks of Hydrogen Bonds. *J. Am. Chem. Soc.* **1998,** *120*, 2486–2487.

18. Clegg, R. S.; Hutchison, J. E. Control of Monolayer Assembly Structure by Hydrogen Bonding Rather Than by Adsorbate-Substrate Templating. *J. Am. Chem. Soc.* **1999,** *121*, 5319–5327.

19. Lewis, P. A.; Smith, R. K.; Kelly, K. F.; Bumm, L. A.; Reed, S. M.; Clegg, R. S.; Gunderson, J. D.; Hutchison, J. E.; Weiss, P. S. The Role of Hydrogen Bonds in Self-Assembled Mixed Composition Thiols on Au{111}. *J. Phys. Chem. B* **2001,** *105*, 10630–10636.

20. Smith, R. K.; Reed, S. M.; Lewis, P. A.; Monnell, J. D.; Clegg, R. S.; Kelly, K. F.; Bumm, L. A.; Hutchison, J. E.; Weiss, P. S. Phase Separation within a Binary Self-Assembled Monolayer on Au{111} Driven by an Amide-Containing Alkanethiol. *J. Phys. Chem. B* **2001,** *105*, 1119–1122.

21. Lewis, P. A.; Inman, C. E.; Yao, Y.; Tour, J. M.; Hutchison, J. E.; Weiss, P. S. Mediating Stochastic Switching of Single Molecules Using Chemical Functionality. *J. Am Chem. Soc.* **2004,** *126*, 12214–12215.

22. Lewis, P. A.; Inman, C. E.; Maya, F.; Tour, J. M.; Hutchison, J. E.; Weiss, P. S. Molecular Engineering of the Polarity and Interactions of Molecular Electronic Switches. *J. Am. Chem. Soc.* **2005,** *127*, 17421–17426.

23. Kim, M.; Hohman, J. N.; Serino, A. C.; Weiss, P. S. Structural Manipulation of Hydrogen-Bonding Networks in Amide-Containing Alkanethiolate Monolayers via Electrochemical Processing. *J. Phys. Chem. C* **2010,** *114*, 19744–19751.

24. Stipe, B. C.; Rezaei, M. A.; Ho, W. Single-Molecule Vibrational Spectroscopy and Microscopy. *Science* **1998,** *280*, 1732–1735.

25. Lee, H. J.; Ho, W. Structural Determination by Single-Molecule Vibrational Spectroscopy and Microscopy: Contrast between Copper and Iron Carbonyls. *Phys. Rev. B* **2000**, *61*, R16347–R16350.

26. Khuong, T.-A. V.; Nuñez, J. E.; Godinez, C. E.; Garcia-Garibay, M. A. Crystalline Molecular Machines: A Quest Toward Solid-State Dynamics and Function. *Acc. Chem. Res.* **2006,** *39*, 413–422.

27. Michl, J.; Sykes, E. C. H. Molecular Rotors and Motors: Recent Advances and Future Challenges. *ACS Nano* **2009,** *3*, 1042–1048.

28. Han, P.; Kurland, A. R.; Giordano, A. N.; Nanayakkara, S. U.; Blake, M. M.; Pochas, C. M.; Weiss, P. S. Heads and Tails: Simultaneous Exposed and Buried Interface Imaging of Monolayers. *ACS Nano* **2009,** *3*, 3115–3121.

29. Thomas, J. C.; Schwartz, J. J.; Hohman, J. N.; Claridge, S. A.; Auluck, H. S.; Serino, A. C.; Spokoyny, A. M.; Tran, G.; Kelly, K. F.; Mirkin, C. A.; Gilles, J.; Osher, S. J.; Weiss, P. S. Defect-Tolerant Aligned Dipoles within Two-Dimensional Plastic Lattices. *ACS Nano* **2015,** *9*, 4734–4742.

30. Han, P.; Akagi, K.; Canova, F. F.; Mutoh, H.; Shiraki, S.; Iwaya, K.; Weiss, P. S.; Asao, N.; Hitosugi, T. Bottom-Up Graphene-Nanoribbon Fabrication Reveals Chiral Edges and Enantioselectivity. *ACS Nano* **2014,** *8*, 9181–9187.

31. Zhang, J.; Chen, P.; Yuan, B.; Ji, W.; Cheng, Z.; Qiu, X. Real-Space Identification of Intermolecular Bonding with Atomic Force Microscopy. *Science* **2013,** *342*, 611–614.

32. Lang, N. D. Apparent Height in Scanning Tunneling Microscopy. *Phys. Rev. B* **1988**, *37*, 10395–10398.

33. Monnell, J. D.; Stapleton, J. J.; Dirk, S. M.; Reinerth, W. A.; Tour, J. M.; Allara, D. L.; Weiss, P. S. Relative Conductances of Alkaneselenolate and Alkanethiolate Monolayers on Au{111}. *J. Phys. Chem. B* **2005**, *109*, 20343–20349.

34. Claridge, S. A.; Thomas, J. C.; Silverman, M. A.; Schwartz, J. J.; Yang, Y.; Wang, C.; Weiss, P. S. Differentiating Amino Acid Residues and Side Chain Orientations in Peptides Using Scanning Tunneling Microscopy. *J. Am. Chem. Soc.* **2013,** *135*, 18528–18535.

35. Glowacki, E. D.; Irimia-Vladu, M.; Bauer, S.; Sariciftci, N. S. Hydrogen-Bonds in Molecular Solids-From Biological Systems to Organic Electronics. *J. Mater. Chem. B* **2013,** *1*, 3742–3753.

36. Harder, M.; Kuhn, B.; Diederich, F. Efficient Stacking on Protein Amide Fragments. *Chem. Med. Chem.* **2013,** *8*, 397–404.

37. Fischer, F. R.; Wood, P. A.; Allen, F. H.; Diederich, F. Orthogonal Dipolar Interactions between Amide Carbonyl Groups. *Proc. Nat. Acad. Sci.* **2008,** *105*, 17290–17294.

38. Etter, M. C. Encoding and Decoding Hydrogen-Bond Patterns of Organic Compounds. *Acc. Chem. Res.* **1990,** *23*, 120–126.

39. Steiner, T.. The Hydrogen Bond in the Solid State. *Angew. Chem. Int. Ed.* **2002,** *41*, 48–76.

40. Liao, W.-S.; Cheunkar, S.; Cao, H. H.; Bednar, H. R.; Weiss, P. S.; Andrews, A. A. Subtractive Patterning via Chemical Lift-Off Lithography. *Science* **2012,** *337*, 1517–1521.

41. Meighan, R. M.; Cole, R. H. Dielectric Properties of Alkyl Amides. I. Vapor Phase Dipole Moments and Polarization in Benzene Solution. *J. Phys. Chem.* **1964**, *68*, 503–508.

42. Sellers, H.; Ulman, A.; Shnidman, Y.; Eilers, J. E. Structure and Binding of Alkanethiolates on Gold and Silver Surfaces: Implications for Self-Assembled Monolayers. *J. Am. Chem. Soc.* **1993**, *115*, 9389–9401.

43. Hohman, J. N.; Kim, M.; Wadsworth, G. A.; Bednar, H. R.; Jiang, J.; LeThai, M. A.; Weiss, P. S. Directing Substrate Morphology via Self-Assembly: Ligand-Mediated Scission of Gallium-Indium Microspheres to the Nanoscale. *Nano Lett.* **2011,** *11*, 5104–5110.

44. Ferris, J. H.; Kushmerick, J. G.; Johnson, J. A.; Yoshikawa Youngquist, M. G.; Kessinger, R. B.; Kingsbury, H. F.; Weiss, P. S. Design, Operation, and Housing of an Ultrastable, Low Temperature, Ultrahigh Vacuum Scanning Tunneling Microscope. *Rev. Sci. Instrum.* **1998,** *69*, 2691–2695.

45. Dragomiretskiy, K.; Zosso, D. Variational Mode Decomposition. *IEEE Trans. Sig. Process.* **2014**, *62*, 531–544.

46. Tai, X.-C.; Bae, E.; Chan, T. F.; Lysaker, M. *Energy Minimization Methods in Computer Vision and Pattern Recognition. Lecture Notes in Computer Science*; Springer International Publishing: Hong Kong, China, 2015, 197–208.

47. Huang, N. E.; Shen, Z.; Long, S. R.; Wu, M. C.; Shih, H. H.; Zheng, Q.; Yen, N.-C.; Tung, C. C.; Liu, H. H. The Empirical Mode Decomposition and the Hilbert Spectrum for Nonlinear and Non-Stationary Time Series Analysis. *Proc. R. Soc. Lond. A* **1998,** *454*, 903–995.

48. Jian, J.; Jian, A. Displacement Measurement and Its Application in Interframe Image Coding. *IEEE Trans. Commun.* **1981,** *29*, 1799–1808.

49. Love, N. S.; Kamath, C. An Empirical Study of Block Matching Techniques for the Detection of Moving Objects. *Proc. SPIE* **2006,** 1–36.

50. Poirier, G. E. Characterization of Organosulfur Molecular Monolayers on Au{111} using Scanning Tunneling Microscopy. *Chem. Rev.* **1997,** *97*, 1117–1128.

51. Han, P.; Mantooth, B. A.; Sykes, E. C. H.; Donhauser, Z. J.; Weiss, P. S. Benzene on Au{111} at 4 K: Monolayer Growth and Tip-Induced Molecular Cascades. *J. Am. Chem. Soc.* **2004,** *126*, 10787–10793.

CHAPTER 7

Summary and Outlook

7.1 Aligned Dipoles

Scanning tunneling microscopy probes surface topography with extraordinary precision, however, was previously unable to determine the orientations of azimuthally symmetric single molecules within a host matrix.[1,2] This advance not only enables the determination of molecular tilt, but we probe the dipolar environment simultaneously to track atomic locations within large-scale SAM systems and thus determine molecular orientation, precisely, without averaging. Though the STM tip proved insignificant in redirecting orientations, within the measurement parameters described earlier, it may be possible to operate under different bias voltages and tunneling current parameters to orient molecules in 2D matrices. Further synthetic approaches and functionalization of the molecular cages (*e.g.*, carborane), with functionality that strengthens intermolecular interactions, may enable control of the placement and orientations of single molecules. Carboranethiols have already shown promise in effective metal work function modification,[3] and may be useful in applications toward directing grain boundaries, defect locations, and subsequent strain in two-dimensional systems.

7.2 Functionalized Derivatives of *p*-Carborane

As noted in Chapter 2, extending the zoology of synthetic cage molecule targets is fundamental to creating systems with tunable functionality. In this regard, the chemical modification of *p*-carboranethiol with a *p*-mercatobenzoic acid moiety is a novel stepping stone. Pockets of molecules within a host *p*-carboranethiol framework show that hydrogen-bonding intermolecular interactions between carboxyl groups help dictate initial assembly, and that pristine monolayer formations, on noble metal surfaces, are possible. Thiol groups dominate the assembly process, where the exposed carboxyl group rotates freely, under reduced dimensionality, after surface

adsorption. Carborane chemistry continues to expand with new synthetic targets and novel applications.[4] Cage-molecule-functionalized SAMs will be useful for a large variety of materials, where, controlling the nearest-neighbor spacing between adsorbates, as a function of molecular backbone, may help control strain at the substrate-SAM interface with functionality that has diverse chemical reactivity.

7.3 Control of Valency within Carboranedithiol Assemblies

In the scope of continuing to explore molecular building blocks, SAM formations composed of surfactants with the same backbone structure, dual functionality, and oppositely oriented dipole moments enables tunable surface-SAM interactions.[5] Monolayers composed of 1O2 and 9O12 contain the same nearest neighbor spacing with opposite carbon positional functionality. Since it was previously shown by Baše *et al.* that both isomers are stable in their relative dithiol and dianion states, the use of acid-base chemistry, prior to chemical deposition, enables binding control. Here, we are able to dictate the fraction of sulfur bound to Au due to increased or decreased valency in equally spaced systems. Deposition of the dithiol, 9O12, forms monolayers that are predominately singly bound (with one free thiol) and deposition of the either the 9O12 or 1O2 dianion results in monolayer formations that are mostly doubly bound. Building off the work described in chapter 4, both isomers may be used as parental precursors in further chemical design. Creating a library of different synthetic targets with the carboranedithiol switchable moeity may enable single-molecule levers with controllable interfacial properties.

7.4 Holey Graphene as a Mask against Chemical Deposition

Graphene that is made porous enables a new pathway for molecular patterning with precise pitch and size. From its inception and discovery,[6] graphene continues to hold promise as a powerful component in two-dimensional materials and scalable electronics.[7] Here, we make use of porous graphene as a means to protect a noble metal against chemical deposition, which enables an exciting pathway to explore graphene in the context of controllable patterning schemes. Graphene, first made porous, was transferred onto a Au substrate, where the lattice spacing of graphene was confirmed by STM. The same sample is exposed to a molecular vapor, which deposited into the exposed pores and not the graphene overlayer. Scanning tunneling topographs measured the expected lattice of graphene in all steps, but also showed an inversion in apparent height from empty to molecular-containing pores. Masks were then regenerated by thermal annealing and subsequent steps were successfully performed. Our experiments confirmed the blocking effect of graphene, and point to future experiments geared towards depositing a large library of different functional surfactants, controlling the size and pitch of graphene pores, and ultimately performing scalable patterning in electronic systems.

7.5 Buried Hydrogen-Bonding Networks

In Chapter 6, we further extend the capabilities of simultaneous topographic and dipolar landscape measurements in STM. While monitoring molecular orientations and tilts have been performed in simple *n*-alkanethiol and carboranethiol systems, the extent of local imaging capability in systems with dual functionality at the buried interface has, until now, been undiscovered. Here, we used STM in LBH mode to measure both the Au-S interface and the buried amide bond dipolar landscape. Monolayers composed of 1ATC9 proved an ideal test bed, since it

is a well-studied system with amide functionality.[8-14] Local barrier-height measurements showed a distinct tilt-phase dependence, which enabled image segmentation based on the local tunneling work function. In areas with greater amide bond contributions to the tunneling current, we imaged two-dimensional networks of bonds that followed the <111> direction of the SAM matrix. Amide bonds were shown to cross conventional substrate-attachment offset domains and areas of local disorder. Motivated the capability to monitor amide bonds within buried networks, it becomes possible to measure bonding within model peptides[15] and ultimately even larger scale proteins. We anticipate that multi-modal STM will have a large impact in the field of single molecule biology, structural biology, and protein functionality.

7.6 References

1. Han, P.; Kurland, A. R.; Giordano, A. N.; Nanayakkara, S. U.; Blake, M. M.; Pochas, C. M.; Weiss, P. S. Heads and Tails: Simultaneous Exposed and Buried Interface Imaging of Monolayers. *ACS Nano* **2009**, *3*, 3115–3121.

2. Thomas, J. C.; Schwartz, J. J.; Hohman, J. N.; Claridge, S. A.; Auluck, H. S.; Serino, A. C.; Spokoyny, A. M.; Tran, G.; Kelly, K. F.; Mirkin, C. A.; Gilles, J.; Osher, S. J.; Weiss, P. S. Defect-Tolerant Aligned Dipoles within Two-Dimensional Plastic Lattices. *ACS Nano* **2015**, *9*, 4734–4742.

3. Kim, J.; Rim, Y. S.; Liu, Y.; Serino, A. C.; Thomas, J. C.; Chen, H.; Yang, Y.; Weiss, P. S. Interface Control in Organic Electronics Using Mixed Monolayers of Carboranethiol Isomers. *Nano Lett.* **2014**, *14*, 2946-2951.

4. Grimes, R. N. Carboranes in the Chemist's Toolbox. *Dalton Trans.* **2015**, *44*, 5939–5956.

5. Baše, T.; Bastl, Z.; Plzák, Z.; Grygar, T.; Plešek, J.; Carr, M.; Malina, V.; Šubrt, J.; Boháček, J.; Večerníková, E.; Kříž, O. Carboranethiol-Modified Gold Surfaces. A Study and Comparison of Modified Cluster and Flat Surfaces. *Langmuir* **2005**, *21*, 7776–7785.

6. Novoselov, K. S.; Geim, A. K.; Morozov, S. V.; Jiang, D.; Zhang, Y.; Dubonos, S. V.; Grigorieva, I. V.; Firsov, A. A. Electric Field Effect in Atomically Thin Carbon Films. *Science* **2004**, *306*, 666–669.

7. Müllen, K. Evolution of Graphene Molecules: Structural and Functional Complexity as Driving Forces behind Nanoscience. *ACS Nano* **2014**, *8*, 6531–6541.

8. Clegg, R. S.; Reed, S. M.; Hutchison, J. E. Self-Assembled Monolayers Stabilized by Three-Dimensional Networks of Hydrogen Bonds. *J. Am. Chem. Soc.* **1998**, *120*, 2486–2487.

9. Clegg, R. S.; Hutchison, J. E. Control of Monolayer Assembly Structure by Hydrogen Bonding Rather Than by Adsorbate-Substrate Templating. *J. Am. Chem. Soc.* **1999**, *121*, 5319–5327.

10. Lewis, P. A.; Smith, R. K.; Kelly, K. F.; Bumm, L. A.; Reed, S. M.; Clegg, R. S.; Gunderson, J. D.; Hutchison, J. E.; Weiss, P. S. The Role of Hydrogen Bonds in Self-Assembled Mixed Composition Thiols on Au{111}. *J. Phys. Chem. B* **2001**, *105*, 10630–10636.

11. Smith, R. K.; Reed, S. M.; Lewis, P. A.; Monnell, J. D.; Clegg, R. S.; Kelly, K. F.; Bumm, L. A.; Hutchison, J. E.; Weiss, P. S. Phase Separation within a Binary Self-Assembled Monolayer on Au{111} Driven by an Amide-Containing Alkanethiol. *J. Phys. Chem. B* **2001**, *105*, 1119–1122.

12. Lewis, P. A.; Inman, C. E.; Yao, Y.; Tour, J. M.; Hutchison, J. E.; Weiss, P. S. Mediating Stochastic Switching of Single Molecules Using Chemical Functionality. *J. Am Chem. Soc.* **2004**, *126*, 12214–12215.

13. Lewis, P. A.; Inman, C. E.; Maya, F.; Tour, J. M.; Hutchison, J. E.; Weiss, P. S. Molecular Engineering of the Polarity and Interactions of Molecular Electronic Switches. *J. Am. Chem. Soc.* **2005**, *127*, 17421–17426.

14. Kim, M.; Hohman, J. N.; Serino, A. C.; Weiss, P. S. Structural Manipulation of Hydrogen-Bonding Networks in Amide-Containing Alkanethiolate Monolayers via Electrochemical Processing. *J. Phys. Chem. C* **2010**, *114*, 19744–19751.

15. Claridge, S. A.; Thomas, J. C.; Silverman, M. A.; Schwartz, J. J.; Yang, Y.; Wang, C.; Weiss, P. S. Differentiating Amino Acid Residues and Side Chain Orientations in Peptides Using Scanning Tunneling Microscopy. *J. Am. Chem. Soc.* **2013**, *135*, 18528–18535.

Appendix A

A.1 Chapter 2 MATLAB Code and Computation

MATLAB Script

```
%=========================================================================
%========================== Skew the image==========================
pskewy = c1.
pskewx = c2;
tform = maketform('affine',[1 pskewy 0;pskewx 1 0; 0 0 1]);
JTopo = imtransform(Topo,tform);
Jlbh = imtransform(lbh,tform);

%=========================================================================%=
========================= Correlation approach ======================
%% At each local max p of Topo, consider the searching
% window centered at p, radius ws. Calculate the correlation between a patch
% centered at p and another patch centered at a point inside that searching
% window. Find the best match.
% correlation matrix
u = corr_matrix(JTopo,Jlbh_crop,maxc_Topo,maxr_Topo,params.ws,params.ps);
[value,indx] = max(u); % indx is in [1, (2*ws+1)^2]
[corr_row corr_col] = ind2sub([2*params.ws+1 2*params.ws+1],indx);% position in the window
search
im_row = maxr_Topo + corr_row - (params.ws+1)*ones(size(maxr_Topo)); % row-index in the
actual image
im_col = maxc_Topo + corr_col - (params.ws+1)*ones(size(maxr_Topo)); % col-index in the
actual image
% draw vectors
X2 = [maxc_lbh; maxr_lbh];
h = figure('name','Correlation Approach');
imshow(lbh_crop,[]); hold on
caxis(autorange(lbh_crop));
plot(maxc_Topo,maxr_Topo,'.r','MarkerSize',14); %,'MarkerSize',18
plot(maxc_lbh,maxr_lbh,'.g','MarkerSize',14); %,'MarkerSize',18
l = 0;% store number of vectors
for i=1:length(maxc_Topo)
 p = [maxc_Topo(i); maxr_Topo(i)]; % local Max in Topo
 qref = [im_col(i); im_row(i)]; % the max correlation corresponds to p
 X1q = repmat(qref,1,length(maxc_lbh));
 X1p = repmat(p,1,length(maxc_lbh));
 tmq = X1q - X2;
 tmp = X1p - X2;
 ntmq = sqrt(sum(tmq.*tmq));
 ntmp = sqrt(sum(tmp.*tmp));
 col = find((ntmq<params.qrad) & (ntmp<params.prad));% col = the positions of q - in the local
Maxima set of im2
```

```
 Q(1:2,l+1:l+length(col)) = X2(1:2,col);% Store all q
 P(1:2,l+1:l+length(col)) = X1p(1:2,col);% Store all p
 for i = 1:length(col) % draw lines connecting p and q
  x = [p(1) Q(1,l+i)];
  y = [p(2) Q(2,l+i)];
  plot(x,y,'c','linewidth',1.2);
 end
 l = l+length(col);
end
legend('Topography','LBH');
hold off

% Compute the correlation between the patch centered at p,
% size (2*ps+1)x(2*ps+1) from image I1 and the same size patch centered at q
% from image I2, where q is on the searching window of size       % (2*ws+1)x(2*ws+1), centered
at p.
%  * * * * * * *  searching window of size (2*ws+1) x (2*ws+1)
%  * * * * * * *
%  * q * * * * *
%  * * * p * * *
%  * * * * * * *
%  * * * * * * *
%  * * * * * * *
%
%  * * *     * * *
%  * q *  vs   * p *    patches of size (2*ps+1) x (2*ps+1)
%  * * *     * * *
function u = corr_matrix(I1,I2,maxc1,maxr1,ws,ps)
I1ext = padarray(I1,[ws+ps ws+ps],'symmetric','both');
I2ext = padarray(I2,[ws+ps ws+ps],'symmetric','both');
[rows,cols] = size(I1ext);
maxc1ext = maxc1 + ws + ps;
maxr1ext = maxr1 + ws + ps;

%% correlation between vectors x and y
corr_vec = @(x,y,l) sum((x-mean(x)).*(y-mean(y)))/((l-1)*std(x)*std(y));
N = length(maxc1); % number of local maxima in topo
u = zeros((2*ws+1)^2,N) - 10;
for k = 1:N
    cc = maxc1(k);
    rr = maxr1(k);
    t1 = [maxr1ext(k) maxc1ext(k)];
    tmp1 = I1ext(t1(1)-ps:t1(1)+ps,t1(2)-ps:t1(2)+ps);
    patch1 = tmp1(:);
    count =0;
    for col = -ws:ws
```

```
      for row = -ws:ws
        count = count+1;
        if ((rr + row <1)|(rr+row>size(I1,1)))
          u(count,k) = -10;
        else
          if ((cc + col<1)|(cc+col>size(I1,2)))
           u(count,k) = -10;
          else
        t2 = t1 + [row col];
        tmp2 = I2ext(t2(1)-ps:t2(1)+ps, t2(2)-ps:t2(2)+ps);
        patch2 = tmp2(:);
        u(count,k) = corr_vec(patch1,patch2,(2*ps+1).^2);
          end
        end
      end
    end
end
return
figure;
subplot(221);
imshow(I1,[]);
hold on; plot(maxc1,maxr1,'.r');
subplot(222);
imshow(I1ext,[]);
hold on; plot(maxc1ext,maxr1ext,'.r');
subplot(223);
imshow(I2,[]);
hold on; plot(maxc2,maxr2,'.b');
subplot(224);
imshow(I2ext,[]);
hold on; plot(maxc2ext,maxr2ext,'.b');
```

Table A.1: Dipole moments and vectors for the *o*-9-carboranethiol (**O9**) isomer calculated with a density functional approach in the B3LYP/6-311G** with Gaussian 09 software packages. Dipoles are defined as oriented toward positive charge.

O9 Dipole Moment and Component Vectors

	Absolute Energy (Hartrees)	Dipole Moment (Debye)	X	Y	Z
DFT	-730.404	5.72	2.96	-0.48	4.87

Cartesian coordinates for the **O9** isomer were optimized at the B3LYP/6-311G** level of theory. Sulfur and hydrogen atoms are numbered according by which carbon or boron atom they are bounded.

Table A.2: Cartesian coordinates for the **O9** isomer

	DFT		
	X	Y	Z
1 C	-0.000659	0.000297	-2.16244
2 C	-1.353825	-0.221407	-1.282775
3 B	-0.216204	-1.511897	-1.376342
4 B	1.353565	-0.684698	-1.400102
5 B	1.064462	1.08053	-1.399972
6 B	-0.687009	1.364614	-1.375585
7 B	-1.329387	0.69106	0.142555
8 B	-1.039885	-1.078869	0.14204
9 B	0.028098	0.004338	1.073718
10 B	0.714609	-1.362286	0.110007
11 B	1.509242	0.246657	0.109921
12 B	0.243152	1.517925	0.10993
S 9	0.089048	0.013953	2.94971
H 1	-0.118598	-0.01888	-3.23529
H 2	-2.26603	-0.370737	-1.840758
H 3	-0.497442	-2.442762	-2.039379
H 4	2.206817	-1.132547	-2.079257
H 5	1.730371	1.777277	-2.07889
H 6	-1.250297	2.157666	-2.038133

H 7	-2.351218	1.1123	0.553459
H 8	-1.874304	-1.80373	0.552829
H 10	1.189846	-2.314894	0.61887
H 11	2.566441	0.420043	0.60808
H 12	0.39045	2.572334	0.618727
H S	-1.227123	-0.189527	3.154824

A.2 Chapter 6 MATLAB Code

MATLAB Script

```
close all; clear all; clc;

im = topo;
im2 = lbh;

[maxc_topo,maxr_topo] = localMax(im,params.wmax_topo);
[maxc_lbh,maxr_lbh] = localMax(im2,params.wmax_lbh);

maxc1 = maxc_topo;
maxr1 = maxr_topo;
maxc2 = maxc_lbh;
maxr2 = maxr_lbh;

X2 = [maxc2; maxr2];
l = 0;
for i=1:length(maxc1)
    p = [maxc1(i); maxr1(i)];
    X1 = repmat(p,1,length(maxc2));
    tmp = X1 - X2;
    ntmp = sqrt(sum(tmp.*tmp));
    col = find(ntmp<radupper & ntmp>radlower);
    V(1:2,l+1:l+length(col)) = tmp(1:2,col)./repmat(ntmp(col),2,1);
    Q(1:2,l+1:l+length(col)) = X2(1:2,col);
    P(1:2,l+1:l+length(col)) = X1(1:2,col);
    tmpAn(1:2,l+1:l+length(col)) = (Q(1:2,l+1:l+length(col)))-
            (P(1:2,l+1:l+length(col)));
    vectorSet(1,l+1:l+length(col)) = tmpAn(1,l+1:l+length(col));
    vectorSet(2,l+1:l+length(col)) = tmpAn(2,l+1:l+length(col));
    vectorSet(3,l+1:l+length(col)) = norm(tmpAn);
    vectorSet(4,l+1:l+length(col)) = P(1,l+1:l+length(col));
    vectorSet(5,l+1:l+length(col)) = P(2,l+1:l+length(col));
    vectorSet(6,l+1:l+length(col)) = Q(1,l+1:l+length(col));
    vectorSet(7,l+1:l+length(col)) = Q(2,l+1:l+length(col));
    vectorSet(8,l+1:l+length(col)) =
            atan2(vectorSet(2,l+1:l+length(col)),vectorSet(1,l+1:l+length(col
            )))*-180/3.14;
    l = l+length(col);
end

%% normalize angles
vectorSet(11,:) = vectorSet(8,:);
for i = 1:length(vectorSet(8,:))
    if vectorSet(8,i) < 0
       vectorSet(8,i) = vectorSet(8,i)+360;
    end
end
vectorSet(9,:) = round(vectorSet(8,:));
```

```
for i = 1:length(vectorSet(9,:))-1
    if (vectorSet(9,i)>(angle-rangea)) && (vectorSet(9,i)<(angle+rangea))
       vectorSet(9,i) = vectorSet(9,i);
    else
       vectorSet(:,i) = NaN;
    end
end

% Direction Image
imshow(im,[]);
hold on;
plot(maxc1,maxr1,'.r','MarkerSize',14);
plot(maxc2,maxr2,'.b','MarkerSize',14);

for t=1:(length(vectorSet)-1)
     x = [vectorSet(4,t) vectorSet(6,t)];
     y = [vectorSet(5,t) vectorSet(7,t)];
     plot(x,y,'c','linewidth',1.2);
     hold on;
     plot(vectorSet(4,t),vectorSet(5,t),'.r','MarkerSize',14);
     plot(vectorSet(6,t),vectorSet(7,t),'.b','MarkerSize',14);
     vectorSet(10,t) = sqrt((x(2)-x(1))^2+(y(2)-y(1))^2);
end

hold off;

 adegrees = vectorSet(9,:);
 aintensity = vectorSet(10,:);
 adegplot = vectorSet(11,:);
 adegrees( :, all( isnan( adegrees ), 1 ) ) = [];
 aintensity( :, all( isnan( aintensity ), 1 ) ) = [];
 adegplot( :, all( isnan( adegplot ), 1 ) ) = [];
 asindeg = acosd(aintensity.*(1/moldist));
 aintensity = aintensity(1,1:(length(aintensity)-1));
 adegrees = adegrees(1,1:(length(adegrees)-1));
 asindeg = asindeg(1,1:(length(asindeg)-1));
 adegplot = adegplot(1,1:(length(adegplot)-1));
```